Major element diffusion in garnet and the exsolution of majoritic garnet from aluminous enstatite in Earth's Upper Mantle

Dissertation

Von der Fakultät für Biologie, Chemie und Geowissenschaften

der Universität Bayreuth

zur Erlangung der Würde

eines Doktors der Naturwissenschaften

- Dr. rer. nat. -

vorgelegt von

Willem Louis van Mierlo

Geboren in Leidschendam / die Niederlande

Bayreuth, 2011

Diese Dissertation wurde am Bayerischen Geoinstitut, Universität Bayreuth im Zeitraum von Januar 2008 bis Mai 2011 unter der Betreuung von Prof. Dr. Falko Langenhorst angefertigt.

Vollständiger Abdruck der von der Fakultät für Chemie, Biologie und Geowissenschaften der Universität Bayreuth genehmigten Dissertation zur Erlangung des Grades eines Doktors der Naturwissenschaften (Dr. rer. nat.).

Dissertation eingereicht am:	25.05.2011
Zulassung durch die Prüfungskommission:	11.07.2011
Wissenschaftliches Kolloquiem:	26.07.2011

Prüfungsausschuss:

Prof. Dr. Falko Langenhorst *(Erstgutachter)*

Prof. Dr. David Rubie *(Zweitgutachter)*

Prof. Dr. Jörgen Senker *(Vorsitz)*

Prof. Dr. Tomoo Katsura

Prof. Dr. Klaus Bitzer

Acknowledgements

I would like to thank the European Commission for providing the funding of the presented PhD project under the Marie Curie Research Training Network 'Crust to Core– the fate of subducted material' (MRTN-CT-2006-035957).

I would like to thank my supervisor during for my PhD, Falko Langenhorst, for his patience and help in teaching me, the many fruitful discussions and the invaluable feedback he gave me, which significantly improved the quality of the dissertation.

Dan Frost, David Rubie, Nobuyoshi Miyajima, Florian Heidelbach, Hans Keppler, Catherin McCammon, Guðmundur Guðfinnson and Detlef Krauße I would like to thank for their advise and instructions on using the different kinds of equipment that was used to produce results presented in this dissertation.

My scientific productivity was greatly increased by the meticulous preparation work done by Uwe Dittmann, Hubert Schulze, Stefan Übelhack and Heinz Fischer in the workshops. Their work is greatly appreciated!

Lydia Kison-Herzing, Petra Buchert, and Stefan Keyssner I thank for their help in solving administrative and other problems not directly related to my scientific work.

I would like to thank all my colleagues and friends at the Bayerisches Geoinstitut for creating a great environment to work in and the nice social life outside BGI.

I also want to thank my friends in Holland, that they are there for me and it is always nice to see them again! To conclude I would like to thank my family for all the help and support they provided through all of my life, without them I would not be where I would be now.

Table of contents

Summary

Majorite is a high pressure polymorph of enstatite with the garnet structure. The amount of enstatite that can be dissolved in garnet as a majorite component increases significantly with pressure, and therefore, majoritic garnet is thought to be a major constituent of the Earth's transition zone. The transport properties of majoritic garnet are, however, not well constrained at the moment. The magnitude of the diffusivity of the majorite component in garnet influences our understanding of the homogenization time scale of Earth's mantle. This is important in subduction zone settings, where the subducting oceanic crust will form a majorite inhomogeneity in the transition zone because of its higher aluminium content. Reaction kinetics in the dry transition zone are diffusion controlled and therefore an improved dataset on the diffusivity of the majorite component in garnet will enable us to better understand the of role of disequilibrium in subduction zones. This dissertation therefore reports the results of diffusion experiments on garnet.

Slow diffusion kinetics of the majorite component in garnet will also will hamper the dissolution of pyroxene in garnet and pyroxene will therefore be metastably preserved during subduction. Natural pyroxenes always contain aluminium, which is expected to cause exsolution of a garnet phase during subduction. Therefore, high pressure and temperature experiments have been conducted on aluminous enstatite, to simulate this process, of which the results are also presented in this dissertation.

Diffusion experiments have been conducted with diffusion couples of majoritic garnet – Dora Maira pyrope, Dora Maira pyrope and Ötztal almandine and Ötztal almandine and majoritic garnet in a multi-anvil press between 1400 – 1900 °C and 12 – 20 GPa. The diffusion experiments with the majoritic garnet – Dora Maira pyrope garnet couples show that the diffusion of the majorite component in garnet is very slow, comparable to the diffusivity of silicon in wadsleyite and ringwoodite. The activation energy, activation volume and the pre-exponential for diffusion of the majorite component in garnet were determined to be 241 ± 54 kJ mol^{-1}, 3.3 ± 0.1 cm^3 mol^{-1} and 2.3 x 10^{-7} cm2 s^{-1}, respectively. The diffusivity of the majorite component in garnet was determined to be 2-3 orders of magnitude slower than the self-diffusivity of Mg, Fe and Ca in garnet at the same conditions. Comparison with diffusion data on wadsleyite and ringwoodite shows that the diffusivity of the majorite component in garnet is very similar to that of the silicon self-diffusivity in the high-pressure polymorphs of olivine.

Another set of diffusion experiments was conducted with Ötztal almandine – majoritic garnet diffusion couples. The diffusion profiles obtained from these experiments are strongly asymmetric, and indicate that there is an increased tracer-diffusivity of Mg and Fe by one order of magnitude in majoritic garnet part of the diffusion couple. The increased diffusivity of Mg and Fe in majoritic garnet appears to be an intrinsic property of majoritic garnet, which can be explained by the fact that the octahedral sites short cut the diffusion path through the garnet structure. In almandine the octahedral sites are all occupied by aluminium, whereas in the majoritic garnet a proportion of the octahedral sites are also occupied by Mg and Fe.

To determine whether solid state diffusion can homogenize the mantle the diffusion distance of the majorite component in garnet, assuming grain boundary diffusion is the dominant diffusion mechanism, has been calculated. The results show that within the range of temperatures prevailing in the transition zone, majorite is able to diffuse 5 – 15 m on the time scale of the age of the Earth. Solid state diffusion is thus not able to homogenize the mantle.

Another important question is whether or not diffusion of the majorite component in garnet is fast enough to enable pyroxene to dissolve in garnet, thus forming majoritic garnet in the subducting oceanic slab. A finite difference code has been developed to assess this question that models diffusion in a spherical grain and diffusion controlled growth of a spherical grain. The results show that during the subduction process all pyroxene can be dissolved in garnet in the case of the lithospheric mantle part of the slab. The oceanic crust shows however a different result, due to its lower temperature, and only a small amount of pyroxene can be dissolved into garnet. Metastable phases will thus be preserved in the subducting oceanic crust during the subduction process.

Natural pyroxenes contain small amounts of aluminium. During subduction pyroxene is thought to dissolve into garnet. However, as the diffusion experiments reported in this thesis show, there is a significant delay in the dissolution of pyroxene in garnet as result of the limited diffusivity of the majorite component in garnet. Therefore, garnet will exsolve from pyroxene before pyroxene is dissolved into garnet, because the aluminium solubility in pyroxene decreases with increasing pressure. Experiments with Dora Maira pyrope – Tanzania enstatite couples have been conducted at 1700 °C and 15 GPa to simulate the process of subduction into the transition zone. The recovered samples reveal in low clinoenstatite extensive twinning on (100) and a high density of stacking faults on (100) with displacement vector R = [½ ½ w]. From crystal structure considerations one finds that *w* is most likely ½. The stacking fault plane in combination with the displacement vector can be explained by the phase transformation of HP high clinoenstatite to low clinoenstatite.

The topotactic relationship between the majoritic garnet precipitates and the low clinoenstatite host was also determined. Though there is not a unique topotactic relationship, most of the garnet precipitates have their <111> direction parallel to the [001] direction in low clinoenstatite. The lack of a unique topotactic relation is probably due to a lack of an oxygen close packing direction in garnet. The observed dominant topotactic relationship is therefore interpreted as the result of the low diffusivity of silicon and is thus a topotactic relation controlled by kinetics.

From the aluminium diffusion profiles measured in low clinoenstatite, the diffusivity of Al in high clinoenstatite was determined to be at least 6×10^{-11} cm^2 s^{-1} at 1700 °C and 15 GPa. Comparison with data in diopside shows there is a discrepancy between diffusion data at high pressure and at low pressure, which might indicate a strong dependence of Al diffusivity in clinopyroxene on Ca contents or a change in diffusion mechanism.

The results of the experiments conducted in this PhD study show that the low diffusivity of components in the Earth may severely hamper reaction kinetics in the Earth in the case where mass transport is required. To better

understand dynamics of the Earth it would therefore be useful study the role of diffusion in other phase transitions in the Earth where mass transport is required.

Zusammenfassung

Majorit ist eine Hochdruck-Modifikation von Enstatit mit Granatstruktur. Mit steigendem Druck nimmt der Enstatit-Gehalt, der als Majorit-Komponente in Granat gelöst sein kann, deutlich zu, weswegen vermutet wird, dass majoritischer Granat eine Hauptkomponente in der Übergangszone der Erde ist. Dennoch sind die Transporteigenschaften von majoritischem Granat noch nicht genau bekannt. Vom Ausmaß des Diffusionsvermögens des majoritischen Anteils in Granat hängt unser Verständnis vom zeitlichen Ablauf der Homogenisation des Erdmantels ab. Dieses spielt in Subduktionszonen eine wichtige Rolle, wo die subduzierte ozeanische Kruste aufgrund ihres höheren Aluminium-Gehalts eine Majorit-Inhomogenität in der Übergangszone bildet. Da Reaktionsabläufe in einer trockenen Übergangszone diffusionskontrolliert sind, werden verbesserte Daten über das Diffusionsverhalten der majoritischen Komponente in Granat dazu beitragen, Ungleichgewichte in Subduktionszonen besser zu verstehen. Die Ergebnisse solcher Diffusions-Experimente werden in dieser Dissertation vorgestellt.

Eine langsame Diffusion der Majorit-Komponente in Granat behindert die Auflösung von Pyroxen in Granat, wodurch Pyroxen während des Subduktionsprozesses metastabil erhalten bleibt. Natürlicher Pyroxen enthält immer Aluminium, das sich während der Subduktion als Granat-Phase entmischt. Um diesen Prozess zu simulieren, wurden Hochdruck- und Hochtemperatur-Experimente an Aluminium-reichem Enstatit durchgeführt. Die Ergebnisse werden ebenfalls in dieser Dissertation präsentiert.

Diffusionsexperimente wurden an den folgenden Diffusions-Paaren durchgeführt: (1) majoritischer Granat – Dora Maira-Pyrop, (2) Dora Maira-Pyrop und Ötztal-Almandin und (3) Ötztal-Almandin und majoritischer Granat in einer Multi-Anvil-Presse bei Temperaturen von 1400 – 1900 °C und Drücken von 12 – 20 GPa durchgeführt. Jene Experimente mit Paaren von majoritischem Granat – Dora Maira-Pyrop zeigen, dass die Diffusion der majoritischen Komponente in Granat sehr langsam vonstatten geht, vergleichbar mit dem Diffusionsvermögen von Silizium in Wadsleyit und Ringwoodit. Die Aktivitätsenergie, das Aktivitätsvolumen und der präexponentielle Faktor der Diffusion der majoritischen Komponente in Granat betragen 241 ± 54 kJ mol^{-1}, beziehungsweise 3.3 ± 0.1 cm^3 mol^{-1} und 2.3 x 10^{-7} cm^2 s^{-1}. Das Diffusionsvermögen der majoritischen Komponente in Granat ist 2 bis 3 Größenordnungen langsamer als die Selbstdiffusion von Mg, Fe und Ca in Granat unter denselben Bedingungen. Vergleiche mit den Diffusionsdaten von Wadsleyit und Ringwoodit zeigen, dass das Diffusionsvermögen der Majorit-Komponente in Granat der Selbstdiffusion von Silizium in den Hochdruck-Polymorphen von Olivin sehr ähnlich ist.

Eine weitere Reihe von Diffusionsexperimenten wurde an Diffusionspaaren von Ötztal-Almandin und majoritischem Granat durchgeführt. Die aus diesen Experimenten hervorgegangenen Diffusionsprofile sind stark asymmetrisch und belegen ein um eine Größenordnung erhöhtes Diffusionsvermögen von Spuren von Mg

und Fe im majoritischem Granat-Teil des Diffusionspaares.

Das erhöhte Diffusionsvermögen von Mg und Fe scheint eine spezifische Eigenschaft von majoritischem Granat zu sein, die dadurch erklärt werden kann, dass die oktaedrischen Plätze den Diffusionspfad durch den Granat vereinfachen. In Almandin sind alle Oktaeder-Plätze mit Aluminium besetzt, während in majoritischem Granat ein Teil dieser Plätze auch mit Mg und Fe belegt sind.

Um herauszufinden, ob der Erdmantel durch Volumendiffusion homogenisiert werden könnte, wurde, unter der Annahme, dass Diffusion an Korngrenzen der Haupt-Diffusionsmechanismus ist, die Diffusions-Strecke der Majorit-Komponente in Granat berechnet. Die Ergebnisse zeigen, dass innerhalb der in der Übergangszone vorherrschenden Temperaturen, in der Zeitspanne seit der Entstehung der Erde, die Majorit-Komponente 5 – 15 m weit diffundieren kann. Daraus folgt, dass Volumendiffusion nicht jener Prozess ist, der den Mantel homogenisiert.

Eine weitere offene Frage ist, ob die Diffusion der majoritischen Komponente in Granat schnell genug abläuft, damit Pyroxen zu Granat zerfällt und sich majoritischer Granat in der subduzierten ozeanischen Platte bildet. Um diese zu beantworten, wurde ein finiter Differential-Code entwickelt, der die Diffusion in einem runden Korn und das diffusions-kontrollierte Wachsen eines solchen Kornes modelliert. Die Ergebnisse zeigen, dass während der Subduktion des lithospärischen Mantels der ganze Pyroxen zu Granat zerfallen kann. Die ozeanische Kruste verhält sich allerdings aufgrund ihrer geringeren Temperatur anders und nur ein geringer Teil des Pyroxens kann zu Granat zerfallen. Deshalb bleiben metastabile Phasen während der Subduktion in subduzierter ozeanischer Kruste erhalten.

Natürlicher Pyroxen enthält geringe Mengen an Aluminium. Es wird angenommen, dass Pyroxen während der Subduktion zu Granat zerfällt. Allerdings zeigen die Diffusionsexperimente in dieser Dissertation, dass der Zerfall von Pyroxen zu Granat wegen des begrenzten Diffusionsvermögens der Majorit-Komponente in Granat signifikant verzögert wird.

Demnach entmischt Granat aus Pyroxen bevor Pyroxen zu Granat zerfällt, weil die Löslichkeit von Aluminium in Pyroxen mit zunehmendem Druck abnimmt. Experimente mit Dora Maira-Pyrop- und Tansania Enstatit – Paaren wurden bei 1700 °C und 15 GPa durchgeführt, um den Prozess der Subduktion bis in die Übergangszone zu simulieren. Die untersuchten Proben zeigen in Klinoenstatit erhebliche Verzwilligungen und eine große Dichte von Stapelfehlern auf (100) mit einem Verschiebungsvektor R = [½ ½ w]. Überlegungen zur Kristallstruktur ergeben, dass *w* höchstwahrscheinlich ½ ist. Die Stapelfehler-Ebene zusammen mit dem Versatz-Vektor ergibt sich durch die Phasentransformation von HP Hoch-Clinoenstatit zu Tief-Clinoenstatit.

Die topotaktische Beziehung zwischen den majoritischen Granat-Entmischungen und dem Tief-Clinoenstatit-Wirt wurde ebenfalls ermittelt. Obwohl keine einzelne topotaktische Beziehung besteht, ist die <111> Richtung des Großteils der Granat-Entmischungen parallel zur [001] Richtung im Tief-Clinoenstatit. Das Fehlen einer einzelnen topotaktischen Beziehung kann vermutlich auf das Fehlen einer dichtesten Sauerstoff-Packung in

Granat zurückgeführt werden. Die beobachtete vorherrschende topotaktische Beziehung wird somit als Ergebnis des geringen Diffusionsvermögens von Silizium interpretiert und ist daher kinetisch kontrolliert.

Das Diffusionsvermögen von Aluminium in Hoch-Clinoenstatit wurde aus den in Tief-Clinoenstatit gemessenen Aluminium – Diffusionsprofilen ermittelt. Es beträgt zumindest 6 x 10^{-11} cm^2 s^{-1} bei 1700 °C und 15 GPa. Der Vergleich mit Daten von Diopsid zeigt, dass ein Unterschied zwischen den Diffusions-Daten bei hohem und niedrigerem Druck besteht, was auf eine starke Abhängigkeit des Al-Diffusionsvermögens in Clinopyroxen von dem Ca-Gehalt oder auf eine Änderung der Diffusionsmechanismen hinweist.

Die Ergebnisse der Experimente, die im Zuge dieser Dissertation durchgeführt wurden, zeigen, dass das geringe Diffusionsvermögen einiger Komponenten die Reaktionskinetik im Inneren der Erde, vor allem dort, wo Massentransport eine bedeutende Rolle spielt, deutlich beeinträchtigen kann. Um die Bewegungsabläufe der Erde noch besser zu verstehen, wäre es sinnvoll, weitere Studien zur Diffusion in den anderen Übergangszonen, wo Massentransport vorausgesetzt wird, durchzuführen.

Samenvatting

Majoriet is een hoge druk polymorf van enstatiet met de granaat structuur. Met toenemende druk neemt de oplosbaarheid van enstatiet in granaat als majorietcomponent sterk toe. Als gevolg hiervan wordt verwacht dat majoritische granaat een van hoofdbestanddelen van de overgangszone van de Aarde is. De transporteigenschappen van majoritische granaat zijn op het moment echter niet goed vastgesteld. De grootte van de diffusiviteit van de majorietcomponent in granaat beïnvloed ons begrip van de tijdschaal waarop de Aardmantel gehomogeniseerd kan worden. Dit speelt in subductiezones een grote rol, waar vanwege zijn hogere aluminium concentratie, de gesubduceerde oceanische korst in de overgangszone een majoriet-inhomogeniteit zal vormen. De reactiekinetiek in de droge overgangszone van de Aarde is bovendien door diffusie gecontroleerd en daarom zal een verbeterde dataset met the diffusiviteit van de majorietcomponent in granaat ons een beter begrip verschaffen over de rol van chemisch non-evenwicht in subductiezones. Deze dissertatie rapporteert daarom over de resultaten van diffusie experimenten met granaat.

Indien de diffusiekinetiek van de majorietcomponent in granaat traag is, zal dit ook de snelheid waarmee pyroxeen in granaat oplost negatief beïnvloeden. Pyroxeen kan daardoor gedurende subductie metastabiel bewaard blijven. Natuurlijke pyroxenen bevatten altijd een kleine hoeveelheid aluminium, waarvan verwacht wordt dat het ontmengt uit pyroxeen als een granaat fase gedurende subductie. Derhalve zijn er ook hoge druk en temperatuur experimenten uitgevoerd op aluminium bevattende enstatiet om dit proces te simuleren, waarvan de resultaten ook gepresenteerd worden in deze dissertatie.

Diffusie-experiment zijn gedaan met diffusiekoppels van (1) majoritische granaat – Dora Maira pyroop, (2) Dora Maira pyroop – Ötztal almandien en (3) Ötztal almandien – majoritische granaat in een multi-anvil-pers tussen 1400 – 1900 °C en 12 – 20 Gpa. De diffusie-experimenten met de majoritische granaat – Dora Maira pyroop koppels laten zien dat de diffusie van de majorietcomponent in granaat zeer traag is, vergelijkbaar met de

diffusiviteit van silicium in wadsleyiet en ringwoodiet. De activatie-energie, het activatievolume en de pre-exponent voor diffusie van de majorietcomponent in granaat zijn respectievelijk vastgesteld op 241 ± 54 kJ mol^{-1}, 3.3 ± 0.1 cm^3 mol^{-1} en 2.3×10^{-7} cm^2 s^{-1}. De diffusiviteit van de majorietcomponent in granaat blijkt 2 – 3 orden van grootte kleiner te zijn als de interdiffusie van Mg, Fe en Ca in granaat onder de zelfde omstandigheden.

Een andere serie diffusie-experimenten is uitgevoerd op Ötztal almandien – majoritische granaat diffusiekoppels. De verkregen diffusieprofielen van deze experimenten zijn sterk asymmetrisch en duiden op een met één orde van grote toegenomen zelfdiffusiviteit van Mg and Fe in het majoritische granaat gedeelte van het diffusiekoppel. De toegenomen diffusiveit van Mg en Fe in majoritische granaat blijkt een intrinsieke eigenschap van majoritische granaat zelf te zijn, welke verklaard kan worden door het feit dat de octaëdrische rooster posities het diffusiepad door de granaat structuur afsnijden. In almandien zijn deze posities bezet door aluminium, in tegenstelling tot in majoritische granaat waar deze posities ook bezet worden door Mg en Fe.

Om te bepalen of volumediffusie de mantel kan homogeniseren is de diffusie-afstand van de majorietcomponent in granaat berekend, ervan uitgaande dat het massatransport overwegend plaats vindt door middel van diffusie door de korrelgrenzen. De resultaten laten zien dat, binnen het temperatuurbereik van de overgangszone, de majoriet component 5 – 15 m kan diffunderen over een tijdbestek gelijk aan de ouderdom van de Aarde. Volumediffusie is dus niet in staat de Aardmantel te homogeniseren.

Een andere belangrijke vraag is die of de diffusie van de majorietcomponent in granaat snel genoeg is zodat pyroxeen volledig in granaat kan oplossen gedurende de subductie van de oceanische plaat in de overgangszone, alwaar het majoritische granaat zal vormen. Hiertoe is een eindige-differentiemethode code ontwikkeld die de diffusie in een bolvormige korrel en de door diffusie gecontroleerde groei van een bolvormige korrel simuleert. De resultaten wijzen uit dat gedurende het subductieproces alle pyroxeen in granaat opgelost kan worden in het lithosferische mantelgedeelte van de subducerende plaat. De oceanische korst laat echter een ander resultaat zien, vanwege zijn lagere temperatuur. Enkel een klein gedeelte van de pyroxeen kan opgelost worden in granaat, metastabiele fasen zullen dus achterblijven in de gesubduceerde oceanische korst gedurende het subductieproces.

Tijdens de subductie wordt verwacht dat pyroxeen oplost in granaat. De resultaten van de diffusie-experimenten in deze dissertatie laten echter zien dat er een aanzienlijke vertraging is in het oplossen van pyroxeen in granaat als gevolg van de lage diffusiviteit van de majorietcomponent in granaat. Aangezien natuurlijke pyroxenen een kleine hoeveelheid aluminium bevatten, wordt verwacht dat granaat zich ontmengt uit pyroxeen voordat pyroxeen volledig in granaat oplost als gevolg van de afnemende oplosbaarheid van aluminium in pyroxeen met toenemende druk. Experimenten met Dora Maira pyroop – Tanzania enstatiet koppels zijn uitgevoerd bij 1700 °C en 15 GPa, om het subductieproces van pyroxenen te simuleren in overgangszone. In het pyroxeengedeelte van de monsters worden na het experiment door het gehele monster kristallografische tweelingen op (100) en stapelfouten op (100) met een verplaatsingsvector R = [½ ½ w]

waargenomen. Gebaseerd op de kristalstructuur kan worden uitgegaan van dat *w* hoogstwaarschijnlijk ook gelijk is aan ½. De combinatie van de stapelfoutvlakken en verplaatsingsvector kan worden verklaard door de faseovergang van de hoge druk vorm van hoog-clinoenstatiet naar de laag-clinoenstatiet.

De topotactische relatie tussen de ontmengde majoritische granaat en de laag-clinoenstatiet gastheer is ook bepaald. Alhoewel er geen unieke topotactische relatie is gevonden, hebben de meeste ontmengde granaatkristallen hun <111> richting parallel aan de [001] richting in de laag-clinoenstatiet gastheer. Het gebrek aan een unieke topotactische relatie is waarschijnlijk te wijten aan het afwezig zijn van een zuurstof-dichte-stapeling-richting in granaat. De waargenomen overwegende topotactische relatie is daarom geïnterpreteerd als het resultaat van de lage diffusiviteit van silicium en is daarom gecontroleerd door kinetiek.

Door middel van het meten van diffusieprofielen van aluminium in laag-clinoenstatiet is een Al-diffusiviteit in hoge druk hoog-clinoenstatiet vastgesteld van tenminste 6×10^{-11} cm^2 s^{-1} bij 1700 °C en 15 GPa. Een vergelijk met aluminium diffusiedata in diopsied duidt op een tegenstrijdigheid in de diffusiedata tussen Al diffusie onder hoge druk en onder lage druk in clinopyroxeen. Dit kan mogelijk duiden op een sterke Ca afhankelijkheid van de Al diffusiviteit in clinopyroxeen of een verandering in het diffusiemechanisme.

De resultaten van de experimenten uitgevoerd voor deze dissertatie laten zien dat de trage diffusie van (chemische) component in de Aarde de reactiekinetiek, vooral in het geval waar massatransport noodzakelijk is, sterk negatief kan beïnvloeden. Een beter begrip van de dynamica van de Aarde kan daarom profiteren van verdere studies naar de rol van diffusie in andere faseovergangen in de Aarde waar massatransport noodzakelijk is en zulke studies worden daarom aangeraden naar aanleiding van de resultaten in deze dissertatie.

Chapter 1:Introduction

The studies on phase relations in the Earth's mantle during the last six decades have shown that olivine and its high pressure polymorphs, pyroxene and garnet are probably the most important phases in the Earth's upper mantle (Frost 2008). In the Earth's transition zone, between 410 – 660 km depth, a super-silicic and aluminium-deficient form of garnet, majoritic garnet, is thought to be the second most abundant phase after the high pressure polymorphs of olivine, constituting about 40 vol. % of the transition zone (Frost 2008). Majorite, the $Mg_4Si_4O_{12}$ end-member of this super-silicic and aluminium-deficient garnet is a high pressure polymorph of enstatite. Because the coeanic crust is aluminium enriched and consist mainly of pyroxenes at near surface conditions, it may even consist for up to 90 vol. % of garnet in the transition zone (Irifune and Ringwood 1993). Clearly majoritic garnet is thus a major phase in the Earth's upper mantle and transition zone. Most major element diffusion studies have however concentrated on olivine and its high pressure polymorphs in the upper mantle and transition zone. Very few diffusion data is available on diffusion in garnets or pyroxenes at the conditions in the deeper upper mantle and the transition zone. This PhD study tries to address this lack of data, at least to some extent, and will discuss the implications of diffusion control on phase transitions that occur in subduction zones in the deeper upper mantle and transition zone.

Because reaction and diffusion kinetics can strongly influence the phase relations in a dynamic setting, a review will be given in this chapter on the different studies that have been performed on phase relations in the earth's upper mantle and transition zone, and diffusion and reaction kinetics in Earth's mantle. Finally the goals of the PhD are explained in more detail. The next chapter will present some general information about garnet and majorite, and the presence of majoritic garnet remnants in UHP terranes. Chapter three focuses on the experimental and analytical methods used in this PhD study. Chapter four will explain the numerical models used to simulate the diffusion profiles obtained from the diffusion experiments and to model the dissolution of pyroxene into garnet. Chapter five presents the results on the garnet diffusion experiments. Finally, chapter six presents the results on the aluminous enstatite experiments.

1.1 Phase relations in the Earth's Transition Zone

Rock suites representative of Earth's mantle that are exposed on Earth's surface are relatively scarce and generally are not of primary origin, i.e. they are usually secondary and reworked rock samples (Wilson 2007). Xenoliths found in kimberlite pipes sample the Earth's mantle at depths of 150 kilometres and greater, i.e. in the diamond stability field. These xenoliths usually consist of peridotites, i.e. an assemblage consisting of olivine + orthopyroxene + clinopyroxene + an aluminium bearing phase, which show evidence for varying amounts of melt extraction (Gurney and Harte 1980, Nixon et al. 1981). Ringwood (1962) proposed a hypothetical mantle composition named pyrolite (table 1.1), which is a mixture of 4 parts dunite, a peridotite consisting of almost purely olivine, and 1 part basalt. The addition of basalt accounts for the depletion due to partial melting of the primitive mantle. The ratio of dunite to basalt is chosen such that the major element composition of the inferred

pyrolitic mantle composition matches that of chondritic meteorites (Wilson 2007). A pyrolite composition has often been used in phase equilibrium studies pertaining to Earth's mantle.

The pyrolite composition is a relative complex composition with many oxides. This complicates the determination of phase relations by experimental studies, and the interpretation of the results. Therefore experimental studies have usually been performed on simplified systems in the past. Table 1.1 shows that the oxides SiO_2 and MgO compose about 83% of the pyrolite composition. The system MgO – SiO_2 is therefore essential in understanding the phase relations in the Earth's transition zone. Forsterite (olivine Mg_2SiO_4) is the most abundant phase in the Earth's upper mantle. Ringwood (1956) proposed that forsterite has an olivine to spinel transition around 520 kilometres depth, based upon the solubility of forsterite in Ni_2GeO_4, which has a spinel structure. The pressure of the olivine – spinel transition was subsequently determined experimentally in the Mg_2SiO_4 – Fe_2SiO_4 system. Early studies generally focussed on the fayalite (Fe_2SiO_4) rich side of the olivine solid solution, where olivine directly transforms to a spinel structured polymorph called ringwoodite (Akimoto and Fujisawa 1966, Ringwood and Major 1966, 1970). The forsterite end of the olivine solid solution series however first transforms to a different polymorph with a modified spinel structure, called wadsleyite, before transforming to ringwoodite (Ringwood and Major 1970, Akaogi et al. 1989, Katsura and Ito 1989). The phase diagram at 1600 °C at upper mantle and transition zone pressures of the Mg_2SiO_4 – Fe_2SiO_4 join is shown in figure 1.1.

Half way the MgO – SiO2 join the mineral enstatite ($Mg_2Si_2O_6$) is located. At pressures up to ~ 8.5 GPa enstatite has the orthopyroxene structure (orthoenstatite, Pbca space group), above which it transforms to a clinopyroxene structure (HP high-clinoenstatite, space group C2/c) (Kanzaki 1991, Angel et al. 1992, Angel and Hugh-Jones 1994). The substitution of Mg^{2+} by a crystal field stabilizing cation like Fe^{2+} or Cr^{2+} significantly lowers the transformation of orthoenstatite to HP high-clinoenstatite (Arlt et al. 1998). Above ~ 17 GPa and 1600 °C high-clinoenstatite transforms to an $MgSiO_3$ polymorph with a garnet structure called majorite (Kato and Kumazawa 1985, Gasparik 1989). Majorite garnet forms a solid-solution with the other natural aluminosilicate garnets found in Earth's mantle. Since majorite is a high pressure polymorph of (ortho)pyroxene, significant amounts of pyroxene can be dissolved in garnet as majorite component at pressures above 10 GPa. The solubility of this majorite component in garnet increases with increasing pressure (Akaogi and Akimoto 1977, Gasparik 2003). For a pyrolite composition this means that in the transition zone all the pyroxene will be dissolved in garnet as majorite component (Irifune 1987,

Table 1.1: Pyrolite composition, after Green and Ringwood (1970).

Oxide	**Wt. %**
SiO_2	45.20
TiO_2	0.71
Al_2O_3	3.54
Cr_2O_3	0.43
Fe_2O_3	0.48
FeO	8.04
MnO	0.14
NiO	0.20
MgO	37.48
CaO	3.08
Na_2O	0.57
K_2O	0.13

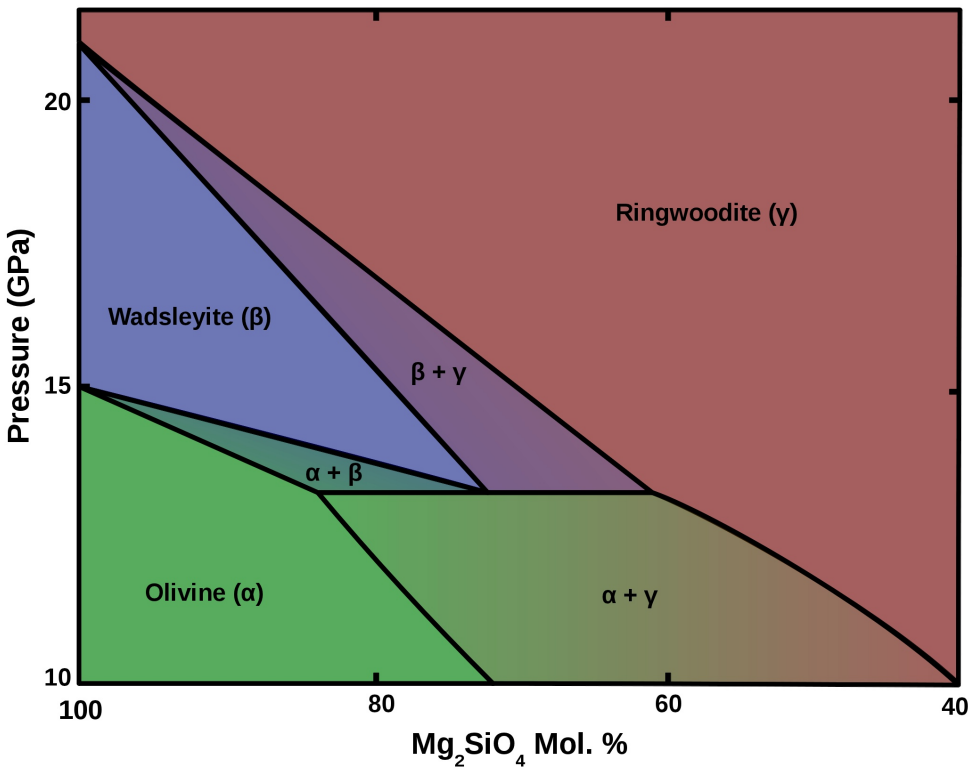

Figure 1.1: Phase diagram of the $Mg_2Si_2O_4$ – Fe_2SiO_4 join at 1600 °C. Modified after Katsura and Ito (1989).

Frost 2008), making majoritic garnet the second most abundant phase in the transition zone after the high pressure polymorphs of olivine, wadsleyite and ringwoodite (figure 1.2).

The mineralogy of the bulk part of Earth's mantle can be described by the system CaO – MgO – Al_2O_3 – SiO_2 (CMAS-system). Iron mainly exchanges with magnesium and therefore affects the size of the stability fields of the phases involved and the depth range over which phase transition occurs (Akaogi et al. 1989, Katsura and Ito 1989, Frost 2003). The presence of iron generally does not lead to the appearance of new phases. The addition of CaO and Al_2O_3 to the system leads to the stability of clinopyroxene and garnet at lower pressures. High pressure experiments in the CMS-system have shown that the HP high-clinoenstatite phase mentioned above, however, does not form a solid-solution with the diopside ($CaMgSi_2O_6$) rich clinopyroxenes stable at lower pressure and are thus two distinct phases (Gasparik 1990). The mutual solubility of HP-clinoenstatite and the clinopyroxene jadeite ($NaAlSi_2O_6$) is significantly higher, however in the transition zone the solubility of jadeite in HP-clinoenstatite is also reduced to virtually zero (Gasparik 1989, 1990).

The breakdown of diopsidic clinopyroxene above 17 – 18 GPa (figure 1.3) results in the formation of a majorite rich garnet ($En_{80}Di_{20}$ when the composition is expressed as pyroxene end-members) in equilibrium with calcium perovskite at temperatures above 1400 °C, and the formation of a calcium perovskite + stishovite + wadsleyite / ringwoodite below 1400 °C. The calcium content of the garnet phase is however strongly dependent on temperature and pressure and increases with increasing temperature and decreasing pressure (Canil 1994, Oguri et al. 1997). Gasparik (1989, 1990) observed the formation of a new non-quenchable phase as breakdown product of diopside with a close to diopside stoichiometry at pressures above 14 GPa, which is however not confirmed by other studies and no crystal structure determination of this new phase was attempted by the

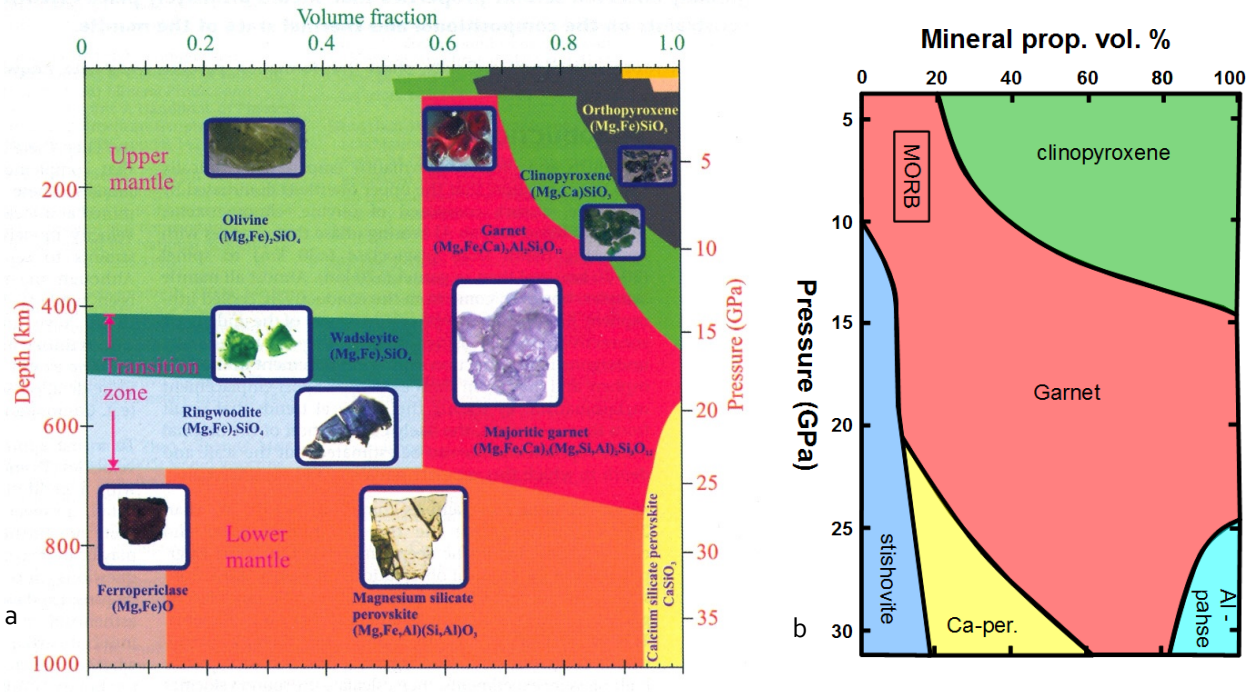

Figure 1.2: a) Mineralogy of the mantle assuming a pyrolite composition (Frost 2008) and b) a MORB composition, the subducted oceanic crust (Irifune & Ringwood 1993), as function of pressure.

authors.

Similar breakdown to garnet at high temperatures and pressures is observed for sodium bearing pyroxenes. On the jadeite – enstatite joint at 1650 °C, pure jadeite transforms to a garnet structure above 21 GPa (Gasparik 1990).The sodium atom is incorporated in a dodecahedral site and the additional silicon atom is incorporated in an octahedral site (Ringwood and Major 1971). Liu (1978) however, showed that at lower temperatures (1000 °C) jadeite disproportionates to stishovite + calcium-ferrite structured $NaAlSiO_4$ above 24 GPa. The stability of garnets with a calcic and sodic clinopyroxene stoichiometry at high pressure and temperature indicates that, like enstatite, the major rock-forming clinopyroxene end-members diopside and jadeite can be dissolved into garnet in the transition zone, also bearing in mind that calcium can be incorporated in garnet as a grossular component. Since MORBs have a relative high aluminium, calcium and sodium content, this has important consequences for the subducted oceanic crust in the transition zone. Irifune and Ringwood (1986) and Irifune et al. (1993) performed high-pressure experiments in a multi-anvil press on materials with a MORB composition, of which the oceanic crust is made. These experiments showed that virtually all pyroxene will be dissolved into garnet in the transition zone, forming a garnetite assemblage consisting of ~ 90 vol. % of garnet between 15 GPa and 20 GPa (figure 1.2). Garnet at these conditions have a strong majorite component (up to ~ 40%). At pressures above 21 GPa (at 1200 °C) majoritic garnet starts to exsolve its $Ca_4Si_4O_{12}$ component as calcium perovskite. At pressures above ~25 GPa an Al-rich phase with a calcium-ferrite structure starts to exsolve from garnet (Irifune and Ringwood 1993, Hirose et al. 1999). At ~ 27 GPa the remaining majoritic garnet transforms to Mg-perovskite (Hirose et al. 1999, Ono et al. 2001). In the subducted oceanic crust, majoritic garnet is thus a dominant phase between 15 GPa and 27 GPa.

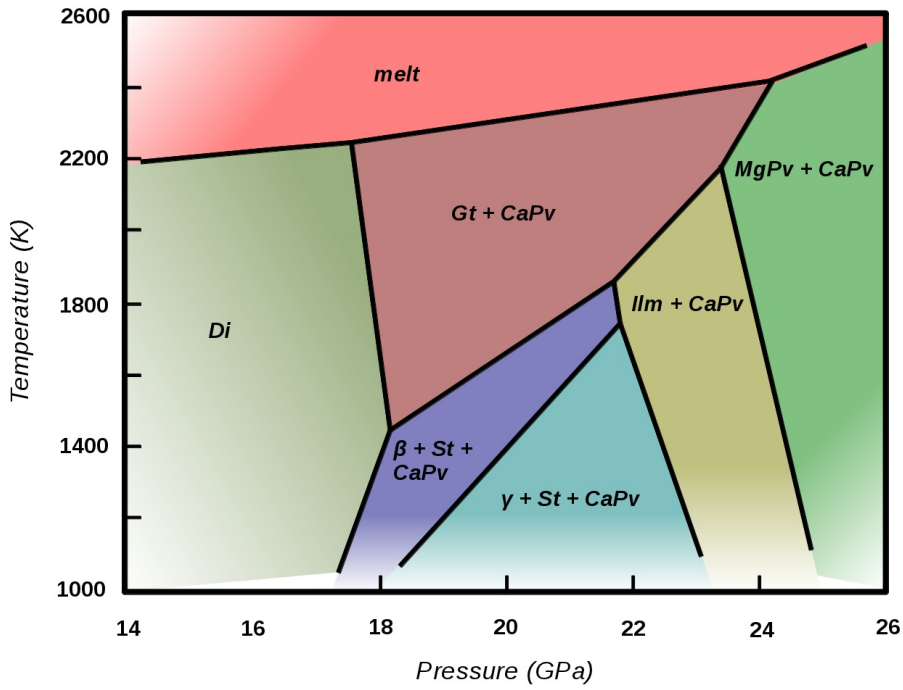

Figure 1.3: Phase diagram of diopside showing the breakdown above ~ 18 GPa. After Oguri et al. (1997).

1.2 Diffusion kinetics of the major elements in Earth's mantle

The diffusion of atoms in minerals control a number processes in the Earth's interior and properties of the Earth in which geologists are interested in. Among these are the reaction kinetics during phase transformations, especially when they require long-range transport of the components (Putnis 1992), order – disorder phase transitions (Sipling and Yund 1973, Carpenter 1982), re-equilibration of metamorphic assemblages and its geothermo-barometric applications (Lasaga 1983, Lasaga and Jiang 1995), geochronology (Dodson 1973) and rheology of phases in the Earth's interior (Weertman et al. 1978, Poirier 1985). This section will give a short review of diffusion data on minerals relevant to the Earth's mantle.

1.2.1 Olivine

As already pointed out above, olivine is the most abundant phase in Earth's upper mantle. It has therefore been the focus of a great number of studies. Buening and Buseck (1973) and Misener (1974) performed pioneering work on the interdiffusion of magnesium and iron in olivine. They showed that diffusion in this system is highly asymmetric and diffusion down the c-axis in olivine is up to one order of magnitude faster than down the a- or b-axis. The highly asymmetric profiles indicated that the iron content is of great influence on the Mg-Fe interdiffusivity in olivine. Buening and Buseck (1973) argued therefore, that the increased interdiffusivity can be attributed to a vacancy process where the oxidation of iron in the olivine structure introduces extrinsic vacancies and thereby increases the Mg-Fe interdiffusivity in olivine. This was also later confirmed by other studies, where vacancy concentrations in olivine as function of oxygen fugacity were determined (Nakamura and Schmalzried 1983, Tsai and Dieckmann 2002) and where the Fe-Mg interdiffusivity as function of oxygen fugacity was observed to increase in a similar way as the vacancy concentrations (Chakraborty 1997, Dohmen et al. 2007).

Buening and Buseck (1973) also found a change in slope in the $\log_{10} D_{Fe\text{-}Mg}$ vs. reciprocal temperature plot around 1125 °C and mentioned that a change in Fe-Mg interdiffusion mechanism in olivine, from an extrinsic mechanism at low temperatures to an intrinsic mechanism at high temperatures, might cause such a kink. A (tentatively interpreted) similar intrinsic – extrinsic transition has been observed for Co – Mg interdiffusion in olivine at 1300 °C by Morioka (1980). The interpretation as intrinsic – extrinsic diffusion regime transition of the observed kink transition has been contested by Chakraborty (1997), who claimed that the kink observed by Buening and Buseck (1973) was probably due to the setup of their experiments. A more recent study, where the oxygen was more carefully controlled, showed that a transition from one extrinsic to a different extrinsic mechanism was present at an oxygen fugacity of 10^{-10} Pa and 900 °C. At lower oxygen fugacities Fe-Mg interdiffusion is independent of the oxygen fugacity, whereas at high oxygen fugacities Fe-Mg interdiffusion becomes dependent on oxygen fugacity. There is also a slight increase in the activation energy for Fe-Mg interdiffusion from ~201 kJ mol^{-1} in the fO_2 dependent regime to ~ 220 kJ mol^{-1} in the fO_2 independent regime (Dohmen and Chakraborty 2007, Dohmen et al. 2007).

Diffusion studies have also been of interest because they shed more light upon the rheological properties of the materials of Earth's mantle. The two deformation mechanism that are deemed to be the most important in the Earth's mantle, i.e. dislocation creep and diffusion creep, are both controlled by the diffusivity of the mineral constituents (Ranalli and Fischer 1984, Ranalli 2001). The slowest diffusing species, usually oxygen or silicon in silicates, will then control the rheological properties. Therefore, a number of experiments have been performed in the past on the oxygen and silicon diffusivity in olivine.

Jaoul et al. (1980) performed diffusion experiments determining the oxygen self diffusivity in forsterite. They determined the oxygen self-diffusivity to be 5 order of magnitude slower than that of Mg-Fe interdiffusion at the 1500 K and room pressure. They also showed, that for iron-free forsterite, the oxygen self-diffusivity is independent of the oxygen fugacity. Houlier et al. (1988) performed silicon and oxygen tracer-diffusion experiments at 1300 °C at a pO_2 ranging from 10^{-4} Pa to 10 Pa in a natural San Carlos olivine crystal. Although they were not able to determine whether there was a dependence of silicon and oxygen tracer-diffusivity on the oxygen fugacity or not, they showed that silicon is the slowest diffusing cation in natural olivine, about 1 – 2 orders of magnitude slower than oxygen. A comparison of the different studies that have been performed on natural olivines, shows that the activation energy for diffusion of oxygen in olivine, ~300 – 320 kJ mol^{-1} (Jaoul et al. 1980, 1983, Gérard and Jaoul 1989), only Ryerson et al. (1989) produced at lower activation energy of 266 kJ mol^{-1}, is higher than that of Fe-Mg interdiffusion which is ~200 – 220 kJ mol^{-1} (Misener 1974, Chakraborty 1997, Dohmen et al. 2007). Houlier et al. (1990) measured an activation energy for silicon self-diffusion of 291 kJ mol^{-1}, whereas Dohmen et al. (2002b) determined the activation energy for silicon self-diffusion to be 531 kJ mol^{-1}. The latter ascribes the relative low activation energy of Houlier et al. (1990) to the fact that diffusion profiles for silicon diffusion in olivine are very short and close to the limits of instrumental precision and analyses, which causes an apparent broadening of the diffusion profiles. Dohmen et al. (2002) took this into account in their study, which would give a similar activation energy otherwise. The results from Dohmen et al. (2002)

correspond better to experimental deformation data on olivine (Mei and Kohlstedt 2000, Karato and Jung 2003).

Except for Misener (1974), the previously mentioned experiments were all conducted at room pressures. Clearly, since diffusivity is generally pressure-dependent, it can not be simply assumed that these diffusion coefficients are representative for the Earth's interior, where pressure are in the GPa range. The activation volume for Fe-Mg interdiffusion in olivine was determined by several authors to be ~5.0 – 5.5 $cm^3\ mol^{-1}$ (Misener 1974, Farber et al. 2000, Holzapfel et al. 2007). This value corresponds well to the value for Mg tracer diffusion in olivine (~ 5 $cm^3\ mol^{-1}$) calculated using atomistic modeling by Béjina et al (2009). The group around Jaoul (Bertran-Alvarez et al. 1992, Jaoul et al. 1995) and Chakraborty et al. (1999) determined lower activation volumes for Fe-Mg interdifusion, however the interdiffusion data by the Jaoul group is anomalously high (Dohmen et al. 2007) and the data by Chakraborty et al (1999) was obtained using misaligned crystals in the diffusion couples, which gave an apparent reduction in the Fe-Mg interdiffusivity at high pressures (Holzapfel et al. 2007).

In contrast to Fe-Mg interdiffusion in olivine at high pressure, high pressure data on silicon is rather scarce and on oxygen is absent. The effect of pressure on the tracer diffusivity of silicon in olivine was studied by Béjina et al (1997, 1999). Their results indicated that the activation volume for silicon tracer-diffusion in olivine is negligible. Figure 1.4 displays the magnitude of the different ionic diffusivities in olivine.

1.2.2 High pressure polymorphs of olivine

Because wadsleyite and ringwoodite compose ~60 vol. % of the Earth's transition zone, they have been the focus of several studies. Chakraborty et al (1999) conducted Fe-Mg interdiffusion experiments on diffusion couples consisting of olivine couples and wadsleyite couples. Their results indicated that Fe-Mg interdiffusion in wadsleyite is roughly 2 orders of magnitude faster than in olivine. This observation was confirmed by Farber et al (2000) in their experiments, who already observed a similar phenomenon on the Mg_2SiO_4 – Ni_2SiO_4 joint earlier, where Mg-Ni interdiffusion in the high pressure phases where observed to be three orders of magnitude faster than in the olivine phase (Farber et al. 1994). Kubo et al. (2004), however, expressed concerns about the effect of water in wadsleyite, since it greatly enhances the Fe-Mg interdiffusivity and wadsleyite is known to have a high water solubility (Inoue et al. 1995, Kohlstedt et al. 1996). Holzapfel et al. (2009) performed more diffusion experiment on nominally dry wadsleyite and showed that when one takes into account the effect of fO_2, fH_2O and iron contents of olivine and wadsleyite in the two phase region in the transition zone,the Fe-Mg interdiffusivity is expected to be 7 orders of magnitude faster in wadsleyite than in olivine. In the same study they also combined all data published on Fe-Mg interdiffusion in wadsleyite to calculate an activation 229 kJ mol^{-1}, which is similar to that for olivine, and an activation volume of 13.9 kJ mol^{-1}, significantly greater than that for olivine. In their diffusion experiments Farber et al. (2000) simultaneously determined the Fe-Mg interdiffusivity of olivine, wadsleyite and ringwoodite. They showed that the Fe-Mg interdiffusivity is very similar in wadsleyite and ringwoodite. Because of the great similarity between both structures, this is in line with expectations.

The silicon and oxygen self-diffusivity in wadsleyite have been determined by Simojuku et al. (2004, 2009). Comparison with Fe-Mg interdiffusion in wadsleyite data (Holzapfel et al. 2009) shows that like in olivine, diffusion of silicon and oxygen in the high pressure polymorphs of olivine is 5 – 6 orders of magnitude slower than Fe-Mg interdiffusion (figure 1.4). They determined an activation enthalpy for diffusion in olivine of 291 kJ mol^{-1} and 409 kJ mol^{-1} for oxygen and silicon, respectively. This difference in activation enthalpy for diffusion between oxygen and silicon leads to a change of silicon being the slowest diffusing species below 1800 °C to oxygen being the slowest diffusing species above 1800 °C at 16 GPa. In their experiments they were also able to determine the grain boundary diffusivity of silicon and wadsleyite. Their results show that grain boundary is 4 – 5 orders of magnitude faster than volume diffusion at the experimental conditions. The activation energies for grain boundary diffusion they determined to be for silicon ~ 80 kJ mol^{-1} lower than that for volume diffusion in both wadsleyite and ringwoodite and for oxygen to be 50 kJ mol^{-1} smaller in wadsleyite and 120 kJ mol^{-1} smaller in ringwoodite than for volume diffusion.

1.2.3 Perovskite ($MgSiO_3$)

Magnesium-silicate perovskite (hereafter perovskite) is the dominant phase in the lower mantle, where it constitute ~ 80 % of the total volume(Fiquet 2001). Therefore it will control to a large extent the rheological

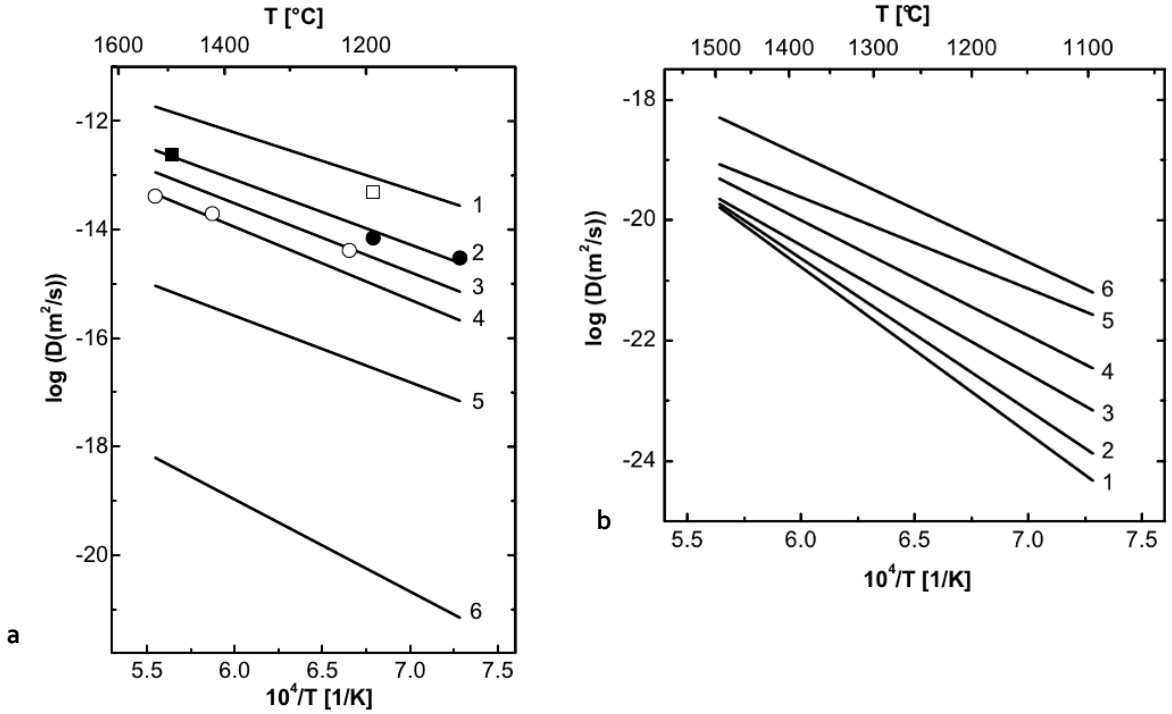

Figure 1.4 : a) Iron – magnesium interdiffusivity in wadsleyite and olivine. (1) wadsleyite 13 GPa (Holzapfel et al. 2009) (2) wadsleyite15 GPa (Holzapfel et al. 2009) (3) wadsleyite 16 GPa (Holzapfel et al. 2009) (4) wadsleyite 17 GPa (Holzapfel et al. 2009) (5) olivine 1 atm (Dohmen et al. 2007) (6) olivine 15 GPa (Holzapfel et al. 2009; Dohmen et al. 2007), open circle: Kubo et al. (2004), solid circle:Chakraborty et al. (1999), open square: Farber et al. (2000), solid square: Holzapfel et al. (2009) b) Oxygen and silicon diffusion in olivine and its high pressure polymorphs. (1) Si, olivine 1 atm (Dohmen, Chakraborty, et al. 2002) (2) Si, ringwoodite 22 GPa (Shimojuku et al. 2009) (3) Si, wadsleyite 16 GPa (Shimojuku et al. 2009) (4) O, ringwoodite 22 GPa (Shimojuku et al. 2009) (5) O, wadsleyite 16 GPa (Shimojuku et al. 2009) (6) O, olivine 1 atm (Dohmen, Chakraborty, et al. 2002). After Chakraborty (2010).

properties of the lower mantle. Since perovskite is only stable at high pressures (above ~ 22 GPa), conducting diffusion experiments on perovskite is challenging and experimentally reported diffusion coefficients are scarce. Yamazaki et al. (2000) were the first to report on silicon self-diffusion in perovskite. They determined that the activation enthalpy for silicon self-diffusion in perovskite is ~ 336 kJ mol^{-1}, which for silicon is a rather low value considering that the experiments were conducted at 25 GPa. The nature of their experiments also made it possible to determine the grain boundary diffusivity of silicon, showing that it was ~4 order of magnitude faster than volume diffusion. The activation enthalpy for grain boundary diffusion was determined to be very similar to the activation enthalpy for volume diffusion, implying that grain boundary diffusion may play an important role independent of temperature.

Holzapfel et al. (2005) measured the Fe-Mg interdiffusivity in perovskite between 22 GPa and 26 GPa between 1700 °C and 2000 °C. They determined that the Fe-Mg interdiffusion coefficient is three orders of magnitude slower than in olivine at 12 GPa and is of the same order magnitude as that of silicon self-diffusion reported by Yamazaki et al. (2000). This is a rather surprising result, since in the other dominant phases present in the Earth's interior, Fe-Mg interdifussion is several orders of magnitude faster than silicon self-diffusion. In the same study they also determined the activation enthalpy for Fe-Mg interdiffusion in perovskite to be ~414 kJ mol^{-1}, which is slightly greater beyond experimental error than that for silicon self-diffusion.

Dobson et al. (2008) performed silicon and oxygen tracer-diffusion experiments similar to the experiments from Yamazaki et al. (2000). For silicon, they basically confirmed the tracer-diffusivities measured by Yamazaki et al. (2000). The oxygen diffusivity was determined to be about two orders of magnitude faster than silicon diffusion, although it has a rather larger activation enthalpy for oxygen diffusion of ~500 kJ mol^{-1}, which is significantly greater than the activation enthalpy for Si determined by Yamazaki et al (2000). Due to the relative large errors on the diffusion coefficients for both Fe-Mg interdiffusion (Holzapfel et al. 2005) and oxygen diffusion (Dobson et al. 2008) it is not possible to determine whether the activation enthalpy of one is greater than the other.

Due to the difficulties in conducting experiments at high pressures it is generally very difficult to measure accurate activation volumes for diffusion in perovskite. People have therefore resorted to atomistic methods the determine the diffusivity of the major elements in perovskite. Earlier atomistic studies were able to calculate migration enthalpies of magnesium and oxygen reasonably well, when diffusion in the extrinsic regime was assumed for magnesium diffusion and either the intrinsic and extrinsic regime for oxygen diffusion (Wright and Price 1993, Dobson 2003, Karki and Khanduja 2007, Dobson et al. 2008). They failed however in reproducing the migration enthalpy for silicon diffusion. Ammann et al. (2009) performed a more thorough search for the silicon saddle point, which defines the activation energy for diffusion. They found a more reasonable value for the activation enthalpy for silicon diffusion of about 453 kJ mol^{-1}, at 26.2 GPa. Ito and Torumi (2010) took a different approach using molecular dynamics simulation that does not make any assumptions about the location of the saddle point and obtained an activation enthalpy at 25 GPa for silicon diffusion in perovskite of ~ 332 kJ mol^{-1}, though their simulation were performed at temperatures (~ 3900 °C –

5600 °C) well above the Earth's geotherm. The activation volumes for silicon diffusion in perovskite determined by the above mentioned atomistic studies are usually below 3.5 $cm^3\ mol^{-1}$ at lower mantle conditions and decreases with increasing pressure. Activation volumes for magnesium diffusion are slightly higher than those for silicon diffusion.

It can thus be concluded that Fe-Mg interdiffusion is anomalously sluggish in perovskite, and it might be the rate limiting process in deformation during diffusion creep or dislocation creep. In this case there might be a strong dependence of the rheological properties of the lower mantle on the oxygen fugacity, since the number of iron and magnesium vacancies is usually dependent on the oxidation state of the mantle.

1.2.4 Magnesiowüstite

Magnesiowüstite or ferropericlase $(Mg,Fe_{1-x})O$ is the second most abundant phase in Earth's lower mantle, constituting about 20 vol.% of the lower mantle. Though not the most abundant phase in the lower mantle, as a weak phase it may still play a significant role in determining the rheological behaviour of the lower mantle (Stretton et al. 2001, Heidelbach et al. 2003). Again the mobility and thus diffusivity of iron, magnesium and oxygen in magnesiowüstite will play an important role in determining the rheological properties of this mineral.

As with the other previously mentioned minerals Mg-Fe interdiffusion profiles in magnesiowüstite are usually highly asymmetric (Rigby and Cutler 1965, Blank and Pask 1969, Mackwell et al. 2005). This is no surprise, as wüstite is one of the classical examples exhibiting non-stoichiometry due to oxidation of divalent iron. Though the earlier study by Rigby and Cutler (1965) showed no dependence of the activation energy for Fe-Mg interdiffusion in magnesiowüstite on iron content, Blank and Pask (1969) showed there was a positive exponential dependence of the activation enthalpy on the iron concentration in magnesiowüstite. This was subsequently also confirmed by other studies, where the effect roughly amounts to a decrease of the activation enthalpy of 1.0 – 1.3 $kJ\ mol^{-1}$ per molar percent of FeO. (Chen and Peterson 1980, Sata and Goto 1982, Holzapfel et al. 2003, Yamazaki and Irifune 2003, Mackwell et al. 2005). The activation energy for Fe-Mg interdiffusion in these studies was determined to be ~210 $kJ\ mol^{-1}$. Different studies have also shown there is a $D = D' fO_2^{1/n}$ dependence of the Fe-Mg interdiffusivity on the oxygen fugacity, for which n is in the range of 5 -6 for geological relevant compositions (Chen and Peterson 1980, Sata and Goto 1982, Mackwell et al. 2005). This indicates that oxidation of ferrous iron in magnesiowüstite is balanced by the formation of vacancies on the metal sites (see also chapter 2).

Not many diffusion experiments have been conducted at pressures relevant to the Earth's lower mantle. Holzapfel et al. (2003) and Yamazaki and Irifune (2003) performed Fe-Mg interdiffusion experiments at conditions relevant to the upper part of the lower mantle. Both studies reported different activation volumes for Fe-Mg interdiffusion, 3.3 $cm^3\ mol^{-1}$ was reported in the former and 1.8 $cm^3\ mol^{-1}$ in the latter study. Mackwell et al. (2005) showed that both studies could be reconciled with each other, if the oxygen dependence of Fe-Mg interdiffusion was taken into account, since both studies were conducted using a different oxygen buffer. Both studies however also reported a different activation energy for diffusion, which would mean that

the activation energy for Fe-Mg interdiffusion is also dependent on the oxygen fugacity. Hints to this were given by Sata and Goto (1982), who found that the decrease of apparent activation energy for Fe-Mg interdiffusion as function of iron content is dependent on the oxygen fugacity.

Oishi et al. (1983) determined the oxygen self-diffusivity in pure end-member MgO. Their results showed that there was a change in activation energy around 1500 °C. The activation energy in the high temperature regime appeared to be independent of the impurity concentration. This break has therefore been interpreted as being a transition from an extrinsic regime below 1500 °C, characterized by an activation energy of ~ 213 kJ mol^{-1}, to an intrinsic regime, characterized by an activation energy of ~ 536 kJ mol^{-1}. Ando et al. (1983) showed that in contrast to Fe-Mg interdiffusion, the oxygen diffusivity is independent on the iron concentration. Van Orman et al. (2003) confirmed that the oxygen diffusivity in MgO is also independent on trivalent impurity content at high pressures. As their study was a tracer diffusion study, they were able to determine the activation volume for magnesium tracer diffusion in MgO, and determined it to be ~ 3.0 cm^3 mol^{-1}., which is in good agreement with the magnesium self-diffusion coefficients obtained from atomistic simulations (Ita and Cohen 1997). The latter predict also a decreasing activation volume for magnesium self-diffusion with increasing pressure.

1.2.5 Garnets

Though garnets constitute an important part of Earth's upper mantle and transition zone, in the latter they constitute up to ~40 vol.%, only a few experiments have been conducted at conditions prevalent in the transition zone. Most of the diffusion studies were conducted at pressure below 4 GPa.

Though diffusion models in garnet based on zoning in natural garnets have been formulated earlier (Anderson and Buckley 1973, Loomis 1978), the first report from diffusion experiments on garnet is by Freer (1979). In this study Fe-Mn interdiffusion was observed in almandine garnet – sintered spessartine garnet diffusion couples at 1 bar and between 822 °C and 1200 °C. A concentration dependent manganese diffusivity was observed, which was fitted against an exponential function, similar to as what has been done in the case for magnesiowüstite and olivine. The manganese diffusivity increases about half an order of magnitude from a garnet containing 5 wt.% of Mn to a garnet containing 20 wt.% Mn at a temperature of 1002 °C. From the constant pressure experiments also an activation energy for Fe – Mn/Mg interdiffusion of 132 ± 45 kJ mol^{-1}, which as will be discussed later, is significantly lower than the other studies on Fe-Mg interdiffusion in garnet.

The early theoretical models (Anderson and Buckley 1973, Loomis 1978, Lasaga 1979) for interdiffusion in garnet note that during diffusion the fluxes of cations cannot be considered to be independent, but are correlated by cross terms in the matrix of diffusion coefficients. This thus introduces a compositional dependence in the diffusivity of the component. This occurs, however, through a different mechanism as Fe-Mg interdiffusion mentioned in the above minerals, where the iron concentration modifies the both vacancy concentration and the activation enthalphy for diffusion and thereby makes Fe-Mg interdiffusion concentration dependent.

In the experiments conducted on Fe-Mg-Mn interdiffusion on spessartine – almandine couples by Elphick et al.

(1985) it was noted that their diffusion profiles could not be fitted by a single composition independent diffusion coefficient. Subsequently they fitted their profiles by two diffusion coefficients, one for both ends of the diffusion couple. Loomis et al. (1985) re-analysed the data of Elphick et al. (1985) and fitted the diffusion models of Lasaga (1979) and Manning (1968) to the data. Doing so, he determined that the tracer diffusivity of manganese is roughly 3 – 5 times larger than the tracer diffusivity of iron and magnesium. The tracer diffusivity of the latter two was determined to be very similar in magnitude in the almandine – spessartine diffusion couples. Using their method, Elphick et al. (1985) determined a difference up to a factor two in interdiffusivities between both sides. Loomis et al. (1985) also determined that the activation enthalpy for (tracer) diffusion at 40 kbar of magnesium is (251 ± 33 kJ mol^{-1}) and iron (257 ± 36 kJ mol^{-1}) is significantly greater than that of manganese (202 ± 33 kJ mol^{-1}). The activation volume for tracer diffusion in garnet they determined to be ~4.7 cm^3 mol^{-1} in the two studies.

The dataset of Loomis et al. (1985) has been extended by Chakraborty and Ganguly (1992) to cover a greater pressure and temperature range. The determined activation energies for tracer diffusion were slightly higher (Fe: 276 ± 36 kJ mol^{-1}, Mg: 285 ± 38 kJ mol^{-1}, Mn: 254 ± 37 kJ mol^{-1}). The activation volumes for diffusion was also a bit higher than in the study by Loomis et al. (1985), but within experimental error of the latter (5 – 6 cm^3 mol^{-1} with a ~ 3 cm^3 mol^{-1} error). Ganguly et al. (1998) extended the dataset further with data from interdiffusion experiments conducted at the almandine – pyrope joint and also include calcium and manganese diffusion data. These diffusion experiments showed a strong contrast in relative diffusivities of magnesium, iron and manganese in almandine – pyrope couples as compared to almandine – spessartine couples by Loomis (1985). The relative tracer diffusivities in the Ganguly et al. (1998) study are approximately $D_{Mg} = 10\ D_{Fe} = 3\ D_{Ca}$ and manganese tracer diffusivity is similar to that of iron, whereas at the almandine – spessartine join iron self-diffusion is similar to magnesium tracer diffusion. The activation energies and volume for diffusion along the C-O buffer in the spessartine – almandine couples and almandine – pyrope couples are equal within each others errors, indicating that the change in relative diffusivities in not very likely caused by a change in diffusion mechanism. Ganguly et al. (1998) also showed that the oxygen fugacity has a profound effect on the determined apparent activation volume for diffusion.

Schwandt et al. (1996) performed calcium tracer diffusion experiments on garnet between 800 – 1000 °C and at 1 bar. They obtained extremely short diffusion profiles (~ 20 nm) which indicated that calcium self-diffusion is at least one order of magnitude slower than magnesium self-diffusion at the same conditions in their earlier experiments (Schwandt et al. 1995). Their activation energy for self-diffusion is significantly lower than that determined in other studies (Freer and Edwards 1999, Perchuk et al. 2008), which might be a result of the extremely short profiles. The Ca self-diffusion coefficients from Freer and Edwards (1999) are however 3 – 4 orders of magnitude faster than obtained by other workers (Schwandt et al. 1996, Ganguly et al. 1998, Vielzeuf et al. 2007, Perchuk et al. 2008). Although there is some discrepancy in calcium diffusion data from the above mentioned workers, they generally agree that calcium is the slowest diffusing divalent cation in garnet.

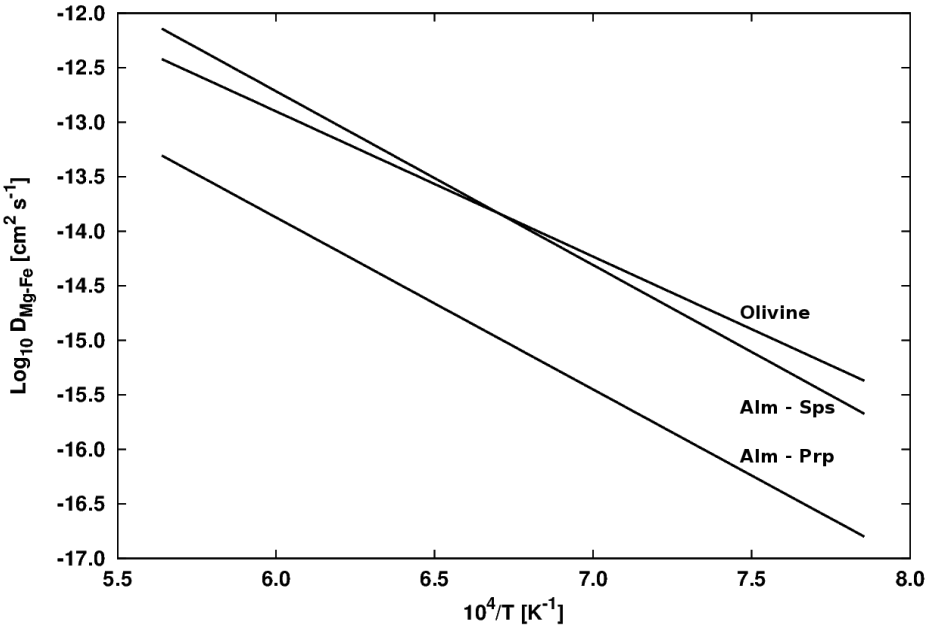

Figure 1.5: Iron – magnesium interdiffusivity in garnet and olivine at 50 kbar between 1000 °C and 1500 °C. Alm – Prp denotes the Fe – Mg interdiffusivity in almandine – pyrope couples (Ganguly et al. 1998) , Alm – Sps of that in the almandine – spessartine diffusion couples (Chakraborty & Ganguly 1992) and olivine of that in olivine (Chakraborty 2010).

Chakraborty and Rubie (1996) performed magnesium tracer diffusion experiments on almandine and pyrope rich garnet at room pressure between 750 °C and 850 °C and at 8.5 GPa. The ^{26}Mg tracer diffusivities they measured interpolated well to the tracer diffusivities determined in the previous studies by Loomis et al. (1985) and Chakraborty and Ganguly (1992). This, together with oxygen fugacity corrected ^{25}Mg tracer diffusion data obtained by Cygan and Lasaga (1985), demonstrates that tracer diffusivities obtained from interdiffusion experiments provide relatively reliable results. The inclusion of the high pressure data at 8.5 GPa allowed for a better determination of the activation volume for diffusion of Mg-tracer diffusion in garnet. The determined activation volume with these data was 8 ± 1 cm^3 mol^{-1}, which is significantly higher than that of the previous studies and shows the importance of doing diffusion experiments over a large enough pressure range. When considered on their own, their low pressure diffusion data produced a rather low activation energy for diffusion of 226 ± 21 kJ mol^{-1}, however when combined with the high pressure data of Chakraborty and Ganguly (1992) they obtained an activation energy for magnesium tracer diffusion of 270 ± 8 kJ mol^{-1}. Their rather low activation energy of their own data they tentatively ascribed to the limited temperature range of their own experiments. Next to this, they also found no dependence of the magnesium tracer diffusivity on the almandine content of garnet.

Schwandt et al. (1995) performed ^{25}Mg diffusion experiments at more oxidizing conditions near the FMQ buffer than the above mentioned experiments, which were conducted mostly near the C-O buffer or at constant oxygen fugacity. They observed that there was a correlation between the reciprocal duration of the experiment and the measured diffusion coefficient. This is an effect that might be caused by profile broadening related to the applied instrumental method or experimental setup (Ganguly et al. 1988, Dohmen et al. 2002a, b, Watson and Dohmen 2010). The broadening of the diffusion profiles will result in an increase of measured diffusion coefficients and a decrease of apparent activation energy for diffusion when diffusion profiles are short. To correct for this effect, Schwandt et al. (1995) extrapolated their data to infinite experiment duration conditions

and thereby obtained an activation energy for magnesium tracer diffusion of 294 ± 54 kJ mol^{-1}, which is very similar to that of Ganguly et al. (1998). The experiments of Chakraborty and Rubie (1996) show a similar decrease of diffusivity with increasing annealing duration. This indicates that their data might also be affected by profile broadening. Thus the actual magnesium tracer diffusivity could be lower and the activation energy for magnesium tracer diffusion might be higher than reported by them. In their study, Schwandt et al. (1995) inspected the influence of oxygen fugacity on the magnesium tracer diffusivity in garnet too. They found no evidence for any influence, which may question the correction of the data of Cygan and Lasaga (1985) for oxygen fugacity using a $D \propto fO_2^{1/6}$ proportionality by Chakraborty and Rubie (1996). The dependence of cation diffusivity in garnet on oxygen fugacity thus remains unresolved.

Perchuck et al. (2008) performed interdiffusion experiments on single crystal garnets in a pyrope powder matrix. Their data showed good correspondence to the other studies mentioned in this section. They sometimes, however, observed plateau like features in their diffusion experiments. To investigate the cause of the features they performed numerical 2D modelling to assess the influence of grain boundary diffusion on the obtained diffusion profiles. These models showed that when great care is not taken when selecting the location of the diffusion profiles, the diffusion profiles may include regions where the effect of grain boundary diffusion is significant, resulting in plateau like features in the measured profiles.

1.2.6 Pyroxenes

Pyroxenes are an important component of the subducting oceanic crust, about 80 vol. % of the oceanic crust consists out of clinopyroxene during the initial stages of subduction (Irifune and Ringwood 1993). The diffusivity of the different elements in pyroxene form an important factor in equilibrating the subducting oceanic crust with its changing environment when it is transported deeper into the mantle.

Major element diffusion data on orthopyroxene are scarce. There is only one report of a magnesium self-diffusion study (Schwandt et al. 1998). The anisotropy that might be expected from the orthopyroxene structure appears to be only small in terms of absolute self-diffusivities. The activation energies for magnesium self diffusion, however, show a significant difference between the a-axis (ΔE = 360 ± 52 kJ mol^{-1}) and c-axis (ΔE = 265 ± 66 kJ mol^{-1}). At 900 °C, magnesium self-diffusion is about one order magnitude faster than magnesium self-diffusion in garnet, as determined in an earlier study (Schwandt et al. 1995).

More data is available on major element diffusion in diopside. Brady and McCallister (1983) performed homogenization experiments on a diopside host with pigeonite exsolution lamellae from which they determined average Ca-Mg interdiffusivities in diopside between 1150 °C and 1250 °C at 25 kbar near the graphite – oxygen buffer. These experiments indicated that the activation energy for Ca-Mg interdiffusion in diopside along either the a- or b-axis (not clearly defined in the paper) is relatively high as compared other minerals (~ 360 kJ mol^{-1}). At 25 kbar and 1200 °C they estimate Ca-Mg interdiffusion to be 1.5 – 2 orders of magnitude slower than magnesium self-diffusion at the same conditions in garnet, and thus slower than Ca self-diffusion in garnet at the same conditions (Chakraborty and Ganguly 1992, Ganguly et al. 1998).

Calcium self-diffusion experiments have been conducted by Dimanov and Ingrin (1995), Dimanov et al. (1996) and Dimanov and Jaoul (1998). These experiments indicated that there is a switch in diffusion mechanism from an extrinsic regime, characterized by oxygen fugacity dependent calcium self-diffusivity with an activation energy for calcium self-diffusion of ~280 kJ mol^{-1}, to an intrinsic regime above 1230 °C with an activation energy of roughly 1000 kJ mol^{-1}. The oxygen fugacity dependence vanishes in this intrinsic regime, as expected. The high temperature regime is explained by Dimanov and Jaoul (1998) as a change to a diffusion mechanism controlled by the Ca-Frenkel defect concentrations, which appear to dominate in the so-called premelting regime of diopside. The actual Ca self diffusivity appeared to be about one order of magnitude slower than determined by Brady and McCallister (1983). The experiments of the Dimanov – Jaoul – Ingrin group did not show any significant anisotropy for calcium self-diffusion in diopside. Zhang et al. (2009) however, determined that there was significant anisotropy in the a-c and b-c planes, with the c-direction being the fastest. This is also manifested by anisotropy in activation energies for calcium self-diffusion in diopside, with a difference of ~ 80 ± 34 kJ mol^{-1} between the fastest (c) and slowest direction (b).

Béjina and Jaoul (1996) measured the silicon self-diffusivity in diopside at 1 bar between 1040 °C – 1250 °C. These experiments showed that silicon is the slowest diffusion species in diopside, roughly one order of magnitude slower than the calcium self-diffusivity in diopside (Dimanov and Ingrin 1995). They determined an activation energy of 211 ± 110 kJ mol^{-1}, which might be higher (280 kJ mol^{-1}) if oxygen fugacity has an effect on the silicon self-diffusivity. Sautter et al. (1988) measured the aluminium self-diffusivity in diopside at 1180 °c which turned out to be as fast as calcium self-diffusion in diopside.

1.3 Reaction kinetics in Earth's mantle

As explained above, the down going slab will undergo a series of phase transitions when it is transported into the transition zone and lower mantle. Most of these phase transitions result in a volume reduction. It has been proposed by several authors that the change in volume or release of heat may induce earthquakes in Earth's deep interior (Bridgman 1945, Evison 1967, Liu 1983). Though being an attractive model for the explanation of deep-focused earthquakes, the focal mechanism observed from deep-focus earthquakes do not correspond to those expected from an implosion through volume reduction (Frohlich 1989). It seems that volume reduction associated with phase transitions can be ruled out as direct cause for deep-focus earthquakes, more complicated models still propose that delayed phase transitions ultimately lead to conditions where catastrophic failure can occur, which is required for the presence of deep-focus earthquake (Sung and Burns 1976, Green II and Burnley 1989, Kirby et al. 1991, Wiens et al. 1993). The most prominent model is the transformational faulting model, which depends on initially sluggish reaction kinetics, release of a large amount of latent heat during transformation and polymorphism to produce a localized runaway process resulting in catastrophic failure at depth (Burnley et al. 1991, Kirby et al. 1996). Though two major deep earthquakes associated with subduction zones near Bolivia and Tonga that occurred in 1994 seem to contradict the transformational faulting model, since the rapture zones extend well beyond the expected width of the

metastable wedge (Wiens et al. 1994, Silver et al. 1995, Wiens and Snider 2001). Next to this, metastable preservation of olivine into the transitions zone as results of sluggish transformation kinetics have been proposed as a factor that may have a significant influence on the dynamics of subduction zones (Sung and Burns 1976, Kirby et al. 1996, Schmeling et al. 1999). Also, the degree of metastable preservation of olivine has a significant effect on the strength of the subduction slab as it influences the microstructure of the transformation products (Vaughan and Coe 1981, Rubie 1984, Ito and Sato 1991, Rubie and Ross 1994). The reaction kinetics of phase transformation in Earth's mantle thus is clearly an important topic in Earth sciences.

Most kinetic studies have focused on the olivine to wadsleyite or ringwoodite transformation that occurs in the Earth. Sung and Burns (1976) fitted a collection of experimental data on the olivine to wadsleyite and ringwoodite transformation to a kinetic model. They concluded that there is a lower limit on temperature, below which nucleation and growth of the new phase is virtually zero. For the olivine to spinel transition they found that this temperature must be around 700 °C. When the downgoing assemblage has reached this temperature, olivine is expected to transform to the spinel phase very rapidly due to a large overstepping of the phase boundary. The rapid transformation is also expected to lead to a temporary local pressure drop in the order of a few GPa in a cold slab.

Poirier (1981) argued that the transformation mechanism for the olivine to spinel transformation is controlled by the motion of stacking faults resulting in shearing of the oxygen sublattice, which leads to the formation of a local spinel-type oxygen sublattice. The cations then only need to diffuse one atomic distance to form the spinel phase (a process called synchroshear). Burnley and Green (1989) concluded that Poiriers mechanism only plays a significant role at very high shears stresses. Only a limited amount of transformation by synchoshear is observed in experiments, therefore it was concluded that the shearing mechanism does not play an important role in the Earth (Rubie and Ross 1994). However, more recent studies have shown that nucleation of ringwoodite platelets on (100) stacking faults in olivine may also occur at low to moderate degrees of differential stress when the phase boundary is overstepped by a few GPa and the grain size is large (Kerschhofer et al. 1996, 1998, 2000). The latter authors investigated in more detail the nucleation kinetics of wadsleyite and ringwoodite in olivine. They find that at 18 – 20 GPa an intracrystalline nucleation mechanism is present where the transformation of olivine to ringwoodite and / or wadsleyite occurs via a sequence of steps: (1) formation of (100) stacking faults in olivine, (2) coherent nucleation of ringwoodite lammelae on those stacking faults and (3) nucleation of wadsleyite on ringwoodite. Furthermore they observed that growth of wadsleyite or ringwoodite grains on olivine grain boundaries, the nucleation mechanism preferred when grainsize is small, slows down and eventually halts as the wadsleyite/ringwoodite grains grow bigger. They interpret this as a result of elastic strain that accumulates due to a difference in density between olivine and the product phases. At geological time scales reaction kinetics may then be controlled by the rate of viscoelastic relaxation of the product phases.

Rubie and Ross (1994) fitted experimental data on the progress the olivine to spinel transformation of Burnley (1990) and Rubie (1990) to transformation rate equations and constructed several models for the olivine to

spinel transformation in a subduction zone. They concluded that the preservation of metastable olivine in subduction zones is strongly temperature dependent. In the cold inner part of the subducting slab, transformation is delayed by ~ 120 km beyond the equilibrium boundary and takes place over a depth interval of ~ 150 km. The transformation rate in the cold inner part of the slab is expected to be controlled by the grain growth of the ringwoodite, resulting in a very fine grained spinel that produces conditions suitable for superplasticity. In the hotter external parts grain growth is faster and the transformation will take part over a limited depth interval. As result of the higher growth rates the spinel is coarse grained, but still stiff due to the relative low temperatures. The upper and lower bounds are expected to be in a thermodynamic equilibrium and are weak owing to the high temperatures. Latent heat production however, may significantly affect the width of the depth range over which the transition occurs. Däßler et al. (1996) included the release of latent heat in their thermal and kinetic model. Their calculations showed that for warm slow slabs, the inclusion of latent heat release increases the depth at which the olivine to ringwoodite or wadsleyite occurs because it slows down kinetics by pushing the assemblages towards the equilibrium boundary in PT-space. They however expect the effect to be small for the olivine to wadsleyite boundary. For a fast cold slab it reduces the depth to which the metastable wedge persists. Mosenfelder et al. (2001) updated the model of Rubie and Ross (1994) with the additional experimental data that has become available by that time and also incorporated the release of latent heat in their model. Their results are consistent with that of Däßler et al. (1996) in that latent heat significantly reduces the depth to which a metastable wedge can persist. Also the new data lead to growth rates that are 5 times as high as the old ones (Rubie and Ross 1994). The overall result is that it is highly like that metastable wedges are present in old and cold slabs, but their sizes are significantly smaller then previously predicted and are unlikely to extend to depths greater than 600 km. For the Tonga trench they predict that the metastable wedge may persist up to ~ 550 km depth (figure 1.6). The 1994 Tonga earthquake, for which the focus is determined at 563 km depth (Wiens et al. 1994), would thus have occurred at the very tip of the metastable wedge in their model and the Bolivian earthquake (metastable wedge predicted up to 450 km) should have occurred well beyond the penetration depth of the metastable wedge. Mosenfelder et al. (2001) add that real slabs may have a more complicated thermal structure that would alter they model.

The above mentioned models used data that was obtained from experiments that had solely olivine or its β- and / or γ-modifications present. Sharp and Rubie (1995) performed experiments with additionally high pressure clinoenstatite present. These experiments indicated that ringwoodite was ubiquitously associated with clinoenstatite and that the latter catalysed the nucleation of the former phase. As already mentioned however, the slow transformation kinetics of olivine to its high pressure polymorphs is probably not controlled by the nucleation kinetics, but by the growth kinetics of the high pressure polymorphs (Rubie and Ross 1994). The catalyses of nucleation may, however, lead to smaller grains in the product phase. In general, it shows that it is necessary to study geologically realistic bulk composition too, when performing studies on reaction kinetics.

Hogrefe et al.(1994) performed experiments on the breakdown of enstatite at transition zone pressures. The results these experiments show that the breakdown of enstatite to wadsleyite plus stishovite is extremely

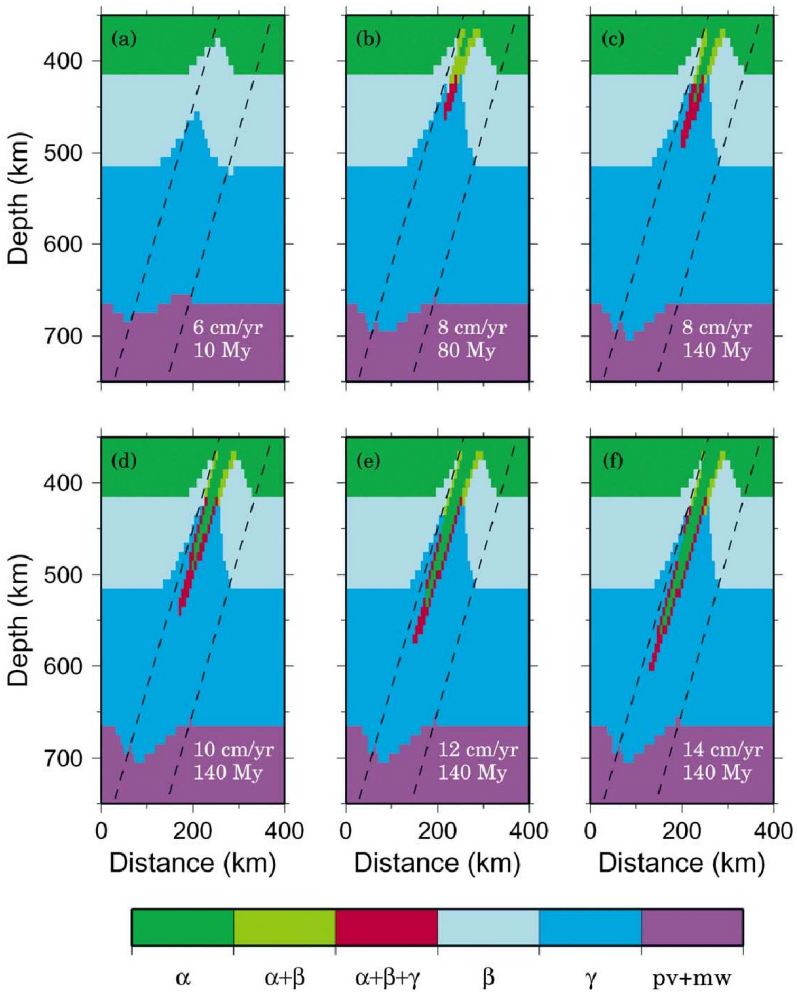

Figure 1.6: The extent of the metastable wedge in a subducted zone as function of lithosphere age at the start of subduction and subduction rate. a) For a hot and young slab the reaction kinetics are expected to be fast enough such that subducting slab in near equilibrium. b – f) For progressively older slab and high subducting rates the extent of metastable wedge increases, up to a maximum of ~ 600 km. Colours indicate the phase field (α = olivine, β = wadsleyite, γ = ringwoodite, pv + mw = perovskite + magnesiowüstite). Figure d correspond to the Tonga-slab. After Mosenfelder et al. (2001)

sluggish and require much higher temperatures than the transformation of olivine to wadsleyite at the same timescales. They conclude it is therefore more likely that enstatite is preserved as metastable phase in the wadsleyite + stishovite field and transforms to akimotoite directly when it enters the akimotoite field. Though volumetrically of less importance, because of the large volumetric difference between clinoenstatite and akimotoite, enstatite might therefore still influence dynamics of subduction and the stress field in the subducting slab.

The above mentioned investigations show that reaction kinetics play an important role in phase transitions that occur in the Earth. It is therefore in most cases a too big simplification to assume that the mineralogical composition of subducting slabs in a dynamic setting, like a subduction zone, are in thermodynamic equilibrium.

1.4 Goals of this PhD study

Because of the stability of a pyroxene polymorph with a garnet structure (majorite) at high pressure, pyroxene is expected to dissolve progressively with increasing pressure in garnet during subduction. The dissolution of pyroxene into garnet is controlled by long range mass transport, therefore the rate of dissolution will be controlled by the diffusivity of the relevant cations in garnet. Since diffusion rates in silicates are generally low,

it may be expected that the dissolution of pyroxene is hindered and thus pyroxene may be present to depths greater than expected for an equilibrium assemblage. As there is a significant density contrast between garnet and pyroxenes, this may have important implications for the dynamics of subduction zones.

The results of Sharp and Rubie (1995) have shown that HP high clinoenstatite catalyses the nucleation of ringwoodite during the transformation of olivine to wadsleyite and/or ringwoodite. Though reaction kinetics of the olivine to wadsleyite and ringwoodite transformation are controlled by the growth kinetics, and therefore the metastable preservation of HP clinoenstatite is unlikely to influence the transformation kinetics, it may result in a reduced grain size of wadsleyite and ringwoodite after transformation. This in turn may enhance superplasticity, which is thought to cause deep-focus earthquakes in subduction zones, as explained.

Furthermore, pyroxene exsolution needles have been found in several UHP provinces (Song et al. 2004, van Roermund 2009, Pandey et al. 2010). The rate of dissolution of pyroxene into garnet and the rate exsolution of pyroxene from garnet in these cases will also be controlled by the diffusivity of the majorite component. The lack of exsolution needles in pre-Scandian garnets from Norway in combination with diffusion data on the majorite component in garnet may be used to constrain the duration of UHP metamorphism in these provinces. It is thus clear our understanding of important geological process occurring in the interior of the Earth will benefit from constraints on the major element diffusivity in garnet at depth.

At present unfortunately, there is neither data on major element diffusion in garnet available at the conditions prevalent in the Earth's transition zone, nor data on the majorite diffusivity in garnet. During this PhD experiments it has been attempted to, at least partially, fill this gap in garnet diffusion data. Additionally, there is no data available on the aluminium diffusivity in HP high clinoenstatite. As reviewed in the reaction kinetics chapter the microstructure of phases in the transition zone controls among others the strength of the subducting slab. It is expected that the aluminium component will be exsolved as majoritic garnet. This requires long-range transport of aluminium in enstatite and the exsolution of garnet from HP high clinoenstatite will therefore be controlled by the aluminium diffusivity in HP high clinoenstatite. In this PhD study it has been attempted to study the microstructure of the majoritic garnet exsolution products from high clinoenstatite and to determine the diffusivity of aluminium in HP high clinoenstatite to gain a better understanding of the properties of metastable HP high clinoenstatite at transition zone conditions.

This dissertation therefore reports on two different studies perfomed during this PhD. The first part reports (chapter 5) on the results of an experimental study on the major element diffusivity in garnet at transition zone conditions. The second study (chapter 6) was an experimental high pressure study performed on aluminous enstatite to get more insight into the evolution of HP clinoenstatite as it is preserved as a metastable phase during subduction and to determine the aluminium diffusivity in HP clinoenstatite at high pressure and temperature.

1.5 References

Akaogi, M., Akimoto, S. (1977), Pyroxene-garnet solid-solution equilibria in the systems $Mg_4Si_4O_{12}$ – $Mg_3Al_2Si_3O_{12}$ and $Fe_4Si_4O_{12}$ – $Fe_3Al_2Si_3O_{12}$ at high pressures and temperatures. Phys Earth Planet Inter 15:90-106. doi: 10.1016/0031-9201(77)90013-9

Akaogi, M., Ito, E., Navrotsky, A. (1989), Olivine-modified spinel-spinel transitions in the system Mg_2SiO_4 - Fe_2SiO_4: Calorimetric measurements, thermochemical calculation, and geophysical application. J Geophys Res 94:15671-15685

Akimoto, S., Fujisawa, H. (1966), Olivine-spinel transition in the system Mg_2SiO_4-Fe_2SiO_4 at 800°C. Earth Planet Sci Lett 1:237-240. doi: 16/0012-821X(66)90076-8

Ammann, M., Brodholt, J., Dobson, D.P. (2009), DFT study of migration enthalpies in $MgSiO_3$ perovskite. Phys Chem Miner 36:151-158. doi: 10.1007/s00269-008-0265-z

Anderson, D.E., Buckley, G.R. (1973), Zoning in garnets-Diffusion models. Contr Mineral Petrol 40:87-104. doi: 10.1007/BF00378168

Ando, K., Kurokawa, Y., Oishi, Y. (1983), Oxygen self-diffusion in Fe-doped MgO single crystals. J Chem Phys 78:6890. doi: 10.1063/1.444635

Angel, R.J., Chopelas, A., Ross, N.L. (1992), Stability of high-density clinoenstatite at upper-mantle pressures. Nature 358:322-324. doi: 10.1038/358322a0

Angel, R.J., Hugh-Jones, D.A. (1994), Equations of state and thermodynamic properties of enstatite pyroxenes. J Geophys Res 99:19777-19783. doi: 199410.1029/94JB01750

Arlt, T., Angel, R.J., Miletich, R., Armbruster, T., Peters, T. (1998), High-pressure $P2_1/c$ – C2/c phase transitions in clinopyroxenes; influence of cation size and electronic structure. Am Mineral 83:1176-1181

Béjina, F., Blanchard, M., Wright, K., Price, G.D. (2009), A computer simulation study of the effect of pressure on Mg diffusion in forsterite. Phys Earth Planet Inter 172:13-19. doi: 10.1016/j.pepi.2008.04.008

Béjina, F., Jaoul, O. (1996), Silicon self-diffusion in quartz and diopside measured by nuclear micro-analysis methods. Phys Earth Planet Inter 97:145-162. doi: 10.1016/0031-9201(96)03137-8

Béjina, F., Jaoul, O., Liebermann, R.C. (1999), Activation volume of Si diffusion in San Carlos olivine: Implications for upper mantle rheology. J Geophys Res 104:PP. 25,529-25,542. doi: 199910.1029/1999JB900270

Béjina, F., Raterron, P., Zhang, J., Jaoul, O., Liebermann, R.C. (1997), Activation volume of silicon diffusion in San Carlos olivine. Geophys Res Lett 24:2597-2600

Bertran-Alvarez, Y., Jaoul, O., Liebermann, R.C. (1992), Fe-Mg interdiffusion in single crystal olivine at very high pressure and controlled oxygen fugacity: technological advances and initial data at 7 GPa. Phys Earth Planet Inter 70:102-118. doi: 10.1016/0031-9201(92)90165-R

Blank, S.L., Pask, J.A. (1969), Diffusion of Iron and Nickel in Magnesium Oxide Single Crystals. J Am Ceram Soc 52:669-675. doi: 10.1111/j.1151-2916.1969.tb16074.x

Brady, J.B., McCallister, R.H. (1983), Diffusion data for clinopyroxenes from homogenization and self-diffusion experiments. Am Mineral 68:95 -105

Bridgman, P.W. (1945), Polymorphic transitions and geological phenomena. Am J Sci 243A:90-97

Buening, D.K., Buseck, P.R. (1973), Fe-Mg Lattice Diffusion in Olivine. J Geophys Res 78:6852-6862. doi: 197310.1029/JB078i029p06852

Burnley, P.C. (1990), The effect of nonhydrostatic stress on the olivine-spinel transformation in magnesium germanate. University of California, Davis

Burnley, P.C., Green, H.W. (1989), Stress dependence of the mechanism of the olivine-spinel transformation. Nature 338:753-756. doi: 10.1038/338753a0

Burnley, P.C., Green, H.W., Prior, D.J. (1991), Faulting Associated with the Olivine to Spinel Transformation in Mg_2GeO_4 and its Implications for Deep-focus Earthquakes. J Geophys Res 96:425-443. doi: 199110.1029/90JB01937

Canil, D. (1994), Stability of clinopyroxene at pressure-temperature conditions of the transition region. Phys Earth Planet Inter 86:25-34. doi: 16/0031-9201(94)05059-7

Carpenter, M.A. (1982), Time-temperature-transformation (TTT) analysis of cation disordering in omphacite. Contrib Mineral Petrol 78:433-440. doi: 10.1007/BF00375205

Chakraborty, S. (1997), Rates and mechanisms of Fe-Mg interdiffusion in olivine at 980°–1300°C. J Geophys Res 102:12,317-12,331. doi: 199710.1029/97JB00208

Chakraborty, S., Ganguly, J. (1992), Cation diffusion in aluminosilicate garnets: experimental determination in spessartine-almandine diffusion couples, evaluation of effective binary diffusion coefficients, and applications. Contrib Mineral Petrol 111:74-86. doi: 10.1007/BF00296579

Chakraborty, S., Knoche, R., Schulze, H., Rubie, D.C., Dobson, D.P., Ross, N.L., Angel, R.J. (1999), Enhancement of Cation Diffusion Rates Across the 410-Kilometer Discontinuity in Earth's Mantle. Science 283:362-365. doi: 10.1126/science.283.5400.362

Chakraborty, S., Rubie, D.C. (1996), Mg tracer diffusion in aluminosilicate garnets at 750-850° C, 1 atm. and 1300° C, 8.5 GPa. Contrib Mineral Petrol 122:406-414. doi: 10.1007/s004100050136

Chen, W.-K., Peterson, N.L. (1980), Iron diffusion and electrical conductivity in magnesio-wüstite solid solutions (Mg, Fe)O. J Phys Chem Solids 41:335-339. doi: 10.1016/0022-3697(80)90206-1

Cygan, R.T., Lasaga, A.C. (1985), Self-diffusion of magnesium in garnet at 750 degrees to 900 degrees C. Am J Sci 285:328 -350. doi: 10.2475/ajs.285.4.328

Däßler, R., Yuen, D.A., Karato, S., Riedel, M.R. (1996), Two-dimensional thermo-kinetic model for the olivine-spinel phase transition in subducting slabs. Phys Earth Planet Inter 94:217-239. doi: 10.1016/0031-9201(95)03103-0

Dimanov, A., Ingrin, J. (1995), Premelting and high-temperature diffusion of Ca in synthetic diopside: An increase of the cation mobility. Phys Chem Miner 22: doi: 10.1007/BF00200321

Dimanov, A., Jaoul, O. (1998), Calcium self-diffusion in diopside at high temperature: implications for transport properties. Phys Chem Miner 26:116-127. doi: 10.1007/s002690050168

Dimanov, A., Jaoul, O., Sautter, V. (1996), Calcium self-diffusion in natural diopside single crystals. Geochem Cosmochem Acta 60:4095-4106. doi: 10.1016/S0016-7037(96)00250-5

Dobson, D.P. (2003), Oxygen ionic conduction in $MgSiO_3$ perovskite. Phys Earth Planet Inter 139:55-64. doi: 10.1016/S0031-9201(03)00144-4

Dobson, D.P., Dohmen, R., Wiedenbeck, M. (2008), Self-diffusion of oxygen and silicon in $MgSiO_3$ perovskite. Earth Planet Sci Lett 270:125-129. doi: 10.1016/j.epsl.2008.03.029

Dodson, M.H. (1973), Closure temperature in cooling geochronological and petrological systems. Contr Mineral and Petrol 40:259-274. doi: 10.1007/BF00373790

Dohmen, R., Becker, H.-W., Chakraborty, S. (2007), Fe–Mg diffusion in olivine I: experimental determination between 700 and 1,200 ° C as a function of composition, crystal orientation and oxygen fugacity. Phys Chem Miner 34:389-407. doi: 10.1007/s00269-007-0157-7

Dohmen, R., Becker, H.-W., Meißner, E., Etzel, T., Chakraborty, S. (2002a), Production of silicate thin films using

pulsed laser deposition (PLD) and applications to studies in mineral kinetics. Eur J Mineral 14:1155 -1168. doi: 10.1127/0935-1221/2002/0014-1155

Dohmen, R., Chakraborty, S. (2007), Fe–Mg diffusion in olivine II: point defect chemistry, change of diffusion mechanisms and a model for calculation of diffusion coefficients in natural olivine. Phys Chem Miner 34:409-430. doi: 10.1007/s00269-007-0158-6

Dohmen, R., Chakraborty, S., Becker, H.-W. (2002b), Si and O diffusion in olivine and implications for characterizing plastic flow in the mantle. Geophys Res Lett 29:4 PP. doi: 200210.1029/2002GL015480

Elphick, S.C., Ganguly, J., Loomis, T.P. (1985), Experimental determination of cation diffusivities in aluminosilicate garnets. Contrib Mineral Petrol 90:36-44. doi: 10.1007/BF00373039

Evison, F.F. (1967), On the occurrence of volume change at the earthquake source. Bulletin of the Seismological Society of America 57:9 -25

Farber, D.L., Williams, Q., Ryerson, F.J. (1994), Diffusion in Mg_2SiO_4 polymorphs and chemical heterogeneity in the mantle transition zone. Nature 371:693-695. doi: 10.1038/371693a0

Farber, D.L., Williams, Q., Ryerson, F.J. (2000), Divalent cation diffusion in Mg_2SiO_4 spinel (ringwoodite), β phase (wadsleyite), and olivine: Implications for the electrical conductivity of the mantle. J Geophys Res 105(B1):513-529

Fiquet, G. (2001), Mineral phases of the Earth´s mantle. Zeitschrift für Kristallographie 216:248-271. doi: 10.1524/zkri.216.5.248.20374

Freer, R. (1979), An experimental measurement of cation diffusion in almandine garnet. Nature 280:220-222. doi: 10.1038/280220a0

Freer, R., Edwards, A. (1999), An experimental study of Ca-(Fe,Mg) interdiffusion in silicate garnets. Contrib Mineral Petrol 134:370-379. doi: 10.1007/s004100050491

Frohlich, C. (1989), The Nature of Deep-Focus Earthquakes. Annu Rev Earth Planet Sci 17:227-254. doi: 10.1146/annurev.ea.17.050189.001303

Frost, D.J. (2003), The structure and sharpness of $(Mg,Fe)_2SiO_4$ phase transformations in the transition zone. Earth Planet Sci Lett 216:313-328. doi: 16/S0012-821X(03)00533-8

Frost, D.J. (2008), The Upper Mantle and Transition Zone. Elements 4:171-176

Ganguly, J., Bhattacharya, R.N., Chakraborty, S. (1988), Convolution effect in the determination of composition profiles and diffusion coefficients by microprobe step scans. Am Mineral 73:901-909

Ganguly, J., Cheng, W., Chakraborty, S. (1998), Cation diffusion in aluminosilicate garnets: experimental determination in pyrope-almandine diffusion couples. Contrib Mineral Petrol 131:171-180. doi: 10.1007/s004100050386

Gasparik, T. (1989), Transformation of enstatite - diopside - jadeite pyroxenes to garnet. Contr Mineral and Petrol 102:389-405. doi: 10.1007/BF00371083

Gasparik, T. (1990), Phase Relations in the Transition Zone. J Geophys Res 95:769

Gasparik, T. (2003), Phase diagrams for geoscientists: an atlas of the earth's interior. Springer, Heidelberg-Berlin

Gérard, O., Jaoul, O. (1989), Oxygen diffusion in san carlos olivine. J Geophys Res 94(B4):4119-4128

Green II, H.W., Burnley, P.C. (1989), A new self-organizing mechanism for deep-focus earthquakes. Nature 341:733-737. doi: 10.1038/341733a0

Gurney, J.J., Harte, B. (1980), Chemical Variations in Upper Mantle Nodules from Southern African Kimberlites. Phil Trans R Soc A A297:273 -293. doi: 10.1098/rsta.1980.0215

Heidelbach, F., Stretton, I., Langenhorst, F., Mackwell, S. (2003), Fabric evolution during high shear strain deformation of magnesiowüstite ($Mg_{0.8}Fe_{0.2}O$). J Geophys Res 108:2154

Hirose, K., Fei, Y., Ma, Y., Mao, H.-K. (1999), The fate of subducted basaltic crust in the Earth's lower mantle. Nature 397:53-56. doi: 10.1038/16225

Hogrefe, A., Rubie, D.C., Sharp, T.G., Seifert, F. (1994), Metastability of enstatite in deep subducting lithosphere. Nature 372:351-353. doi: 10.1038/372351a0

Holzapfel, C., Chakraborty, S., Rubie, D.C., Frost, D.J. (2007), Effect of pressure on Fe–Mg, Ni and Mn diffusion in $(Fe_xMg_{1-x})_2SiO_4$ olivine. Phys Earth Planet Inter 162:186-198. doi: 10.1016/j.pepi.2007.04.009

Holzapfel, C., Chakraborty, S., Rubie, D.C., Frost, D.J. (2009), Fe–Mg interdiffusion in wadsleyite: The role of pressure, temperature and composition and the magnitude of jump in diffusion rates at the 410km discontinuity. Phys Earth Planet Inter 172:28-33. doi: 10.1016/j.pepi.2008.09.005

Holzapfel, C., Rubie, D.C., Elphick, S.C., Frost, D.J. (2003), Effect of pressure on Fe–Mg interdiffusion in $(Fe_xMg_{1-x})O$, ferropericlase. Phys Earth Planet Inter 139:21-34. doi: 10.1016/S0031-9201(03)00142-0

Holzapfel, C., Rubie, D.C., Frost, D.J., Langenhorst, F. (2005), Fe-Mg Interdiffusion in $(Mg,Fe)SiO_3$ Perovskite and Lower Mantle Reequilibration. Science 309:1707 -1710. doi: 10.1126/science.1111895

Houlier, B., Cheraghmakani, M., Jaoul, O. (1990), Silicon diffusion in San Carlos olivine. Phys Earth Planet Inter 62:329-340. doi: 10.1016/0031-9201(90)90177-Y

Houlier, B., Jaoul, O., Abel, F., Liebermann, R.C. (1988), Oxygen and silicon self-diffusion in natural olivine at T = 1300°C. Phys Earth Planet Inter 50:240-250. doi: 10.1016/0031-9201(88)90105-7

Inoue, T., Yurimoto, H., Kudoh, Y. (1995), Hydrous modified spinel, $Mg_{1.75}SiH_{0.5}O_4$: A new water reservoir in the mantle transition region. Geophys Res Lett 22:117-120

Irifune, T. (1987), An experimental investigation of the pyroxene-garnet transformation in a pyrolite composition and its bearing on the constitution of the mantle. Phys Earth Planet Inter 45:324-336. doi: 10.1016/0031-9201(87)90040-9

Irifune, T., Ringwood, A.E. (1993), Phase transformations in subducted oceanic crust and buoyancy relationships at depths of 600-800 km in the mantle. Earth Planet Sci Lett 117:101-110. doi: 10.1016/0012-821X(93)90120-X

Irifune, T., Sekine, T., Ringwood, A.E., Hibberson, W.O. (1986), The eclogite-garnetite transformation at high pressure and some geophysical implications. Earth Planet Sci Lett 77:245-256. doi: 10.1016/0012-821X(86)90165-2

Ita, J., Cohen, R.E. (1997), Effects of Pressure on Diffusion and Vacancy Formation in MgO from Nonempirical Free-Energy Integrations. Phys Rev Lett 79:3198-3201. doi: 10.1103/PhysRevLett.79.3198

Ito, E., Sato, H. (1991), Aseismicity in the lower mantle by superplasticity of the descending slab. Nature 351:140-141. doi: 10.1038/351140a0

Ito, Y., Toriumi, M. (2010), Silicon self-diffusion of $MgSiO_3$ perovskite by molecular dynamics and its implication for lower mantle rheology. J Geophys Res 115:B12205

Jaoul, O., Bertran-Alvarez, Y., Liebermann, R.C., Price, G.D. (1995), Fe-Mg interdiffusion in olivine up to 9 GPa at T = 600–900°C; experimental data and comparison with defect calculations. Phys Earth Planet Inter 89:199-218. doi: 10.1016/0031-9201(94)03008-7

Jaoul, O., Froidevaux, C., Durham, W.B., Michaut, M. (1980), Oxygen self-diffusion in forsterite: Implications for the high-temperature creep mechanism. Earth Planet Sci Lett 47:391-397. doi: 10.1016/0012-821X(80)90026-6

Jaoul, O., Houlier, B., Abel, F. (1983), Study of ^{18}O diffusion in magnesium orthosilicate by nuclear microanalysis. J Geophys Res 613-624

Kanzaki, M. (1991), Ortho/clinoenstatite transition. Phys Chem Minerals 17:726-730. doi: 10.1007/BF00202244

Karato, S.-I., Jung, H. (2003), Effects of pressure on high-temperature dislocation creep in olivine. Phil Mag 83:401-414. doi: 10.1080/0141861021000025829

Karki, B.B., Khanduja, G. (2007), A computational study of ionic vacancies and diffusion in $MgSiO_3$ perovskite and post-perovskite. Earth Planet Sci Lett 260:201-211. doi: 10.1016/j.epsl.2007.05.031

Kato, T., Kumazawa, M. (1985), Garnet phase of $MgSiO_3$ filling the pyroxene-ilmenite gap at very high temperature. Nature 316:803-805. doi: 10.1038/316803a0

Katsura, T., Ito, E. (1989), The System Mg_2SiO_4 – Fe_2SiO_4 at High Pressures and Temperatures: Precise Determination of Stabilities of Olivine, Modified Spinel, and Spinel. J Geophys Res 94:670

Kerschhofer, L., Dupas, C., Sharp, T.G., Durham, W.B., Rubie, D.C. (1998), Polymorphic transformations between olivine, wadsleyite and ringwoodite: mechanisms of intracrystalline nucleation and the role of elastic strain. Mineral Mag

Kerschhofer, L., Rubie, D.C., Sharp, T.G., McConnell, J.D.C., Dupas-Bruzek, C. (2000), Kinetics of intracrystalline olivine-ringwoodite transformation. Phys Earth Planet Inter 121:59-76. doi: 10.1016/S0031-9201(00)00160-6

Kerschhofer, L., Sharp, T.G., Rubie, D.C. (1996), Intracrystalline Transformation of Olivine to Wadsleyite and Ringwoodite Under Subduction Zone Conditions. Science 274:79 -81. doi: 10.1126/science.274.5284.79

Kirby, S.H., Durham, W.B., Stern, L.A. (1991), Mantle Phase Changes and Deep-Earthquake Faulting in Subducting Lithosphere. Science 252:216 -225. doi: 10.1126/science.252.5003.216

Kirby, S.H., Stein, S., Okal, E.A., Rubie, D.C. (1996), Metastable mantle phase transformations and deep earthquakes in subducting oceanic lithosphere. Rev Geophys 34:261-306. doi: 199610.1029/96RG01050

Kohlstedt, D.L., Keppler, H., Rubie, D.C. (1996), Solubility of water in the α, β and γ phases of $(Mg,Fe)_2SiO_4$. Contrib Mineral Petrol 123:345-357. doi: 10.1007/s004100050161

Kubo, T., Shimojuku, A., Ohtani, E. (2004), Mg–Fe interdiffusion rates in wadsleyite and the diffusivity jump at the 410-km discontinuity. Phys Chem Miner 31:456-464. doi: 10.1007/s00269-004-0412-0

Lasaga, A.C. (1979), Multicomponent exchange and diffusion in silicates. Geochem Cosmochem Acta 43:455-469. doi: 10.1016/0016-7037(79)90158-3

Lasaga, A.C. (1983), Geospeedometry: An Extension of Geothermometry. in: Saxena S.K.(ed.) Kinetics and Equilibrium in Mineral Reactions, Advances in Physical Geochemistry pp. 81-114

Lasaga, A.C., Jiang, J. (1995), Thermal history of rocks; P-T-t paths for geospeedometry, petrologic data, and inverse theory techniques. Am J Sci 295:697-741. doi: 10.2475/ajs.295.6.697

Liu, L. (1983), Phase transformations, earthquakes and the descending lithosphere. Phys Earth Planet Inter 32:226-240. doi: 10.1016/0031-9201(83)90128-0

Liu, L.-G. (1978), High-pressure phase transformations of albite, jadeite and nepheline. Earth Planet Sci Lett 37:438-444. doi: 10.1016/0012-821X(78)90059-6

Loomis, T.P. (1978), Multicomponent diffusion in garnet; I, Formulation of isothermal models. Am J Sci 278:1099-1118

Loomis, T.P., Ganguly, J., Elphick, S.C. (1985), Experimental determination of cation diffusivities in aluminosilicate garnets. Contrib Mineral Petrol 90:45-51. doi: 10.1007/BF00373040

Mackwell, S., Bystricky, M., Sproni, C. (2005), Fe–Mg Interdiffusion in (Mg,Fe)O. Phys Chem Miner 32:418-425. doi: 10.1007/s00269-005-0013-6

Manning, J.R. (1968), Diffusion kinetics for atoms in crystals. Van Nostrand, Princeton

Mei, S., Kohlstedt, D.L. (2000), Influence of water on plastic deformation of olivine aggregates 2. Dislocation creep regime. J Geophys Res 105(B9):21471-21481

Misener, D.J. (1974), Cationic diffusion in olivine to 1400 °C and 35 kbar. in: Geochemical Transport and Kinetics, Carnegie Institution of Washington, Washington, pp. 117-129

Morioka, M. (1980), Cation diffusion in olivine—I. Cobalt and magnesium. Geochim Cosmochem Acta 44:759-762. doi: 10.1016/0016-7037(80)90165-9

Mosenfelder, J.L., Marton, F.C., Ross, C.R., Kerschhofer, L., Rubie, D.C. (2001), Experimental constraints on the depth of olivine metastability in subducting lithosphere. Phys Earth Planet Inter 127:165-180. doi: 10.1016/S0031-9201(01)00226-6

Nakamura, A., Schmalzried, H. (1983), On the nonstoichiometry and point defects of olivine. Phys Chem Miner 10:27-37. doi: 10.1007/BF01204323

Nixon, P.H., Rogers, N.W., Gibson, I.L., Grey, A. (1981), Depleted and Fertile Mantle Xenoliths from Southern African Kimberlites. Annu Rev Earth Planet Sci 9:285-309. doi: 10.1146/annurev.ea.09.050181.001441

Oguri, K., Funamori, N., Sakai, F., Kondo, T., Uchida, T., Yagi, T. (1997), High-pressure and high-temperature phase relations in diopside $CaMgSi_2O_6$. Phys Earth Planet Inter 104:363-370. doi: 16/S0031-9201(97)00029-0

Oishi, Y., Ando, K., Kurokawa, H., Hirsco, Y. (1983), Oxygen Self-Diffusion in MgO Single Crystals. J Am Ceram Soc 66:C-60-C-62. doi: 10.1111/j.1151-2916.1983.tb15695.x

Ono, S., Ito, E., Katsura, T. (2001), Mineralogy of subducted basaltic crust (MORB) from 25 to 37 GPa, and chemical heterogeneity of the lower mantle. Earth and Planetary Science Letters 190:57-63. doi: 10.1016/S0012-821X(01)00375-2

Orman, J.A.V., Fei, Y., Hauri, E.H., Wang, J. (2003), Diffusion in MgO at high pressures: Constraints on deformation mechanisms and chemical transport at the core-mantle boundary. Geophys Res Lett 30:4 PP. doi: 200310.1029/2002GL016343

Pandey, A., Leech, M., Milton, A., Singh, P., Verma, P.K. (2010), Evidence of former majoritic garnet in Himalayan eclogite points to 200-km-deep subduction of Indian continental crust. Geology 38:399 -402. doi: 10.1130/G30584.1

Perchuk, A.L., Burchard, M., Schertl, H.-P., Maresch, W.V., Gerya, T.V., Bernhardt, H.-J., Vidal, O. (2008), Diffusion of divalent cations in garnet: multi-couple experiments. Contrib Mineral Petrol 157:573-592. doi: 10.1007/s00410-008-0353-6

Poirier, J.-P. (1985), Creep of Crystals: High-Temperature Deformation Processes in Metals, Ceramics and Minerals. Cambridge University Press, Cambridge

Poirier, J.P. (1981), On the kinetics of olivine-spinel transition. Phys Earth Planet Inter 26:179-187. doi: 10.1016/0031-9201(81)90006-6

Putnis, A. (1992), An Introduction to Mineral Sciences. Cambridge University Press, Cambridge

Ranalli, G. (2001), Mantle rheology: radial and lateral viscosity variations inferred from microphysical creep laws. J Geodyn 32:425-444. doi: 10.1016/S0264-3707(01)00042-4

Ranalli, G., Fischer, B. (1984), Diffusion creep, dislocation creep, and mantle rheology. Phys Earth Planet Inter 34:77-84. doi: 10.1016/0031-9201(84)90086-4

Rigby, E.B., Cutler, I.B. (1965), Interdiffusion Studies of the System Fe_xO-MgO. J Am Ceram Soc 48:95-99. doi: 10.1111/j.1151-2916.1965.tb11806.x

Ringwood, A.E. (1956), The Olivine-Spinel Transition in the Earth's Mantle. Nature 178:1303-1304. doi: 10.1038/1781303a0

Ringwood, A.E. (1962), A Model for the Upper Mantle. J Geophys Res 67:PP. 857-867. doi: 196210.1029/JZ067i002p00857

Ringwood, A.E., Major, A. (1966), Synthesis of Mg_2SiO_4 – Fe_2SiO_4 spinel solid solutions. Earth Planet Sci Lett 1:241-245. doi: 16/0012-821X(66)90077-X

Ringwood, A.E., Major, A. (1970), The system Mg_2SiO_4 – Fe_2SiO_4 at high pressures and temperatures. Phys Earth Planet Inter 3:89-108. doi: 16/0031-9201(70)90046-4

Ringwood, A.E., Major, A. (1971), Synthesis of majorite and other high pressure garnets and perovskites. Earth Planet Sci Lett 12:411-418. doi: 10.1016/0012-821X(71)90026-4

Roermund, H. van (2009), Mantle-wedge garnet peridotites from the northernmost ultra-high pressure domain of the Western Gneiss Region, SW Norway. Eur J Mineral 21:1085-1096. doi: 10.1127/0935-1221/2009/0021-1976

Rubie, D.C. (1984), The olivine --> spinel transformation and the rheology of subducting lithosphere. Nature 308:505-508. doi: 10.1038/308505a0

Rubie, D.C. (1990), Mechanisms of reaction-enhanced deformability in minerals and rocks. in: Barber D.J., Meredith P.G.(eds.) Deformation Processes in Minerals, Ceramics and Rocks, Unwin Hyman, London, pp. 262-295

Rubie, D.C., Ross, C.R. (1994), Kinetics of the olivine-spinel transformation in subducting lithosphere: experimental constraints and implications for deep slab processes. Phys Earth Planet Inter 86:223-243. doi: 10.1016/0031-9201(94)05070-8

Ryerson, F.J., Durham, W.B., Cherniak, D.J., Lanford, W.A. (1989), Oxygen Diffusion in Olivine: Effect of Oxygen Fugacity and Implications for Creep. J Geophys Res 94(B4):4105-4118

Sata, N., Goto, K.S. (1982), Oxygen-Pressure Dependence of Cation Interdiffusivity in Magnesiowustite Solid Solutions. J Am Ceram Soc 65:158-162. doi: 10.1111/j.1151-2916.1982.tb10386.x

Sautter, V., Jaoul, O., Abel, F. (1988), Aluminum diffusion in diopside using the $^{27}Al(p,\gamma)^{28}Si$ nuclear reaction: preliminary results. Earth Planet Sci Lett 89:109-114. doi: 10.1016/0012-821X(88)90036-2

Schmeling, H., Monz, R., Rubie, D.C. (1999), The influence of olivine metastability on the dynamics of subduction. Earth Planet Sci Lett 165:55-66. doi: 10.1016/S0012-821X(98)00249-0

Schwandt, C.S., Cygan, R.T., Westrich, H.R. (1995), Mg self-diffusion in pyrope garnet. Am Mineral 80:483 -490

Schwandt, C.S., Cygan, R.T., Westrich, H.R. (1996), Ca self-diffusion in grossular garnet. Am Mineral 81:448 -451

Schwandt, C.S., Cygan, R.T., Westrich, H.R. (1998), Magnesium self-diffusion in orthoenstatite. Contrib Mineral Petrol 130:390-396. doi: 10.1007/s004100050373

Sharp, T.G., Rubie, D.C. (1995), Catalysis of the Olivine to Spinel Transformation by High Clinoenstatite. Science 269:1095 -1098. doi: 10.1126/science.269.5227.1095

Shimojuku, A., Kubo, T., Ohtani, E., Nakamura, T., Okazaki, R., Dohmen, R., Chakraborty, S. (2009), Si and O diffusion in $(Mg,Fe)_2SiO_4$ wadsleyite and ringwoodite and its implications for the rheology of the mantle transition zone. Earth Planet Sci Lett 284:103-112. doi: 10.1016/j.epsl.2009.04.014

Shimojuku, A., Kubo, T., Ohtani, E., Yurimoto, H. (2004), Silicon self-diffusion in wadsleyite: Implications for rheology of the mantle transition zone and subducting plates. Geophys Res Lett L13606

Silver, P.G., Beck, S.L., Wallace, T.C., Meade, C., Myers, S.C., James, D.E., Kuehnel, R. (1995), Rupture Characteristics of the Deep Bolivian Earthquake of 9 June 1994 and the Mechanism of Deep-Focus Earthquakes. Science 268:69 -73. doi: 10.1126/science.268.5207.69

Sipling, P.J., Yund, R.A. (1973), Kinetics of Al/Si disordering in alkali feldspars. 185-193

Song, S., zhang, L., Niu, Y. (2004), Ultra-deep origin of garnet peridotite from the North Qaidam ultrahigh-pressure belt, Northern Tibetan Plateau, NW China. Am Mineral 89:1330-1336

Stretton, I., Heidelbach, F., Mackwell, S., Langenhorst, F. (2001), Dislocation creep of magnesiowüstite (Mg0.8Fe0.2O). Earth Planet Sci Lett 194:229-240. doi: 10.1016/S0012-821X(01)00533-7

Sung, C.-M., Burns, R.G. (1976), Kinetics of high-pressure phase transformations: Implications to the evolution of the olivine → spinel transition in the downgoing lithosphere and its consequences on the dynamics of the mantle. Tectonophysics 31:1-32. doi: 10.1016/0040-1951(76)90165-7

Tsai, T.-L., Dieckmann, R. (2002), Variation of the oxygen content and point defects in olivines, $(Fe_xMg_{1-x})_2SiO_4$, $0.2 \leq x \leq 1.0$. Phys Chem Miner 29:680-694. doi: 10.1007/s00269-002-0283-1

Vaughan, P.J., Coe, R.S. (1981), Creep mechanism in Mg_2GeO_4: Effects of a phase transition. J Geophys Res 86:389-404. doi: 198110.1029/JB086iB01p00389

Vielzeuf, D., Baronnet, A., Perchuk, A.L., Laporte, D., Baker, M.B. (2007), Calcium diffusivity in alumino-silicate garnets: an experimental and ATEM study. Contrib Mineral Petrol 154:153-170. doi: 10.1007/s00410-007-0184-x

Watson, E.B., Dohmen, R. (2010), Non-traditional and Emerging Methods for Characterizing Diffusion in Minerals and Mineral Aggregates. Rev Mineral Geochem 72:61 -105. doi: 10.2138/rmg.2010.72.3

Weertman, J., White, S., Cook, A.H. (1978), Creep Laws for the Mantle of the Earth [and Discussion]. Phil Trans R Soc A 288:9 -26. doi: 10.1098/rsta.1978.0003

Wiens, D.A., McGuire, J.J., Shore, P.J. (1993), Evidence for transformational faulting from a deep double seismic zone in Tonga. Nature 364:790-793. doi: 10.1038/364790a0

Wiens, D.A., McGuire, J.J., Shore, P.J., Bevis, M.G., Draunidalo, K., Prasad, G., Helu, S.P. (1994), A deep earthquake aftershock sequence and implications for the rupture mechanism of deep earthquakes. Nature 372:540-543. doi: 10.1038/372540a0

Wiens, D.A., Snider, N.O. (2001), Repeating Deep Earthquakes: Evidence for Fault Reactivation at Great Depth. Science 293:1463 -1466. doi: 10.1126/science.1063042

Wilson, B.M. (2007), Igneous Petrogenesis A Global Tectonic Approach. Springer

Wright, K., Price, G.D. (1993), Computer Simulation of Defects and Diffusion in Perovskites. J Geophys Res 98:22

Yamazaki, D., Irifune, T. (2003), Fe–Mg interdiffusion in magnesiowüstite up to 35 GPa. Earth Planet Sci Lett 216:301-311. doi: 10.1016/S0012-821X(03)00534-X

Yamazaki, D., Kato, T., Yurimoto, H., Ohtani, E., Toriumi, M. (2000), Silicon self-diffusion in $MgSiO_3$ perovskite at 25 GPa. Phys Earth Planet Inter 119:299-309. doi: 10.1016/S0031-9201(00)00135-7

Zhang, X., Ganguly, J., Ito, M. (2009), Ca–Mg diffusion in diopside: tracer and chemical inter-diffusion coefficients. Contrib Mineral Petrol 159:175-186. doi: 10.1007/s00410-009-0422-5

Chapter 2: Garnets and diffusion kinetics

2.1 Garnets and majorite, a high pressure polymorph of enstatite

2.1.1 Garnet

Garnet minerals form an important group of rock forming minerals. Since natural garnets are metastable at ambient conditions, they are only found at the Earth's surface in metamorphic terranes of amphibolite facies and higher grade. This paragraph summarizes the most important properties of natural garnets, for a more comprehensive discussion the reader is referred to Geller (1967), Rickwood (1968) and Novak and Gibbs (1971). Most of the information in this paragraph can be found in these references, unless stated otherwise.

Table 2.1: Chemical composition of the most important garnet end-members.

End-member name	Chemical formula
Pyrope	$Mg_3Al_2Si_3O_{12}$
Almandine	$Fe^{2+}_3Al_2Si_3O_{12}$
Grossular	$Ca_3Al_2Si_3O_{12}$
Spessartine	$Mn_3Al_2Si_3O_{12}$
Andradite	$Ca_3Fe^{3+}_2Si_3O_{12}$
Uvarovite	$Ca_3Cr_2Si_3O_{12}$
Skiagite	$Fe^{2+}_3Fe3+_2Si_3O_{12}$
Hydrogrossular	$Ca_3Al_2H_{12}O_{12}$
Hydroandradite	$Ca_3Fe^{3+}_2H_{12}O_{12}$

Natural garnets are often described in terms of end-member components, which are listed in table 2.1 .

The space group of natural garnet is $Ia\bar{3}d$, which is one of the cubic Bravais lattices, and the unit cell contains 8 formula units (160 atoms). Its lattice parameters depend on composition (and physical conditions), but range at ambient conditions between a = 11.4 Å for pyrope to a = 12.7 Å for the (hypothetical) end-member hydrogrossular.

The 96 oxygen atoms in garnet occupy the h-position in this unit cell, and the metal cations either occupy the 16 a-positions (octahedral sites), 24 c-positions (dodecahedral sites) or 24 d-positions (tetrahedral sites). Though natural garnets have 96 oxygen atoms and 64 metal cations in its unit cell, it can conveniently be described by the general chemical formula $X_3Y_2Z_3O_{12}$. The X metal cations (Mg, Fe2+, Ca and Mn) occupy the distorted cubic c sites of garnets, the Y metallic cations (Al^{3+}, Fe^{3+}, Cr^{3+}) occupy the octahedral sites, and the Z metallic cations (mostly Si^{4+}) occupy the tetrahedral sites. The tetrahedra share two edges with the neighbouring dodecahedra, the octahedra share six edges with neighbouring dodecahedra and the dodecahedra share two edges with neighbouring tetrahedra, four with neighbouring and four with other neighbouring dodecahedra (figure 2.1).

Since garnet is a common mineral in high pressure metamorphic terranes and its end-members form a complete solid-solution with each other, they are often used when in equilibrium with other phases as geothermometers. O'Neill and Wood (1979) calibrated a thermometer for the Mg-Fe exchange between garnet and olivine, and geothermometer were developed for Fe-Mg exchange between garnet and biotite (Holdaway 2000), between clinopyroxene and garnet (Ellis and Green 1979, Powell 1985)., and between orthopyroxene and garnet (Harley 1984). Next to its use as a geothermometer, garnet is also often used as a geochronometer dating metamorphic event, using the Lu-Hf, Sm-Nd and U-Pb systems. Therefore, garnet constitute an

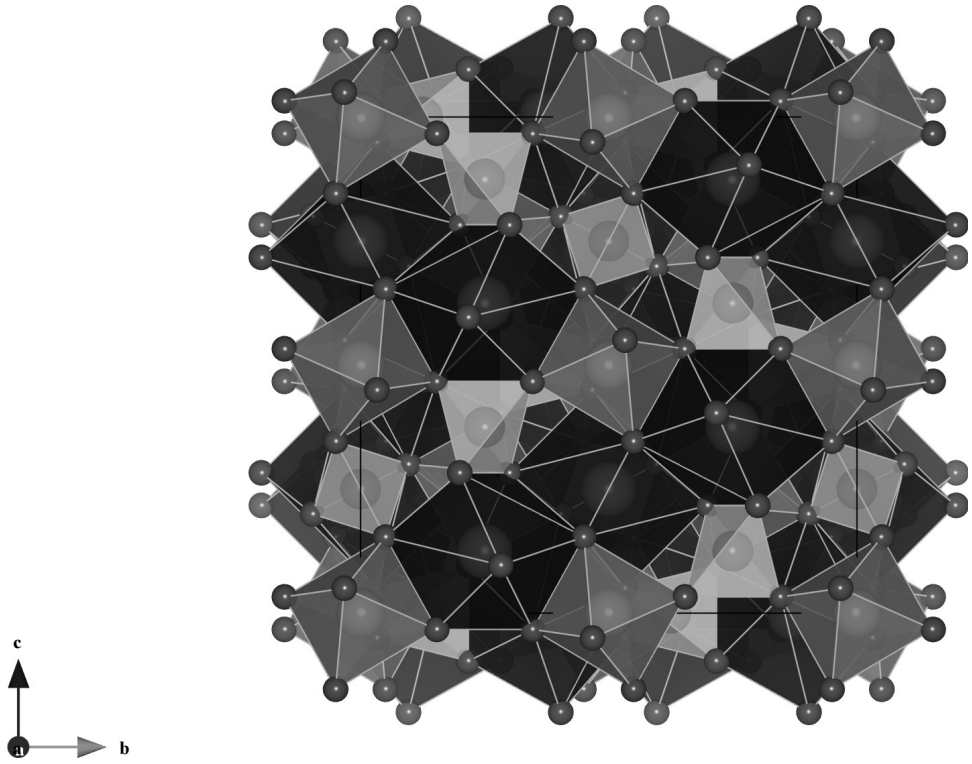

Figure 2.1: Structural model of the garnet unit cell looking down one of the a axes, dark gray cubic sites are occupied by divalent cation, middle gray octahedral sites by trivalent cations and light gray tetrahedral sites by Si^{4+} for natural garnets.

important mineral group elucidating the history of the Earth.

2.1.2 Majorite

Majorite ($Mg_4Si_4O_{12}$) is a high pressure polymorph of enstatite ($MgSiO_3$) with the garnet structure and hints to its existence were first reported by Ringwood and Major (1966), when they synthesized a high pressure garnet phase with an alumina deficient pyrope composition. The first natural occurrence of majorite was reported by Mason et al. (1968) in the Coorare meteorite, though they misinterpreted it as having an olivine composition and thus identified it as a being a high pressure polymorph of olivine. Smith and Mason (1970) later identified it correctly as being a high pressure polymorph of enstatite and assigned the name Majorite to it, in honour of Alan Major. The first successful synthesis of end-member majorite was done by Kato and Kumazawa (1985) during melting experiments on $MgSiO_3$, though the recovered garnet phase was not cubic (like pyrope) but tetragonal. Angel et al. (1989) investigated twinning observed in quenched high temperature majorite, and showed that it has tetragonal symmetry with space group $I4_1/a$ at ambient conditions. They concluded that ordering of Mg and Si on the octahedral sites reduces the symmetry of the structure from $Ia\bar{3}d$ to $I4_1/a$. Heinemann (1996) and Heinemann et al. (1997) performed a more detailed study to the twinning observed in majorite and to the phase change of cubic majorite to tetragonal majorite. Both Heinemann et al. (1997) and Angel et al. (1989) describe two morphologically distinct sets of twins, i.e. one set of twins with irregularly curved domain boundaries corresponding to perfect merohedral twins with {110} as reflection planes and a set of pseudomerohedral twins with a lamellar geometry related to each other by a twin law involving a three fold

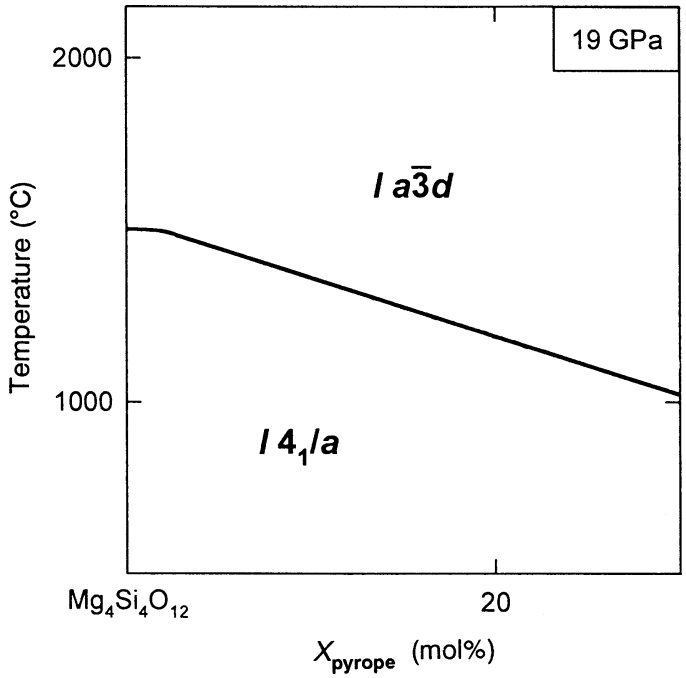

Figure 2.2: The stability domains of tetragonal ($I4_1/a$) and cubic ($Ia\bar{3}d$) majoritic garnet in composition – temperature space at 19 GPa.
After Heinemann et al. (1997)

rotation axis about [111]. Heinemann et al. (1997) showed that the pseudomerohedral twins were the result of transformational twinning during quenching of the sample, during which a cubic majorite phase having space group $Ia\bar{3}d$ transformed to tetragonal $I4_1/a$ majorite, and thus proving the stability of a cubic majorite phase at higher temperatures.

They also showed that the transition from $I4_1/a$ to $Ia\bar{3}d$ was dependent on the alumina content of the majoritic garnet and determined the critical transformation concentration to be at 20 mol% pyrope in majoritic garnet at 19 GPa and ± 1200 °C, as well as that the phase transformation was of second order, i.e. gradual both in terms of composition and temperature. Figure 2.2 shows the position of the phase transition from $Ia\bar{3}d$ to $I4_1/a$ as function of composition and temperature.

Because majorite has the same structure and very similar lattice parameters, a = 11.52 Å and c = 11.42 Å for the tetragonal end-member (Heinemann et al. 1997), as the other natural garnets, it forms a solid-solution with them. Though end-member majorite ($Mg_4Si_4O_{12}$) is only stable at conditions above 17 GPa and 1600 °C (Gasparik 2003), alumina or equivalently, the addition of a pyrope component stabilizes the garnet structured high-pressure polymorph of enstatite to lower pressures and temperatures (Ringwood and Major 1966, Akaogi and Akimoto 1977, Gasparik 2003). The majorite component in garnet that is in equilibrium with enstatite increases therefore with increasing pressure (figure 2.3). As a result, more enstatite can be incorporated into garnet as a majorite component with increasing pressure. In Earth's upper mantle, a majoritic garnet phase is therefore thought to be the second most abundant phase after the high pressure polymorphs of olivine (wadsleyite and ringwoodite) in the Transition Zone (Irifune 1987, Frost 2008).

2.1.3 Majoritic garnet and UHP rocks

In the last one and a half decades majoritic garnet has become in the focus of metamorphic petrologists, since

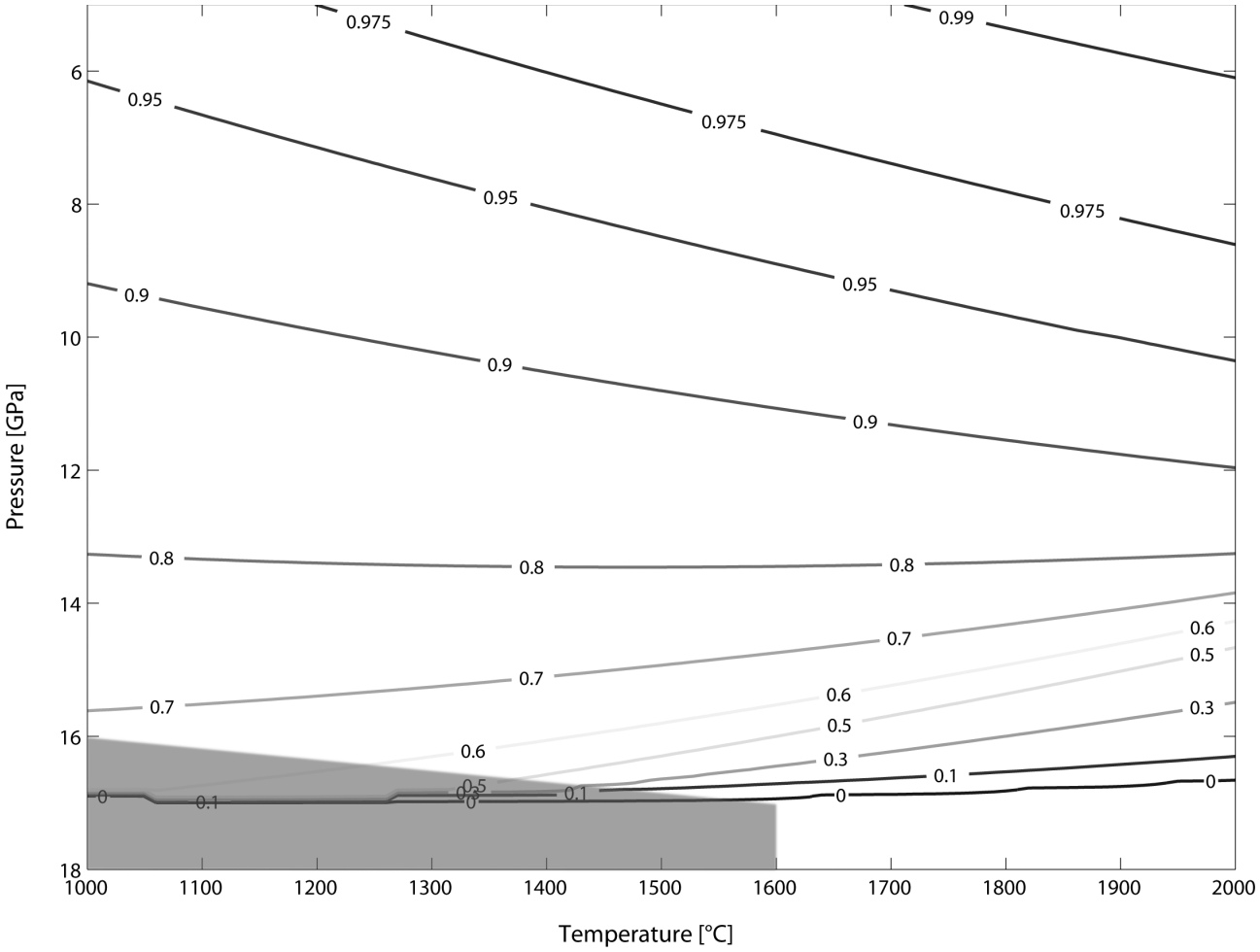

Figure 2.3: The composition of garnet in equilibrium with ortho / clino-enstatite as function of pressure and temperature in the MAS system on the pyrope – enstatite join. Majorite – (ortho/clino)-enstatite equilibrium thermodynamic data from Gasparik (2003), composition of ortho-enstatite calculated using the geothermobarometer of Brey et al. (2008), above 10 GPa pyroxene composition is assumed to be pure end-member (clino/ortho)-enstatite. The concentration of the contours shows the pyrope content of the garnet phase, a concentration of zero means pure end-member majorite ($Mg_4Si_4O_{12}$) is stable. The gray shaded area indicates the region where clino-enstatite and/or majoritic garnet is not stable.

needles and lamellae of pyroxene in garnet with a topotactic relation to the garnet have been found in ulta-high pressure (UHP) metamorphic terranes. Van Roermund and Drury (1998) found that garnets in peridotite bodies in the northern-most UHP domain of the Western Gneiss Region (WGR) of the Scandinavian Caledonides in Norway contain pyroxene lamellae with a topotaxial relation to their host garnet and which are interpreted as being exsolution products during exhumation of garnets with a majorite component. Later, intercrystalline pyroxene with an extremely depleted LREE signature indicating that the intercrystalline pyroxene also exsolved from the garnet host and cannot be attributed to melt addition. This indicated that the minimal depth of origin of these garnet peridotite should be in the order of 350 km (Van Roermund et al. 2000, Spengler 2006, Spengler et al. 2006). Spengler (2006) also demonstrated on the basis of LREE partitioning between garnet and its exsolution products that exsolution took place at temperatures above 1300 °C. They fitted this in a model of a rising diapir or convection cell originating from the mantle transition zone. Dating of the exsolution assemblage by Spengler (2006) (referred as the M_2 assemblage by him) indicated that this happened during mid-

Proterozoic times; 1405 ± 13 Ma. More recently, Scambelluri et al. (2008) also identified a younger generation of pyroxene exsolutions from garnet (referred to by them as M_3 garnets), which can be demonstrated to be Scandian in age since they are filling cracks that cross cut earlier Scandian structures. The amount of pyroxene that is present in the M_3 pyroxene exsolution needles in garnet indicates peak metamorphic conditions during the Scandian event of 5.5 – 6.5 GPa and 900 – 1000 °C. Similar conditions for Scandian metamorphism have recently also been found by other geothermobarometric methods (Vrijmoed et al. 2006, Spengler et al. 2009). Up to present, pyroxene exsolutions from garnet indicating a majoritic parent garnet have only been confirmed in the northern-most UHP domain (Nordøyane) and only in one case could the formation of majoritic garnet be dated to Scandian UHP metamorphism (van Roermund 2009). The juxtapositioning of (U)HP rocks next to low pressure upper crustal rocks with only a couple of kilometers stratigraphical thickness in between them in the WGR (e.g. in the Nordfjord area) requires that during the late stages of Scandian tectonism exhumational displacement along the Nordfjord-Sogn Detachment Zone (NSDZ), the principal extensional structure in the WGR, must have amounted to at least 100 – 150 km of displacement in order to bring UHP rocks to their current stratigraphical position (Hacker et al. 2003, 2010, Andersen 2010).

The Scandinavian Caledonides is not the only orogen where UHP metamorphic conditions in the majoritic garnet stability field have been deduced. Song et al. (2003, 2004) have reported UHP conditions for the North Qaidam orogenic belt in Tibet, including the observation of pyroxene exsolution lamellae from garnet, again indicating the stability of a majorite component in garnet. The presence of pyroxene exsolutions after majoritic garnet has also been reported for the Sulu UHP belt in China (Ye et al. 2000). Rather recently, clinopyroxene exsolution needles in garnet have also been described for the Himalaya's (Pandey et al. 2010).

2.2 Diffusion in minerals

At elevated temperatures during a metamorphic event and in the deep Earth, significant solid state diffusion occurs in minerals present in the Earth over geological time scales. The rate at which mineral assemblages equilibrate under changed conditions during metamorphic events is usually limited, and therefore controlled, by the diffusivity of the components in the respective minerals. Chemical zoning observed in many minerals from metamorphic terranes is usually interpreted as a result of non-complete equilibration under metamorphic conditions and may give more detailed information of the (thermal) geological history of a geological terrane (Lasaga 1983, Sautter and Harte 1990, Lasaga and Jiang 1995). In this section a more detailed overview is given about diffusion in geological materials.

2.2.1 The different diffusion coefficients

In the literature one often finds different diffusion coefficients due to differences in experimental setup , measurement methods and simply convention of usage. These can unfortunately not all be directly related to each other. The self diffusion coefficient is defined as the coefficient describing the diffusivity of an element as response to its own concentration gradients *sensu stricto*. It is a kind of theoretical quantity, which cannot be

determined experimentally. The tracer diffusion coefficient is determined tracer diffusion experiment, where one measures the diffusivity of elements using different isotopes of the same atom in a chemically homogeneous media. Diffusion in these kind of experiments is solely due to differences in concentration of the isotopes of interest, and usually assumed to be equal to the self diffusion coefficient, however, for light elements a significant isotopic effect may exist (Richter et al. 2003, Teng et al. 2006). The chemical diffusion coefficient is determined in experiment where there is a gradient in the chemical potential of the element of interest. In these kind of experiments the gradient in chemical potential serves as an additional driving force for diffusion, next to the concentration gradient. Finally, sometimes interdiffusion coefficients are reported, these are diffusion coefficients when more then one element or component are diffusing at the same time. Considering mass conservation as well as the Gibbs – Duhem equation one can see that the fluxes in an interdiffusion experiment have to be coupled and so the relevant diffusion coefficients have to be coupled. Because of the nature of interdiffusion experiments, interdiffusion coefficients are also chemical diffusion coefficients.

2.2.2 Fick's laws

The most basic phenomenological description of diffusion is given by Fick's laws. The first law describes flux of material J in response to a concentration gradient:

$$J = D \nabla C \tag{2.1}$$

The coefficient D is called the diffusion coefficient. Fick's second law can be obtained by considering conservation of mass in an arbitrary volume V which is bound by a surface S.

The concentration change per unit time in V is equal to the flux in or out of the volume

$$\int_V \frac{\partial C}{\partial t} dV = \int_S J \cdot n \, dS$$

Applying Gauss' theorem and by considering that this equation should hold for any arbitrary volume one obtains:

$$\frac{\partial C}{\partial t} = \nabla \cdot (D \nabla C) = \nabla D \nabla C + D \nabla^2 C \tag{2.2}$$

When gradients in D can be neglected this reduces to:

$$\frac{\partial C}{\partial t} = D \nabla^2 C \tag{2.3}$$

Which is known as Fick's second law.

2.2.3 Pressure and temperature dependence

The diffusivity of a species usually increases with increasing temperature and decreases with increasing pressure. The temperature dependence of the diffusion coefficient is usually described by an Arrhenian type relation:

$$D(T) = D_0 \exp\left(-\frac{\Delta H}{RT}\right) \tag{2.4}$$

where ΔH is the activation enthalpy of diffusion, R the gas constant and T temperature. D_o is a pre-exponential factor that among others can be related to the entropy increase due to diffusion, geometric factors and jump frequency of the atom (Mehrer 2005). The pressure dependence can be obtained from 2.4 and the following equation relating thermodynamic potentials:

$$\Delta H = \Delta E - p\,\Delta V$$

leading to:

$$D(T, p) = D_0 \exp\left(-\frac{\Delta E - p\,\Delta V}{RT}\right) \tag{2.5}$$

where ΔE is the activation energy, p pressure and ΔV the activation volume. Since the activation volume is generally small, pressure effects only become significant when considering diffusion phenomena over a range of several GPa.

2.2.4 Vacancies and oxygen fugacity

Minerals that contain elements that can have multiple oxidations states, most importantly iron, the oxygen fugacity can have also a significant on the diffusivity of elements. The diffusivity of ions in a crystal lattice is controlled by the concentration of vacancies, since an ion can only hop to an adjacent site if there is a vacancy on this site. Therefore the diffusion coefficient can also be described in terms of the number of vacancies and the diffusivity of vacancies (Schmalzried 1981)

$$D_i = D_v N_v \tag{2.6}$$

Where D_v is the diffusion coefficient for the vacancy and N_v is the mole fraction of vacant sites. Vacancies can either be intrinsic or extrinsic. Intrinsic vacancies exist because a small amount of vacancies will increase the disorder in the structure and thus increase the total entropy of the system, which outweighs the energy that is needed to create a vacancy. The mole fraction of intrinsic vacancies can be described by the following equation (Kittel 2005):

$$N_v = e^{-\Delta E_v / RT} \tag{2.7}$$

where ΔE_V is the energy required to make a vacancy and to put the displaced atom on the surface, R is the gas constant and T is temperature. Extrinsic vacancies are due to impurities in the crystal with a valence state different than the ion that would normally occupy the site, for example Al^{3+} on a Si^{4+} site. The incorporation of such an impurity requires either a second impurity to be incorporated or the creation of a vacancy to charge balance the structure. A second kind of extrinsic vacancies are produced by elements that have multiple valence states, iron being the (geologically) most important. In an oxidizing environment Fe^{2+} will be oxidized to Fe^{3+} creating a vacancy on the iron site for charge balance. Using Kröger-Vink notation, it can be written (Morioka and Nagasawa 1991):

$$3\,Fe_{Fe} + \tfrac{1}{2}\,O_2(gas) \leftrightharpoons 2\,Fe^{\bullet}_{Fe} + V''_{Fe} + FeO \qquad (2.8)$$

for which the equilibrium constant can be written as:

$$K = \frac{[Fe^{\bullet}_{Fe}]^2 [V''_{Fe}]\, a_{FeO}}{fO_2^{1/2}} \qquad (2.9)$$

Where [ ] denotes the concentrations of the reactants. Subscripts in the two above equations denote the site that is occupied by the ion (V for vacancy) and the superscript denotes the electrical charge of the site. A solid circle denotes that the site is positively charged (every solid circle corresponds to an electron hole), a prime denotes a negatively charged site (every prime corresponds to a surplus electron).

From equation 2.8 it can be seen that $[Fe^{\bullet}_{Fe}] = 2\ [V''_{Fe}]$ and assuming that activity of FeO does not change significantly with oxygen fugacity fO_2 they write the concentration of iron or metal vacancies as function of oxygen fugacity as:

$$[V''_{Fe}] \propto fO_2^{1/6} \qquad (2.10)$$

This mechanism requires that Fe^{3+} can be accommodated on an Fe^{2+} site, which might be questionable for normal garnets, since as of yet, there is no convincing evidence that Fe^{3+} can occupy the dodecahedral site in garnet (C. McCammon, pers. comm.). However, for majoritic garnet it has been found that there is charge transfer between adjacent docecahedrally coordinated Fe^{2+} and octahedral coordinated Fe^{3+} (Keppler and McCammon 1996), so the dodecahedrally coordinated Fe^{3+} ion (directly after oxidation) might receive an electron from its neighbouring octahedrally coordinated Fe^{2+} ion, effectively exchanging its 3+ charge with the 2+ charge of its octahedral neighbour. However the strong partitioning between Mg and Fe on the octahedral site in majorite, with Mg preferentially on the octahedral site (O'Neill et al. 1993), might inhibit this mechanism. Also the presence of octahedrally coordinated ferrous iron in majorite might enable the above mentioned mechanism at higher pressure. Mackwell et al. (2005) developed the following general expression based upon point defect chemistry:

$$\tilde{D} = D_V^0 e^{-Q_m/RT}\left(k_1^0 + k_2^0 fO_2^m x^p e^{-(Q_f + \alpha x)/RT}\right) \qquad (2.11)$$

where k°_1 and k°_2 are equilibrium constants for the intrinsic and extrinsic vacancy mechanisms respectively, m and p are constants depending on the vacancy mechanism (1/6 for equation 2.8), Q_m is the migration enthalpy for a metal vacancy, Q_f the formation enthalpy for metal vacancies at low iron concentrations, x is the iron concentration and the term $-\alpha \cdot x$ in the exponential corrects for change in formation enthalpy at higher iron and vacancy levels.

2.2.5 Multi-component models

When more than one component or element is diffusing at the same time, as a result of mass conservation and from the Gibbs-Duhem equation, their fluxes have to be coupled. Irreversible thermodynamics shows that fluxes can often be linearly related to their driving forces (Groot and Mazur 1984). In the absence of temperature gradients and external forces the driving force for diffusion in an n-component system becomes

the gradient in chemical potential μ_i of the components (Groot and Mazur 1984, Ganguly 2002):

$$J_i = -\sum_{k}^{n-1} L_{ik}\left(\frac{\nabla(\mu_k - \mu_n)}{T} \right) \tag{2.12}$$

Where L is a matrix of phenomenological coefficients. The last flux is calculated considering conservation of mass. In the case that the off diagonal elements in L can be neglected the equation leads to the following expression for the diffusion coefficient D_i:

$$D_i = D_i^{+}\left(1 + \frac{\partial \ln \gamma_i}{\partial \ln C_i} \right) \tag{2.13a}$$

where γ_i is the activity coefficient and

$$D_i^{+} = \frac{RL_i}{C_i} \tag{2.13b}$$

where R is the gas constant. Equation (2.13a) splits the chemical diffusion coefficient in two parts, an ideal part and a thermodynamic part, the part within brackets is usually referred to the thermodynamic factor. Note that although off diagonal terms in L are negligible, the diffusion coefficients and fluxes still coupled through the activity coefficients.

In the case that the off diagonal terms in L are not negligible one needs to rewrite (2.1) as:

$$J_i = -\sum_{j} D_{ij} \nabla C_j \tag{2.14}$$

Loomis (1978) derived an expression for the diffusion coefficient matrix **D** from irreversible thermodynamics:

$$D_{ij} = \delta_{ij} D_i^0 + D_i^0 X_i \left[\frac{\partial \ln \gamma_i}{\partial X_j} - \frac{\partial \ln \gamma_i}{\partial X_n} \right] - X_i \sum_{k=1}^{n-1} X_k (D_k^0 - D_n^0) \left[\frac{\delta_{jk}}{X_k} + \frac{\partial \ln \gamma_k}{\partial X_j} - \frac{\partial \ln \gamma_k}{\partial X_n} \right] \tag{2.15a}$$

δ_{ij} is kronecker's delta ($\delta_{ij} = 0$ for $i \neq j$, $\delta_{ij} = 1$ for $i = j$) and D_i° denotes the tracer diffusion coefficient for component i. In the case of ideal solutions this reduces to:

$$D_{ij} = \delta_{ij} D_i^0 + X_i (D_n^0 - D_j^0) \tag{2.15b}$$

Lasaga (1979) derived, also from irreversible thermodynamics, a different expression for the D matrix in the case of ionic diffusion, which is more appropriate to minerals:

$$\begin{aligned} D_{ij} = D_i^0 \delta_{ij} + D_i^0 c_i \left[\frac{\partial \ln \gamma_i}{\partial c_j} - \frac{\partial \ln \gamma_i}{\partial c_n} \cdot \frac{z_j}{z_n} \right] - \left(\frac{D_i^0 z_i c_i}{\sum_{k=1}^{n} z_k^2 c_k D_k^0} \right) \times \\ \left\{ z_j (D_j^0 - D_n^0) + \sum_{k=1}^{n} z_k c_k D_k^0 \left[\frac{\partial \ln \gamma_k}{\partial c_j} - \frac{\partial \ln \gamma_k}{\partial c_n} \cdot \frac{z_i}{z_n} \right] \right\} \end{aligned} \tag{2.16a}$$

which reduces for (near) ideal solutions or negligible activity coefficient gradients to a more comprehensible form:

$$D_{ij} = D_i^0 \delta_{ij} - \frac{D_i^0 z_i z_j}{\sum_{k=1}^{n} z_k^2 c_k D_k^0} \cdot (D_j^0 - D_n^0) \qquad (2.16b)$$

In the equations z_i is the charge of ion i and the size of the diffusion matrix D is (n – 1)x(n – 1), the last profile is calculated by charge balance. In the case that there are only two ions diffusing, both with an equal charge, equation 2.10b becomes the well known expression for binary interdiffusion of charged species (Manning 1968):

$$D_{11} = D_{binary}^{ionic} = \frac{D_1^0 D_2^0}{X_1 D_1^0 + X_2 D_2^0} \qquad (2.17)$$

where X_i is the cation mole fraction of cation i, i.e. $X_1 = c_1 / (c_1 + c_2)$. Chakraborty and Ganguly (1992) used the ideal Lasaga model successfully to model Fe – Mg – Mn diffusion profiles in garnet and to obtain tracer diffusion coefficients for Fe, Mg and Mn. The validity of the model for garnets was confirmed by a Mg tracer diffusion study on garnet by Chakraborty and Rubie (1996).

2.3 References

Akaogi, M., Akimoto, S. (1977), Pyroxene-garnet solid-solution equilibria in the systems $Mg_4Si_4O_{12}$ – $Mg_3Al_2Si_3O_{12}$ and $Fe_4Si_4O_{12}$ – $Fe_3Al_2Si_3O_{12}$ at high pressures and temperatures. Phys Earth Planet Inter 15:90-106. doi: 10.1016/0031-9201(77)90013-9

Andersen, T.B. (2010), Excursion Guide, Western Norway 3-4 June 2010. Burial and exhumation of High and Ultra-High-Pressure Rocks.

Angel, R.J., Finger, L.W., Hazen, R.M., Kanzaki, M., Weidner, D.J., Liebermann, R.C., Veblen, D.R. (1989), Structure and twinning of single-crystal $MgSiO_3$ garnet synthesized at 17 GPa and 1800 °C. Am Mineral 74:509-512

Chakraborty, S., Ganguly, J. (1992), Cation diffusion in aluminosilicate garnets: experimental determination in spessartine-almandine diffusion couples, evaluation of effective binary diffusion coefficients, and applications. Contrib Mineral Petrol 111:74-86. doi: 10.1007/BF00296579

Chakraborty, S., Rubie, D.C. (1996), Mg tracer diffusion in aluminosilicate garnets at 750-850° C, 1 atm. and 1300° C, 8.5 GPa. Contrib Mineral Petrol 122:406-414. doi: 10.1007/s004100050136

Ellis, D.J., Green, D.H. (1979), An experimental study of the effect of Ca upon garnet-clinopyroxene Fe-Mg exchange equilibria. Contr Mineral Petrol 71:13-22. doi: 10.1007/BF00371878

Frost, D.J. (2008), The Upper Mantle and Transition Zone. Elements 4:171-176

Ganguly, J. (2002), Diffusion kinetics in minerals: Principles and applications to tectono-metamorphic processes. in: Gramaccioli C.M.(ed.) Energy Modelling in Minerals, EMU notes in mineralogy 4, European Mineralogical Union, Vienna

Gasparik, T. (2003), Phase diagrams for geoscientists: an atlas of the earth's interior. Springer, Heidelberg-Berlin

Geller, S. (1967), Crystal chemistry of the garnets. Z Kristallogr 125:1-47

Groot, S.R.D., Mazur, P. (1984), Non-Equilibrium Thermodynamics. Dover Publications

Hacker, B.R., Andersen, T.B., Johnston, S., Kylander-Clark, A.R.C., Peterman, E.M., Walsh, E.O., Young, D. (2010), High-temperature deformation during continental-margin subduction & exhumation: The ultrahigh-pressure Western Gneiss Region of Norway. Tectonophysics 480:149-171. doi: 10.1016/j.tecto.2009.08.012

Hacker, B.R., Andersen, T.B., Root, D.B., Mehl, L., Mattinson, J.M., Wooden, J.L. (2003), Exhumation of high-pressure rocks beneath the Solund Basin, Western Gneiss Region of Norway. J Metamorph Geol 21:613-629. doi: 10.1046/j.1525-1314.2003.00468.x

Harley, S.L. (1984), An experimental study of the partitioning of Fe and Mg between garnet and orthopyroxene. Contrib Mineral Petrol 86:359-373. doi: 10.1007/BF01187140

Heinemann, S. (1996), Der Phasenünergang kubisch - tetragonal im System der Granate Majorit ($Mg_4Si_4O_{12}$) - Pyrop ($Mg_3Al_2Si_3O_{12}$). Bayreuth

Heinemann, S., Sharp, T.G., Seifert, F., Rubie, D.C. (1997), The cubic-tetragonal phase transition in the system majorite ($Mg_4Si_4O_{12}$) – pyrope ($Mg_3Al_2Si_3O_{12}$), and garnet symmetry in the Earth's transition zone. Phys Chem Miner 24:206-221. doi: 10.1007/s002690050034

Holdaway, M.J. (2000), Application of new experimental and garnet Margules data to the garnet-biotite geothermometer. Am Mineral 85:881-892

Irifune, T. (1987), An experimental investigation of the pyroxene-garnet transformation in a pyrolite composition and its bearing on the constitution of the mantle. Phys Earth Planet Inter 45:324-336. doi: 10.1016/0031-9201(87)90040-9

Kato, T., Kumazawa, M. (1985), Garnet phase of $MgSiO_3$ filling the pyroxene-ilmenite gap at very high temperature. Nature 316:803-805. doi: 10.1038/316803a0

Keppler, H., McCammon, C.A. (1996), Crystal field and charge transfer spectrum of (Mg, Fe)SiO_3 majorite. Phys Chem Miner 23: doi: 10.1007/BF00202304

Kittel, C. (2005), Introduction to solid state physics. Wiley, New York

Lasaga, A.C. (1979), Multicomponent exchange and diffusion in silicates. Geochem Cosmochem Acta 43:455-469. doi: 10.1016/0016-7037(79)90158-3

Lasaga, A.C. (1983), Geospeedometry: An Extension of Geothermometry. in: Saxena S.K.(ed.) Kinetics and Equilibrium in Mineral Reactions, Advances in Physical Geochemistry pp. 81-114

Lasaga, A.C., Jiang, J. (1995), Thermal history of rocks; P-T-t paths for geospeedometry, petrologic data, and

inverse theory techniques. Am J Sci 295:697-741. doi: 10.2475/ajs.295.6.697

Loomis, T.P. (1978), Multicomponent diffusion in garnet; I, Formulation of isothermal models. Am J Sci 278:1099-1118

Mackwell, S., Bystricky, M., Sproni, C. (2005), Fe–Mg Interdiffusion in (Mg,Fe)O. Phys Chem Miner 32:418-425. doi: 10.1007/s00269-005-0013-6

Manning, J.R. (1968), Diffusion kinetics for atoms in crystals. Van Nostrand, Princeton

Mason, B., Nelen, J., White, J.S. (1968), Olivine-Garnet Transformation in a Meteorite. Science 160:66 -67. doi: 10.1126/science.160.3823.66

Mehrer, H. (2005), Diffusion: Introduction and Case Studies in Metals and Binary Alloys. in: Heitjans P., Kärger J. (eds.) Diffusion in Condensed Matter: methods, materials, models, Springer, pp. 3-65

Morioka, M., Nagasawa, H. (1991), Ionic Diffusion in Olivine. in: Ganguly J.(ed.) Diffusion, Atomic Ordering and Mass Transport, Advances in Physical Geochemistry 8, Springer-Verlag, New York, p.

Novak, G.A., Gibbs, G.V. (1971), The crystal chemistry of the silicate garnets. Am Mineral 56:791-825

O'Neill, H.S.C., McCammon, C.A., Canil, D., Rubie, D.C., Ross, C.R., Seifert, F. (1993), Mössbauer spectroscopy of mantle transition zone phases and determination of minimum Fe^{3+} content. Am Mineral 78:456-461

O'Neill, H.S.C., Wood, B.J. (1979), An experimental study of Fe-Mg partitioning between garnet and olivine and its calibration as a geothermometer. Contrib Mineral Petrol 70:59-70. doi: 10.1007/BF00371872

Pandey, A., Leech, M., Milton, A., Singh, P., Verma, P.K. (2010), Evidence of former majoritic garnet in Himalayan eclogite points to 200-km-deep subduction of Indian continental crust. Geology 38:399 -402. doi: 10.1130/G30584.1

Powell, R. (1985), Regression diagnostics and robust regression in geothermometer/geobarometer calibration: the garnet-clinopyroxene geothermometer revisited. J Metamorph Geol 3:231-243. doi: 10.1111/j.1525-1314.1985.tb00319.x

Richter, F.M., Davis, A.M., DePaolo, D.J., Watson, E.B. (2003), Isotope fractionation by chemical diffusion between molten basalt and rhyolite. Geochem Cosmochem Acta 67:3905-3923. doi: 10.1016/S0016-7037(03)00174-1

Rickwood, P.C. (1968), On recasting analyses of garnet into end-member molecules. Contrib Mineral Petrol 18:175-198. doi: 10.1007/BF00371808

Ringwood, A.E., Major, A. (1966), High-pressure transformations in pyroxenes. Earth Planet Sci Lett 1:351-357. doi: doi: DOI: 10.1016/0012-821X(66)90023-9

Roermund, H. van (2009), Mantle-wedge garnet peridotites from the northernmost ultra-high pressure domain of the Western Gneiss Region, SW Norway. Eur J Mineral 21:1085-1096. doi: 10.1127/0935-1221/2009/0021-1976

Roermund, Van, Drury (1998), Ultra-high pressure (P > 6 GPa) garnet peridotites in Western Norway: exhumation of mantle rocks from > 185 km depth. Terra Nova 10:295-301. doi: 10.1046/j.1365-3121.1998.00213.x

Roermund, Van, Drury, Barnhoorn, Ronde, De (2000), Super-silicic garnet microstructures from an orogenic garnet peridotite, evidence for an ultra-deep (>6 GPa) origin. J Metamorph Geol 18:135-147. doi: 10.1046/j.1525-1314.2000.00251.x

Sautter, V., Harte, B. (1990), Diffusion gradients in an eclogite xenolith from the Roberts Victor kimberlite pipe: (2) kinetics and implications for petrogenesis. Contrib Mineral Petrol 105:637-649. doi: 10.1007/BF00306530

Scambelluri, M., Pettke, T., Roermund, H.L.M. van (2008), Majoritic garnets monitor deep subduction fluid flow and mantle dynamics. Geology 36:59-62. doi: 10.1130/G24056A.1

Schmalzried, H. (1981), Solid state reactions. Verlag Chemie, Weinheim/Bergstr. [West Germany] ▪

Smith, J.V., Mason, B. (1970), Pyroxene-Garnet Transformation in Coorara Meteorite. Science 168:832 -833. doi: 10.1126/science.168.3933.832

Song, S.G., Yang, J.S., Xu, Z.Q., Liou, J.G., Shi, R.D. (2003), Metamorphic evolution of the coesite-bearing ultrahigh-pressure terrane in the North Qaidam, Northern Tibet, NW China. J Metamorph Geol 21:631-644. doi: 10.1046/j.1525-1314.2003.00469.x

Song, S., zhang, L., Niu, Y. (2004), Ultra-deep origin of garnet peridotite from the North Qaidam ultrahigh-pressure belt, Northern Tibetan Plateau, NW China. Am Mineral 89:1330-1336

Spengler, D. (2006), Origin and Evolution of Deep Upper Mantle Rocks from Western Norway. PhD Thesis, Utrecht

Spengler, D., Brueckner, H.K., Roermund, H.L.M. van, Drury, M.R., Mason, P.R.D. (2009), Long-lived, cold burial of Baltica to 200 km depth. Earth Planet Sci Lett 281:27-35. doi: doi: DOI: 10.1016/j.epsl.2009.02.001

Spengler, D., Roermund, H.L.M. van, Drury, M.R., Ottolini, L., Mason, P.R.D., Davies, G.R. (2006), Deep origin and hot melting of an Archaean orogenic peridotite massif in Norway. Nature 440:913-917. doi: 10.1038/nature04644

Teng, F.-Z., McDonough, W.F., Rudnick, R.L., Walker, R.J. (2006), Diffusion-driven extreme lithium isotopic fractionation in country rocks of the Tin Mountain pegmatite. Earth Planet Sci Lett 243:701-710. doi: 10.1016/j.epsl.2006.01.036

Vrijmoed, J.C., Roermund, H.L.M. Van, Davies, G.R. (2006), Evidence for diamond-grade ultra-high pressure metamorphism and fluid interaction in the Svartberget Fe–Ti garnet peridotite–websterite body, Western Gneiss Region, Norway. Mineral Petrol 88:381-405. doi: 10.1007/s00710-006-0160-6

Ye, K., Cong, B., Ye, D. (2000), The possible subduction of continental material to depths greater than 200 km. Nature 407:734-736. doi: 10.1038/35037566

Chapter 3: Experimental and analytical techniques

3.1 High pressure – high temperature experiments

To simulate actual geological processes that are occurring in the Earth's upper mantle and transition zone one needs to reproduce the conditions prevalent there. It is usually assumed that heat transport due to thermal conduction is negligible in the Earth's mantle (Fowler 2005). The temperature profile in the mantle can thus be well approximated by an adiabatic temperature profile for which the temperature gradient as a function of depth r is given by (Fowler 2005):

$$\left(\frac{\partial T}{\partial r}\right)_S = \frac{-T\alpha g}{C_p} \tag{3.1}$$

where T is temperature, α is the coefficient of thermal expansion for the bulk mantle, g acceleration due to gravity and C_p the heat capacity at constant pressure. The figure below shows three different mantle adiabats for different potential temperatures, i.e. the temperature of the adiabat extrapolated to the surface, thought to be representative for the Earth's present mantle (McKenzie and Bickle 1988, Anderson 2000, Fowler 2005, Katsura et al. 2010).

To simulate the conditions prevalent in the mantle transition zone one thus needs a device to generate pressures in the range of 15 – 24 GPa (ca. 410 – 670 km) and temperatures in the range of 1450 – 1800 °C. Two different devices are generally used to reach these conditions, i.e. the diamond anvil cell and the multi-anvil apparatus. The last device has been used for this dissertation and is therefore explained in more detail below.

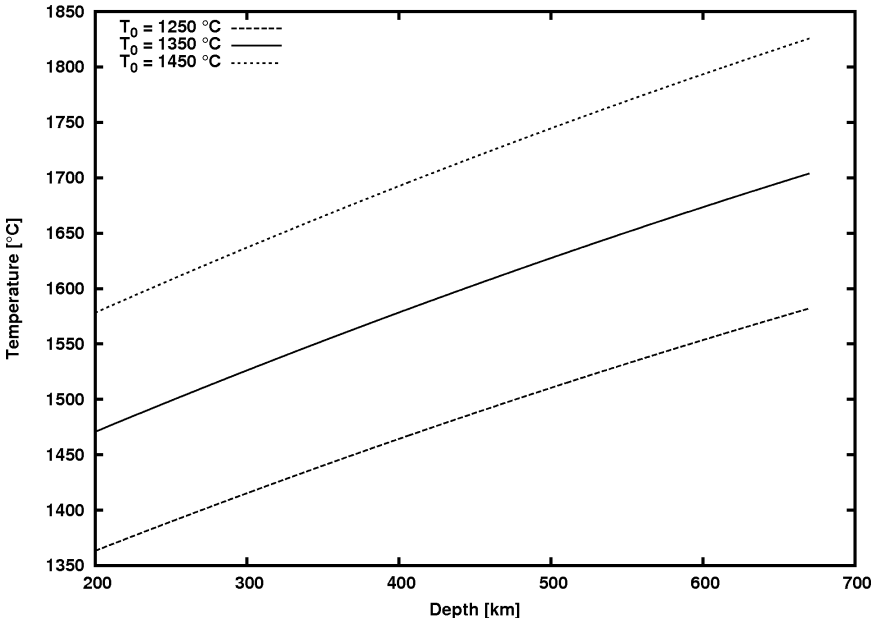

Figure 3.1:The mantle adiabat calculated for three different potential temperatures (temperatures extrapolated to the Earth's surface). The thermal expansion coefficient is taken from Katsura et al. (2010) and approximated by an exponentially decaying function as function of depth.

3.1.1 The Multi-anvil apparatus

High pressure devices can generate high pressures following two different approaches which can be understood from the general equation for pressure:

$$p = \frac{F}{A} \tag{3.2}$$

where p is pressure, F is force and A is the surface area over which the force is applied. The first approach would be to apply a reasonable force over a very small surface area, an example of such a device is the diamond anvil cell (DAC). The down side of this type of devices is that the sample volume is also very small, which might pose a problem with analytical techniques, and large pressure and temperature gradients exist in a DAC. The second approach is to generate a large force and apply this on a (reasonable) small surface area. Such a device is the multi – anvil press, which was used in this diffusion study. The sample volume that can be used in the multi-anvil apparatus is considerably larger than that of the DAC, and in addition it generates more hydrostatic conditions and temperature gradients within the assembly are smaller (Ito 2007).The down side of the multi-anvil apparatus is that in-situ measurements are more complicated than in the DAC, and generally require a high brilliance x-ray source like a synchrotron in the case of a study requiring x-rays (Keppler and Frost 2005).

The first modern multi-anvil device used in most laboratories now, was designed by Kawai and Endo (1970). It consisted of a 6 / 8 type split-sphere multi-anvil device. This means that a set of six hardened steel outer anvils that form a sphere when assembled were used as first stage anvils. The six outer anvils are truncated in such a way, that in the centre of the sphere they create a cubic cavity. In this cubic cavity a set of eight second stage tungsten carbide anvils are put. Each of the eight WC cubes has (at least) one of its corners truncated. Assembled, these WC cubes form an octahedral cavity in its centre in which the pressure medium with the

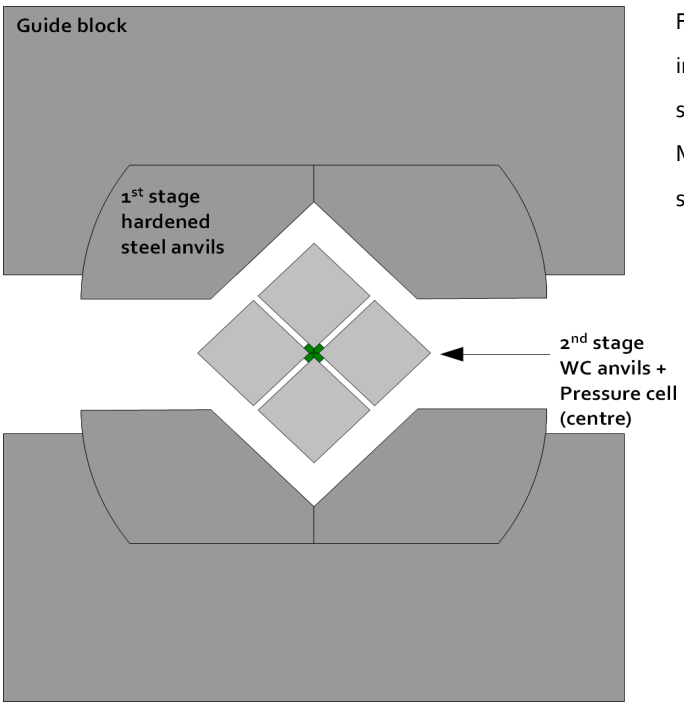

Figure 3.2: sketch of the 6 / 8 split-sphere design incorporated in a metal guide block. The top and lower part of the first stage anvils are truncated to inhibit rotation of the anvils. The MgO pressure cell has been put in the centre of the 8 WC cube second stage anvils, with truncated corners.

experimental load is placed. In the original design of Kawai and Endo the spherical assembly was contained in a rubber shell and then submerged in an oil reservoir. This oil reservoir was pressurized and the pressure exerted by the oil reservoir is then transmitted and concentrated by the anvils on the octahedral pressure medium contained within the octahedral cavity created by the WC anvils. In later designs the oil reservoir was replaced by guide blocks in which the lower and upper half of the spherical anvil assembly was placed, greatly reducing the cumbersome preparation of the experiments (Kawai et al. 1973). The upper and lower guide blocks are driven together by a uni-axial hydraulic press. The hydrostatic conditions in this case must be provided by using appropriate pressure media. In later designs the top and lower parts of the first stage anvils were truncated in order to inhibit the rotation of the anvils (Keppler and Frost 2005). Using traditional WC anvils the maximum attainable pressures are around 28 – 30 GPa, which is sufficient for the upper mantle, transition zone and top part of the lower mantle. Higher pressures however, can be obtained by using sintered diamond anvils, which are also more costly. Recently, pressures up to 90 GPa have been reached using a multi-anvil apparatus equipped with sintered diamond second stage anvils (Ito et al. 2010).

The cavity in the second stage anvils is filled with a (usually) MgO pressure cell, which needs to be longer than the truncation lengths of the WC anvils to generate the high pressure conditions. The maximum attainable pressure is dependent on the ratio of octahedral edge length to truncation edge length and their absolute sizes, the compressibility of the pressure medium, the resistance to plastic deformation of the anvils, the sealing action of the gasket material, and the maximum load of the press. As the pressure medium will get compressed during loading, the pressure medium will be extruded out of the octahedral cavity, forming a gasket. Usually an additional set of pyrophyllite gasket strips are placed around the octahedral cavity, to give better lateral support to the second stage anvil assembly and to prevent blow-outs (Ito 2007). At high loads most of the applied force by the press will be put in extruding the gasket material, and thus reducing the pressure generating efficiency of the press and the deformation properties of the gasket is thus an important factor in determining the maximum attainable pressure (Ito 2007).

In the early designs of Kawai and Endo (1970) and Kawai et al.(1973) the used pressure medium was pyrophyllite ($Al_2Si_4O_{10}(OH)_2$), which is a phyllosilicate mineral. However, pyrophyllite breaks down above 600 °C and 10 GPa successively into stishovite + an unknown hydrous aluminosilicate and stishovite + Al5Si5O17(OH) and above 20 GPa into stishovite + corundum, which resulted in a reduction of pressure during high pressure runs (Ito 2007). Nowadays, semi-sintered MgO (with a porosity of ~ 35%) is being used as pressure media. Under high temperatures MgO has a very low shear strength and thus generates a good hydrostatic pressure regime (Keppler and Frost 2005). Through the centre of one of the faces of the octahedron a cylindrical hole is drilled in which a hollow cylinder of ZrO_2 is put surrounding the heater. The role of the ZrO_2 cylinder is to thermally isolate the resistance heater, since the thermal conductivity of MgO is high, making it very difficult to heat the experiment above 1000 °C without the thermal insulator. Different materials can function as heater, the most common being a metal foil (e.g. platinum or rhenium), $LaCrO_3$, TiC_3 / diamond mixture or graphite heater. At the Bayerisches Geoinstitut usually $LaCrO_3$ heaters were used. $LaCrO_3$ also reduces temperature gradients within

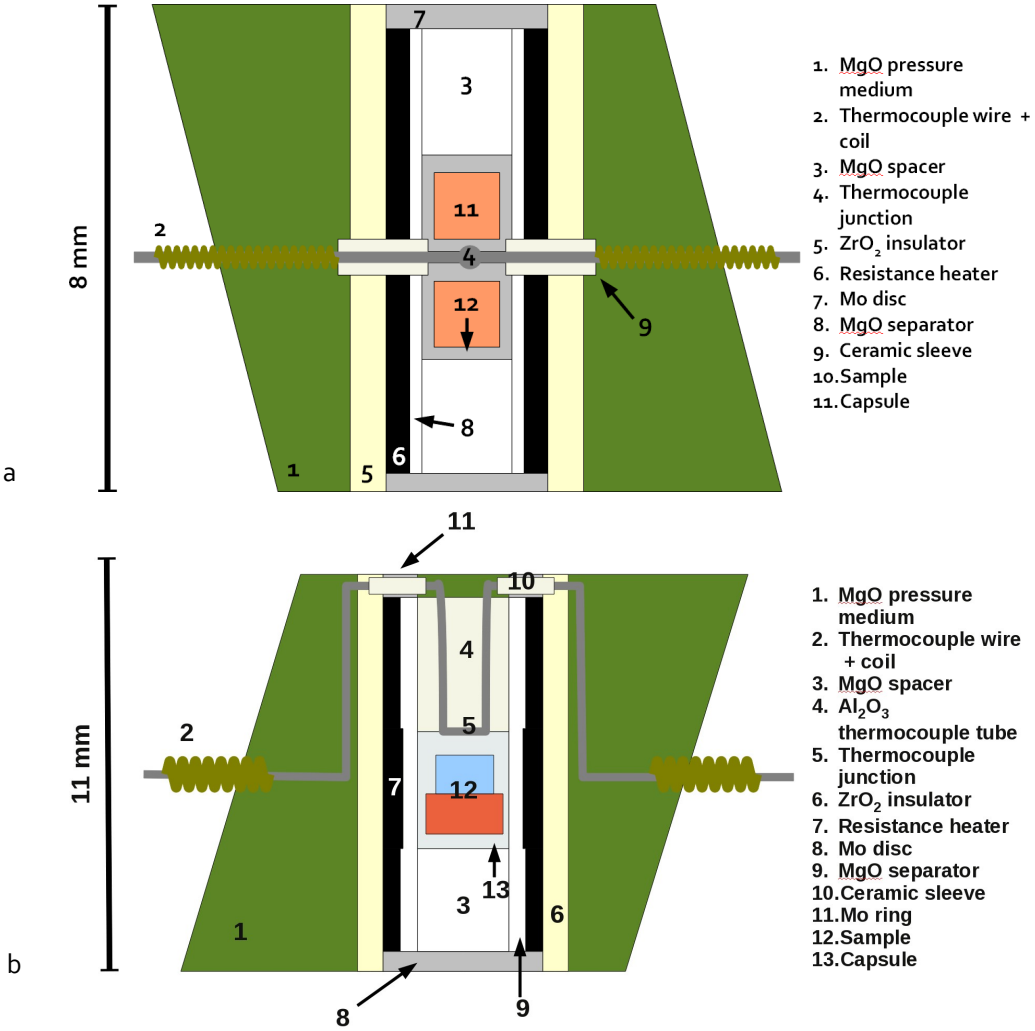

Figure 3.3: Two sketches of the MgO pressure cell used in the multi-anvil apparatus. a) Pressure cell with where the thermocouple is brought in radially. b) Pressure cell where the thermocouple is brought in axially. The former one is used at the Bayerisches Geoinstitut for smaller assemblies.

the furnace because of its negative resistance dependence on temperature, especially for smaller pressure cells (Kawashima and Yagi 1988). Further reduction of temperature gradients inside the furnace can be achieved by using a stepped heater, where the heater consists of three cylinders of which the thickness of the wall of the middle one is greater than the outer ones (Kawashima et al. 1990).

The temperature is measured by thermocouples in the multi-anvil apparatus. Thermocouples work because thermal gradients in (semi-)conductors induce an electrostatic potential difference between the hot and cold end, also known as the Seebeck effect. If two conductors (or metal) with different Seebeck coefficients are used to create a circuit, an electrical current will start to flow, of which the magnitude is dependent on the actual temperature gradient along the thermocouple wire. Thermocouples used in the multi-anvil usually consist of W3%Re – W25%Re thermocouple wires or W5%Re – W26%Re thermocouple wires because of their high melting points and the small pressure effect of thermocouple voltage on pressure, which is unknown quantitatively (Keppler and Frost 2005). The thermocouple can be incorporated in two ways in the octahedral pressure cell. The first way, and as used in the diffusion study in this dissertation, the thermocouple is put close to the capsule

in an axial direction, i.e. where the wire comes into the furnace from the top (figure 3.3a). To prevent the thermocouple from short circuiting on the molybdenum ring (which creates a good electrically conducting contact between the WC anvils and the heater), isolating ceramic tubes are put around the thermocouple wires, where the wires cross the ring. The thermocouple wires are then guided to the middle of one of the octahedron edges through a groove cut into the octahedron. In the second method, the thermocouple is put in the central portion of the pressure cell by drilling a hole through the heater and positioning the junction of the thermocouple through this hole next to the capsule. The hole in the heater however makes the heater more susceptible to breaking and it is impossible to do high temperature experiments, like melting experiments, with it (Ito 2007). With both methods a coil is put around the thermocouple wires where they exit the octahedron, to prevent the wires from breaking when the octahedron is (partially) extruded out from the octahedrally shaped cavity during the experiment. In the axial configuration, the thermocouple wires are led through a MgO or corundum tube from the top, where the thermocouple junction is made just above the capsule. If the capsule is made of a soft material, a disc-shaped rhenium foil can be put between the thermocouple junction and the capsule in order to prevent the thermocouple from penetrating the capsule.

The capsule material itself is also an important factor in the experiment. First of all, different materials have different melting temperatures, when doing high temperature experiments this has to be taken into account. When using sample material with elements that have different oxidation states, like iron or chromium, one usually makes capsules with a material that can buffer the oxygen fugacity, like iron, nickel, rhenium or graphite. Additionally, one can disperse oxygen fugacity buffering materials in the sample material to improve the buffering capability during the experiment (Frost et al. 2001). Multiple sample chamber assemblies have also been used, where the sample chambers were spark-eroded from a rhenium wire (Keppler and Frost 2005). Since the sample chambers in such a capsule are small, the absolute temperature gradients over these sample chambers are smaller, too. Moreover, one can do multiple experiments in one run using such a capsule. In the case that the capsule should not touch the heater, since it can short circuit it or react with the heater, isolating material like MgO is put between the heater and capsule. The same holds for the tube through which the thermocouple wires are guided from the top. Any remaining space within the furnace is usually filled up with (densified) MgO.

Since the heaters used in the pressure cell are resistance heaters, the individual WC cubes need to be isolated from each other, as not to short circuit the resistant heater. This is done by placing cardboard and / or Teflon tape on each of the three faces of the WC anvils facing each other. Using cardboard also prevents the gaskets from flowing easily, when placed behind the gaskets on the WC anvils. After assembling the eight WC cubes, sheets of mica or fibreglass epoxy sheets are put on the faces of the cubic assembly that are facing the first stage anvils to make it possible for the WC anvils to move and automatically centre themselves. A contact between the first stage anvils and the WC anvils, that are touching the molybdenum disc in the pressure cell, is made with the use of a piece of copper foil through the sheets.

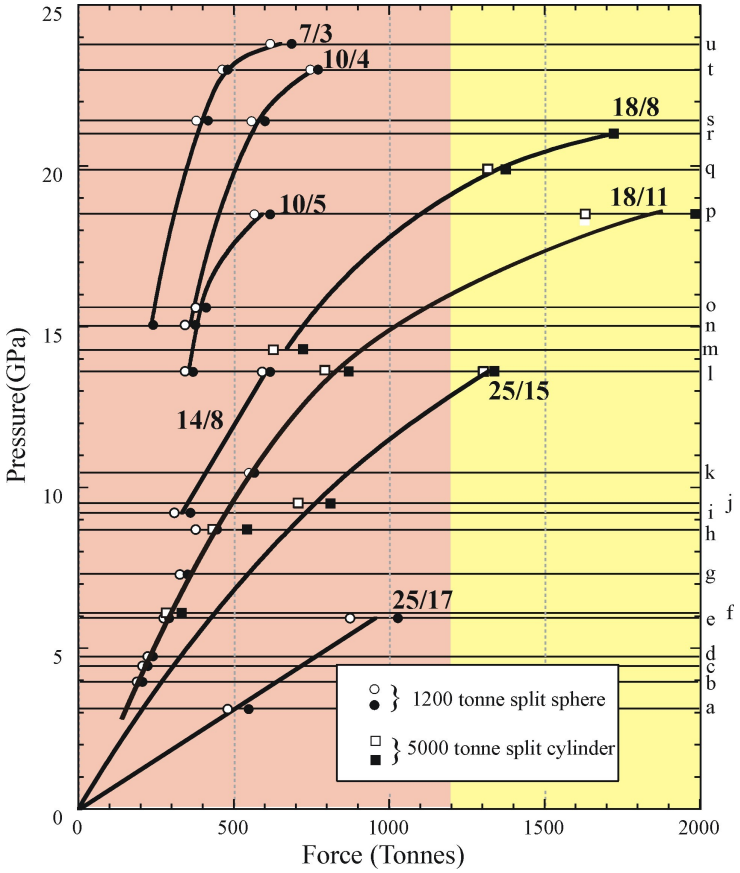

Figure 3.4: Pressure calibration curve for the 1000, 1200 and 5000 ton presses available at the Bayerisches Geoinstitut. Open and closed symbols denote the stability of high pressure side and low pressure sides of the phase transformation. The right light gray area denotes the pressure range only attainable in the 5000 ton press.

Since pressure generation in a multi-anvil apparatus is not 100% efficiently, the apparatus have to be calibrated for the assemblies used in it. In order to do so, known phase transitions are used to see which mechanical load corresponds to which sample pressure. This can be done in an in-situ way, where usually a phase transition alters the electrical conductivity of the sample material. Examples include the bismuth III – IV transition, and the semiconductor to metal phase change in the GaAs system (Ito 2007). When a multi-anvil apparatus is placed in a synchrotron beam line, one can also make use of x-ray diffraction to detect phase changes, enlarging the number of phase changes that can be used for pressure calibration. X-ray diffraction can also be used to calibrate pressure on the basis of unit cell volume of a phase, when the equation of state of the used phase is well known. When phase transitions are quenchable, they can also be used for calibration. The olivine to wadsleyite and clino-enstatite to majorite phase transitions are examples of phase transitions used for pressure calibration (Ito 2007).

Additional complications arise because there is no absolute pressure scale at high temperatures, which have lead to different labs placing different HPHT phase transitions at different pressures. Especially above 20 GPa the fact that an absolute pressure scale is not known results in a deviation in pressure calibrations between different labs (Keppler and Frost 2005). Calibration curves used at the Bayerisches Geoinstitut are shown in figure 3.4. Thought different presses are available, the variations in the applied load – pressure calibrations between the different presses are smaller than the errors of the calibration itself, and thus a single calibration curve can be used for each apparatus (Keppler and Frost 2005). As is apparent from figure 3.4, the calibration

curves flatten off towards higher applied load, since at higher load more force is put in deforming the gaskets because more material is extruded from the octahedral pressure chamber, and pressure generation is thus less efficient (Keppler and Frost 2005).

3.2 Transmission electron microscopy

The main analytical device used for obtaining the results presented in this dissertation was the Philips CM20 FEG transmission electron microscope (TEM). The TEM can both be used as an imaging device, which can image the microstructure of the specimen down to the nanometer scale, as well as an analytical device with a nanometer scale spatial resolution. This combination of techniques makes it a very powerful and versatile instrument. In this part I will go into more detail on the functioning of the TEM.

3.2.1 Sample preparation

To be able to observe the sample under the TEM one needs to thin it to a thickness where it becomes transparent to electrons, which means it needs to be thinned from ~ 30 µm, the typical thickness of a thin section, down to a thickness of ~ 100 nm. The step of sample preparation is one of most important steps in obtaining good data for a TEM study, especially when studying interfaces within materials, since these get amorphized preferentially (Malherbe 1994, Barna et al. 1999). Several techniques are available for reducing the thickness of a sample, however, all of them use in one way or another a beam of ionized atoms that are accelerated to an energy of several keV to tens of keV, after which they strike the sample and ablate material from the surface of the sample. In the studies presented in this thesis two methods have been used, using Ar ion-milling to thin a prepared thin section to electron transparency and cutting foils with the help of a dual beam Focussed Ion Beam / Scanning Electron Microscope (FIB/SEM) device.

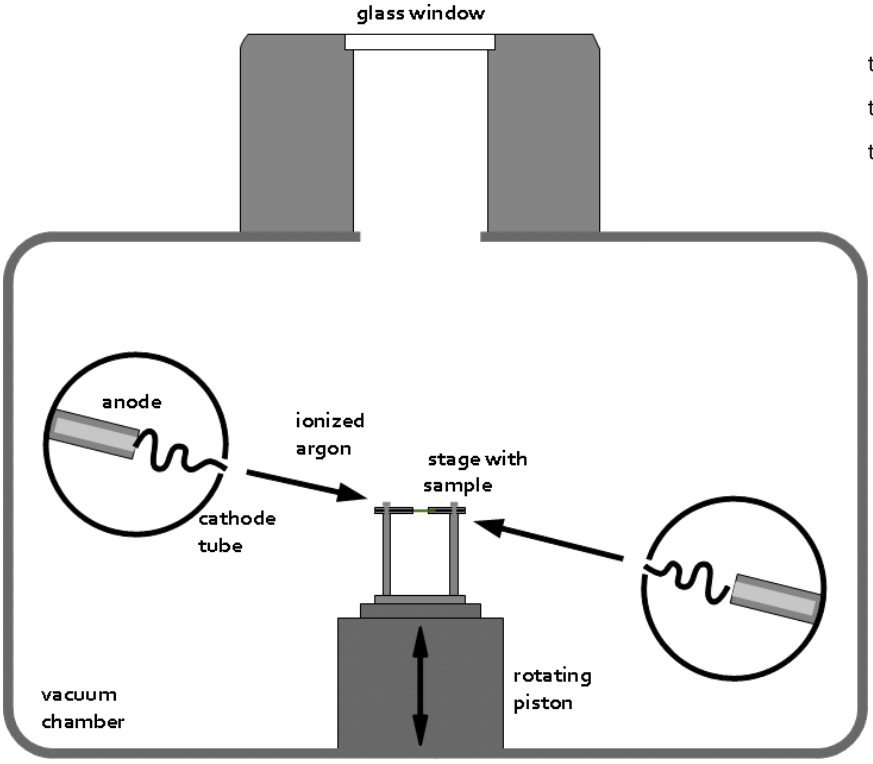

Figure 3.5: A schematic section through the Ar-ion milling vacuum chamber where the TEM specimen is thinned to electron transparency.

In an Ar ion-milling device the sample is loaded on a stage and lowered into a vacuum chamber. In this vacuum there are two Ar ion guns, on opposing sides of the sample. Each gun consists of an anode inside of a cathode tube with a small hole in it (figure 3.5). The anode is connected to an Ar supply, and since there is a several kV difference between the anode and cathode, Ar is ionized and accelerated through a hole in the cathode tube and directed at the specimen. As the accelerated Ar ions hit the surface of the specimen, they sputter the top surface layer of atoms away, by which the specimen is thinned. Ion milling usually results in two kinds of damage to the specimen, creation of topography on an initially flat surface and secondly the creation of an amorphous layer of material on the surface (Barna et al. 1999, Williams and Carter 2009). The first kind of damage can be reduced by rotating the sample while thinning and using a low incidence angle of the ion beam on the specimen, however due to the geometry of the holder, the lowest incidence angle that can be used for thinning in the ion milling device is 12 degrees. Rotation of the specimen reduces the creation of topography since the sputtering rate is dependent on the orientation of the incident ion beam relative to the crystal lattice of the crystallites in an aggregate (Barna and Menyhard 1994). Rotation of the specimen thus averages out (or at least reduces) the orientation dependent sputtering rate. Creation of a damaged or amorphous layer is harder to reduce. Typical operating conditions of ion miller are 2 – 5 kV, in this range ionization of the target can happen by electron exchange between the incident electron and specimen, and thus modifying the direct surface layer of the specimen (Malherbe 1994). As the incident ions impinge on the surface, the ion will lose its energy in two different way, either through electron interactions with atoms of the specimen, or by nuclear interaction (momentum transfer) with specimen atoms before it finally becomes trapped (implanted) within the specimen. Electronic interaction results in the ionization of specimen atoms. Nuclear interaction, or collision, between the incident ion and atoms of the specimen result in a momentum or energy transfer from the impinging ion to a specimen atom. Momentum transfer sets the atoms of the specimen in motion and leads to sputtering of the specimen atoms if the atoms is freed from the surface, or otherwise may lead to a cascade of collisions inside the specimen. If the impinging ion transfers enough energy, not a single cascade of collision will occur, but a group of atoms will be set simultaneously in motion, a so-called 'spike', which may completely amorphize a portion of the lattice (Malherbe 1994). The above mentioned processes are dependent on the incident angle, charge, mass and energy of the incident ion, and the properties of the target (Barna and Menyhard 1994, Barna et al. 1999, Williams and Carter 2009). The thickness of the damaged or amorphized layer thus will also vary with these variables. A higher energy of the incident ion increases penetration depth and thus the thickness of the damaged layer, whereas as higher mass of the incident ion decreases it penetration depth. A lower incident angle will decrease the thickness, though below an incident angle of 10° the dependence on the incidence angle becomes very weak (Barna et al. 1999). A multiply ionized incident ion will have a higher energy and thus create a thicker damage layer. Next to this, energy transfer of the incident ion to the specimen, may also result in heating of the specimen, which may also damage or modify the specimen, cooling therefore is required for some specimens (Williams and Carter 2009).

The dual beam FIB/SEM is a device that has both an electron optical system, serving as scanning electron

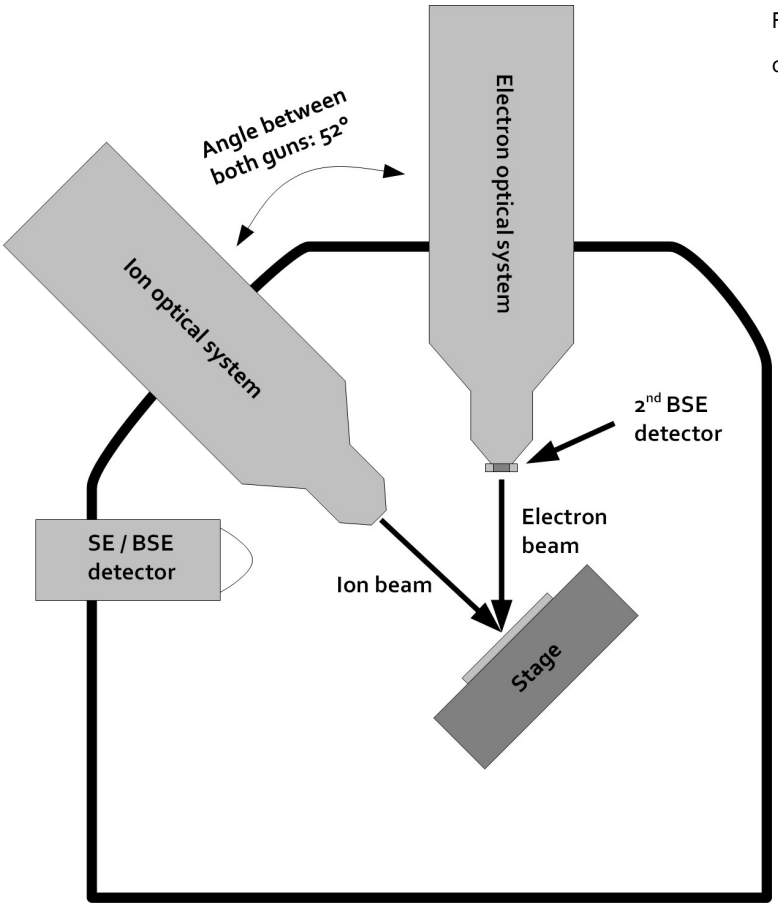

Figure 3.6 : A schematic overview of the sample chamber of the dual beam FIB/SEM.

microprobe, and an ion optical system, serving as focused ion beam, that can be operated simultaneously. Its main advantage over conventional Ar ion-milling, is that it can cut thin foils at very precise locations, i.e. submicron-level precision. Besides this, the combination of a well focused ion beam and small milling angles make it possible to produce thin foils that have nearly flat parallel faces. Preferential thinning of one phase is not a major issue in the FIB/SEM as can be the case for Ar ion-milling. In contrast to the ion-milling system which usually uses a beam of Ar ions, this kind of system uses a focused beam of Ga ions. The FIB system usually has two modes of operation, those being milling with the Ga beam and etch / deposition mode, where the interaction of a gas with the Ga ion beam results in the deposition of material, e.g. platinum or gold, or the injected gas etches the specimen. The ion beam and electron beam columns are usually at some angle to each other, in the FEI Quanta3D FEG system available at the Bayerisches Geoinstitut this is an angle of 52°, which simplifies the process of creating thin films for the TEM. During the first step of this process the feature of interest is searched for and then a platinum protection cap is deposited upon this feature. After this two wedge shaped trenches are cut on either side of the protective cap. Subsequently, the faces of the section that has been cut are cleaned from any contamination, and undercuts are made. A needle is then inserted and a physical connection is made with platinum between the needle and section. After this the section is cut loose from the bulk specimen and transferred to a grid where it is further cleaned and thinned to the desired thickness. Since the FIB/SEM also operates with an ion beam, it has the same disadvantage as the Ar ion milling device, in the sense that it also creates an amorphous layer on the surface of the section. However, since the operating

voltage of the FIB/SEM is 20 – 30 kV, penetration of the Ga ions is much deeper than for Ar ion milling. Different studies have shown that the thickness of the amorphous layer in nanometer on either side of the thin film is roughly equal to the operating voltage of the ion beam (Mayer et al. 2007). A 30 keV beam, would thus result in an amorphous layer 60 nm thick, which would make HRTEM on these specimens impossible. To remove this layer, the operating voltage of the ion beam can be lowered towards the final steps of preparation (Mayer et al. 2007). Another method that has been proposed is to perform the final step of creating a thin film in an Ar ion-milling device, where it is easier to produce very thin foils then in an FIB/SEM (Miyajima et al. 2010).

3.2.2 Basic principles of the TEM

The limit of detail that is visible in an optical microscope, also called the resolving power, was first studied by Ernst Abbe (1873), the founder together with Carl Zeiss of the Carl Zeiss company, probably most well known for its optical systems. The resolving power of a microscope can be approximated by (Hawkes 1972):

$$d = k\frac{\lambda}{n_0 \sin\theta_0} \tag{3.3}$$

where k is a geometric factor somewhere between 0.6 – 0.8, λ is the wavelength of the light employed and n_0 is the refractive index of the medium between the specimen and objective lense and θ_0 the maximum angle of the rays leaving the specimen that pass through the objective lens to contribute to the image, the product in the denominator is also called the numerical aperture. This means that the smallest detail we can see using a normal optical microscope is in the order of 200 nm, for a numerical aperature of 1.4. To obtain a higher resolving power, one thus need to either increase the numerical aperture or use a particle which has a smaller wavelength. Increasing the numerical aperture further is difficult, since the most non-corrosive immersion liquids have a refraction index smaller than 1.8, current day research grade microscopes have a numerical aperture of 1.4 – 1.5.

The problems in increasing the resolving power using electromagnetic radiation prompted Knoll and Ruska (1932) to develop a microscope not based upon electromagnetic radiation, but upon accelerated electrons. Louis de Broglie introduced in his 1925 doctoral thesis the concept of wave-particle duality, i.e. that with every moving particle a wave can be associated of which the phase moves through space faster than the speed of light, where he relates the wavelength λ of a particle to its momentum p, λ = h / p, where h is Planck's constant. The wavelength of accelerated electrons can thus described by:

$$\lambda = \frac{h}{(2 m_0 e V_r)^{1/2}} \tag{3.4a}$$

Where m_0 is the rest mass of an electron, e the charge of an electron and V_r is the 'relativistic accelerating voltage', i.e. the energy of the electron corrected for relativistic effect, which are significant in a TEM:

$$V_r = V_0 + \left(\frac{e}{2 m_0 c^2} \right) V_0^2 \tag{3.4b}$$

Where V_0 is the acceleration voltage and c the speed of light. Typical operating conditions for TEM are 80 kV to

200 kV (though high voltage TEMs go up to 3 MeV), which would thus correspond to a wavelength of 4.2 pm and 2.5 pm respectively. To compare, the radius of a silicon atom is 111 pm (1.1 Å).

Since high energy electrons cannot be focused by glass lenses (they would be absorbed and backscattered like in the case of bulk samples), magnetic lenses are used in a TEM. Those lenses consist of a hollow cylindrically symmetric soft magnetic core, i.e. the core is easily magnetized and demagnetized, surrounded by a copper coil which generates a radially symmetric magnetic field when a current flows through it. The objective lens is the most important and complicated lens in the TEM since it produces the image and diffraction pattern, which the other image forming lenses merely magnify (Williams and Carter 2009).

3.2.3 Elastic scattering within the specimen

As the electrons enter the specimen they will interact with the electrostatic potential of the specimen lattice, resulting in elastic scattering of the incident electrons. This kind of scattering is associated with only a negligible loss of energy of the incident electron beam. The other kind of scattering, inelastic scattering, where there is a significant transfer of energy between the involved particles is giving another kind of information, and is treated later. The TEM has four different modes of imaging:

- Diffraction mode
- Amplitude contrast imaging (BD/DF mode)
- High resolution mode (HRTEM)
- STEM mode

In diffraction mode an image of the back-focal plane of the objective lens is produced on the imaging plane. In the case that the incident electron beam is illuminating the specimen parallel, the image produced will consist of a pattern of spots. Each such a spot corresponds to a beam that is refracted from a plane that (nearly) satisfies the Bragg condition:

$$n\lambda = 2d\sin\theta_B \tag{3.5}$$

where n is an integer, d is the spacing of the refracting lattice planes and θ_B is the refraction angle (know as Bragg's angle). The diffraction pattern is defined by the intersection of the reciprocal lattice and the Ewald sphere, which can be shown to be a geometrical reconstruction of the Bragg conditions.

Amplitude contrast imaging can be done by either selecting the direct beam or one of the diffracted beams by the use of an objective aperture. In the former case it is called bright field (BF) imaging, in the latter case dark field (DF) imaging. The names originate from the fact that in DF imaging, holes in the foil appear black and the picture is generally darker than for BF imaging. These two imaging techniques can be used to image strain fields within crystals. Strain is defined by the displacement of an atom from its position that would be expected from the ordinary periodicity of the crystal. Causes of such a strain field can be dislocations, planar defects or other imperfections in the crystal lattice.

The distortion of the lattice around a dislocation core may alter the lattice in such a way that diffracted beams that are in the undistorted lattice not excited, become exited in the distorted lattice. The displacement field around a dislocation core for an isotropic solid is given by (Williams and Carter 2009):

$$\boldsymbol{R} = \frac{1}{2\pi}\left(\boldsymbol{b}\,\phi + \frac{1}{4(1-\nu)}\{\boldsymbol{b_e} + \boldsymbol{b}\times\boldsymbol{u}(2(1-2\nu)\ln r + \cos 2\phi)\}\right) \tag{3.6}$$

where $\mathbf{b}_e$ is the edge component of the burgers vector, ν Poisson's ratio and r and ϕ are the spherical coordinates along the dislocation line. The Howie-Whelan (HW) equations, the equations that describe the intensity of the direct and diffracted beam and thus the contrast in amplitude contrast images, can be modified to include a lattice distortion (Williams and Carter 2009):

$$\frac{d\phi_g}{dz} = \frac{\pi i}{\xi_0}\phi_g + \frac{\pi i}{\xi_g}\exp\left[-2\pi i(sz + \boldsymbol{g}\cdot\boldsymbol{R})\right] \tag{3.7}$$

where **g** is the diffracted beam used to image. The only difference to the HW-equations for an undistorted lattice is the additional **g**·**R** term, and thus only a change in contrast will be observed when the scalar product of the diffraction vector and displacement field will be non-zero. If the displacement field is the one corresponding to a pure screw dislocation **R** reduces to **R** = **b**ϕ / 2π. The dislocation for a screw dislocation will thus not be visible is the Burgers vector is perpendicular to the diffracted beam. In the case of a pure edge dislocation we need the complete form of 3.6, so the invisibility criteria become **g**·**b** = 0 and **g**·(**b** x **u**) = 0. The last term can be ascribed to the buckling of lattice planes perpendicular to both the Burgers vector and dislocation line (Williams and Carter 2009). Using dark field imaging, one can thus determine the Burgers vector and slip system of the studied phase.

Another type of defects are planar defects. Examples are stacking faults, anti-phase domain boundaries and grain boundaries. Again one can use a displacement vector **R** to describe the translation of the lattice over the planar defect, a point $\mathbf{r}_n$ corresponds on the other side of the planar fault to the point $\mathbf{r}_n' = \mathbf{r}_n + \mathbf{R}$. Since **R** on either side of the planar defect is independent of z, equation 3.7 comes down to adding a phase term to Howie-Whelan equations for the diffracted beam, which can be written as $e^{i\alpha}$; where α = 2π**g**·**R**. Again, no change will be visible when α = 0. When α ≠ 0, there will be a change in contrast depending on the depth of the planar defect. In the case of an inclined planar defect, light and dark fringes will be visible, since one needs to integrate 3.7 over the amount of foil under the planar defect. Similarly to dislocations, one can determine the displacement vector by a more detailed investigation of the fringes with different **g**·**R** conditions.

Bright field, dark field and weak beam dark field imaging are all amplitude contrast imaging techniques, which is one of the two main imaging modes of the TEM, as already explained. The other imaging mode is phase contrast imaging, where the contrast in the image is caused by interference of multiple beams. To do so, one uses an aperture if the back focal plane of the objective lens to let some of the diffracted beams pass through and block the others. When one selects a 2D array of diffracted beams in the objective aperture, a phase contrast image will be formed with a two dimensional structure. The image formed in HRTEM images can be

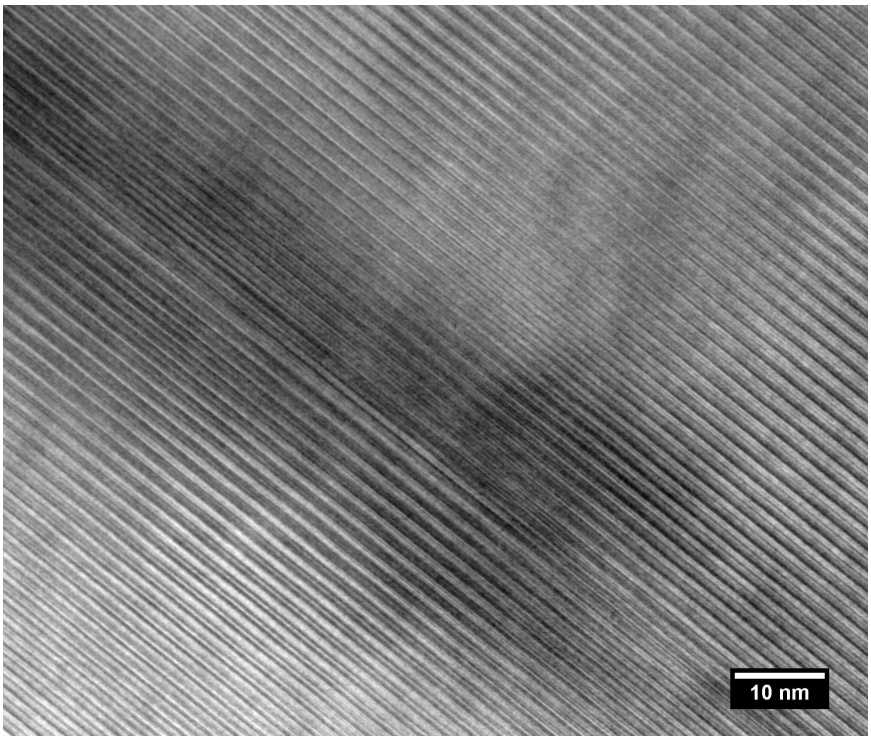

Figure 3.7 :Lattice fringes in enstatite. The dominant structure visible are lattice fringes related to the 18.2 Å lattice repeat ((1 0 0) plane spacings). Stacking faults run from the top left to the bottom right.

expressed as the product of several contributions. The first one being the specimen function describing how the specimen interacts with the incident electron beam and what wave function of the electron beam is after they emerge from the specimen. The other contributions arise because of the electron optical system and its main components are those from the apertures, attenuation of the wave in the lens and aberration of the lens from a perfect lens (Williams and Carter 2009). The image one observes in the end can be written as a convolution of these contributions:

$$g(\boldsymbol{r}) = \int f(\boldsymbol{r}')h(\boldsymbol{r}-\boldsymbol{r}')d\boldsymbol{r}' = f(\boldsymbol{r}) * h(\boldsymbol{r}) \tag{3.8}$$

where f is the specimen function and h is the function describing the electron optical system, the * denotes the convolution f with h. The convolution can be written as the product of the Fourier transform of the functions that are convolved together. If we break down h into the contributions mentioned above one can write:

$$G(\boldsymbol{u}) = A(\boldsymbol{u})E(\boldsymbol{u})B(\boldsymbol{u})F(\boldsymbol{u}) \tag{3.9}$$

where A is the Fourier transform of the aperture function, E the Fourier transform of the envelope (attenuation) function, B the fourier transform of the aberration function, F the Fourier transform of the specimen function an **u** a reciprocal lattice vector. Equation 3.9 decribes how the detail on a certain scale (**u**) is affected by the electron optical system. The specimen function can be written in the phase object approximation (POA), which holds for thin specimens and when absorption can be neglected (Spence 2009, Williams and Carter 2009):

$$f(\boldsymbol{r}) = \exp\left(-i\sigma V_p(\boldsymbol{r})\right) \tag{3.10}$$

where V_p is the projected electrostatic potential of the lattice parallel to the x-y plane (perpendicular to the incident electron beam) and $\sigma = \pi/\lambda E$ the interaction constant. The specimen function is thus directly related to the (projected) electrostatic potential inside the specimen itself.

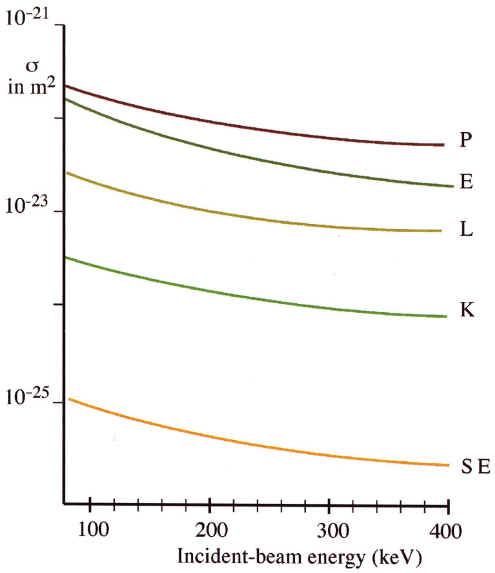

Figure 3.8: Scattering cross sections in Al in the case of forward scattering (θ = 0°) for different types of electron - specimen interactions. P = plasmon scattering, E = elastic scattering, K and L are K and L shell ionization and SE is secondary electron generation. Plasmon generation and elastic scattering are the dominant scattering processes in the TEM. Reproduced from Williams and Carter (2009).

The final mode is the scanning transmission electron microscope (STEM) mode. In this mode the electron optical system creates a condensed probe which scans the specimen, similar to in an SEM. For every pixel the intensity of either the direct beam (bright field STEM) or diffracted beams (dark field STEM) are measured using an angular detector. In this way the image is build by scanning over the specimen with the condensed beam. This mode has been used to measure the diffusion profiles presented in chapter 4.

3.2.4 Inelastic scattering – Energy dispersive spectroscopy

Al already stated, the other type of interaction between high energy incident electrons and the atoms of the specimen is inelastic scattering. The main difference between elastic scattering and inelastic scattering is that the latter one involves a significant amount of energy transfer from the incident electron to the particle with which it interacts.

To get an impression of the importance of the different types of scattering, one can have a look at the probability that a particular process will occur and scatters an incident high energy electron, which is given by the scattering cross section. An overview of the importance of the different scattering processes is given in figure 3.8.

Inelastic scattering can occur due to energy transfer during electron – atom interactions, electron – electron interactions, and interactions with multiple atoms or electrons simultaneously. The first kind of interaction is also the cause for elastic scattering, and in a crystal lattice it will result in a sharply peaked distribution of scattering directions, called diffraction as described in the previous section. During high angle scattering, enough energy can be transferred to the atoms such that the atom is knocked out of its position in the specimen lattice, resulting in knock-on or displacement damage within the specimen. (Egerton 1996), a process that can lead to complications during the chemical analyses of specimens. In appendix 5.1 a method is described to correct for this kind and other kinds of radiation damage. The second kind of interactions, electron – electron interactions, results in the transfer of energy from the incident electron to electrons of the scattering atom in

the specimen. The energy transferred in this process can be the result of two kinds of interactions with the electrons of an atom:

- If the energy transfer is small, it can be used for intra- and interband electronic transitions in the atom being excited, or in the ejection of an outer (valance) electron from the atom (secondary electron). It can also lead to the collective oscillation of outer shell electrons of many atoms, a process which is called plasmon resonance.
- At higher amounts of transferred energies, i.e. few hundred eV to tens of kEv, inner shell electrons (K, L or M) can be excited to a higher unoccupied bound state or to the continuum level, the latter one resulting in ionization of the atom.

The last type of interaction form the basis of two widely used spectroscopic techniques in the TEM, i.e. Electron Energy Loss Spectroscopy (EELS) and Energy Dispersive Spectroscopy (EDS), whereby the name of the latter refers to the device used to measure the spectra and will be handled in more detail in this section.

Figure 3.9 shows the physical process which forms the basis for EDS. A high energy electron in the incident electron beam passes through the electron cloud of an atom. Due to Coulombic interaction with other electrons in the electron cloud, the incident electron gets deflected and transfers a part of its energy to an electron in the electron cloud. The latter electron then can get ejected from the atom if the transferred energy is greater than the ionization energy of the particular shell. The creation of a hole in the shell represents an excited state of an atom, i.e. it is in an energy state higher than its ground state. The atom can get back to its ground state by

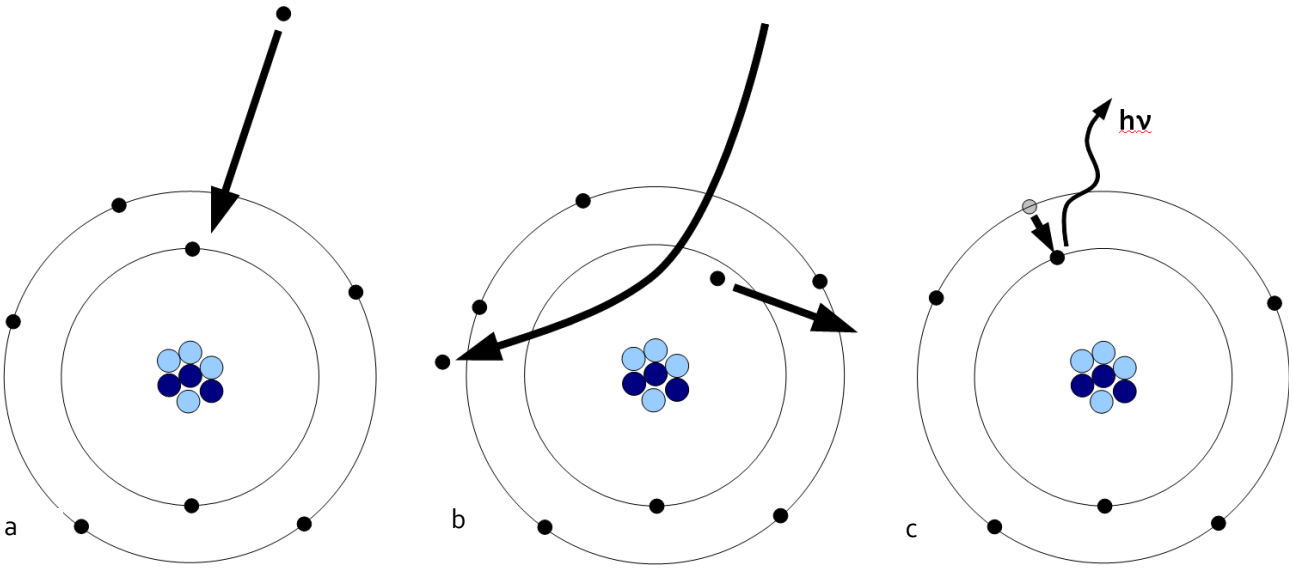

Figure 3.9: Generation of x-rays by inner shell ionization of a specimen atom. a) A high energy incident electron penetrates the electron clouds and passes close to the inner shell electron. b) Coulombic interaction with inner shell electrons causes a change of incident electron direction and transfer of energy from the incident electron to the inner shell electron, ejecting the latter one from the specimen. c) An electron from a higher shell falls back to fill the electron hole in the inner shell and thereby releasing the potential energy as an x-ray.

moving an electron from one of its higher shells to fill the electron hole, which was created by the interaction with the incident high energy electron. Moving an electron from a higher shell to a lower shell results in the lowering of the potential energy of the atom. This energy can be released from the atom by either the emission of a photon of a characteristic energy or another electron from a higher shell, the released electron is called an Auger electron and the transition is called a non-radiative transition. The probability of a radiative (one during which a photon is emitted) vs. non-radiative transition is given by the fluorescence yield ω, and for the following approximation can be used (Williams and Carter 2009):

$$\omega = \frac{Z^4}{a + Z^4} \tag{3.11}$$

where a is a constant dependent on the shell and Z is the atomic number. The fluorescence yield is thus a strong function of atomic number and the intensity of the CKα line is therefore much less intense than that of the FeKα. The low probability of a radiative transition for light elements in combination with strong absorption in the specimen and detector window of x-rays with low energies makes EDS not the ideal technique to measure light elements. In such case, the complimentary technique to analyse light elements is EELS.

Next to characteristic x-ray lines through which elements in the specimen can be uniquely determined, another kind of radiation is emitted by the incident high energy electron when it interacts with the specimen, called Bremsstrahlung (German for breaking-radiation). Interaction of the incident electron with the electric field of the nucleus results in a change of propagation direction of the incident electron. The centripetal acceleration that is associated with this change in direction or momentum results in the loss of energy of the incident electron, which is emitted as electromagnetic radiation (Egerton 1996). The generated intensity I as function of photon energy is given by Kramers (Williams and Carter 2009):

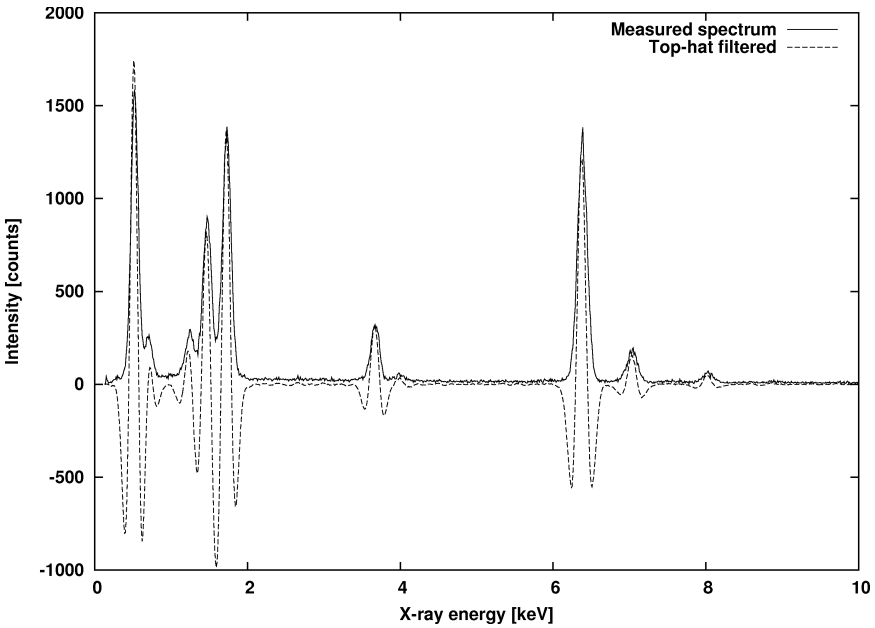

Figure 3.10: Top-hat filter applied to a measured EDS spectrum of almandine, applying the top-hat filter removes the background but changes the shape of the x-ray peaks. Quantification of the x-ray peak intensity is then done by comparing the filtered spectrum to other filtered (elemental) reference spectra.

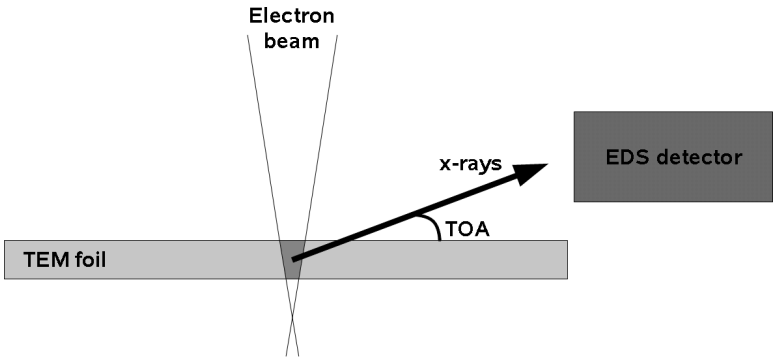

Figure 3.11: Sketch of the sample – detector geometry during an EDS measurements. The incident electron beam ionizes and excites a volume in the TEM foil (dark gray area), which emits x-rays when atoms again return to their lowest energy state. The angle between the x-rays reaching the detector and the sample surface is called the take-off angle (TOA). Note that ion-milled foils don't have parallel surface but are wedge shaped.

$$I(E) = KZ\frac{E_0 - E}{E} \tag{3.12}$$

where Eo is the energy of the incident electron, E the energy of the emitted Bremsstrahlung, Z the average atomic number and K is Kramers' constant, which may itself also be a function of the average atomic number (Small et al. 1987). The total spectrum is a sum of the characteristic x-ray lines and the Bremsstrahlung or background radiation.

The bremsstrahlung can be removed from the spectrum by either fitting an equation related to 3.12 or to remove the background from the spectrum by a digital filter method. The latter one uses a top-hat filter which removes any linear component from the spectrum including the Bremsstrahlung component since the latter one is nearly a linear function of energy with minor deviations only at low energies (Reed 1993). If the Bremssstrahlung background was stripped using a modified form of 3.12, Gaussian peaks are fitted to the characteristic x-ray lines and the area under the peaks gives the intensity of each line. If the filter-fit method is used, top-hat filtered reference spectra are used to fit the filtered measured spectra and from this the intensity of each characteristic x-ray is determined. For the results presented in this dissertation the background modelling in combination with fitting of Gaussian peaks have been used, since the filter-fit methods requires good elemental reference spectra that were not available.

Unless the specimen is very thin, absorption of x-rays in the specimen must be considered, which can be expressed by following the equation:

$$I = \frac{I_0}{\mu_A \rho \, cosec\, \alpha}\left[1 - e^{-\mu_A \rho t \, cosec\, \alpha}\right] \tag{3.13}$$

where Io is the generated x-ray intensity, μ_A the mass absorption coefficient for element A in the specimen, ρ the mass density, t the thickness of the thin foil and α the take-off angle of the x-rays from the foil to the x-ray detector (see figure 3.11). Since foils in the TEM are generally thin and therefore energy loss of the electron beam within the foil can be neglected one can write for the concentration of an element:

$$\frac{C_A}{C_R} = k_{AR} \cdot f_{AR} \cdot \frac{I_A}{I_R} \tag{3.14}$$

with

$$f_{AR} = \frac{\mu_A^{spec}}{\mu_R^{spec}} \left[\frac{1 - \exp(\mu_R^{spec} \rho \, t \, cosec \, \alpha)}{1 - \exp(\mu_A^{spec} \rho \, t \, cosec \, \alpha)} \right]$$

k_{AR} is the Cliff-Lorimer factor for element A using R as ratio element, f_{AR} represents an absorption correction factor, I_A and I_R are the net counts of element A and element R and μ_{spec}^i is the mass absorption coefficient for element i in the specimen, which can be calculated from the mass absorption coefficients in a pure standard j (μ_i^j):

$$\mu_i^{spec} = \sum_j C_j \mu_i^j \tag{3.15}$$

Using as additional constraint that the total concentration should add up to 100%, one can calculate the composition for an unknown specimen, if the thickness is known. Though it is possible to determine the thickness by EELS, thickness fringes or convergent beam electron diffraction (Williams and Carter 2009), these methods are often cumbersome and impractical when it comes down to measuring many points. Van Cappellen and Doukhan (1994) proposed to use the net charge of all elements as an alternative constraint to determine the thickness of the specimen, or x-ray absorption thickness of the specimen. Using an approximation to 3.14 they expressed the total charge as function of specimen thickness as a second order polynomial and from this they determined the thickness and composition of the specimen at the place of analyses. A program was developed during the work on the diffusion study that employs a modified version of their method (see appendix 5.2)

A major issue with high pressure phases is their instability under the intense electron beam, which can lead to preferential loss of some elements. In this dissertation a method is developed to correct for a change in composition due to radiation damage during EDS analyses, and which is described in more detail in appendix 5.1.

3.2.5 Electron energy loss spectroscopy

A complementary analytical technique to EDS is EELS, where not the produced x-ray intensity is measured, but the energy loss of the transmitted electrons. The physical process underlying EELS is the same as the one underlying EDS, i.e. inelastic scattering of the incident beam. Since EELS is independent of the fluorescence yield of a certain electronic transition, EELS can also be used for light elements, which have a low fluorescence yield and where absorption by the specimen and the window in front of the EDS detector may cause problems. The fact that low energy losses of the high energy incident beam are more likely than high energy losses, also makes EELS a favourable method to determine the concentration of light elements.

The EELS spectrum is usually divided in two parts, a low loss part below ± 50 eV and a core loss spectrum, the measured energy loss region above ± 50 eV. The low loss spectrum contains the zero-loss peak, which represent the transmitted electrons that did not loose any energy, and is by far the most intense peak in the spectrum. The width of the ZLP gives the ultimate resolution of the analyses. The peak after the ZLP and usually located somewhere between 5 and 35 eV energy loss is the plasmon peak. High energy electrons penetrating the

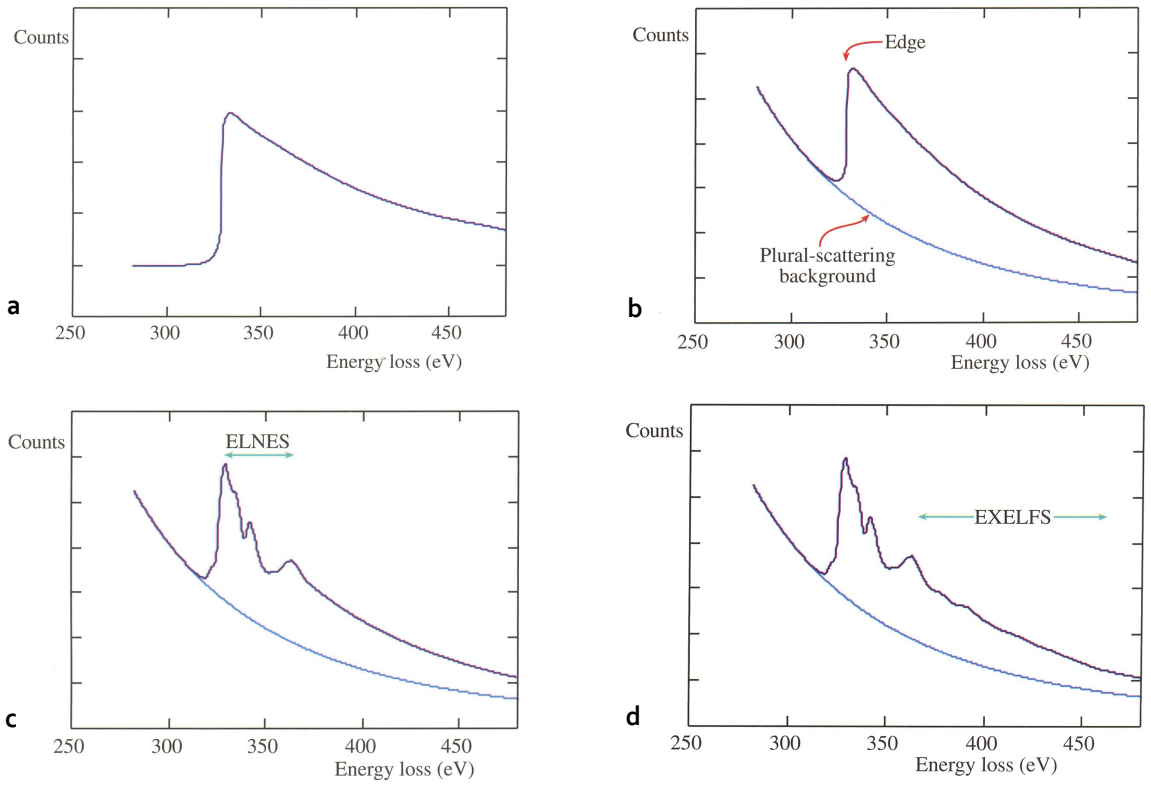

Figure 3.12:The structure of core loss spectra. a) The shape of hydrogenetic absorption edge. b) The hydrogenetic is superimposed on the tail of other absorption edges and the plasmon peak, due to plural-scattering. c) When electrons can be exited to bound unoccupied states, this leads to the superposition of white lines on top of the absorption edge, the ELNES structure. d) Beyond the ELNES structure is the EXELFS structure. Modified after Williams and Carter (2009).

specimen induce collective oscillations of the outer shell electrons of the specimen, so called plasmons, which give rise to the plasmon peak. The shape of the plasmon peak is controlled among others by the type of bonding and can be used for phase identification (Egerton 2009, Williams and Carter 2009).

Figure 3.12 shows the features of a typical core-loss spectrum. The shape of an edge when without any contributions of bonding, unfilled higher states and background of previous edges would look like (A), a sharp increase at the ionization edge energy followed by a long tail which can be approximated by a power-law decay in intensity after the ionization edge. In (B) the background is added to this ionization edge, which is the sum of the tails of previous edges and the plasmon peak, and can thus also be approximated by a power-law function (Egerton 1996). If the core-level electron is ejected from its shell, but did not gain enough energy to get into the vacuum level, it will end up in some unfilled state above the Fermi level, but still bound to the nucleus by Coulomb forces. The probability that an electron will go to a certain state within an associated energy range is dependent on the number of states in this energy range, and is thus given by the Density Of States (DOS) of the system. This will give rise to additional spectral structure upon the background and ionization edge (C), the Energy-Loss Near-Edge Structure (ELNES) up to 30-50 eV after the onset of the ionization edge and Extended Energy-Loss Fine structure (EXELFS) beyond there (D). In the case that these empty states are well defined empty states (in the sense of their energy), they will give rise to peaks, or white lines, on top of the ionization

edge, which can give valuable information on for example the bond type or oxidation state (Egerton 1996, Williams and Carter 2009).

In this dissertation EELS has been used to determine the oxidation state of iron in garnet. Van Aken et al. (1998) and Van Aken and Liebscher (2002) used the shape of the $FeL_{2,3}$ edge to determine the ferric / ferrous in different minerals of known ferric/ferrous iron ratio, and produced a universal curve to determine the ferric/ferrous iron ratio in unknown minerals. The FeL_3 edge at 707.8 eV consists of several white lines, of which the most prominent are one at 707.8 eV and one at 709.5 eV. The latter one becomes more intense with increasing Fe3+ content. A similar behaviour is seen for the FeL_2 edge, which also consist of multiple peaks, of which the ones at 720 eV and 721.5 eV react most strongly to the Fe^{3+} content, the latter one becoming more intense with increasing Fe^{3+} content. Van Aken et al. (1998) used the integrated intensity ratio in two energy windows at 708.5 – 710.5 eV and 719.7 – 721.7 eV to produce a universal curve from which one can determine the Fe3+ / Fe2+ ratio using the same method. To correct for transitions to the continuum state, they fit a double arctan function to the regions outside of the edge after the power-law background has been removed:

$$f(\Delta E)=\frac{h_1}{\pi}\cdot\left[\arctan\left(\frac{\pi}{w_1}(\Delta E-E_1)\right)+\frac{\pi}{2}\right]+\frac{h_2}{\pi}\cdot\left[\arctan\left(\frac{\pi}{w_2}(\Delta E-E_2)\right)+\frac{\pi}{2}\right] \quad (3.16)$$

where h_1 and h_2 are the heights of the peaks, w_1 and w_2 the widths of the continuum transition, ΔE the energy lost and E_1 = 708.65 eV and E_2 = 721.65 eV the positions of the continuum transitions.

In specimens that are not very thin, multiple scattering plays an important role, and therefore the measured core-loss spectra are a convolution of the single scattering core-loss spectra, i.e. the detected electron only lost energy by a single inner shell scattering event, and the low-loss spectra since the low energy loss scattering events are most likely to occur. For good quantification of the Fe^{3+}/Fe^{2+} ratio in the specimen the multiple scattering effect needs to be removed, or deconvolved. This can be achieved by using the Fourier-ratio technique (Egerton 1996):

$$k^1(\nu)=I_0\, j_k(\nu)/\, j_l(\nu) \quad (3.17)$$

where $k^1(\nu)$ is the Fourier transform of the single-scattering core-loss spectrum, I_0 the intensity of the zero-loss peak, $j_k(\nu)$ the Fourier transform of the measured core-loss spectrum and $j_l(\nu)$ the Fourier transform of the low-loss spectrum. Doing this, however, is not straight forward and requires additional treatment of the spectra which is beyond the scope of this dissertation but can be found in more detail in Egerton (1996).

3.3 The electron microprobe

Chemical characterization on the sample scale of the recovered samples was done by electron microprobe analysis (EMPA) using wavelength dispersive spectroscopy (WDS). The electron microprobe is an electron microscope like the TEM. The main differences are that it works on bulk samples, i.e. the sample is not transparent to electrons, and the electron optical system therefore consists only of a set of condenser and objective lenses that focus the electron beam on the sample. The operating voltage of an electron microprobe is

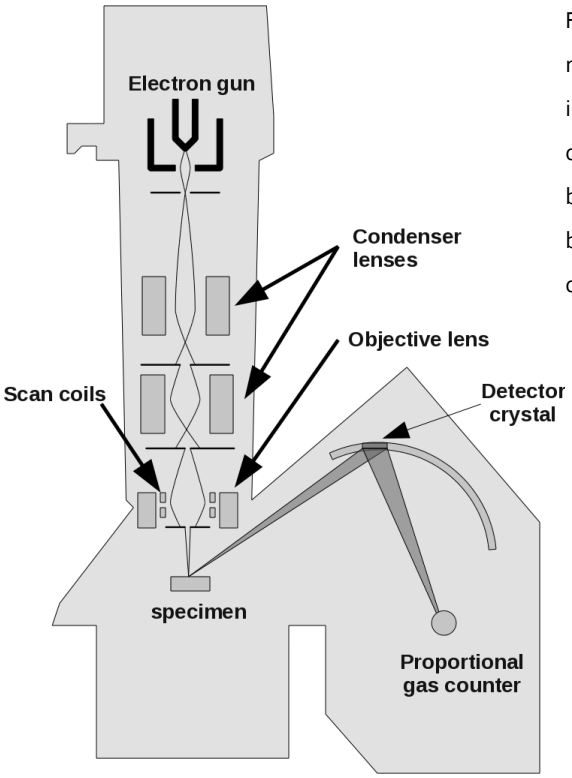

Figure 3.13: A schematic overview of the basic parts of the electron microprobe. The cross over directly below the electron gun acts a source image for the two condenser lenses and objective lens that produce a demagnified image/spot of it at the specimen. Interaction of the electron beam with the specimen then results in the production of x-rays (gray beam emerging from the specimen) that are detected by the WDS detector consisting of a detector crystal and a proportional gas counter.

usually in the range of 10 – 30 kV, as compared to > 80 kV for TEMs.

Chemical analyses by the electron microprobe are based upon the same principle as chemical analyses using EDS on the TEM, i.e. inner shell ionization of the specimen atoms by the incoming high energy electrons and de-excitation of the excited atom by the emission of a photon. The Jeol JXA-8200 electron microprobe at the Bayerisches Geoinstut is equipped with 5 wavelength dispersive spectrometers. In the WDS spectrometer (figure 3.13), x-rays of a desired energy are reflected by a crystal towards the proportional gas counter, which converts the incoming x-rays to voltage pulses which in turn are converted by the single channel analyzer to voltage pulses that can be counted by a computer system. The crystal ensures that the only x-ray with a predefined energy / wavelength are reflected, those for which Bragg's law is fulfilled. The main difference with the EDS system to the user is that, for the user, the EDS system obtains the complete spectrum in parallel, whereas the WDS system only collects the x-ray intensity at specified energies and it is a serial way of measuring x-ray intensity (one position at a time).

Since with EMPA bulk samples are measured, matrix effects play a more important role than for EDS measurements on the TEM. Matrix corrections for EMPA are usually done by the ZAF method, where the weight fraction of element i relative to a standard is expressed as:

$$\frac{C_i^u}{C_i^s} = [ZAF]_i \frac{I_i^u}{I_i^s} \tag{3.18}$$

where the superscript u designates the unknown, the superscript s the standard, I the measured x-ray intensity of elements i using a characteristic peak and ZAF the matrix correction factor, where Z is the atomic number effect, A the absorption correction and F fluorescence correction.

Whereas in a TEM foil the energy loss of the incident electron is insignificant, in a bulk foil this plays an important role and is dependent on the average atomic number. Moreover, a significant portion of the incident are backscattered out of the sample before they loose all their energy. These two corrections are contained in the atomic number correction. The atomic number correction can be calculated from the individual correction for stopping power and backscattering (Goldstein et al. 2003), or as a ϕ(ρz)-curve that expresses the generation of x-rays (ϕ) as function depth (z) x density (Pouchou and Pichoir 1984, Bastin et al. 1998). Absorption of x-rays traversing a distance t in the specimen can be calculated by:

$$\frac{I}{I_0} = \exp\left[-(\mu/\rho)(\rho t)\right] \tag{3.19}$$

where μ is the mass attenuation coefficient and ρ the density. This expression can be integrated in a simplified analytical expression or in the ϕ(ρz)-curve method (Duncumb 1994, Goldstein et al. 2003). For most samples the fluorescence correction is only minor (Duncumb 1994).

The spot size and the interaction volume are the two most important factors controlling the spatial resolution

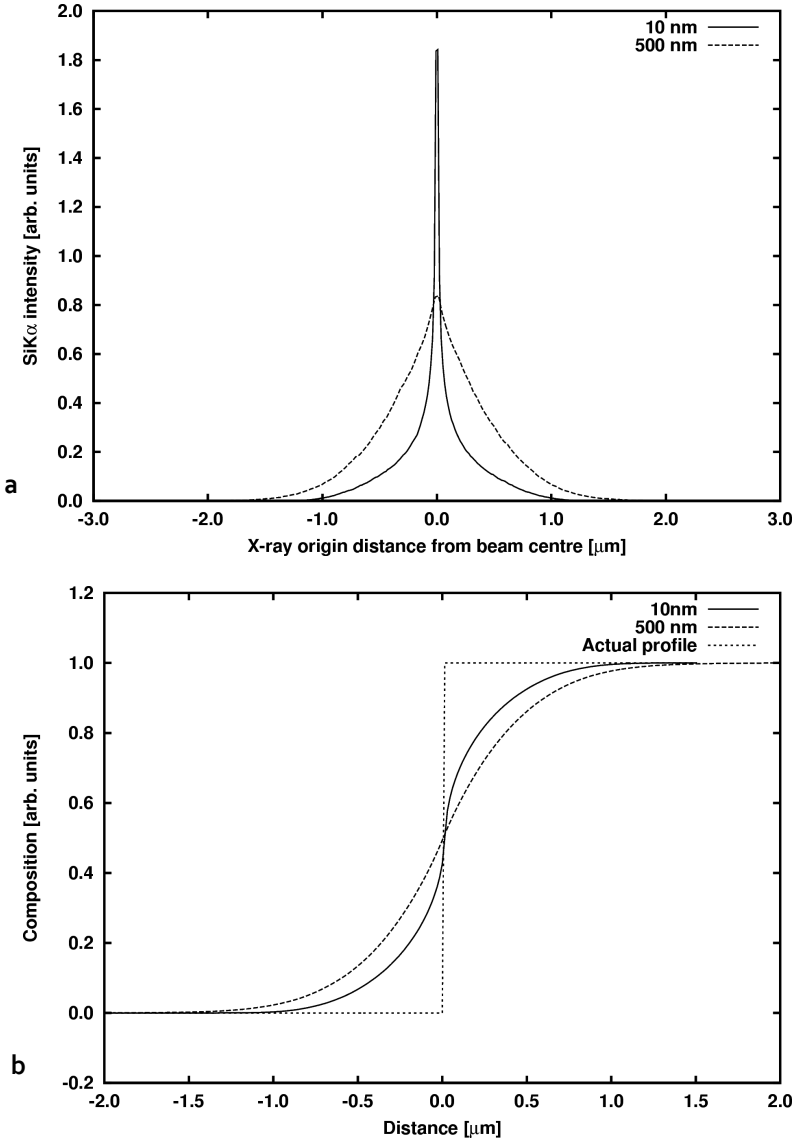

Figure 3.14: Combined effect of the beam diameter and interaction volume on the spatial resolution of EMPA on pyrope using an acceleration voltage of 15 kV, determined using Monte Carlo modelling. a) The radial distribution of x-rays produced in the interaction volume that are detected by the detector for a beam diameter of 10 nm (FEG electron source) and 500 nm (thermionic electron source). b) The spreading of a step change in concentration over a range due to the above mentioned effect. It shows that at 15 kV, the resolution of EMPA is about 1 - 2 μm with only a small dependence on spot size.

of the EMPA. The intensity distribution of the probe is usually assumed to be Gaussian in nature (Goldstein et al. 2003) and the spot size is then defined as the FWHM of the intensity distribution. The spot size is controlled by the electron source (thermionic, LaB_6 or FEG in order of decreasing spot size) and the lens aberrations of the electron optical system. In bulk specimens the incident electrons are scattered until they are backscattered from the surface or until they have deposited all their energy in the bulk specimen. The scattering in the bulk specimen causes spreading of the electron beam into a pear shaped volume in which it interacts with the specimen, the interaction volume. Because of this, the spatial resolution of EMPA is limited to about 1 µm more or less independent of the spot width, which is illustrated in figure 3.14. Therefore the very short diffusion profiles in the diffusion experiments presented in this dissertation cannot be measured by EMPA. Profiles in the micrometer range measured by EMPA should be corrected for this by deconvolution of the measured profiles or convolving the modelled profile with a function that simulates the effect of the finite interaction volume and beam size (Ganguly et al. 1988).

3.4 References

Abbe, E. (1873), Beiträge zur Theorie des Mikroskops und der mikroskopischen Wahrnehmung. Archiv f mikrosk Anatomie 9:440-456. doi: 10.1007/BF02956175

Aken, P.A. van, Liebscher, B. (2002), Quantification of ferrous/ferric ratios in minerals: new evaluation schemes of FeL_{23} electron energy-loss near-edge spectra. Phys Chem Miner 29:188-200. doi: 10.1007/s00269-001-0222-6

Aken, P.A. van, Liebscher, B., Styrsa, V.J. (1998), Quantitative determination of iron oxidation states in minerals using $FeL_{2,3}$ -edge electron energy-loss near-edge structure spectroscopy. Phys Chem Miner 25:323-327. doi: 10.1007/s002690050122

Anderson, D.L. (2000), The thermal state of the upper mantle; No role for mantle plumes. Geophys Res Lett 27:PP. 3623-3626. doi: 200010.1029/2000GL011533

Barna, A., Menyhard, M. (1994), Auger Depth Profile Analysis of Deeply Buried Interfaces. Phys Stat Sol (a) 145:263-274. doi: 10.1002/pssa.2211450206

Barna, Á., Pécz, B., Menyhard, M. (1999), TEM sample preparation by ion milling/amorphization. Micron 30:267-276. doi: 10.1016/S0968-4328(99)00011-6

Bastin, G.F., Dijkstra, J.M., Heijligers, H.J.M. (1998), PROZA96: an improved matrix correction program for electron probe microanalysis, based on a double Gaussian $\phi(\rho z)$ approach. X-Ray Spectrom 27:3-10

Cappellen, E. Van, Doukhan, J.C. (1994), Quantitative transmission X-ray microanalysis of ionic compounds. Ultramicroscopy 53:343-349. doi: 10.1016/0304-3991(94)90047-7

Duncumb, P. (1994), Correction procedures in electron probe microanalysis of bulk samples. Mikrochim Acta 114-115:3-20. doi: 10.1007/BF01244530

Egerton, R.F. (1996), Electron energy-loss spectroscopy in the electron microscope. Plenum Press, New York

Egerton, R.F. (2009), Electron energy-loss spectroscopy in the TEM. Rep Prog Phys 72:016502. doi: 10.1088/0034-4885/72/1/016502

Fowler, C.M.R. (2005), The solid earth: an introduction to global geophysics. Cambridge University Press

Frost, D.J., Langenhorst, F., Aken, P.A. van (2001), Fe–Mg partitioning between ringwoodite and magnesiowüstite and the effect of pressure, temperature and oxygen fugacity. Phys Chem Miner 28:455-470. doi: 10.1007/s002690100181

Ganguly, J., Bhattacharya, R.N., Chakraborty, S. (1988), Convolution effect in the determination of composition profiles and diffusion coefficients by microprobe step scans. Am Mineral 73:901-909

Goldstein, J., Newbury, D.E., Echlin, P., Joy, D.C., Lyman, C.E., Lifshin, E.E., Sawyer, L., Michael, J.R. (2003), Scanning electron microscopy and x-ray microanalysis. Springer

Hawkes, P.W. (1972), Electron optics and electron microscopy. Taylor and Francis

Ito, E. (2007), Theory and Practice – Multianvil Cells and High-Pressure Experimental Methods. in: Mineral Physics, Treatise on Geophysics Elsevier Science, Haarlem, pp. 197-230

Ito, E., Yamazaki, D., Yoshino, T., Fukui, H., Zhai, S., Shatzkiy, A., Katsura, T., Tange, Y., Funakoshi, K. (2010), Pressure generation and investigation of the post-perovskite transformation in $MgGeO_3$ by squeezing the Kawai-cell equipped with sintered diamond anvils. Earth Planet Sci Lett 293:84-89. doi: 10.1016/j.epsl.2010.02.023

Katsura, T., Yoneda, A., Yamazaki, D., Yoshino, T., Ito, E. (2010), Adiabatic temperature profile in the mantle. Phys Earth Planet Inter 183:212-218. doi: 10.1016/j.pepi.2010.07.001

Kawai, N., Endo, S. (1970), The Generation of Ultrahigh Hydrostatic Pressures by a Split Sphere Apparatus. Rev Sci Instrum 41:1178. doi: 10.1063/1.1684753

Kawai, N., Togaya, M., Onodera, A. (1973), A New Device for Pressure Vessels. Proc Japan Acad 49:623-626

Kawashima, Y., Tsuchida, Y., Utsumi, W., Yagi, T. (1990), A cylindrical furnace with homogeneous temperature distribution for use in a cubic high-pressure press. Rev Sci Instrum 61:830. doi: 10.1063/1.1141502

Kawashima, Y., Yagi, T. (1988), Temperature distribution in a cylindrical furnace for high-pressure use. Review of Scientific Instruments 59:1186-1188. doi: 10.1063/1.1139747

Keppler, H., Frost, D.J. (2005), Introduction to minerals under extreme conditions. in: Miletich R.(ed.) Mineral Behaviour at Extreme Conditions, EMU Notes in Mineralogy 7, pp. 1-30

Knoll, M., Ruska, E. (1932), Das Elektronenmikroskop. Z Physik 78:318-339. doi: 10.1007/BF01342199

Malherbe, J.B. (1994), Sputtering of compound semiconductor surfaces. I. Ion-solid interactions and sputtering yields. Crit Rev Solid State 19:55. doi: 10.1080/10408439408244588

Mayer, J., Giannuzzi, L.A., Kamino, T., Michael, J. (2007), TEM sample preparation and FIB-induced damage. MRS BULLETIN 32:400-407

McKenzie, D., Bickle, M.J. (1988), The Volume and Composition of Melt Generated by Extension of the Lithosphere. J Petrol 29:625 -679. doi: 10.1093/petrology/29.3.625

Miyajima, N., Holzapfel, C., Asahara, Y., Dubrovinsky, L.S., Frost, D.J., Rubie, D.C., Drechsler, M., Niwa, K., Ichihara, M., Yagi, T. (2010), Combining FIB milling and conventional Argon ion milling techniques to prepare high-quality site-specific TEM samples for quantitative EELS analysis of oxygen in molten iron. J Microsc 238:200-209. doi: 10.1111/j.1365-2818.2009.03341.x

Pouchou, J.L., Pichoir, F. (1984), A new model for quantitative X-ray microanalysis. I Application to the analysis of homogeneous samples. Rech Aerosp 3:13-38

Reed, S.J. (1993), Electron microprobe analysis. Cambridge Univ. Press, Cambridge

Small, J.A., Leigh, S.D., Newbury, D.E., Myklebust, R.L. (1987), Modeling of the bremsstrahlung radiation produced in pure-element targets by 10–40 keV electrons. J Appl Phys 61:459. doi: 10.1063/1.338245

Spence, J.C.H. (2009), High-Resolution Electron Microscopy. Oxford University Press

Williams, D.B., Carter, C.B. (2009), Transmission electron microscopy: a textbook for materials science. Springer, Heidelberg

Chapter 4: Numerical modeling of diffusion phenomena

In order to model and fit diffusion profiles in several geometries (planar, cylindrical and spherical) programs have been developed which solve the required partial differential equations, using an implicit finite difference scheme. Discretization of the partial differential equations using a finite difference scheme is done by a Taylor series expansion on a grid with a distance of Δx between each node:

$$f_{i+n} = f_i + \sum_{j=1}^{\infty} \frac{(n\Delta x)^j}{j!} \frac{\partial^j f}{\partial x^j} \tag{4.1}$$

where f_i denotes the value of function f at node i. Using combinations of (truncated) Taylor series expansion one can replace partial differential equations by their finite difference approximations, leading to a set of linear equations that can be solved with the use of linear algebra codes. The exact codes are described in more detail below.

4.1 Planar 1-D multi-component diffusion

A computer program (mcdiff) was developed to fit the diffusion profiles measured. The program employs an implicit finite difference scheme to solve the general 1-D multi-component diffusion equation:

$$\frac{\partial C_i}{\partial t} = \sum_{j=1}^{n-1} \frac{\partial C_j}{\partial x} \cdot \frac{\partial D_{ij}}{\partial x} + D_{ij} \frac{\partial^2 C_j}{\partial x^2} \tag{4.2}$$

The last profile is calculated from charge balance. This equation is discretized in the following way:

$${}^{n-1}C_i^k = {}^nC_i^k + \sum_{j=1}^{l} {}^n_i\beta_j^{k-1}\ {}^nC_j^{k-1} + {}^n_i\beta_j^k\ {}^nC_j^k + {}^n_i\beta_j^{k+1}\ {}^nC_j^{k+1} \tag{4.3}$$

where

$${}^n_i\beta_j^{k-1} = \alpha\left(\frac{1}{4}{}^n\Delta D_{ij}^k - {}^nD_{ij}^k\right)$$

$${}^n_i\beta_j^k = 2\alpha\,{}^nD_{ij}^k$$

$${}^n_i\beta_j^{k+1} = -\alpha\left(\frac{1}{4}{}^n\Delta D_{ij}^k + {}^nD_{ij}^k\right)$$

$$\alpha = \frac{\Delta t}{(\Delta x)^2}$$

$${}^n\Delta D_{ij}^k = {}^nD_{ij}^{k+1} - {}^nD_{ij}^{k-1}$$

In these equations k is the node (spatial discretization), n is the time step (temporal discretization) and i and j are indices for the diffusing components. Equation 4.3 forms a set of linear equations that can be solved using standard methods, for example available in the LAPACK package (Anderson et al. 1999). The matrix of diffusion coefficients is calculated by iterating every time step till it converges to a stable value, before going to the next time step. The code has been tested against an analytical solution for the standard diffusion equation with a constant diffusion coefficient.

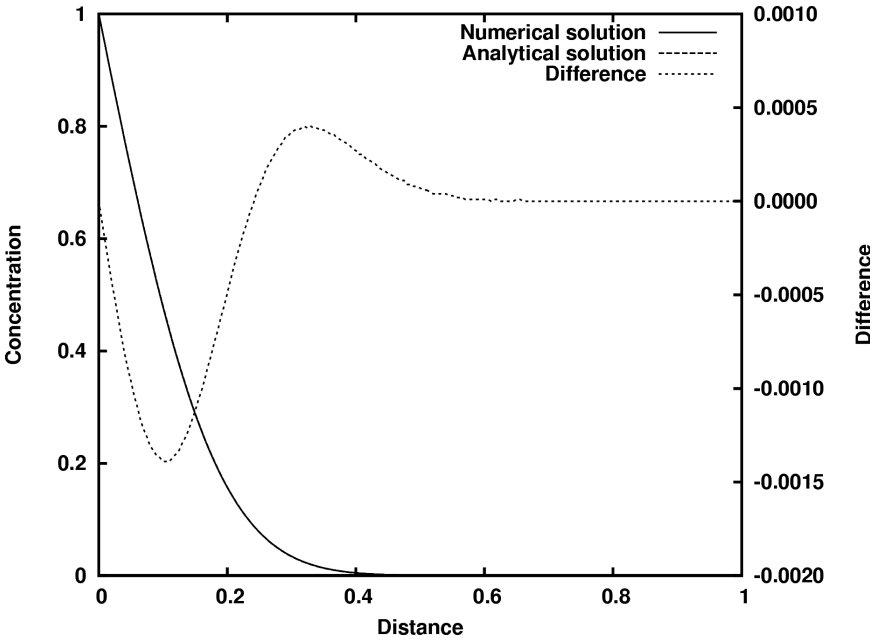

Figure 4.1: The results of the numerical vs. analytical solution for the multi-component diffusion program mcdiff. The analytical solution is not visible since it overlaps with the numerical solution at the scale of the figure. The difference between the two is plotted on the right y-axis. The difference between the analytical and numerical solution is less than 0.15%. Simulation conditions: grid spacing dx = 0.005, time step 0.01, time interval 0 – 1, diffusion coefficient 0.01.

The numerical scheme has been tested against an analytical solution for a semi-infinite half space problem with a constant boundary concentration C_0 and an initial concentration profile of C(t=0) = 0 (Crank 1980):

$$C = C_0 \, erfc\left(\frac{x}{2\sqrt{Dt}}\right) \tag{4.4}$$

where x is the spatial coordinate, D is the diffusion coefficient, t time and erfc is the complementary error function erfc x = 1 – erf x. As figure 4.1 shows, the error is smaller than 0.0015 on a total range of 1.0, which corresponds to an error of less than 0.15%. The error can be further reduced by taking a finer grid or take smaller time steps.

The program allows for different diffusion models to be used, by calculating the matrix of diffusion coefficients using the relations corresponding to each diffusion model. Currently four models are supported:(1) the most simple diffusion model with constant diffusion coefficients independent of composition and all off-diagonal elements of D equal to zero, (2) the diffusion model of Lasaga (1979) for ideal solutions, (3) the diffusion model of Lasaga (1979) using a symmetric non-ideal solution described by Margules parameters and (4) the diffusion model by Loomis (1978) for an ideal solution. The program also has options to modify the tracer diffusion coefficients used in the different diffusion models to model the diffusivity dependence of elements on other elements that can have multiple valence states, for example iron. Following Mackwell et al. (2005) the following equation is used to model this:

$$\tilde{D}_i^0 = D_i^0 k_1 C_{mv}^{k_2} e^{-k_3 C_{mv}} \tag{4.5}$$

where k_1, k_2 and k_3 are adjustable parameters for the model and C_{mv} is the concentration of the multi-valent ion. Next to this a different kind of compositional dependence can also be modelled, according to the following equation:

$$\tilde{D}_i^0 = D_i^0\left(1+\sum_{j=1}^{n} k_{ij}C_j\right) \tag{4.6}$$

where k_{ij} are adjustable parameters.

A second program (mcfitter) was developed to fit the measured diffusion profiles to calculated profiles. The program uses the routines in the mcdiff program to calculate a profile and then to fit this profile to measured profiles. It allows for fitting the tracer diffusivities used in the diffusion models, initial compositions and the adjustable parameters in equation 4.5. A gap in the diffusion profile can also be fitted, as well as a shift in the profile to fit the initial interface. The profiles are simultaneously fitted by minimizing the χ^2 value defined by:

$$\chi^2 = \sum_{i=1}^{k}\sum_{i=1}^{l}\left(\frac{(O_{ij}-M_{ij})}{e_{ij}}\right)^2 \tag{4.7}$$

where k is the number of components, l the number of measurements, O_{ij} is the measured concentration of component i in measurement j, M_{ij} is the modelled concentration of component i in measurement j and e_{ij} is the error in the measurement of component i in measurement j. The minimization is done using the Levenberg – Marquardt method contained in the MINPACK fortran software routine package[1].

The errors on the fitted parameters are calculated using the bootstrap method (Efron and Tibshirani 1994) which is a resampling method to calculate errors on fitted parameters. After the profiles have been fitted, the residuals are calculated and scaled to their measurement error. New 'pseudo-profiles' are then calculated using the fitted profile and the residuals by random sampling the scaled residuals and adding this to fitted values of the measured profiles. The 'pseudo-profiles' are then again fitted to obtain the 'pseudo-parameters'. This was repeated for 5000 'pseudo-profiles' and the errors in the fitted parameters are then determined by finding the symmetric interval around the originally fitted parameters that encompasses 90% (for the 90% confidence interval) of the fitted 'pseudo-parameters'.

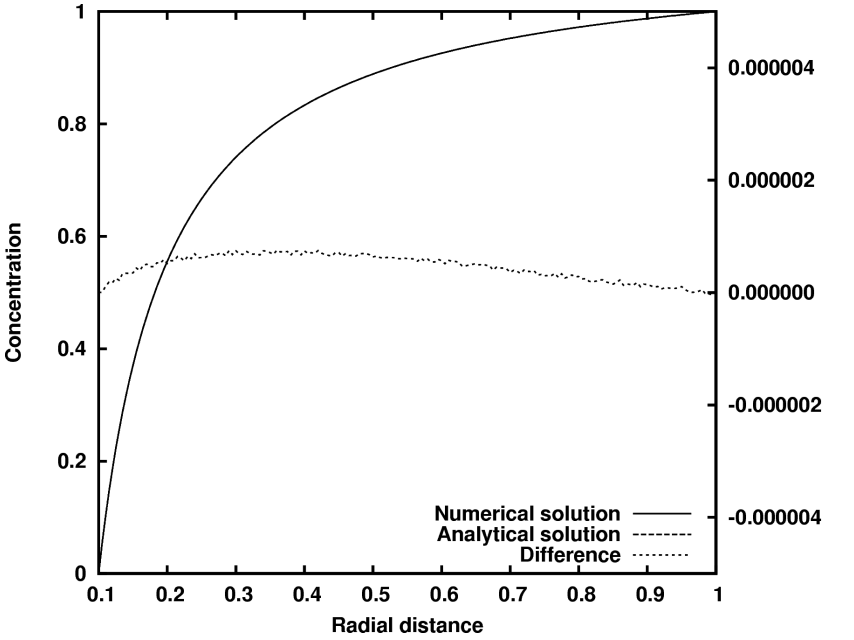

Figure 4.2: The results of the numerical vs. analytical solution for the 3D spherical radially symmetric diffusion program raddiff. The analytical solution is not visible since it overlaps with the numerical solution at the scale of the figure. The difference between the two is plotted on the right y-axis. The absolute error (difference between numerical and analytical solution) is less than 0.0002% for the steady state solution. Simulation conditions: grid spacing dr = 0.005, time step 0.01, time interval 0 – 100, diffusion coefficient 0.01.

1 http://www.netlib.org/minpack/

4.2 Diffusion in a spherical or cylindrical geometry

To model diffusion in a grain and diffusion controlled growth of a grain or needle a finite difference model was used. The basic equation that governs diffusion in a spherical and cylindrical geometry assuming a constant diffusion coefficient D is given by (Crank 1980):

$$\frac{\partial C}{\partial t} = D\left(\frac{n}{r}\frac{\partial C}{\partial r} + \frac{\partial^2 C}{\partial r^2}\right) \tag{4.8}$$

where C is the concentration, r the radius from the centre, t time, D the diffusion coefficient, and n = 1 for a cylindrical geometry and n = 2 for a spherical geometry. Equation 4.8 has been discretized using a fully implicit scheme:

$$C_i^k = -\alpha\left(\frac{1}{\Delta r} + \frac{n}{2r_i}\right)C_{i+1}^{k+1} + \left(1 - \frac{2\alpha}{\Delta r}\right)C_i^{k+1} - \alpha\left(\frac{1}{\Delta r} - \frac{n}{2r_i}\right)C_{i-1}^{k+1} \qquad \text{With} \quad \alpha = \frac{D\Delta t}{\Delta r} \tag{4.9}$$

where k is the time index, i the spatial index, Δr the distance between two nodes, and Δt the time step for temporal discretization. Equation 4.9 describes a tridiagonal linear system and can be solved using standard methods included in the LAPACK software library for example.

The code has been tested against a steady state analytical solution for a hollow sphere and hollow cylinder, which are respectively given by (Crank 1980):

$$C = \frac{a C_1 (b - r) + b C_2 (r - a)}{r(b - a)} \tag{4.10}$$

and

$$C = \frac{C_1 \ln(b/r) + C_2 \ln(r/a)}{\ln(b/a)} \tag{4.11}$$

where *r* is the radial distance from the centre of the sphere/cylinder, C_1 is the concentration on the inside surface, C_2 the concentration on the outside surface, *a* the radial distance from the centre of the sphere or cylinder to the inside surface and *b* the radial distance from the centre of the sphere/cylinder to the outer surface. Figure 4.2 shows the result for the spherical geometry, the error is less than 0.0002% for the steady state solution. For the cylindrical solution the error is less than 0.002% in the case of the steady state solution (see figure 4.3).

Grain growth (or shrinkage) was modelled by dividing the domain into three parts; the internal part, the boundary and the external part (figure 4.4). The internal part corresponds to the grain and for this part equation 4.9 is solved for every time step. The boundary has a constant concentration, corresponding to the composition of the internal phase when in equilibrium with the external phase, and its position determines the size of the external and internal parts. The external part corresponds to the external phase and also has a constant concentration, not necessarily equal to the boundary concentration. Since the boundary concentration is

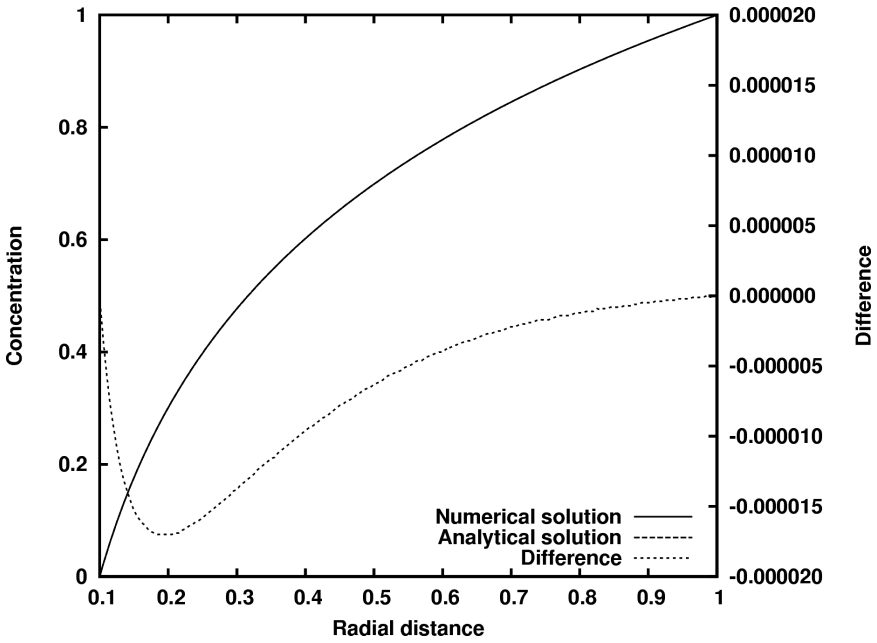

Figure 4.3 : The results of the numerical vs. analytical solution for the 3D cylindirical radially symmetric diffusion program raddiff. The analytical solution is not visible since it overlaps with the numerical solution at the scale of the figure. The difference between the two is plotted on the right y-axis. The absolute error is less than 0.002% for the steady state solution. Simulation conditions: grid spacing dr = 0.005, time step 0.01, time interval 0 – 100, diffusion coefficient 0.01.

different from the concentration of the internal part, material will flow in or out of the grain. The total flux of material that has flown in/out off the grain is determined after every time step by integration of the concentration profile over the complete grain, taking into account the proper geometry. The boundary position is then updated for the next time step based on the total flux of material that has flown in/out of the grain (M_{int}) and the concentration or density of material in the external part (ρ_{ext}):

$$\Delta V_{grain} = \frac{M_{\text{int}} - M_0}{\rho_{ext}} \tag{4.12}$$

M_0 is the starting concentration of material in the grain. In the case of grain growth, the composition of the new nodal points in the internal part is set to the boundary composition.

The growth of the grain can be stopped after a certain amount of material has flown into the grain. The boundary position is kept constant after this point has reached. To stop material from flowing in or out of the

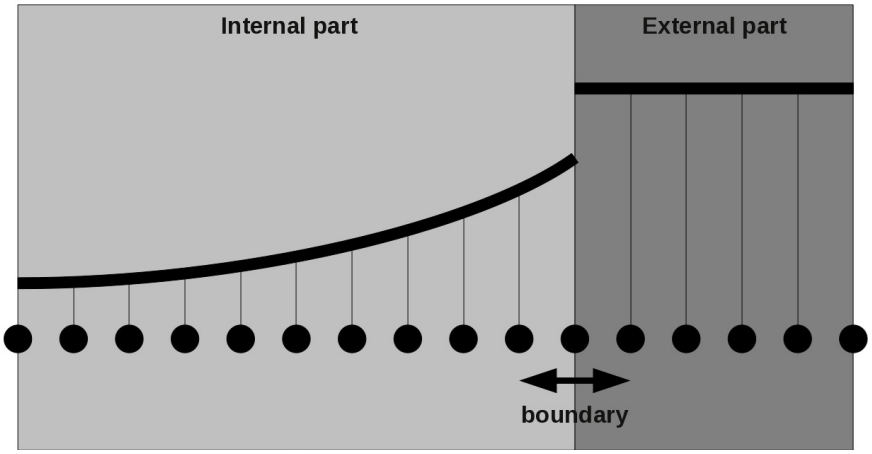

Figure 4.4 : Sketch of the setup of the domain. Solid black circles denote nodal points at which the solution is calculated. In the internal part the relevant descretized differential equation is solved, whereas the external part functions as a kind of reservoir to accommodate grain growth or shrinkage. The position of the boundary is calculated by determining the amount of material at flowed into the internal part.

grain, the boundary flux is forced to be zero using a Neumann boundary condition:

$$C_b^{k+1} - C_{b-1}^{k+1} = 0 \tag{4.13}$$

where b is the boundary node. In the case that the internal part contains the first node, also a Neumann type boundary condition was used for the first node.

4.3 References

Anderson, E., Bai, Z., Bischof, C., Blackford, S., Demmel, J., Dongarra, J., Croz, J. Du, Greenbaum, A., Hammarling, S., McKenney, A., Sorensen, D. (1999), LAPACK Users' Guide. Society for Industrial and Applied Mathematics, Philadelphia, PA

Crank, J. (1980), The Mathematics of Diffusion. Oxford University Press, USA

Efron, B., Tibshirani, R.J. (1994), An Introduction to the Bootstrap. Chapman and Hall/CRC, London

Lasaga, A.C. (1979), Multicomponent exchange and diffusion in silicates. Geochem Cosmochem Acta 43:455-469. doi: 10.1016/0016-7037(79)90158-3

Loomis, T.P. (1978), Multicomponent diffusion in garnet; I, Formulation of isothermal models. Am J Sci 278:1099-1118

Mackwell, S., Bystricky, M., Sproni, C. (2005), Fe–Mg Interdiffusion in (Mg,Fe)O. Phys Chem Miner 32:418-425. doi: 10.1007/s00269-005-0013-6

Chapter 5: Diffusion of the majorite component in garnet

5.1 Introduction

Majorite is a high pressure polymorph of enstatite ($Mg_2Si_2O_6$) and forms a solid solution with the other garnets in Earth's mantle. Garnet with a large majorite component, so called majoritic garnet, is thought to constitute up to 40 - 60 volume % of the Earth's transition zone (Bass and Parise 2008, Frost 2008), whereas subducted oceanic crust might contain up to 80 volume % majoritic garnet in the transition zone (Irifune and Ringwood 1993). Also, the recognition of pyroxene lamellae and needles within garnet with a clear topotaxial relationship as being the products of exsolution from majoritic garnets (Song et al. 2004, Scambelluri et al. 2008, van Roermund 2009), refocused the interest of the scientific community to the solubility of the majorite component in garnet. Different studies have shown that the solubility of the majorite component in garnet increases with increasing pressure (Akaogi and Akimoto 1977, Gasparik 2003), which is the reason why majoritic garnet is an important phase in Earth's transition zone. A subducting (oceanic) slab should thus dissolve its (clino)pyroxene into garnet, by a mechanism which under dry conditions is probably diffusion controlled. The preservation of exsolved pyroxene lamellae from earlier events as well as lack of new precipitates after a UHP metamorphic event, as in the case of the Western Gneiss Region (Scambelluri et al. 2008, van Roermund 2009), might thus give important information on the duration of this UHP metamorphic event, provided that the diffusivity and solubility of the majorite component in garnet at the relevant conditions is known. As the subducting slab descends deeper into the mantle, diffusion of the majorite component into garnet will also be an important factor in the thermodynamic equilibration of the slab. However, the mass transport properties of majoritic garnet and especially diffusion properties of the majorite component in garnet at high pressure are not well constrained. Therefore diffusion experiments have been conducted at transition zone conditions to determine the diffusivity of the majorite component in garnet as function of temperature, pressure and also composition.

5.1.1 Diffusion in minerals

In the absence of a fluid phase, volume diffusion is the main mechanism to reduce concentration gradients and to equilibrate mineral assemblages in the solid earth. The diffusivity of components in minerals is thus an important factor controlling the rate at which mineral assemblages equilibrate and diffusion profiles have therefore been used to place constraints on the rate at which geological processes occur in the Earth (Lasaga and Jiang 1995, Chakraborty 2008). Garnets, as one of the important minerals found on the surface of the Earth, has been in the focus of several diffusion studies (Elphick et al. 1985, Loomis et al. 1985, Chakraborty and Ganguly 1992, Chakraborty and Rubie 1996). However, the application of these data was directed towards the interpretation of diffusion profiles that developed in garnet during a metamorphic event, and therefore the pressure range at which these studies were done was limited to below 4 GPa, with one point at 8.5 GPa by Chakraborty and Rubie (1996). For the same reason, the above mentioned studies only focused on the diffusivity of divalent cations, that occupy the dodecahedral site in garnet. The study presented here

investigates the diffusion at higher pressure conditions, as well as the diffusivity of the majorite component, which involves diffusion of divalent, trivalent and tetravalent ions occupying both the dodecahedral and octahedral sites.

Since the experiments presented here involve diffusion of more than one component, the profiles are treated as multi-component diffusion profiles. The general one dimensional form for a n-component system is:

$$\frac{\partial C_i}{\partial t} = \sum_{i}^{n-1} \frac{\partial}{\partial x}\left(D_{ij} \frac{\partial C_j}{\partial x} \right) \tag{5.1}$$

where C_i is the concentration of component i, t time, x the spatial coordinate and D is a (n – 1) x (n – 1) matrix of diffusion coefficients, which makes it a system of coupled partial differential equations. The off-diagonal elements in D represent the influence of one diffusing component on the other. The last component (C_n) is calculated from charge balance. The matrix D is calculated using either the ideal multi-component model of Lasaga (1979) or, if from visual inspection there was no reason to think that there is a compositional dependence of the diffusion coefficient, constant diffusion coefficients were used, where the off-diagonal elements of D were set to zero, effectively reducing 5.1 to:

$$\frac{\partial C_i}{\partial t} = \frac{\partial}{\partial x}\left(D_i \frac{\partial C_i}{\partial x} \right) \tag{5.2}$$

In the case that the diffusion model with constant parameters did not give a satisfactory fit, the model of Lasaga (1979) for ideal ionic (solid) solutions was used:

$$D_{ij} = D_i^0 \delta_{ij} - \frac{D_i^0 z_i z_j}{\sum_{k=1}^{n} z_k^2 c_k D_k^0} \cdot (D_j^0 - D_n^0) \tag{5.3}$$

where D^0_i is the tracer diffusivity of component i, i.e. when component i would diffuse independently from all other components, δ_{ij} is Kronecker's delta ($\delta_{ij} = 1$ if i = j, otherwise zero) and z_i the charge of component i. In the case of a binary system, equation 5.1 reduces to 5.2 with D_1 given by:

$$D_1 = \frac{D_0^0 D_1^0}{X_0 D_0^0 + X_1 D_1^0} \tag{5.4}$$

where X_0 and X_1 are the cationic mole fractions ($X_0 = C_0 / (C_0 + C_1)$). This model was already successfully used by Chakraborty and Ganguly (1992) to model multi-component diffusion profiles in garnets. The modelling and fitting of the diffusion profiles was done by two programs that were developed, mcdiff and mcfitter, that solve equation 4.1 and allows for different models for the calculations of the D matrix. A more detailed explanation of the programs was given in chapter 4.

One of the objectives of this study is, next to determining the actual diffusion coefficients themselves, to determine the activation enthalpy of diffusion ΔH, which is a measure of the temperature dependence of the diffusivity of the components. The temperature dependence can be expressed by an Arrhenius style relation:

$$\ln D_i^0(T) = \ln D'^0_i - \frac{\Delta H}{RT} \quad (5.5)$$

The activation enthalpy for diffusion is determined from the slope in a log D – 1/T plot, which gives a straight line. The pressure dependence, expressed through the activation volume ΔV, can be obtained through the standard relation of thermodynamic potentials and leads to:

$$\ln D_i^0 = \ln D'^0_i - \frac{\Delta E + (P-1)\Delta V}{RT} \quad (5.6)$$

where ΔE is the activation energy and P pressure in bars, and which also defines a straight line in a log D – (P - 1) plot at constant temperature.

5.2 Experimental methods

5.2.1 Starting materials

Three different sets of experiments were conducted with various starting materials, all experiments were conducted using the diffusion couple method, i.e. two cylinders of garnet were placed together with their polished faces facing each other in a capsule and then annealed at transition zone conditions. The first set of experiments was conducted with polished cylinders of synthetic majoritic garnet (composition $Py_{55}Mj_{45}$) and natural pyrope garnet ($Py_{93}Alm_5Gr_2$) from the Dora Maira Massif in Italy (Schertl et al. 1991) to determine the pyrope – majorite interdiffusivity. Natural almandine garnet ($Alm_{70}Py_{15}Gr_{15}$) from the Ötztal in Austria together with the same majoritic garnet were used in the second set of experiments to determine almandine – majorite interdiffusivity. The last set of experiments was a single experiment to determine the pyrope – majorite interdiffusivity, the starting materials for this experiment were Dora Maira pyrope garnet and Ötztal almandine garnet also used in the other sets of experiments.

The cylinders were mirror-polished on the sides where they contact each other. Before the experiment the ferric iron contents have been determined by Mössbauer spectroscopy. The Dora Maira garnet contains no detectable

Table 5.1: Composition determined by electron microprobe of the starting materials used in the diffusion experiments

Element	**Dora Maira garnet**		**Ötztal almandine**		**Majoritic garnet**	
	Wt. %	per 12 O	Wt. %	per 12 O	Wt. %	per 12 O
MgO	27.88	2.83	3.32	0.39	35.43	3.52
FeO	1.93	0.11	43.37	2.14	0.01	0.00
CaO	0.62	0.05	5.20	0.44	0.00	0.00
MnO	0.04	0.00	0.21	0.01	0.00	0.00
Al2O3	25.04	2.01	21.56	2.01	12.61	0.99
TiO2	0.02	0.00	0.08	0.00	0.04	0.00
SiO2	44.05	3.00	37.83	2.99	52.54	3.50
Total	99.58	8.00	100.57	8.00	100.63	8.01

amount of ferric iron (detection limit 0.5 %) whereas the almandine garnet from Ötztal contains 2 ± 1 % of ferric iron. The water contents of Dora Maira pyrope was determined by Lu & Keppler (1997) to be 58 ppm, which corresponds to a protonation of 0.02% of the tetrahedral sites assuming that the hydrogarnet substitution is the dominant substitution mechanism.

Since majoritic garnet is not commonly found in nature, it was necessary to synthesize it using the multi-anvil apparatus. First reagent grade MgO, Al_2O_3 and SiO_2 oxide powders were mixed in a mortar together with ethanol to create a suspension. Subsequently the ethanol was evaporated using an infra-red lamp and after this the mixed powders were fused in a furnace at 1650 °C. The glass obtained was then crushed and grounded to a fine powder under ethanol, after which the ethanol was again evaporated. The powder was then again fused in a 1650°C furnace, after which it was crushed again and ground to a fine powder. This powder was then loaded into a Pt capsule (inner diameter 0.8 mm, outer diameter 1.2 mm, length 2.2 mm) for synthesizing majoritic garnet. Just before the synthesis experiments, the tube with powder was put for 5 minutes in a 1000 °C furnace to dry the powder, afterwards it was sealed by putting the Pt tube in a capsule die and pressing it in a bench vice. Majoritic garnet was then synthesized in a multi-anvil apparatus using a 10/5 assembly (numbers denote octahedron edge length and WC cube truncation edge length, respectively) at 1800 °C and 16 GPa for 8 hours. After recovery of the platinum capsule, it was cut into discs of 0.5 mm thickness and a single side was polished.

The grain size of the synthetic majoritic garnet was 5 – 10 µm and the grains were, as far as could be determined by TEM, randomly orientated. The cylinders of natural garnet were single crystal, though some of the crystals were cracked. The crystal size of the natural garnets was generally bigger than 200 µm. The Dora Maira pyrope garnet contained a minor amount of hydrous minerals, which were destroyed before the experiments by

Table 5.2: Run conditions of the diffusion experiments. [1]Type of diffusion couple: Py – Mj = Dora Maira pyrope – majoritic garnet diffusion couple, Py – Alm = Dora Maira pyrope – Ötztal almandine diffusion couple, Alm – Mj = Ötztal almandine – majoritic garnet diffusion couple. [2]Octahedron edge size / inner anvil truncation size notation

Run number	Diffusion couple[1]	Pressure cell[2]	Pressure	Temperature	Run duration
H2986	Py - Mj	14/8	15 GPa	1600 °C	4 h
H3050	Py - Mj	14/8	15 GPa	1800 °C	2 h
H3076	Py - Mj	14/8	15 GPa	1500 °C	24 h
H3084	Py - Mj	10/5	20 GPa	1800 °C	20 h
H3086	Py – Alm	14/8	15 GPa	1500 °C	12 h
H3088	Alm - Mj	14/8	15 GPa	1600 °C	7 h
H3106	Py – Mj	14/8	15 GPa	1900 °C	2 h
H3119	Alm - Mj	14/8	15 GPa	1600 °C	4 h
H3201	Py - Mj	14/8	12 GPa	1800 °C	4 h
H3244	Alm - Mj	10/5	15 GPa	1400 °C	24 h
H3257	Py - Mj	10/5	15 GPa	1400 °C	24 h

putting the cylinders in a furnace at 1000 °C for 5 minutes. After this treatment no peaks of hydrous minerals could be found by x-ray diffraction and also inspection by SEM could not identify any hydrous minerals.

5.2.2 Apparatus and pressure cell

The diffusion experiments were carried out in a 1000 ton multi-anvil apparatus at the Bayerisches Geoinstitut in Bayreuth. The multi-anvil apparatus used was of the 6/8 split-sphere type (Kawai et al. 1973, Keppler and Frost 2005), referring to the number of outer and inner anvils and guidie block geometry. The inner anvils consisted of 8 tungsten carbide cubes with their corners truncated, to form an octahedral shaped pressure chamber in which the pressure cell resided. The length of the thermocouple was increased such that the thermocouple junction was inside the central heater, the capsule was therefore made smaller than in the standard assembly. The diffusion couple was contained within a platinum capsule in the case of the pyrope – majoritic garnet diffusion couples and within an iron capsule in case of the almandine – majoritic garnet diffusion couples, the length of the capsules was 1.7 mm, the diameter 1.6 mm, and the wall thickness was 0.2 mm. The iron capsule in the experiments with almandine should have buffered the oxygen fugacity near the iron-wüstite (IW) buffer. A tungsten 3% rhenium - tungsten 25% rhenium thermocouple was used to measure the temperature, the pressure effect on the EMF is unknown and has therefore not been corrected for. To prevent the platinum capsule from entering into the thermocouple tube or from reacting with the iron capsule the thermocouple has been separated from the capsule with a 25 µm thick rhenium disc in the former case and a 200 µm thick densified Al_2O_3 disc in the latter case.

Before the experiments, the samples were dried in a vacuum oven at 175 °C for 24 hours, after which the capsules were pressure sealed as fast as possible in a bench vice. Since the iron capsules oxidized even in a vacuum oven, they were not dried but stored in a desiccator with silica gel. After the pressure cell was loaded in the multi-anvil apparatus and was pressurized to the desired pressure, increasing the temperature was done at a rate of 100 °C / minute, with the last 200 °C in one minute. Quenching was done by cutting of the power, the sample was quenched in this way to ~ 100 °C in roughly 10 seconds. Temperature was controlled automatically with a Eurotherm controller. For a more detailed account of the calibration of the multi-anvil apparatus the reader is referred to chapter 3 or Keppler & Frost (2005).

5.3 Analytical methods

After recovery of the sample the capsule was cut perpendicular to the contact interface between the two halves of the diffusion couple (hereafter referred to as the diffusion interface) and prepared as a 30 µm thick thin section. These thin sections were subsequently analysed by a JEOL JXA-8200 electron microprobe to gain insight into the length of the diffusion profiles. Since in all cases the diffusion profiles were too short to be measured by electron microprobe, the samples were further prepared for TEM. Molybdenum meshes with a mesh size of 135 µm were glued with epoxy glue on the thin section after which the sample with mesh was separated from the slide by dissolving the crystalbond glue in acetone. The sample was then further milled down in an Ar ion-miller at 4.5 keV and 1.0 mA to electron transparency. From experiments H3201 about 250-

300 nm thick TEM foils were produced with a FEI Quanta 3D FEG dual beam device (FIB/SEM). Diffusion profiles were then measured by using a Philips CM20 FEG TEM operating at 200 kV and equipped with an EDS system and Noran System Six software. To ensure that the beam direction, and thus excitation volume for EDS analysis, was perpendicular to the diffusion gradient, the TEM foil was orientated in such a way that the y-rotation axis of the specimen holder was parallel to the orientation of the diffusion interface and the x-axis was perpendicular to it. The foil was then rotated around the x-axis by 15°, such that it faces towards the EDS detector. Diffusion profiles were measured in STEM mode with a theoretical spot size of 2.2 nm. Since diffusion profiles were generally shorter than 400 nm, a circular scanning pattern of 40 nm in diameter was used and the beam was underfocused by ± 3.5 µm to reduce beam damage. However, a scanning pattern of 40 nm still resulted in a significant amount of beam damage when analysing majoritic garnet,resulting in a low magnesium content and relatively high silicon content. Therefore a method was developed to correct for beam damage, which is described in more detail in appendix 5.1. Quantification is done by using a modified version of the method proposed by Van Cappelen and Doukhan (1994) which is described in more detail in appendix 5.2.

The garnet component mole fractions are calculated from the elemental compositions using a least squares technique. Since Fe has a strong prevalence for the dodecahedral site (O'Neill et al. 1993), it is assumed that the Fe-majorite component ($FeSiO_3$) is negligible for the majoritic garnet phase. For the pyrope – majoritic garnet analyses, the grossular and almandine components have been taken together as one virtual component $(Ca+Fe)_3Al_2SiO_3$, leading to the following components to be calculated from the elemental compositions:

$Mg_w(Ca+Fe)_xAl_ySi_zO_{12}$ = a $Mg_3Al2Si3O12$ + b $(Ca+Fe)_3Al_2Si_3$ + c $Mg_4Si_4O_{12}$
for which the following matrix equation can be written and solved:

$$\begin{pmatrix} 3 & 0 & 4 \\ 0 & 3 & 0 \\ 2 & 2 & 0 \\ 3 & 3 & 4 \end{pmatrix} \cdot \begin{pmatrix} a \\ b \\ c \end{pmatrix} = \begin{pmatrix} w \\ x \\ y \\ z \end{pmatrix} \qquad (5.7)$$

$$A\,c_{comp} = c_{element}$$

In the case of almandine – majoritic garnet diffusion experiments, a similar expression can be derived.

The errors on the component compositions are calculated using the following formula, which can be obtained from the propagation of errors:

$$M^{comp} = A^{+} \cdot M^{element} \cdot (A^{+})^{T} \qquad (5.8)$$

where $M^{element}$ is the covariance matrix of the elemental concentrations, where the diagonal elements (variances) are the squared errors of the elemental concentrations, which was estimated from the relative error of the counting statistics, and the off-diagonal elements were set to zero (zero covariance between elements). A^{+} denotes the Moore – Penrose pseudoinverse of A, and the superscript T denotes the transpose.

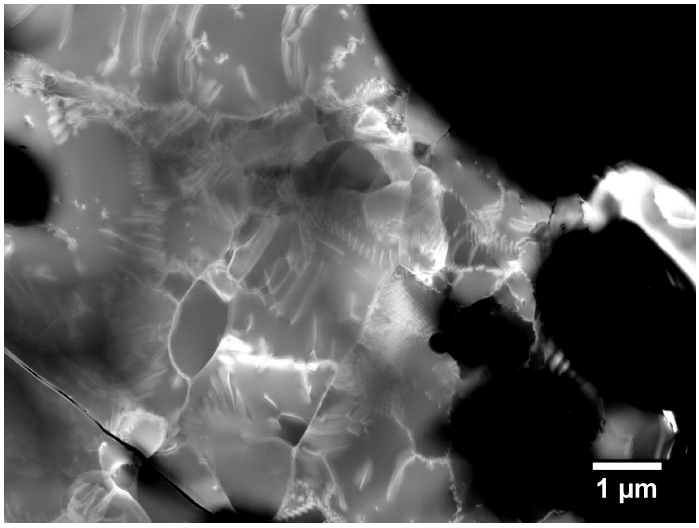

Figure 5.1: Microtextural evolution of the majoritic garnet – almandine diffusion couple near the edge of the majoritic garnet - almandine interface. See text for discussion.

5.4 Results

5.4.1 Characterization of the samples after the experiments

After the samples were recovered, cut perpendicular to the interface and polished, they were characterized by SEM / electron microprobe and TEM. The observations showed a microtextural evolution of most of the samples during the experiments. In most of the samples recrystallization was observed near the edges of the majoritic garnet half. This might have been caused by the shape of the majoritic garnet half of the diffusion couple, which is smaller than the almandine or pyrope half and may act as a kind of indenter to the other half during the initial stage of cold compression, where the conditions are less hydrostatic.

Figure 5.1 shows a STEM DF images of one of the recrystallized zones near the edge of the majoritic garnet – almandine interface. There is a big difference in the density of dislocations and the average grain size between the recrystallized part and the more pristine part. Also a high amount of dislocation arrays forming sub-grain boundaries can be seen. During the measurement of diffusion profiles, the regions with a high density of dislocations and recrystallization have been avoided. The experiments with iron capsules show a greater amount of these zones, which might be related to the higher strength of the iron capsules.

Ion addition to the above mentioned 'deformation zones', another phenomenon can also be observed. Most of the diffusion gradients lie within grains after the diffusion experiment. This has been interpreted as being the result of topotactic growth of the majoritic garnet grain on the pyrope or the almandine part of the diffusion couple (figure 5.2). The driving force for this is possibly the reduction of (surface) energy by reducing the total area of grain boundaries. Sometimes growth of the grain towards the almandine or pyrope side is also observed, but this might be related to the volume of dislocations in both sides of the diffusion couple, since the polycrystalline majoritic side can also accommodate deformation by grain boundary sliding, which is not possible in the single crystal pyrope or almandine. The amount of topotactic growth usually increases with temperature and the Dora Maira pyrope – majoritic garnet experiments usually show a higher amount of topotactic growth than the almandine – majoritic garnet experiment. This might be caused by the greater mismatch in lattice parameters between the calcium bearing almandine garnet ($a \approx 11.53$ Å) and majoritic

garnet (a ≈ 11.47 Å), than between pyrope (a ≈11.46 Å) and majoritic garnet (Novak and Gibbs 1971, Heinemann et al. 1997). However, considering the relatively small width of dry grain boundaries (few nm) compared to the length of the diffusion profiles (300 – 500 nm), it is not expected that the motion of the grain boundaries has an influence on the determined diffusion coefficients. Moreover, in most samples the motion of the grain boundaries was much faster than the diffusion rate, which can be deduced from the length of the diffusion profiles and the position of the grain boundary after the diffusion anneal. Therefore, the grain boundary would have only been for a short amount of time at the position where actual diffusion between both parts of the diffusion couple occur, which makes it even more unlikely that the motion of the grain boundary significantly

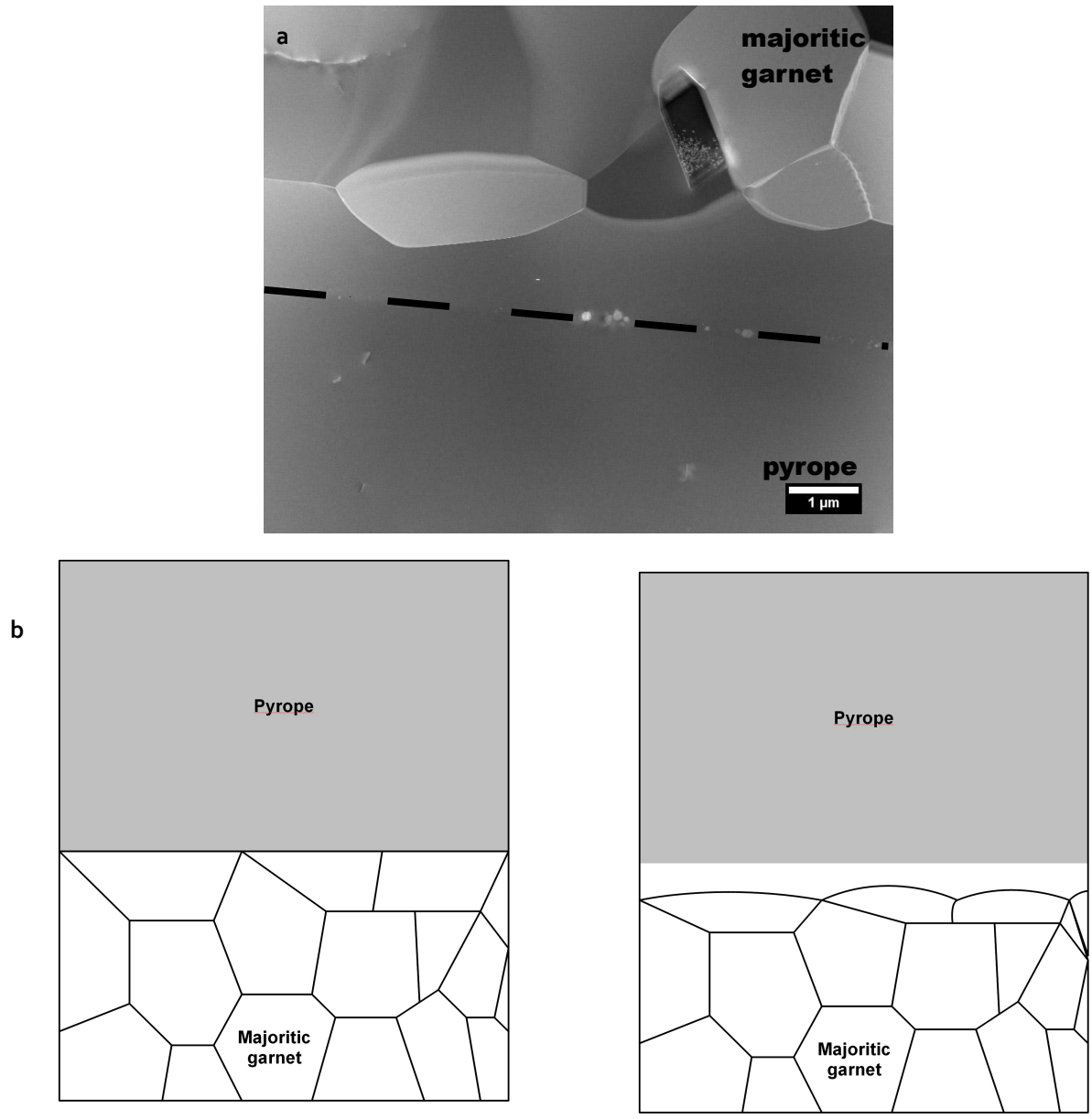

Figure 5.2: a) Dark-field STEM image of diffusion couple H3257 showing the topotaxic growth of majorite on pyrope. The original interface is marked by the dashed black line. Its position could be determined by the location of the diffusion profile and the presence of nm-sized inclusion on a linear array at the location of the former boundary. (b) Sketch of the topotaxic growth of majoritic garnet on pyrope, the grain boundary on the original interface between both couples migrates into the majoritic garnet side.

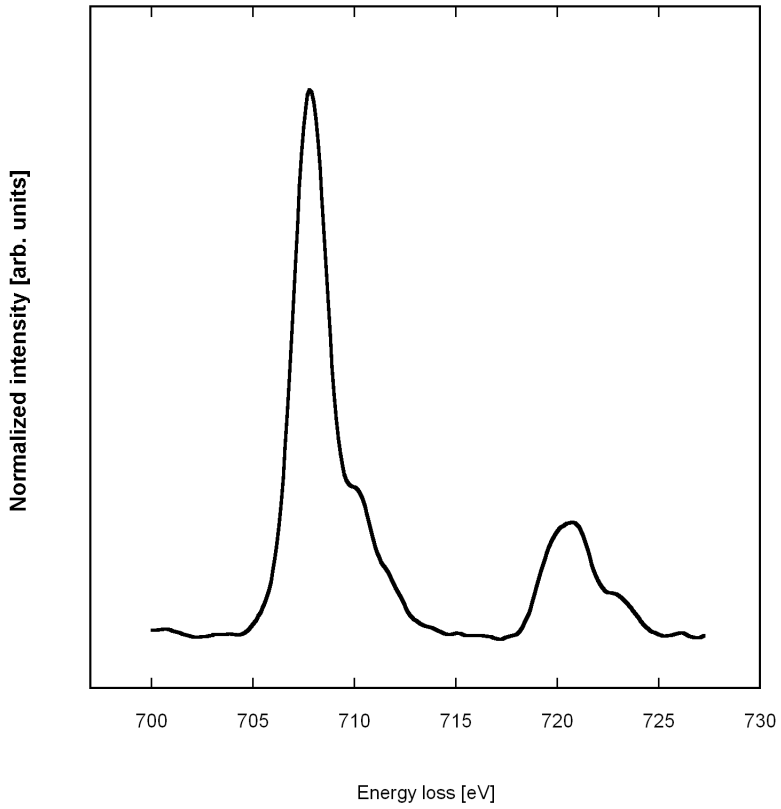

Figure 5.3: EELS spectrum of the region around the $FeL_{2,3}$ edge in the almandine side of experiment H3088, profile is deconvolved and corrected for multiple scattering using the fourier-ratio described in Egerton (1996). The Fe^{2+}/ (Fe^{2+} + Fe^{3+}) ratio was determine from the relative intensity of the white lines centered around 707.8 eV / 709.5 eV (white lines on L_3 edge) and 720.5 eV / 723eV (white lines on L_2 edge) described by van Aken and Liebscher (2002). Zero-loss FWHM peak width was 0.8 eV.

influences diffusion during the experiments.

The Fe^{3+} / (Fe^{2+} + Fe^{3+}) ratio was determined using EELS for the sample H3088 after the experiment and the EELS spectrum is shown in figure 5.3. The relative intensities of the white lines present at the $FeL_{2,3}$ edges was used to determine the Fe^{3+} / (Fe^{2+} + Fe^{3+}) ratio in this sample using the universal curve determined by Van Aken et al. (2002). The obtained ratio for almandine was 6 ± 4 %, which is within error similar to that determined by Mößbauer spectroscopy (2 ± 1 %) for the almandine starting material. So clearly, the iron capsule buffered the oxygen fugacity well and no significant change in ferric iron content occurred during the experiment.

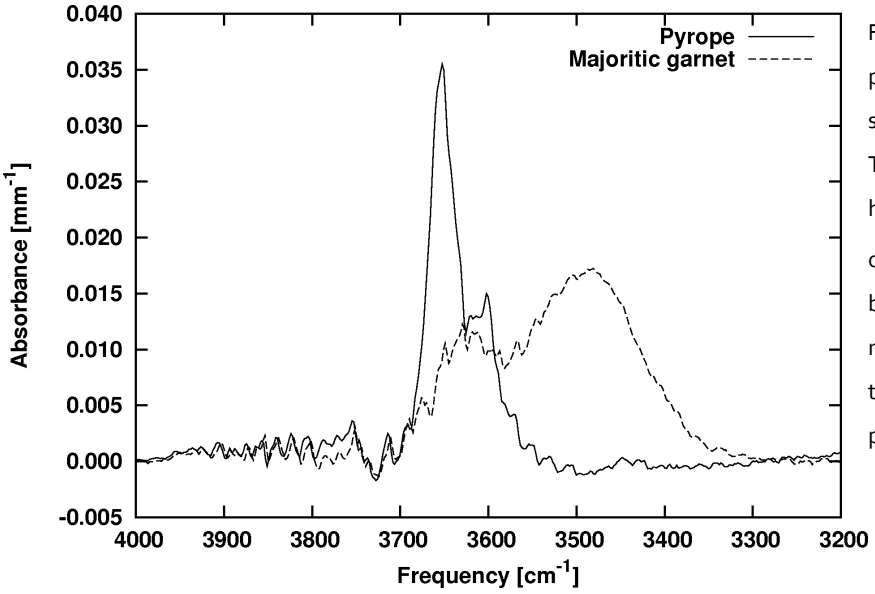

Figure 5.4: FTIR spectrum of the central pyrope and majoritic garnet parts of the sample H3106 after the diffusion anneal. The most dominant peak is that of the hydrogarnet band system in the spectrum of the pyrope part. Around 3500 cm^{-1} is a broad band system which might be related to water in the grain boundaries in the FTIR spectrum of the central majorite part of sample H3106.

The water content after the experiment was determined for sample H3106 using FTIR by measuring the integrated area under the OH band system between frequencies 3558 cm^{-1} and 3685 cm^{-1} and using the calibration of Bell et al. (1995). The obtained FTIR spectra indicate for the pyrope side a water content of 58 ± 6 ppm wt. in the centre and 47 ± 5 ppm wt. more towards the interface between the majorite and the pyrope part. The majorite part has a lower water content, about 37 ± 4 ppmw in the middle and 24 ± 3 ppmw near the interface. However, as is apparent from the spectra (figure 5.4) the quality of the majorite spectra is lower with a broad band centered around 3500 cm^{-1} , possibly related to water in the grain boundaries, partly overlapping the position of the band related to hydrogarnet substitution, so the exact amount of water that is present in the majoritic garnet half is less well constrained. The Dora Maira pyrope spectrum shows one dominant peak at 3651 cm^{-1} and one less dominant at 3602 cm^{-1}, which can be related to the hydrogarnet subsitution and is also observed for other Dora Maira pyrope garnets (Lu and Keppler 1997). However, the bands here are much broader than reported by Lu and Keppler (1997), their high frequency system is not much more intense as is the case in the run products of the diffusion anneal, and the individual bands in the high frequency system (at 36450.5, 3650.8 and 3660.6 cm^{-1}) are not discernible in the run product here.

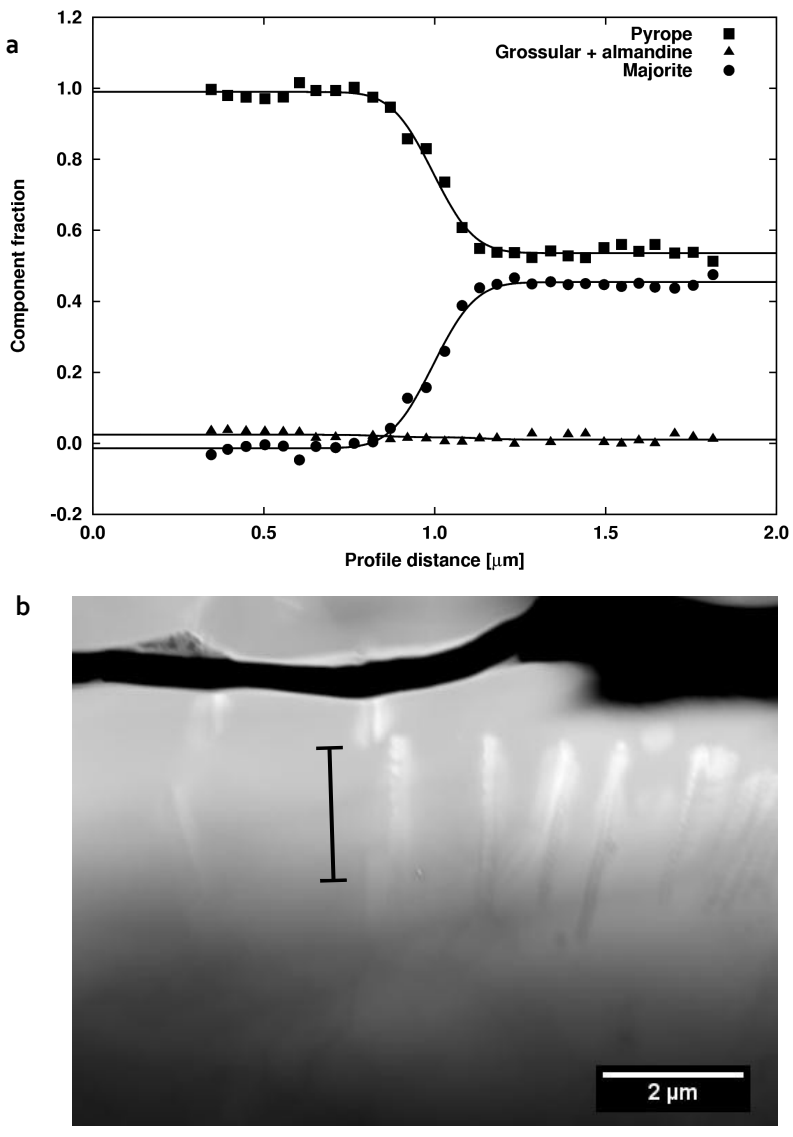

Figure 5.5: a) The measured diffusion profile for sample H3050, run at 1800 °C and 15 GPa. The solid lines are the fits to the measured profiles using constant diffusion coefficients. The best fit value are for pyrope $D_{Py} = 6\ (2) \times 10^{-15}\ cm^2\ s^{-1}$, and for majorite $D_{Mj} = 7\ (1) \times 10^{-15}\ cm^2\ s^{-1}$. b) The location of the diffusion profile (black line). White to dark gray spots are contamination marks of other analyses.

Table 5.3: Fitted diffusion coefficients for the experiments run at 15 GPa

Run number	Pressure	Temperature	D_{Py} [cm² s⁻¹]	D_{Mj} [cm² s⁻¹]
H3257	15 GPa	1400 °C	2.5 (8) x 10^{-16}	3.4 (8) x 10^{-16}
H3076	15 GPa	1500 °C	4 (2) x 10^{-16}	3 (1) x 10^{-16}
H2986	15 GPa	1600 °C	1.4 (2) x 10^{-15}	1.4 (2) x 10^{-15}
H3050	15 GPa	1800 °C	6 (2) x 10^{-15}	7 (1) x 10^{-15}
H3106	15 GPa	1900 °C	3.7 (7) x 10^{-14}	4 (1) x 10^{-14}

5.4.2 Temperature dependence

The temperature dependence of the diffusivity of the majorite component in garnet was determined at 15 GPa by performing several experiments between 1400 °C and 1900 °C. All the profiles in these runs were fitted using the method described above with a constant diffusion coefficient for each component. Using compositionally dependent diffusion coefficients did not give significantly better fits.

The measured diffusion profile, expressed in terms of garnet components (pyrope, majorite and grossular + almandine), is shown in figure 5.5 for experiment H3050, which was run at 1800 °C for 2 hours. Due to the topotactic growth of the majoritic garnet part onto the pyrope part, the original interface was not longer visible as a grain boundary. For this sample, and for the other samples where this was the case, the orientation of the interface was determined by measuring two more diffusion profile on either side of the first one and from the position of the compositional gradients the orientation and the approximate position of the original interface were determined. The exact position of the interface was then taken as a free variable in the fitting process. From the profiles the diffusion coefficient in run H3050 for the pyrope component was determined to be D_{Py} = 6(2) x 10^{-15} cm² s^{-1} and for the majorite component it was determined to be D_{Mj} = 7(1) x 10^{-15} cm² s^{-1}. The diffusion coefficients for pyrope and majorite are equal within their respective errors, however this is most likely because the grossular + almandine component is very small in all these experiments, such that the experiment is basically a binary diffusion experiment, which can be characterized by a single diffusion coefficient.

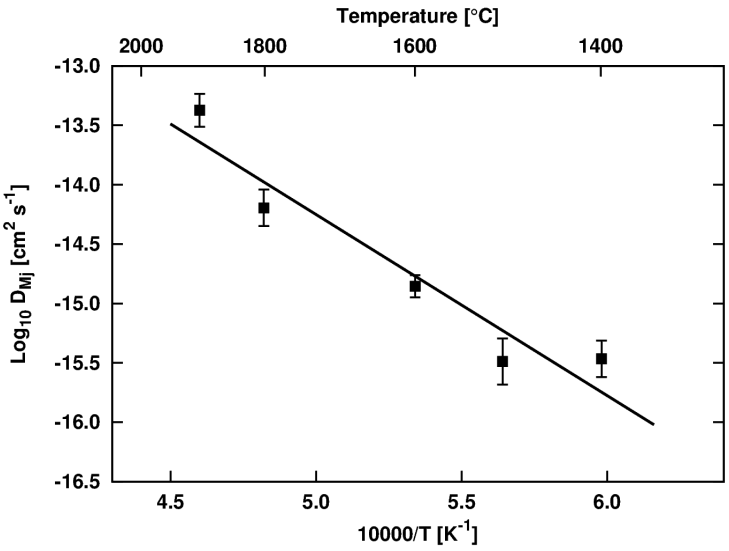

Figure 5.6: Diffusivity of the majorite component in garnet as function of temperature. From this plot an activation enthalpy at 15 GPa of 291 ± 51 kJ mol^{-1} was determined.

The results for the other pyrope – majoritic garnet experiments at 15 GPa are given in table 5.3. As expected, there is clearly a temperature dependence of the diffusion coefficient for both majorite and pyrope in garnet. The activation enthalpy obtained by fitting the measured 'binary' diffusion coefficient to equation (4.5) was 291± 51 kJ mol^{-1} with the pre-expontial being 2.3 x 10^{-7} cm^2 s^{-1} when using the diffusion coefficients for the majorite component. For the pyrope component the values are 302 ± 61 kJ mol^{-1} for the activation enthalpy and 4.3 x 10^{-7} cm^2 s^{-1} for the pre-exponential.

5.4.3 Pressure dependence

In order to determine the effect of pressure on the diffusivity of the majorite and pyrope components diffusion experiments were conducted at 12 and 20 GPa, both at 1800 °C using the same pyrope – majoritic garnet diffusion couples as in the experiments described above. The measured profiles for experiment H3201 are shown in figure 5.7, run at 12 GPa and 1800 °C for 4 hours, and can be compared to the profile shown in figure 5.5 for run H3050, which was an experiment at 15 GPa and 1800 °C for 2 hours. The diffusion profiles for experiment H3050, run at 15 GPa, are about half the length of the diffusion profiles obtained from experiment

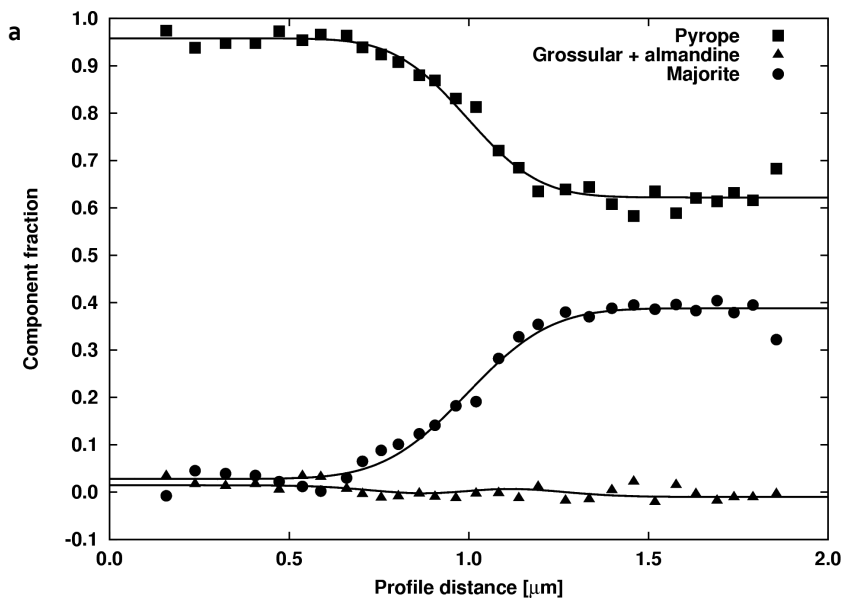

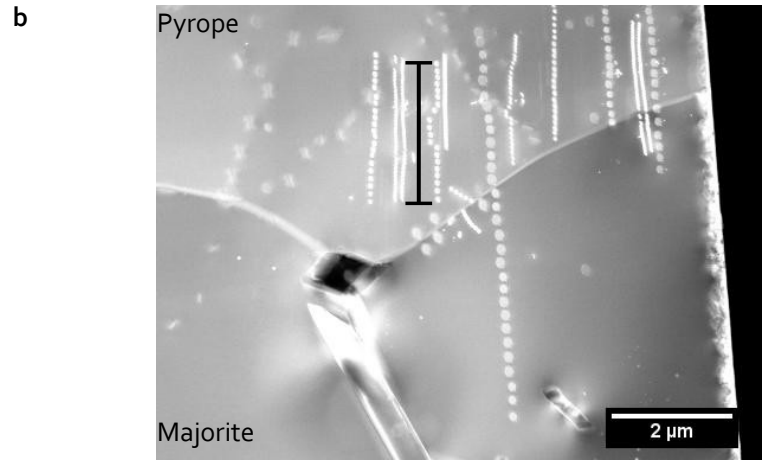

Figure 5.7: Diffusion profiles for run H3201, ran at 12 GPa and 1800 °C. a) Shows the measured diffusion profile expressed as garnet end-member fraction. b) The location (black line) of the measured diffusion profile. The white spots are contamination marks of other analyses.

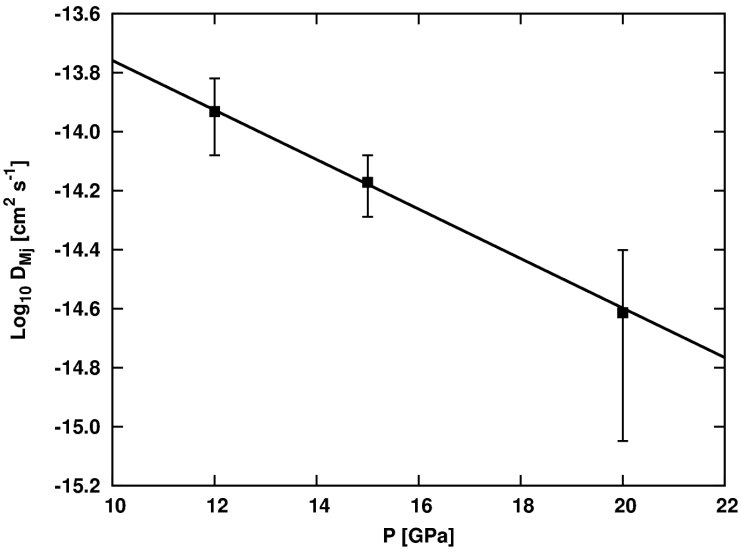

Figure 5.8: Pressure dependence of the diffusivity of the majorite component in garnet. The obtained activation volume for diffusion is 3.3(1) cm^2 mol^{-1}.

H3201, which was run at 12 GPa. Since the diffusion distance is proportional to √(Dt), where D is the diffusion coefficient and t the run length of the experiment, one can estimate that a 3 GPa increase in pressure leads to a factor ~1.4 decrease in diffusivity.

Figure 5.8 shows the fitted diffusion coefficients for the majorite component in garnet in a Log_{10} D – P plot for the experiments conducted at 1800 °C between 12 – 20 GPa. From this plot, using equation 5.6, the activation volume for diffusion of the majorite component in garnet was determined to be 3.3 (1) cm^3 mol^{-1}. Combining this with the already previously determined activation enthalpy at 15 GPa, one can deduce an activation energy for diffusion of the majorite component in garnet of 241 ± 54 kJ mol^{-1} and a pre-exponential factor of 1.4 x 10^{-7} cm^2 s^{-1}.

5.4.4 Magnesium – iron interdiffusion

To determine the magnitude of the diffusivity of the majorite component relative to that of magnesium – iron interdiffusion in garnet, an experiment (H3086) on a pyrope – almandine diffusion couple was conducted at 15 GPa and 1500 °C. Since the diffusion profiles obtained from the recovered sample of this experiment were much longer than those obtained from the Dora Maira pyrope – majoritic garnet runs, it was possible to measure profiles with a larger scanning pattern and radiation damage correction was not necessary.

Since both halves of the diffusion couple separated during decompression there was a gap in the diffusion profile of unknown width. The position of the gap is denoted in figure 5.9 by the dashed vertical line. The mcfitter program was modified for this, to fit the width of the gap along with the other variables. For this sample the ideal model of Lasaga (1979) was used, since it gave a significantly better result than the simple constant diffusion coefficient model (a decrease of 49% in the χ^2 value). The tracer diffusion coefficient obtained by fitting the profiles are D_{Mg} = 2.1 x 10^{-13} cm^2 s^{-1}, D_{Fe} = 4.8 x 10^{-13} cm^2 s^{-1} and D_{Ca} = 3.6 x 10^{-14} cm^2 s^{-1}, i.e. the diffusivity of dodecahedrally coordinated Mg and Fe in garnet is 2 – 3 orders of magnitude faster than the diffusivity of the majorite component at the same conditions (run H3076) and the diffusivity of Ca is 1 – 2 orders of magnitude faster than that of the majorite component.

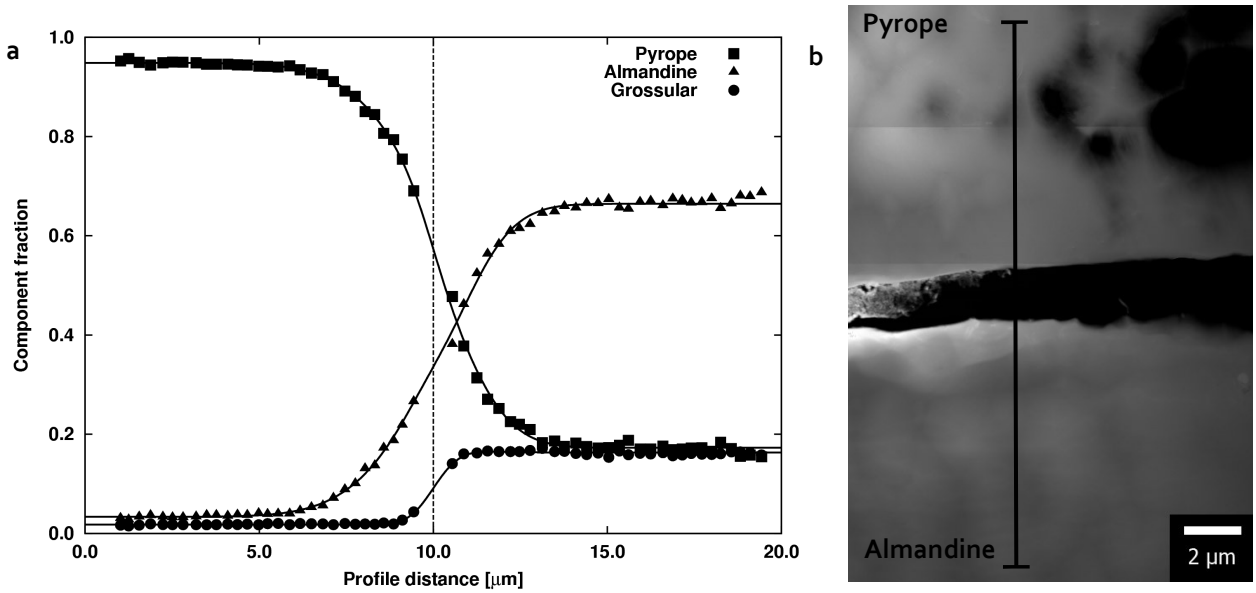

Figure 5.9 : a) the measured diffusion profiles of the divalent cations in experiment H3086 at 15 GPa and 1500 °C. The cation fractions are calculated as $X_{Mg} = X_{Mg} / (X_{Mg} + X_{Fe} + X_{Ca})$. The fitted tracer diffusion coefficients are $D_{Mg} = 2.1 \times 10^{-13}$ cm² s^{-1}, $D_{Fe} = 4.8 \times 10^{-13}$ cm² s^{-1} and $D_{Ca} = 3.6 \times 10^{-14}$ cm² s^{-1}. The vertical dashed line indicates the position of the gap in the profile. b) A dark-field STEM image of the location of the diffusion profile (black line) in experiment H3086. The horizontal lines are due to the picture being a mosaic of several pictures.

5.4.5 Almandine – (Mg) majorite diffusion

Experiments H3088 (15 GPa, 1600 °C), H3119 (15 GPa, 1600 °C) and H3244 (15 GPa, 1400 °C) were conducted with almandine – majorite diffusion couples, to investigate the effect of iron on diffusion. The diffusion profile for experiment H3244 is shown in figure 5.10, and is distinctly different from the diffusion profiles with the pyrope – majorite couples and the almandine – pyrope couples. The asymmetry in the profiles is clear, with the gradients in Fe and Mg (and to al lesser extent Ca too) extending much farther into the majoritic garnet half than into the almandine part. Due to the complexity of the diffusion profile the fitting was adjusted manually done, since the mcfitter program did not produce realistic fits near the diffusion interface and on the almandine side of the diffusion couple. The values for the diffusion coefficients for Mg, Fe and Ca were chosen by keeping in mind the relative magnitudes of the diffusion coefficients of Mg, Fe and Ca obtained from the pyrope – almandine diffusion experiment (H3086). The asymmetry of the diffusion profile could only be modelled when a strong dependence of the diffusion coefficient of the divalent cations on majorite composition was assumed. The concentration dependence of the diffusion coefficient was expressed in the following form:

$$D = D_0\left(1 + \sum_{i=1}^{N} \alpha_i C_i\right) \tag{5.9}$$

where N is the number of components in the system, α_i is a coefficient determined by fitting and C_i is the concentration of component i. Though the fit is not perfect, the main characteristics are well reproduced and it is still possible to make some qualitative inferences. The fitted tracer diffusivities for Mg, Fe and Ca are 3.5×10^{-14} cm² s^{-1}, 9.3×10^{-14} cm² s^{-1} and 9.3×10^{-15} cm² s^{-1} respectively. For Al and Si these are 2.3×10^{-15} cm² s^{-1} and 4.6×10^{-15} cm² s^{-1}, respectively. The absolute magnitude of the diffusion coefficients may however not be

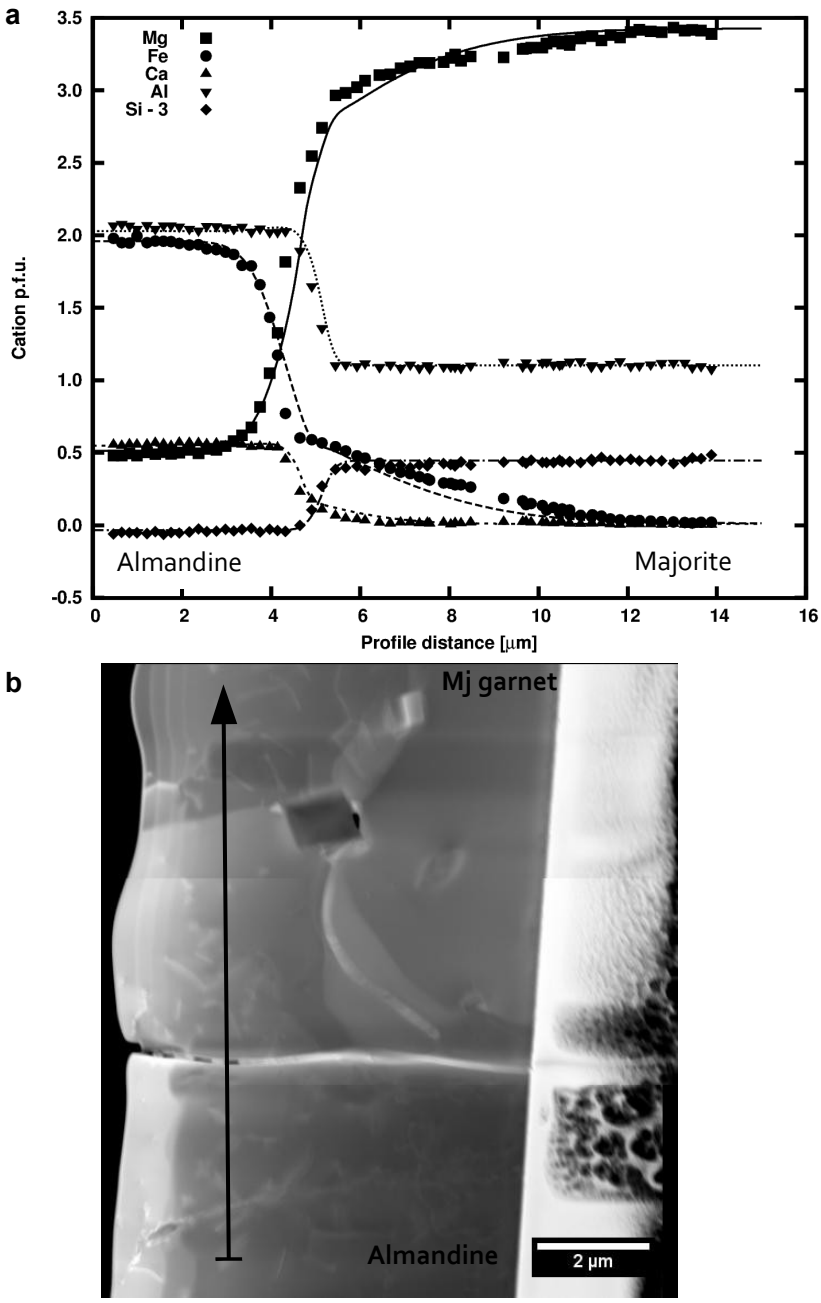

Figure 5.10:The measured diffusion profile (a) and location (black line) (b) for experiment H3244, run at 1400 °C and 15 GPa for 24 hours. Note the shoulder of Fe in the diffusion profile extending into the majoritic garnet part of the diffusion couple.

representative of the bulk diffusion coefficient, since both sides contain a relatively high density of dislocations. The ' shoulder' in Fe and Mg extending into the majoritic garnet side could only be modelled if the diffusivity in majoritic garnet for Mg was at least a factor 15 faster than in the almandine side (α_{Mg} = 30 -50) and the diffusivity for Fe a factor 5 higher. (α_{Fe} = 10-15).

The compositions were also expressed in terms of pyrope, almandine, grossular and Mg-majorite components (fugure 5.11). The addition of an andradite component did not change the profiles (the andradite component was nearly equal to zero), which is also supported by the EELS measurements in the other almandine – pyrope and almandine – majoritic garnet diffusion couples that were run in Fe capsules which showed a Fe^{3+} / (Fe^{2+} + Fe^{3+}) ratio of nearly zero. The addition of an Fe-majorite component produced a large negative Mg-majorite component at the almandine side of the diffusion profile, and was thus considered unrealistic. Expressing the

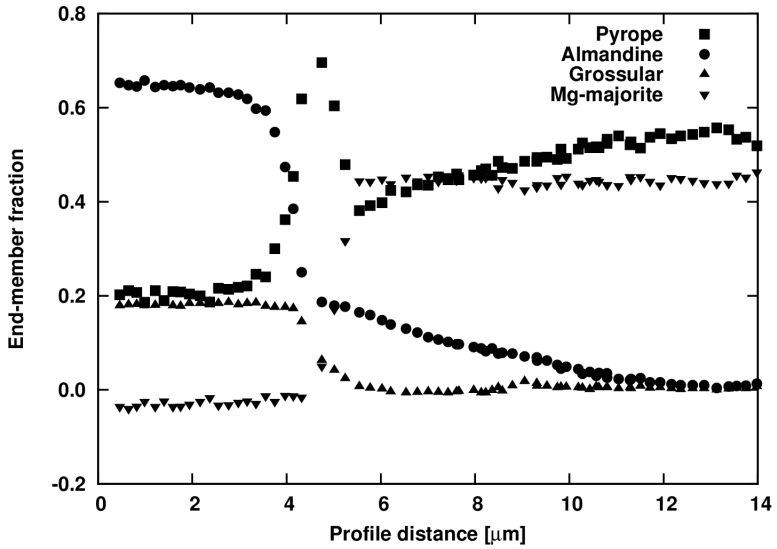

Figure 5.11: Profile H3244 expressed in terms of pyrope, almandine, grossular and Mg-majorite components. Note the spike in the pyrope component at the location where the Mg-majorite component decreases to zero.

composition in terms of garnet components resulted in a pyrope peak near the point where the Mg-majorite component drops to zero. In principle this could be the result of presence of a miscibility gap between almandine rich garnet and Mg-majorite rich garnet. However, there is no evidence for a miscibility gap between majorite rich garnet and almandine rich garnet, Ringwood and Major (1971) synthesized majoritic garnets near the almandine – majorite join at 1000 °C. Because miscibility gaps tend to close at higher temperatures it is thus unlikely that one exists at the conditions of the diffusion anneals. Moreover, the existence of a miscibility gap would also require next to the precipitation of a pyrope rich phase, the precipitation of a Fe-majorite rich phase which is not observed and is not very likely considering that end-member Fe-majorite is not stable (Ohtani et al. 1991). Diffusion in the almandine – majoritic garnet experiments has therefore not been interpreted in terms of diffusion of garnet components, as in the experiments described above, but in terms of the diffusion of cations. The fitting has been done without regard to end-member components, i.e. magnesium in the Mg-majorite and pyrope component has been treated as a single diffusing component.

Experiment H3119 (see figure 5.12) shows a similarly shaped profile, with again a shoulder for Mg, Fe and Ca

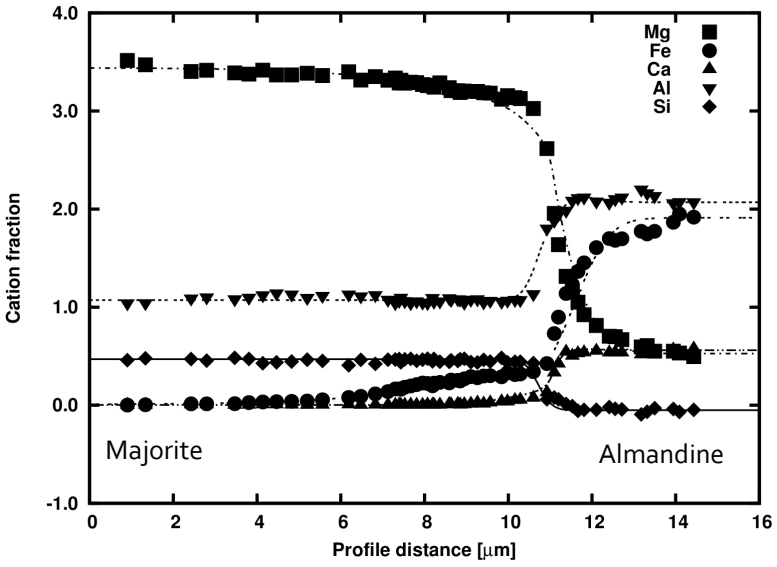

Figure 5.12: Diffusion profile obtained from experiment H3119, ran at 1600 °C and 15 GPa for 4 hours. The shape of the diffusion profiles show great similarity with those from experiment H3244. Again, the diffusion profiles could only be modelled by assuming a strong dependency of the diffusivity of Mg, Fe and Ca on the majorite content.

penetrating deeper into the majoritic garnet side than into the almandine side. The diffusion profile has again been fitted by hand using the above mentioned method. The obtained tracer diffusion coefficients are for Mg, Fe and Ca 2.1 x 10^{-13} cm^2 s^{-1}, 5.6 x 10^{-13} cm^2 s^{-1} and 3.1 x 10^{-14} cm^2 s^{-1}, respectively. For Al and Si 2.8 x 10^{-14} cm^2 s^{-1} and 2.4 x 10^{-14} cm^2 s^{-1}, respectively. The values for Mg, Fe and Ca are very similar to those obtained in the almandine – pyrope diffusion experiment, however this run was performed at a temperature 100 °C higher. However it must again be stressed that the fit of the model to the measured diffusion profiles for this run is not optimal which might be caused by the used minimization routine or negligence of the effect of iron on the diffusivity of the elements. The other almandine – majoritic garnet run shows a similar diffusion profile.

5.5 Discussion

Although the diffusion experiments were conducted at relatively high temperatures, the diffusion profiles were still too short to be measured by electron microprobe, indicating that diffusion of the majorite component is much slower than the interdiffusion of the divalent cations in garnet (Mg, Ca, Fe and Mn, which diffuse fast enough such that they can be measured after experiments on a microprobe at these conditions). This is also confirmed by the pyrope – almandine diffusion couple (H3086), which produced profiles that are considerably longer and of which the fitted diffusion coefficients for the dodecahedrally coordinated cations are 2 – 3 orders of magnitude faster for Mg and Fe, and 1 – 2 orders of magnitude faster for Ca, as compared to the diffusivity of the majorite component in garnet. The actual values at 1600 °C and 15 GPa, D_{Mj} = 1.4 x 10^{-15} cm^2 s^{-1}, are

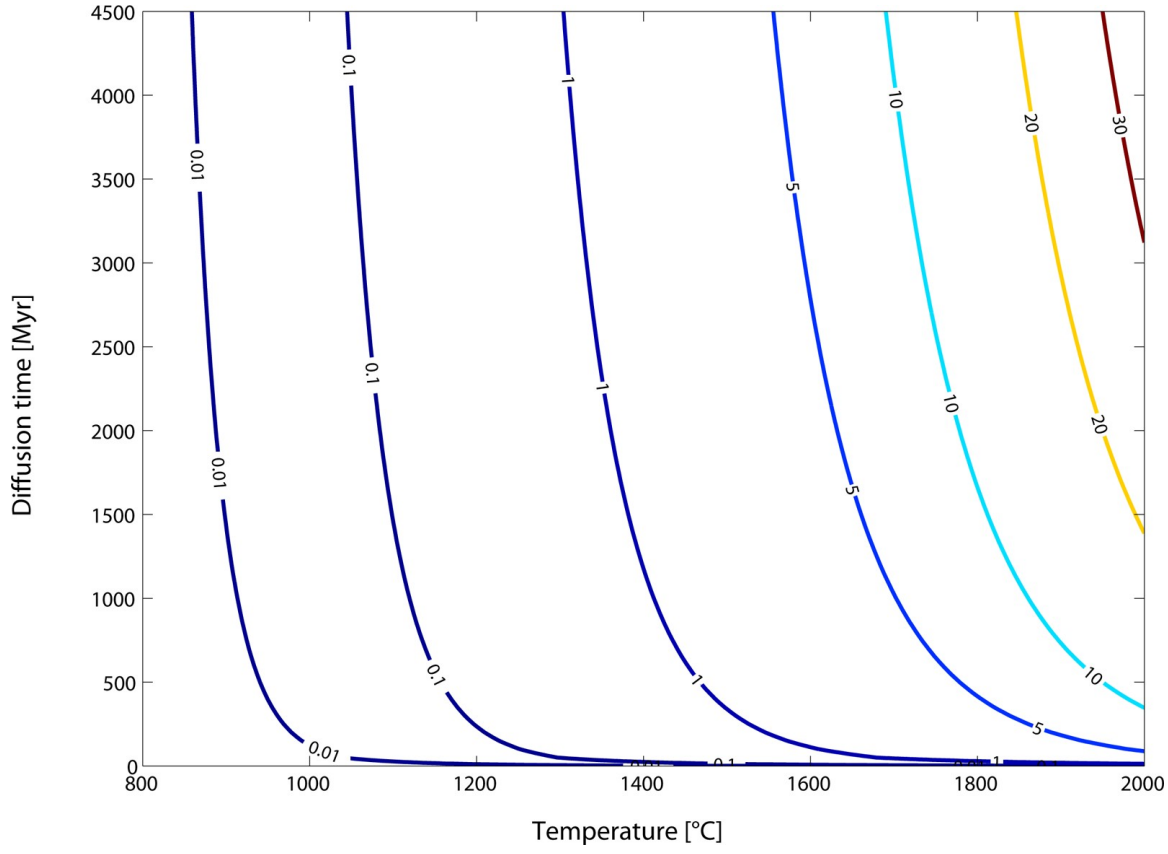

Figure 5.13: The diffusion distance of the majorite component as function temperature and time. The numbers on the lines are in meters. See text for more explanation.

comparable to the (tracer) diffusivity of Si in wadsleyite at 1600 °C and 16 GPa, which was also determined to be 1.4 x 10^{-15} cm^2 s^{-1} (Shimojuku et al. 2009). This again stresses that diffusion of the majorite component in garnet is slow.

5.5.1 Homogenization of the upper mantle

Because of its higher alumina content, the oceanic crust will consist of 80 – 90 vol. % garnet in the transition zone (Irifune et al. 1986). Therefore, when the oceanic crust is subducted, it will form a majorite inhomogeneity in the Earth's mantle. For the understanding of the differentiation of the mantle, it is important to know whether the oceanic crust will persist as an inhomogeneity in the mantle or not over geological time scales. The diffusion distance of the majorite component has been calculated as function of temperature and time at 18 GPa using the diffusion data presented in this chapter. When diffusion occurs over a length scale that is significantly longer then the grain size, grain boundary diffusion is the dominant diffusion mechanism at conditions where grain boundary diffusion is significantly faster (Harrison 1961). The grain boundary coefficient has been taken as 10^4 x the bulk diffusion coefficient, based on grain boundary diffusion experiments on YAG-garnet crystals at 1500 °C (Marquardt (née Hartmann) et al. 2011). The diffusion distance was calculated as:

$$x = \sqrt{D_{gb} t} \tag{5.10}$$

where D_{gb} is the grain boundary coefficient and t diffusion time. The results are plotted in figure 5.13. Estimates for the temperature on the mantle adiabat at 18 GPa range from 1500 °C to 1800 °C (chapter 3). The figure shows that at these conditions, the majorite component will only be able to diffuse over a distance of 5 – 15 meters on the time scale of the age of the Earth. It is clearly not possible to homogenize the mantle by solid state diffusion and the oceanic crust will persist as a majorite homogeneity in the Earth's mantle.

5.5.2 Rheology of garnet in the transition zone

In deformation processes controlled by dislocation creep (through dislocation climb) and diffusion creep mechanisms, the volume diffusivity of the slowest diffusing ion is an important rate controlling factor (Weertman 1957, Poirier 1985). As will be explained below, there are arguments to assume that octahedral and tetrahedral Si do not diffuse as independent components, but diffuse as one component, which might be even faster than the diffusion of Al in garnet. It can thus be assumed that the diffusivity of the majorite component is representative of the diffusivity of the slowest component. The creep rates for dislocation creep (by the Weertman model) and diffusion creep are given by respectively:

$$\dot{\epsilon} = \alpha_{disl} \frac{D_{sd}}{b^{3.5} M^{0.5}} \left(\frac{\sigma}{\mu} \right)^{4.5} \frac{\mu \Omega}{kT}$$

and (5.11)

$$\dot{\epsilon} = \alpha_{diff} \frac{D_{sd} \sigma \Omega}{d^2 k T}$$

where α is a geometric factor, D_{sd} the self-diffusivity of the rate controlling ion, b the burgers vector of the dislocation, M the density of dislocation sources, σ the applied stress, μ the shear modulus, k Boltzmann's

constant, T temperature, d grain size, Ω volume of the vacancy. Using a shear modulus at 16 GPa and 1600 °C of 85 GPa for majoritic garnet and 104 GPa for wadsleyite (Nishihara et al. 2008, Hunt et al. 2010), and the <1 1 1> or <1 0 0> Burgers vectors for the activated slip systems in (majoritic) garnet (Cordier et al. 1996) and <1 1 1> or [1 0 0] for wadsleyite (Demouchy et al. no date), and assuming similar dislocation source densities, grain size and volume of vacancies for garnet and wadsleyite one finds that if the diffusivity of tetrahedrally coordinated Si in garnet is less than in wadsleyite, majoritic garnet will be more resistant to flow than wadsleyite (i.e. 'stronger'). The relative deformation rates are then given by the following equation:

$$\frac{\dot{\epsilon}_{gt}}{\dot{\epsilon}_{wads}} \approx 0.2 \frac{D_{sd}^{gt}}{D_{sd}^{wads}} \tag{5.12}$$

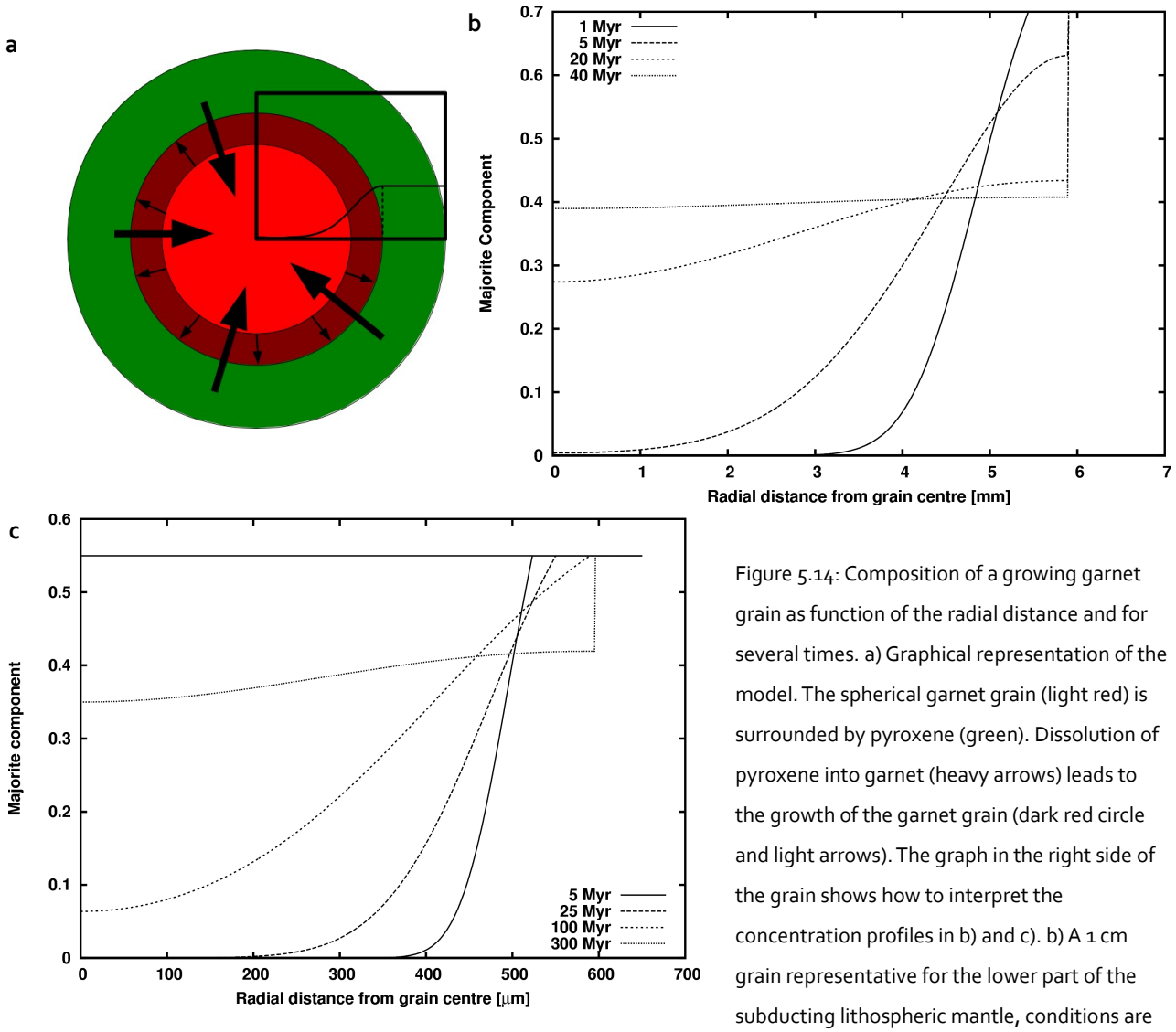

Figure 5.14: Composition of a growing garnet grain as function of the radial distance and for several times. a) Graphical representation of the model. The spherical garnet grain (light red) is surrounded by pyroxene (green). Dissolution of pyroxene into garnet (heavy arrows) leads to the growth of the garnet grain (dark red circle and light arrows). The graph in the right side of the grain shows how to interpret the concentration profiles in b) and c). b) A 1 cm grain representative for the lower part of the subducting lithospheric mantle, conditions are 18 GPa and 1400 °C, and c) is representative for the subducted oceanic crust, conditions are 18 GPa and 1000 °C. Grain growth is stopped after an amount of majorite component corresponding to a homegonous composition of $Py_{60}Mj_{40}$ has fluxed into the grain. After this the grain is let to homogenize. The grain size can be determined by finding the position where the profiles cut the upper 70% majorite line (b) or the 55% majorite (c) line.

for dislocation creep, and

$$\frac{\dot{\epsilon}_{gt}}{\dot{\epsilon}_{wads}} \approx \frac{D_{sd}^{gt}}{D_{sd}^{wads}}$$

for diffusion creep.

If the diffusivity of the majorite component in garnet is of the same order as that of the diffusivity of Si in wadsleyite, there will be no great contrast between majoritic garnet and wadsleyite. However, if due to the low diffusivity of the majorite component the garnet phase did not equilibrate, one might expect a lower diffusivity for Si, since it will be confined to the tetrahedral site. The strength of garnet in subduction zones, the location where most likely there will be lack of equilibration due to lower temperatures and its dynamic character, in this case will be controlled by the degree of equilibration and thus the diffusivity and grain size of garnet. To model this, a program has been developed that simultaneously models diffusion in a (spherical) grain, and diffusion controlled growth of the same grain. A more detailed explanation of the code is given in chapter 4.2.

Figure 5.14 shows how long it will take for enstatite to dissolve into a garnet grain and then homogenize the grain for two different scenarios. Scenario A (figure 5.14b) correspond to a grain in the middle to lower part of the subducting lithospheric mantle. Conditions here are assumed to be 1400 °C and 18 GPa, which correspond to conditions on an average subduction geotherm (Emmerson and McKenzie 2007). The composition of the newly grown majoritic garnet ($Py_{30}Mj_{70}$) was inferred from phase diagrams by Gasparik (2003) and Akaogi and Akimoto (1977). The maximum influx of majorite component was chosen such that the final composition after homogenization was $Py_{60}Mj_{40}$, corresponding to high-pressure experiments on pyrolitic compositions (Irifune 1987). The initial grain size is 1 cm. The results of the modelling show that it takes about 4 Myr for the grain to grow to its final size. However, after this it still has a large core of almost pure pyrope composition. It takes about 20 Myr before the grain is homogenized. Assuming an average rate of burial due to subduction of 20 mm y^{-1}, it would take 12.5 Myr to pass the transition zone. For the subducted lithospheric mantle homogenization is thus roughly at the same timescale as the subduction process.

Things, however, are different for the subducted oceanic crust (scenario B, figure 5.14c). Conditions in this case are 1000 °C and 18 GPa, again from the computed subduction geotherm of Emmerson and McKenzie (2007). The composition of the newly grown majoritic garnet was $Py_{45}Mj_{55}$, from Akaogi and Akimoto (1977) and the maximum influx was again chosen such that the final composition would be $Py_{60}Mj_{40}$, corresponding to experiments conducted on refractory MORB material after partial melting and transformation to an eclogite assemblage, representative of the subducted oceanic crust (Irifune et al. 1986). The initial grain size was taken as 1 mm, which is also a typical grain size for eclogites. The plot in figure 5.14b shows that it takes over 300 Myrs for complete equilibration. After 12.5 Myr only about 38% of the pyroxene would have dissolved into garnet. It might thus be more likely that the basaltic crust will preserve a metastable assemblage of garnet + clinopyroxene + orthopyroxene during its subduction instead of the garnetite assemblage or, since enstatite breaks down to stishovite + wadsleyite or ringwoodite above 17 GPa at these conditions (Akaogi and Akimoto 1977), garnet + clinopyroxene + wadsleyite/ringwoodite + stishovite. The sluggish reaction kinetics of enstatite

breakdown may then also result in the formation akimotoite at greater depths (Hogrefe et al. 1994).

The middle to lower part of the subducting slab is thus expected to be able to dissolve all its enstatite into garnet during the time that, though with a significant delay. This would mean that there would be no significant contrast in strength between garnet and wadsleyite in the transition zone, except perhaps for the upper ~80 km of the transition zone. Diffusion of the majorite component in garnet is too slow to dissolve al the pyroxene into garnet in the oceanic crust during subduction. It might therefore be expected that a significant amount of pyroxene we be preserved as metastable phase. This would make garnet relatively strong, however since pyroxenes are relatively weak (Ohuchi et al. 2010), the preservation of pyroxene may make the oceanic crust weaker than expected in the transition zone.

Extrapolation of the diffusion data in this study to the higher pressures prevailing in the ringwoodite stability field shows that the diffusivity of the majorite component at these conditions is again similar to the diffusivity of silicon self-diffusion in ringwoodite, i.e. 3.5×10^{-17} cm^2 s^{-1} for majoritic garnet vs. 8.5×10^{-17} cm^2 s^{-1} at 22 GPa and 1500 °C (Shimojuku et al. 2009). The conclusions in the previous paragraph thus also hold for ringwoodite stability field.

5.5.3 Comparison with previous experimental data

Chakraborty and Ganguly (1992) determined the value of the activation volume for diffusion of Mg in garnet to be 5.3 ± 3.0 cm^3 mol^{-1}. Chakraborty and Rubie (1996) extended their data with their own to include Mg tracer diffusivity data done over a broader range of pressures to reduce the error in activation volume determined by Chakraborty and Ganguly (1992). They determined from the combined data set an activation volume for Mg tracer diffusion in garnet of 8 ± 1 cm^3 mol^{-1}. The pressure dependence of the majorite component, 3.3 ± 0.1 cm^3 mol^{-1}, determined in this study is thus significantly lower. Chakraborty and Ganguly (1992) also determined the activation enthalpy of Mg diffusion in garnet to be 285 ± 38 kJ mol^{-1} from a multi-component diffusion study, Chakraborty and Rubie (1996), in their tracer diffusion study, determined a lower value of the activation enthalpy for Mg diffusion of 226 ± 21 kJ mol^{-1}. Comparing these to the values determined in this study show that they are very similar, i.e. 241 ± 54 kJ mol for the diffusion of the majorite component in garnet. The fact that diffusion of the majorite component involves diffusion of both dodecahedrally and octahedrally coordinated cations does not seem to influence the activation energy profoundly. The difference in activation volumes between diffusion of the majorite component and diffusion of the eight-fold coordinated Mg, as determined by Chakraborty and Rubie (1996), suggest a different diffusion mechanism involving a less compressible site. Hazen and Finger (1978) indeed report that the octahedral site of garnet is less compressible than the dodecahedral site, which might explain the difference in activation volumes.

5.5.4 Effect of majorite content on diffusivity of the elements

Though the diffusion profiles obtained from the almandine – majoritic garnet diffusion couples were too complex to model well enough to determine absolute diffusion coefficients from, it is still possible to reach some qualitative conclusions. One of the prominent features of all diffusion profiles in the almandine – majoritic

garnet series is the shoulders of Mg, Fe and Ca profiles that extend into the majoritic garnet part of the diffusion couples. These kind of shoulders can only be modelled if it is assumed that the tracer diffusivity of Mg, Fe and Ca was a strong increasing function of majorite content, resulting in the diffusivity of Mg, Fe and Ca being at least one order faster in the majoritic garnet than in almandine. Since the majoritic garnet part of the couple is not a single crystal, but an aggregate of majoritic garnet grain, it might be expected that grain boundary diffusion may also play an important role in the apparently enhanced diffusivity of Mg, Fe and Ca in the majoritic garnet part. Hart (1957) showed that in the case that the length scale over which diffusion occurred is significantly longer than the grain size diffusion can be described by using an effective diffusion coefficient:

$$D_{eff} = fD_{gb} + (1-f)\,D_l \tag{5.13}$$

where f is the volume fraction of grain boundaries or dislocations, D_{gb} the diffusion coefficient for the grain boundary and D_l the diffusion coefficient for lattice diffusion. Harrison (1961) classified diffusion in aggregates in three different types, type A where diffusion can be described by Hart effective diffusivity and where the diffusion length scale is thus significantly longer than the grain size, type C where the diffusion length scale is significantly shorter than the grain size and diffusion can thus be well described by the lattice diffusion coefficient (the pyrope – majoritic garnet and pyrope - almandine experiments fall in this category) inside of the grains and the grain boundary diffusion coefficient outside of the grains. Lastly he described an intermediate type B where the diffusion length scale is of the order of the grain size. This last type of diffusion cannot be described by a simple diffusion equation and has to be treated specially, see for example the treatment of Fisher (1951). That the diffusion experiments were conducted in a type A regime seems to be unlikely, considering the length of the diffusion profile in experiment H3119 (about 5 - 6 μm) as compared to the distance from the interface to the first long dislocation (ca. 3 μm). The same can be concluded from experiment H3244, where the size of the majoritic garnet grain directly after the diffusion interface is 4.5 μm and the length of the shoulder extending into the majoritic garnet size is 7 – 8 μm. The high dislocation density region directly adjacent to the interface also does not seem to affect the diffusivity of Mg and Fe significantly, otherwise one would expect a break in the slope of the Mg and Fe shoulder extending into the majoritic garnet directly beyond the high dislocation density region. If one would be in the type B diffusion regime, one would expect increased Fe and decreased Mg contents near the grain boundaries in the majoritic garnet side of the diffusion couple. This is not observed either, and therefore it is concluded that the increased diffusivity of Fe, Mg and Ca in majoritic garnet is an intrinsic property of majoritic garnet itself.

Also the fact that casting the composition of the garnet analyses in terms of end-member compositions produces diffusion profiles with a spike in pyrope component near the point where the majorite component goes to zero may be important. If it would be due to presence of a miscibility gap one would expect the precipitation of a second garnet phase enriched in Fe-majorite component, which is not observed in the diffusion couples. This is also very unlikely considering that the Fe-majorite end-member is not stable and it thus is improbable that a phase with a lower Fe-majorite component would exsolve into a phase with a strong pyrope component and a second phase with a strong Fe-majorite component. Moreover, there is also no

experimental evidence for such a miscibility gap. Considering all the cations as single components independent of the garnet end-member component produces reasonable fits to the experimental data however. It may thus be simply inappropriate to look at the diffusion in the almandine – majoritic garnet system as the diffusion of garnet end-members, but it should be interpreted as the diffusion of cations in the garnet lattice independent of their actual coordination. This might also shed some light on the actual diffusion mechanism, since if Mg of both the majorite component and the pyrope component diffuse equally fast it is unlikely that they are restricted to a single coordination and thus more likely hop from a dodecahedral site to an octahedral site during the diffusion through the garnet lattice, which would also make Mg of the Mg-majorite component and pyrope component indistinguishable from each other. The garnet structure can be viewed as tubular columns of interlayered rings of silica tetrahedra with dodecahedral sites (figure 6.9). The octahedral sites form direct connections through the silica rings between the layers of dodecahedral sites in this structure, and therefore create short cuts through the garnet structure. If (part of) the octahedral sites can be occupied by Mg and Fe, like in the majoritic garnet, Mg and Fe can diffuse through garnet by using these short cuts and an increased diffusivity of those elements is expected. One might expect that a similar increase in diffusivity of Si will be observed in majoritic garnet, i.e. because Si can cross the silica rings through the octahedral sites instead of diffusing along the rings, however this is not observed in the pyrope – majoritic garnet profiles. However, diffusion might be limited here by the diffusivity of Al and an increase in majorite component may still lead to the increase in silicon diffusivity. If this would be the case, one would expect a weakening of the garnet (equations 5.12) phase as more pyroxene gets dissolved in it during subduction. Hunt et al. (2010) indeed observed that majoritic garnet weakens with increasing majorite content and this may thus be explained by the increased diffusivity of Si in majoritic garnet where the diffusion paths can involve both the octahedral sites and the tetrahedral sites.

5.6 Conclusions

The experiments with pyrope – majoritic garnet, pyrope – almandine and almandine – majoritic garnet couples conducted in this study showed that:

1. Diffusion of the majorite component is a slow process, comparable with the rate silicon diffusion in wadsleyite and ringwoodite at similar pressure and temperature conditions.
2. Although majorite diffusivity in garnet is low, the determined activation energy has only a value of 241 ± 54 Kj mol^{-1}, which is similar to the Mg tracer diffusion activation energy determined in previous studies (Chakraborty and Ganguly 1992, Chakraborty and Rubie 1996). The determined activation volume of diffusion of 3.3 ± 0.1 cm^3 mol^{-1} however, is significantly lower than that determined for Mg tracer diffusivity (8 ± 1 cm^3 mol^{-1}) in garnet determined in those studies, indicating that less compressible sites are involved in the diffusion mechanism of majorite diffusion in garnet.
3. The diffusivity of the majorite component is 2 – 3 orders of magnitude slower than the tracer diffusivity

of Mg and Fe at the same conditions, and 1 – 2 orders of magnitude slower than Ca tracer diffusion in garnet at the same conditions.

4. Solid state diffusion cannot homogenize the mantle, and subducted oceanic crust will persist to exist as (at least) a majorite homogeneity in the Earth's mantle.

5. Due to the slow diffusivity of the majorite component in garnet, it is unlikely that subducted oceanic crust will be equilibrated during subduction in the mantle transition zone, and is more likely to happen only after the slab has become stagnant at the bottom of the transition zone. Diffusion in the (lower) lithospheric part of the subducted slab is probably fast enough such it can be equilibrated on a time scale of a couple of million years.

6. The diffusivity of Mg and Fe is significantly faster in majoritic garnet (Py55Mj45) than in pyrope at the same conditions in our experiments, which is an intrinsic property of majoritic garnet. From the shape of the almandine – majoritic garnet diffusion profiles in combination with the increased diffusivity of Mg and Fe in majoritic garnet it is most likely that the diffusion pathway in Mg and Fe involve both the dodecahedral and the octahedral sites in garnet. It is possible that a similar change in diffusion mechanism would also occur for silicon in majoritic garnet, which could explain the observed weakening of majorite with Al content.

7. Judging from the relative diffusivity of silicon diffusivity in wadsleyite and ringwoodite and the diffusivity of the majorite component in garnet, it is not expected that there will be a major contrast in strength between wadsleyite and garnet or ringwoodite and garnet in the mantle transition zone.

5.7 References

Akaogi, M., Akimoto, S. (1977), Pyroxene-garnet solid-solution equilibria in the systems $Mg_4Si_4O_{12}$ – $Mg_3Al_2Si_3O_{12}$ and $Fe_4Si_4O_{12}$ – $Fe_3Al_2Si_3O_{12}$ at high pressures and temperatures. Phys Earth Planet Inter 15:90-106. doi: 10.1016/0031-9201(77)90013-9

Aken, P.A. van, Liebscher, B. (2002), Quantification of ferrous/ferric ratios in minerals: new evaluation schemes of FeL_{23} electron energy-loss near-edge spectra. Phys Chem Miner 29:188-200. doi: 10.1007/s00269-001-0222-6

Bass, J.D., Parise, J.B. (2008), Deep Earth and Recent Developments in Mineral Physics. Elements 4:157-165

Bell, D.R., Ihinger, P.D., Rossman, G.R. (1995), Quantitative analysis of trace OH in garnet and pyroxenes. Am Mineral 80:465-474

Cappellen, E. Van, Doukhan, J.C. (1994), Quantitative transmission X-ray microanalysis of ionic compounds. Ultramicroscopy 53:343-349. doi: 10.1016/0304-3991(94)90047-7

Chakraborty, S. (2008), Diffusion in Solid Silicates: A Tool to Track Timescales of Processes Comes of Age. Annual Rev Earth Planet Sci 36:153-190. doi: 10.1146/annurev.earth.36.031207.124125

Chakraborty, S., Ganguly, J. (1992), Cation diffusion in aluminosilicate garnets: experimental determination in spessartine-almandine diffusion couples, evaluation of effective binary diffusion coefficients, and applications. Contrib Mineral Petrol 111:74-86. doi: 10.1007/BF00296579

Chakraborty, S., Rubie, D.C. (1996), Mg tracer diffusion in aluminosilicate garnets at 750-850° C, 1 atm. and 1300° C, 8.5 GPa. Contrib Mineral Petrol 122:406-414. doi: 10.1007/s004100050136

Cordier, P., Raterron, P., Wang, Y. (1996), TEM investigation of dislocation microstructure of experimentally

deformed silicate garnet. Phys Earth Planet Inter 97:121-131. doi: 10.1016/0031-9201(96)03154-8

Demouchy, S., Mainprice, D., Tommasi, A., Couvy, H., Barou, F., Frost, D.J., Cordier, P. (no date), Forsterite to Wadsleyite Phase Transformation Under Shear Stress and Consequences for the Earth's Mantle Transition Zone. Phys Earth Planet Inter In Press, Accepted Manuscript: doi: doi: DOI: 10.1016/j.pepi.2010.11.001

Egerton, R.F. (1996), Electron energy-loss spectroscopy in the electron microscope. Plenum Press, New York

Egerton, R.F., Li, P., Malac, M. (2004), Radiation damage in the TEM and SEM. Micron 35:399-409. doi: 10.1016/j.micron.2004.02.003

Elphick, S.C., Ganguly, J., Loomis, T.P. (1985), Experimental determination of cation diffusivities in aluminosilicate garnets. Contrib Mineral Petrol 90:36-44. doi: 10.1007/BF00373039

Emmerson, B., McKenzie, D. (2007), Thermal structure and seismicity of subducting lithosphere. Phys Earth Planet Inter 163:191-208. doi: 10.1016/j.pepi.2007.05.007

Fisher, J.C. (1951), Calculation of Diffusion Penetration Curves for Surface and Grain Boundary Diffusion. J Appl Phys 22:74. doi: 10.1063/1.1699825

Frost, D.J. (2008), The Upper Mantle and Transition Zone. Elements 4:171-176

Gasparik, T. (2003), Phase diagrams for geoscientists: an atlas of the earth's interior. Springer, Heidelberg-Berlin

Harrison, L.G. (1961), Influence of dislocations on diffusion kinetics in solids with particular reference to the alkali halides. Trans Faraday Soc 57:1191. doi: 10.1039/tf9615701191

Hart, E.W. (1957), On the role of dislocations in bulk diffusion. Acta Metall 5:597. doi: 10.1016/0001-6160(57)90127-X

Hazen, R.M., Finger, L.W. (1978), Crystal structures and compressibilities of pyrope and grossular to 60 kbar. Am Mineral 63:297-303

Heinemann, S., Sharp, T.G., Seifert, F., Rubie, D.C. (1997), The cubic-tetragonal phase transition in the system majorite ($Mg_4Si_4O_{12}$) – pyrope ($Mg_3Al_2Si_3O_{12}$), and garnet symmetry in the Earth's transition zone. Phys Chem Miner 24:206-221. doi: 10.1007/s002690050034

Hogrefe, A., Rubie, D.C., Sharp, T.G., Seifert, F. (1994), Metastability of enstatite in deep subducting lithosphere. Nature 372:351-353. doi: 10.1038/372351a0

Hunt, S.A., Dobson, D.P., Li, L., Weidner, D.J., Brodholt, J.P. (2010), Relative strength of the pyrope-majorite solid solution and the flow-law of majorite containing garnets. Phys Earth Planet Inter 179:87-95. doi: 10.1016/j.pepi.2009.12.001

Irifune, T. (1987), An experimental investigation of the pyroxene-garnet transformation in a pyrolite composition and its bearing on the constitution of the mantle. Phys Earth Planet Inter 45:324-336. doi: 10.1016/0031-9201(87)90040-9

Irifune, T., Ringwood, A.E. (1993), Phase transformations in subducted oceanic crust and buoyancy relationships at depths of 600-800 km in the mantle. Earth Planet Sci Lett 117:101-110. doi: 10.1016/0012-821X(93)90120-X

Irifune, T., Sekine, T., Ringwood, A.E., Hibberson, W.O. (1986), The eclogite-garnetite transformation at high pressure and some geophysical implications. Earth Planet Sci Lett 77:245-256. doi: 10.1016/0012-821X(86)90165-2

Kawai, N., Togaya, M., Onodera, A. (1973), A New Device for Pressure Vessels. Proc Japan Acad 49:623-626

Keppler, H., Frost, D.J. (2005), Introduction to minerals under extreme conditions. in: Miletich R.(ed.) Mineral Behaviour at Extreme Conditions, EMU Notes in Mineralogy 7, pp. 1-30

Lasaga, A.C. (1979), Multicomponent exchange and diffusion in silicates. Geochem Cosmochem Acta 43:455-469. doi: 10.1016/0016-7037(79)90158-3

Lasaga, A.C., Jiang, J. (1995), Thermal history of rocks; P-T-t paths for geospeedometry, petrologic data, and inverse theory techniques. Am J Sci 295:697-741. doi: 10.2475/ajs.295.6.697

Loomis, T.P., Ganguly, J., Elphick, S.C. (1985), Experimental determination of cation diffusivities in

aluminosilicate garnets. Contrib Mineral Petrol 90:45-51. doi: 10.1007/BF00373040

Lu, R., Keppler, H. (1997), Water solubility in pyrope to 100 kbar. Contrib Mineral Petrol 129:35-42. doi: 10.1007/s004100050321

Marquardt (née Hartmann), K., Petrishcheva, E., Gardés, E., Wirth, R., Abart, R., Heinrich, W. (2011), Grain boundary and volume diffusion experiments in yttrium aluminium garnet bicrystals at 1,723 K: a miniaturized study. Contrib Mineral Petrol . doi: 10.1007/s00410-011-0622-7

Nishihara, Y., Tinker, D., Kawazoe, T., Xu, Y., Jing, Z., Matsukage, K.N., Karato, S. (2008), Plastic deformation of wadsleyite and olivine at high-pressure and high-temperature using a rotational Drickamer apparatus (RDA). Phys Earth Planet Inter 170:156-169. doi: 10.1016/j.pepi.2008.03.003

Novak, G.A., Gibbs, G.V. (1971), The crystal chemistry of the silicate garnets. Am Mineral 56:791-825

Ohtani, E., Kagawa, N., Fujino, K. (1991), Stability of majorite (Mg, Fe)SiO_3 at high pressures and 1800°C. Earth Planet Sci Lett 102:158-166. doi: 10.1016/0012-821X(91)90005-3

Ohuchi, T., Karato, S., Fujino, K. (2010), Strength of single-crystal orthopyroxene under lithospheric conditions. Contrib Mineral Petrol 161:961-975. doi: 10.1007/s00410-010-0574-3

O'Neill, H.S.C., McCammon, C.A., Canil, D., Rubie, D.C., Ross, C.R., Seifert, F. (1993), Mössbauer spectroscopy of mantle transition zone phases and determination of minimum Fe^{3+} content. Am Mineral 78:456-461

Poirier, J.-P. (1985), Creep of Crystals: High-Temperature Deformation Processes in Metals, Ceramics and Minerals. Cambridge University Press, Cambridge

Press, W.H., Flannery, B.P., Teukolsky, S.A., Vetterling, W.T. (1992), Numerical Recipes in C: The Art of Scientific Computing. Cambridge University Press

Ringwood, A.E., Major, A. (1971), Synthesis of majorite and other high pressure garnets and perovskites. Earth Planet Sci Lett 12:411-418. doi: 10.1016/0012-821X(71)90026-4

Roermund, H. van (2009), Mantle-wedge garnet peridotites from the northernmost ultra-high pressure domain of the Western Gneiss Region, SW Norway. Eur J Mineral 21:1085-1096. doi: 10.1127/0935-1221/2009/0021-1976

Scambelluri, M., Pettke, T., Roermund, H.L.M. van (2008), Majoritic garnets monitor deep subduction fluid flow and mantle dynamics. Geology 36:59-62. doi: 10.1130/G24056A.1

Schertl, H.-P., Schreyer, W., Chopin, C. (1991), The pyrope-coesite rocks and their country rocks at Parigi, Dora Maira Massif, Western Alps: detailed petrography, mineral chemistry and PT-path. Contrib Mineral Petrol 108:1-21. doi: 10.1007/BF00307322

Shimojuku, A., Kubo, T., Ohtani, E., Nakamura, T., Okazaki, R., Dohmen, R., Chakraborty, S. (2009), Si and O diffusion in $(Mg,Fe)_2SiO_4$ wadsleyite and ringwoodite and its implications for the rheology of the mantle transition zone. Earth Planet Sci Lett 284:103-112. doi: 10.1016/j.epsl.2009.04.014

Song, S., zhang, L., Niu, Y. (2004), Ultra-deep origin of garnet peridotite from the North Qaidam ultrahigh-pressure belt, Northern Tibetan Plateau, NW China. Am Mineral 89:1330-1336

Weertman, J. (1957), Steady-State Creep through Dislocation Climb. J Appl Phys 28:362. doi: 10.1063/1.1722747

Williams, D.B., Carter, C.B. (2009), Transmission electron microscopy: a textbook for materials science. Springer, Heidelberg

Appendix 5.1: Radiation damage correction

The transmission electron microscope exposes a high dose of high energy electron to the specimen, which increases as one increases the magnification. This high dose of high energy electrons can exert a damage to the specimen called beam or radiation damage. The physical causes of beam damage include heating of the specimen, electrolyses of bonds and knocking atoms out of their sites, knock-on damage, due to momentum transfer during electron – atom collision (Egerton et al. 2004, Williams and Carter 2009). Radiation damage affects EDS analyses because some elements are preferentially lost, for example magnesium in silicates, which occur often in significant in high pressure phases. Even though cooling of the sample in a liquid N_2 holder was done, and using a lower electron dose was used to measure the chemical composition does decrease radiation damage, it was not possible to perform damage free EDS analyses on majoritic garnet with a small scanning pattern (40 nm) in STEM mode. Therefore, a correction procedure was developed to correct for preferential element loss from majoritic garnet, though it should work as well for other minerals, which is explained below.

Majoritic garnet can contain Mg in two different coordinations, six fold coordination and eight fold coordination. Normal garnet only contains Mg in eight fold coordination, and Mg loss during EDS analyses is very minor when compared to majoritic garnet. Therefore it is assumed that Mg is stable in eight fold coordination, i.e. count rates for eight fold coordinated Mg remain constant with time, whereas count rates of 6 fold coordinated Mg decreases with time. If the fraction of atoms lost with time is constant, one can describe this with the following differential equation:

$$\frac{dI^u}{dt} = -kI^u \tag{5.14}$$

where I^u is the count rate of the element in the unstable site, t is time and k is a constant. This leads to the following expression for the evolution of count rate of the element with time:

$$I^u = I_0^u e^{-kt} \tag{5.15}$$

and the total count rate of the element with time then becomes:

$$I = I^s + I_0^u e^{-kt} \tag{5.16}$$

where I^s is the count rate of the elements in the stable site. To obtain the number of counts in the measurement interval between $t = t_1$ and $t = t_1 + \Delta t$ one integrates 5.16 between those limits:

$$I = \int_{t_1}^{t_1+\Delta t} I^s + I_0^u e^{-kt}\, dt = I^s \Delta t_1 + \frac{I_0^u}{k} e^{-kt_1}\left(1 - e^{-k\Delta t}\right) \tag{5.17}$$

When dead time is sufficiently low such that it can be neglected, equation 5.17, can be fitted to measurements when several short measurements with counting time Δt are done at the same place. Usually at least 8 measurements per spot are required to obtain a satisfactory fit (figure 5.15). If no radiation damage would occur, the count rate of the unstable site would be constant with time, so the corrected total count rate is given

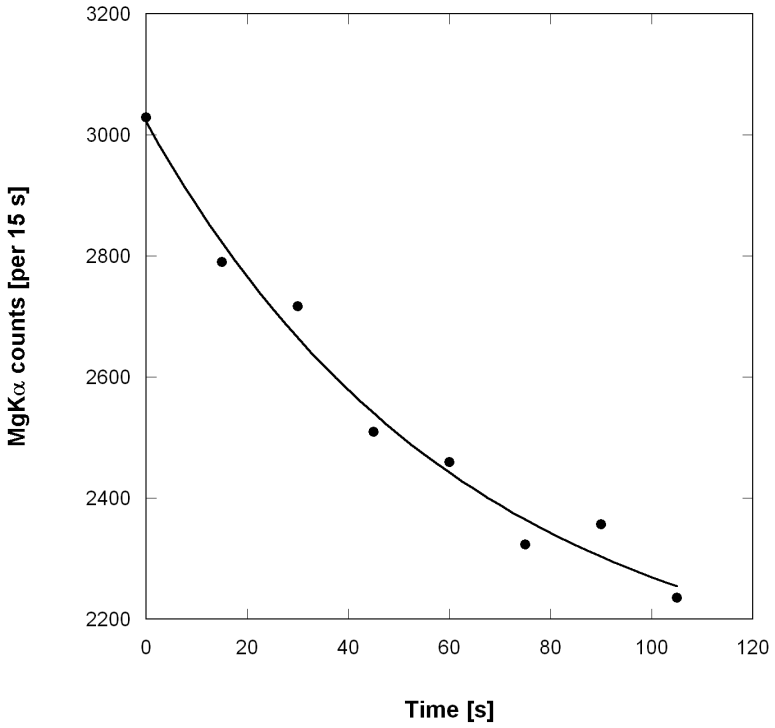

Figure 5.15 :The intensity of the MgKα peak in majoritic garnet as function of the time elapsed since the start of the measurement. Solid dots correspond to the actual measurements, each dot correspond to the cumulative counts over a 15 second interval. The solid line is the fitted intensity using the model proposed here.

by:

$$I_{cor} = I^s + I_0^u \tag{5.18}$$

Fitting of 5.17 to the data has been done by minimizing the χ^2 – value, which is defined as:

$$\chi^2 = \sum_i^n \frac{(O_i - E_i)^2}{O_i} \tag{5.19}$$

Where O_i is the observed intensity of the characteristic x-ray line and E_i is the expected or fitted intensity of the characteristic x-ray line. The minimization is done by using the non-linear Levenberg – Marquandt minimization algorithm available in the Matlab software package.

There are now two scenarios. In the first scenario, the standard case, beam damage is not significant and we can use the standard method, i.e. using the simple arithmetic mean of all measurement, to calculate the intensity of the measured x-ray peak. In the second one, where radiation damage is significant, equation 5.17 should be used to determine the radiation corrected intensity for the measured x-ray peak. To do this, we can use the ratio of the χ^2 – value for both models corrected for the degrees of freedom in both models in an F-test with the following F statistic:

$$F = \frac{\chi_n^2}{\chi_c^2} \cdot \frac{n-3}{n-1} \tag{5.20}$$

Where χ_n^2 is the χ^2 value for the normal case and χ_c^2 is the χ^2 value for the radiation damage corrected case. The expected value for F when using 8 measurements per spot is 1 2/3 when there is no difference between the

models. The radiation damage corrected model is used when the F value exceeds a certain minimum value, which can be obtained from standard tables for the F-distribution (in this thesis 4.88, which corresponds to a 95% confidence level when using 8 measurements per spot).

Appendix 5.2: Quantification of the EDS analyses

The actual elemental concentration can be calculated from the intensities of the characteristic x-ray peaks using Cliff-Lorimer k-factors when absorption can be neglected:

$$\frac{C_A}{C_R} = k_{AR}\frac{I_A}{I_R} \tag{5.21}$$

where A and R denotes element A and the ratio-element R respectively, C are the concentrations, I the characteristic x-ray intensities and k_{AR} is the Cliff-Lorimer k-factor for element A using R as ratio-element. The Cliff-Lorimer k-factors are determined by measuring specimens with a known composition. As additional constraint to calculate the actual concentrations can be used that the concentrations of all elements should add up to 100%. Usually absorption can not be completely neglected and one should correct the k-factors for absorption:

$$k^*_{AR} = k_{AR}\frac{\mu_A^{spec}}{\mu_R^{spec}}\frac{1-\exp(-\mu_R^{spec}\rho\, t\, cosec\,\alpha)}{1-\exp(-\mu_A^{spec}\rho\, t\, cosec\,\alpha)} \tag{5.22}$$

where k^*_{AR} is the corrected k-factor, μ^{spec}_i is the mass absorption coefficient (MAC) for characteristic line i in the specimen, ρt the mass thickness of the foil and α the take-off angle of the x-rays that hit the detector. The MAC is calculated as follows:

$$\mu_i^{spec} = \sum_j C_j \mu_i^j \tag{5.23}$$

where C_j is the concentration of element j and μ_i^j is the MAC for the characteristic line of element I by pure element j.

As can be seen in these equations, one needs to know the thickness of the specimen. Because measuring the exact thickness of the foil is often difficult, Van Cappellen and Doukhan (1994) used net neutral charge as an additional criterion to determine the thickness. For easier calculation, they approximated equation 5.22 with a first order Taylor expansion, which makes the net charge as function of thickness quadratic in nature and easily solvable. In this thesis the Brent root finding algorithm (Press et al. 1992) in combination with the full expression of 5.22 is used to quantify the elemental concentrations. The source code of the program (TemQuant) is available upon request.

Appendix 5.3:Precision of TEM EDS measurements

The diffusion profiles for the majoritic garnet – pyrope diffusion experiments were modelled with a constant composition independent diffusion coefficient. Though binary diffusion profiles can be modelled by a single diffusion coefficient, it should still be composition dependent through equation 5.0, unless the diffusion

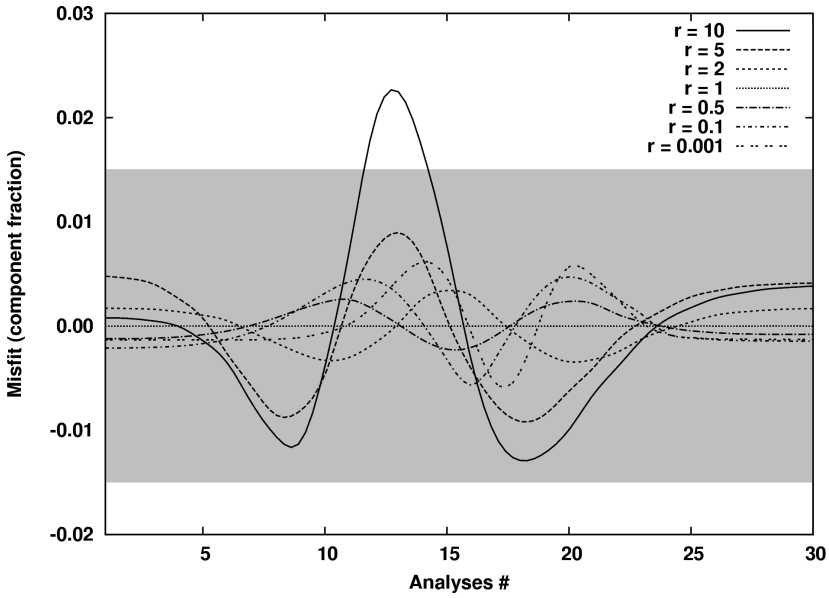

Figure 5.16: A plot of the misfit by fitting a composition independent diffusion model to data generated from a composition dependent model. The r value is the ratio of D_{Py} to D_{Mj} and the gray area denotes the precision of the TEM for Al in majoritic garnet.

coefficients for the majorite component and pyrope component are equal. Chakraborty and Ganguly (1992), for example, modelled their diffusion profiles for diffusion in the almandine – spessartine diffusion couples with two different diffusion coefficient for each side of the couple, pointing out the compositional dependence of the diffusion coefficients. However, the precision of the analyses on the TEM may let it appear as if the binary diffusion coefficient is composition independent, since only slightly asymmetric profiles are not distinguishable from perfectly symmetric profiles.

To determine what the sensitivity is of the profiles measured by the TEM to the composition dependence of the binary diffusion coefficient, several profiles have been modelled with a different composition dependence with the use of the Lasaga model. From the calculated profile a set of 25 points has been taken as 'measurement data' and this data has been fitted by the composition independent diffusion model. The fit or misfit is plotted in figure 5.16. The gray area line gives the typical error for the analytical TEM using EDS, which is 1.5 % under optimal conditions.

Table 5.4 : The obtained values when using the constant diffusion coefficient model when fitting data to the Lasaga multi-component model. On the left side the $D_{Mj} – D_{Py}$ ratio used to model the 'measured' data with the use of the ideal multi-component model by Lasaga, on the right side the diffusion coefficient obtained by fitting the measured data to a constant composition independent diffusion coefficient relative to the D_{Py} value used as input for the Lasaga model.

$D_{Mj} – D_{Py}$ ratio	Fitted coefficient
0.01	0.013
0.1	0.13
0.5	0.56
1	1.0
2	1.63
5	2.67
10	3.32

The best element to check for this would be Al, since for every 1 % of majorite component incorporated, the Al fraction will be reduced by 0.02 per formula unit. Figure 5.16 shows that the ratio r of D_{Py} to D_{Mj} should be below 10, otherwise asymmetry of the diffusion profiles would be too strong to remain undetected by the TEM. However the error in the determined diffusion coefficient would be smaller, as is pointed out in table 4.4, since the determined diffusion coefficient using the composition independent diffusion

coefficient model would lie between the actual values of D_{Py} and D_{mj}.

Appendix 5.4: Majoritic garnet – Dora Maira pyrope diffusion couple profiles

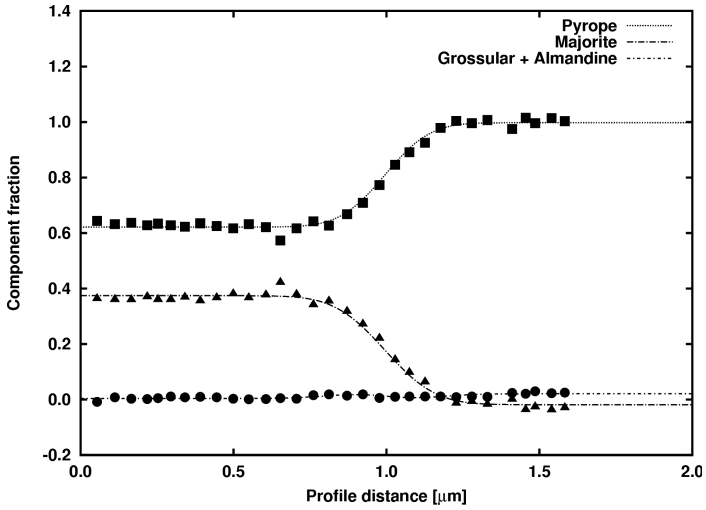

H2986
P = 15 GPa
T = 1600 °C
t = 4h
D_{Py} = 1.4(2) x 10^{-15} cm^2 s^{-1}
D_{Mj} = 1.4(2) x 10^{-15} cm^2 s^{-1}

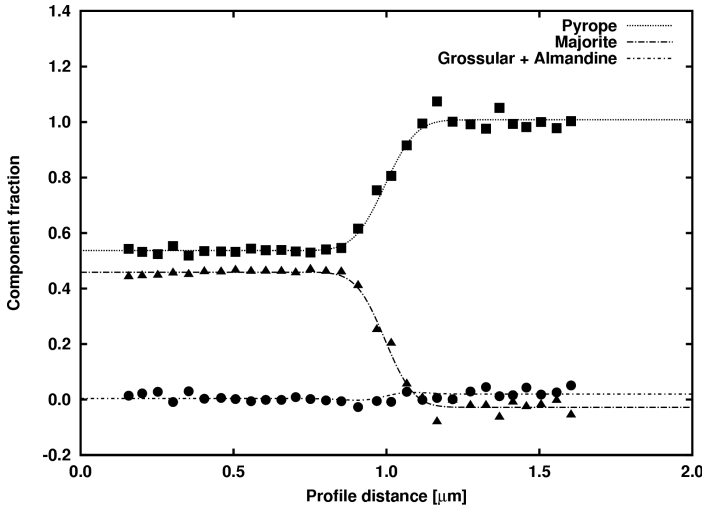

H3076
P = 15 GPa
T = 1500 °C
t = 24 h
D_{Py} = 4(2) x 10^{-16} cm^2 s^{-1}
D_{Mj} = 3(1) x 10^{-16} cm^2 s^{-1}

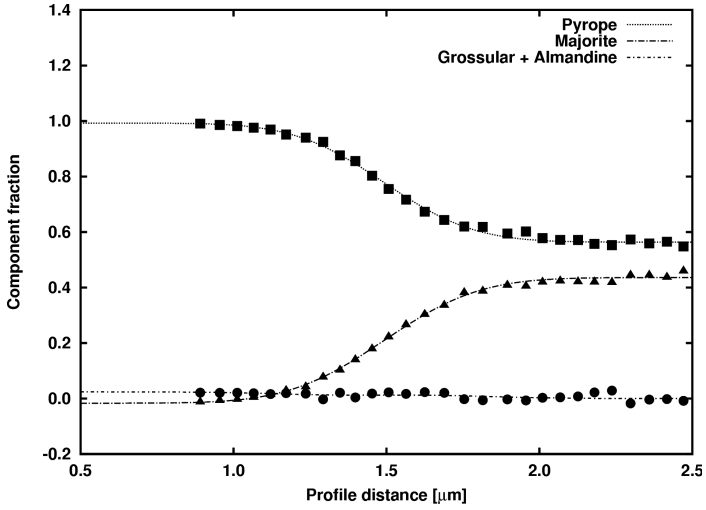

H3106
P = 15 GPa
T = 1900 °C
t = 2h
D_{Py} = 3.7(7) x 10^{-14} cm^2 s^{-1}
D_{Mj} = 4(1) x 10^{-14} cm^2 s^{-1}

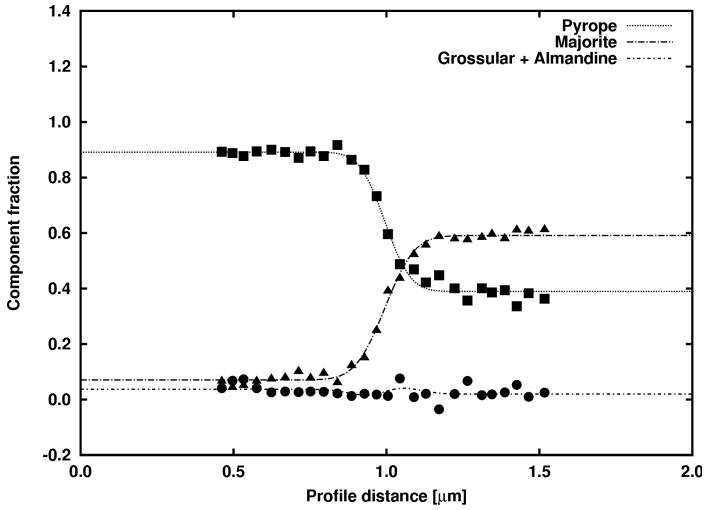

H3257
P = 15 GPa
T = 1400 °C
t = 24 h
D_{Py} = 2.5(8) x 10^{-16} cm^2 s^{-1}
D_{Mj} = 3.4(8) x 10^{-16} cm2 s^{-1}

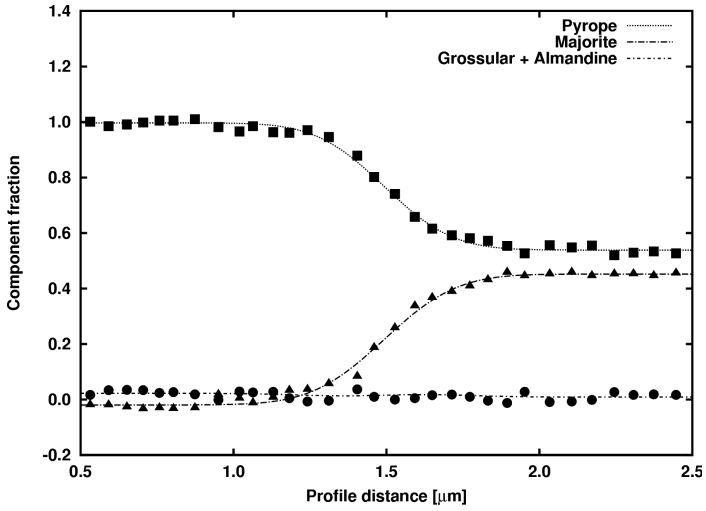

H3084
P = 20 GPa
T = 1800 °C
t = 20 h
D_{Py} = 2.2(7) x 10^{-15} cm^2 s^{-1}
D_{Mj} = 2(1) x 10^{-15} cm^2 s^{-1}

Chapter 6: Exsolution of garnet from orthopyroxene

6.1 Introduction

Orthopyroxene, with spacegroup Pbca and composition ranging from end-members enstatite $Mg_2Si_2O_6$ to ferrosilite $Fe_2Si_2O_6$ can incorporate aluminium by two different substitution mechanisms. The first mechanism is the calcium or magnesium Tschermak substitution mechanism (end-members $CaAl_2SiO_6$ and $MgAl_2SiO_6$). Both Ca/Mg and Si atoms are substituted for two Al atoms in the pyroxene structure. The Al incorporated in the tetrahedral chains strongly prefers the Si(B) site, in accordance with the Al-avoidance principle (Okamura et al. 1974). The aluminium in the octahedral layers has a preference for the M1 site, however the M2 sites accommodate Al too (Okamura et al. 1974, Ganguly and Ghose 1979). In the presence of excess silica, aluminium can also be incorporated (by the second mechanism) by a calcium Eskola component ($Ca_{0.5}AlSi_2O_6$), where discrepancy in charge on the M sites between Al^{3+} and Ca^{2+} is balanced by a vacancy on the M2 site (Gasparik and Lindsley 1980).

The enstatite end-member of the pyroxene series has different polymorphs depending on the pressure and temperature conditions. Figure 6.1 shows the phase diagram of $MgSiO_3$ at upper-mantle pressure. Up to ± 15 GPa the different pyroxene polymorphs are stable, after which it breaks down to either majorite or wadsleyite/ringwoodite + stishovite. The different polymorphs that are stable are orthoenstatite (space group Pbca), protoenstatite (space group Pbcn), low clinoenstatite (space group P21/c), high temperature high clinoenstatite (space group C2/c) and high pressure high clinoenstatite (space group C2/c). Though the last two polymorphs have the same space group, their oxygen packing sequence is different, i.e. the high pressure polymorph has a cubic close packing sequence and the high temperature form has a hexagonal close packing sequence (Thompson and Downs 2003). Though the pure end-member HT clinoenstatite $MgSiO_3$ has only a

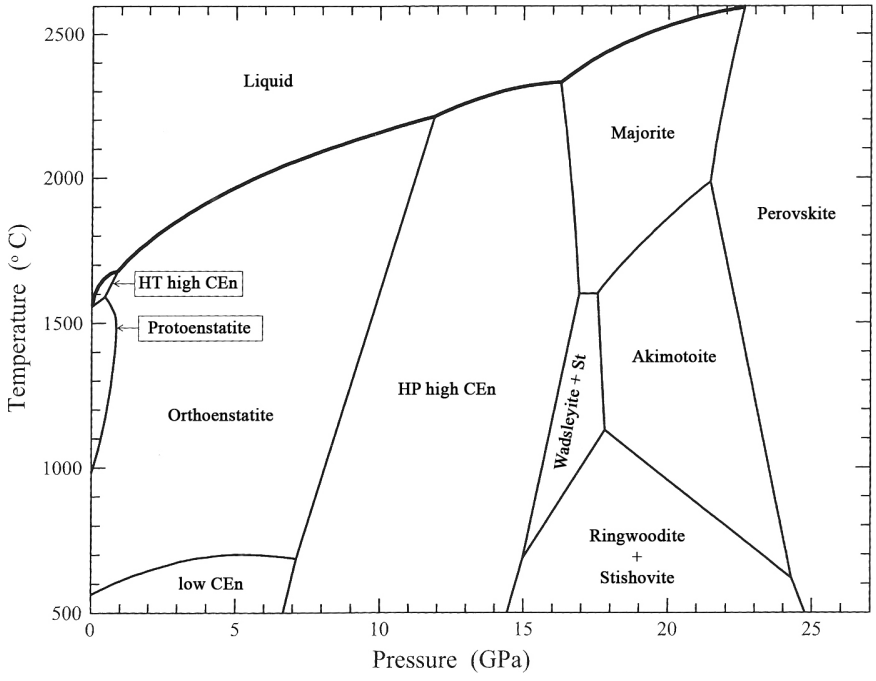

Figure 6.1: The phase diagram of $MgSiO_3$ at the condition of Earth's upper mantle showing the stability of the different enstatite polymorphs, after Gasparik 2003.

Table 6.1 : Chemical composition of the Tanzania enstatite, after Rauch (2000)

Oxide	Wt. %
SiO_2	58.10
FeO	2.00
MgO	38.50
Al_2O_3	1.50
MnO	0.10
CaO	0.15
Na_2O	0.01
Total	*100.35*
Fe^{3+}/Fe_{tot}	23%

very limited stability field, the substitution of Mg by Fe expands the stability field of HT high clinoenstatite significantly (Arlt et al. 1998). Previous studies have shown that both high clinoenstatite polymorphs are not quenchable and transform back to the $P2_1/c$ low enstatite polymorph upon return to room conditions (Kanzaki 1991, Arlt et al. 1998). For the sake of simplicity in the rest of this chapter, when high clinoenstatite is mentioned, the high pressure form of high clinoenstatite is meant.

As argued in chapter 5, slow diffusion kinetics of the majorite component in garnet hampers the dissolution of pyroxene in garnet in the cold subducted slab. Therefore the pyroxene component in the subducted slab can be viewed as a (semi-)isolated system. Experimental studies (Irifune et al. 1986; Irifune 1987) have shown that the amount of aluminium that can be dissolved in pyroxene decreases with increasing pressure. As a result of this, garnet will be exsolved from pyroxene while the slab is subducted into the mantle. The rate at which this will occur in pyroxene will be controlled by the diffusivity of aluminium in high clinoenstatite at enhanced pressures, for which there are currently no data available. For pyroxene exsolutions in garnet it has been shown that there is a topotactic relationship between the garnet host and the pyroxene exsolutions (Spengler 2006). However, the topotactic relation between pyroxene and exsolved garnet at high pressure, i.e. in the Earth's transition zone, where pyroxene has a monoclinic structure (high clinoenstatite C2/c) is unknown at present. Therefore, experiments on natural aluminous enstatite have been conducted to investigate what happens to orthopyroxene that is present in the subducted slab when it is transported into the mantle. Experiments were conducted in the presence of garnet, to closer simulate what occurs in the Earth during subduction.

6.2 Experimental setup

Experiments have been conducted in a 1000-ton multi-anvil device at the Bayerisches Geoinstitut, using a 14 / 8 pressure cell, indicating the octahedron edge length and the truncation edge length of the tungsten-carbide anvils in millimetres, respectively. The pressure cells were MgO octahedra with a central hole into which sample and a $LaCrO_3$ stepped furnace was placed, for a more detailed description see chapter 3 on experimental methods. The length of the platinum capsules was 2.4 mm, the diameter 1.6 mm and the wall thickness 0.2 mm. Temperature was measured by W3%Re – W25%Re thermocouples with a junction just on top of the capsule. The thermocouple wires were isolated from the capsules by a 25 µm rhenium disc to prevent platinum from intruding into the thermocouple tubes. The starting materials were couples of single crystal mirror polished Dora Maira pyrope and Tanzania enstatite cylinders. The Dora Maira pyrope crystals were the same as used in the diffusion experiments described in chapter 5. The chemical composition (see table 6.1) of the Tanzania enstatite crystals were determined by electron microprobe and correspond to those determined by

Table 6.2: Run conditions of the experiments

Run number	Pressure	Temperature	Duration
H2975	15 GPa	1700 °C	19 h
S4378	15 GPa	1700 °C	19 h
S4391	15 GPa	1700 °C	1h

Rauch (2000).

The experiments were conducted at 1700 °C and 15 GPa, with run durations between 1 hour and 19 hours, the conditions are listed in table 6.2. After the end of the run the sample was quenched by cutting of the power, resulting in a temperature drop in 10 seconds to roughly 100 °C.

6.3 Analytical setup

After recovery of the samples the capsule were cut by a diamond wire saw along the length of the capsule and mounted in an epoxy block, polished and further prepared for analyses by electron microprobe and SEM. The chemical compositions of the samples were measured by means of an electron microprobe, using 20 s counting time for the peak position and 10 s counting time for the background position, 15 kV acceleration voltage and 15 nA beam current. The standards and characteristic x-ray peaks used to determine the chemical composition are listed in table 6.3.

Two experiments, H2975 and S4378, were also prepared for further examination by TEM. The TEM samples were first polished down to a thickness of 30 µm, after which a molybdenum mesh with a square size of 135 µm was glued upon them using Araldite epoxy glue. The crystalbond glue between the sample and the glass slide which was used for polishing down the sample to 30 µm was then dissolved by acetone. The sample was then Ar-ion milled to electron transparency in a Gatan Duomill 600, under an angle of 14 ° at 4.5 kV and 1.0 A. Microstructural characterization and determination of topotactic relations between the (clino-)enstatite host and the garnet exsolutions were performed using a Philips CM20 FEG TEM operating at an acceleration voltage of 200 kV.

Table 6.3 : Electron microprobe standards & peaks

Element	Standard	Characteristic peak
Mg	Forsterite	MgKα
Fe	Metallic iron	FeKα
Ca	Diopside	CaKα
Al	Pyrope	AlKα
Mn	$MnTiO_3$	MnKα
Si	Forsterite	SiKα
Ti	Rutile	TiKα

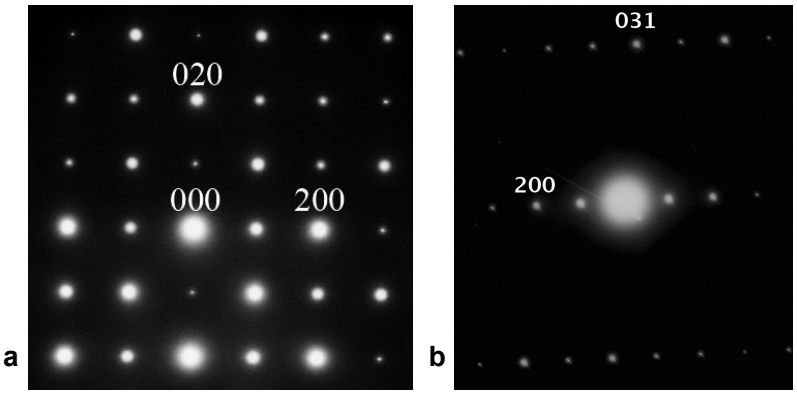

Figure 6.2: Diffraction patterns of the recovered low clinoenstatite sample that show it is the low clinoenstatite polymorph (see text). a) Diffraction pattern down the [001] direction in low clinoenstatite and b) down the <013> direction.

6.4 Results

6.4.1 Determination of the enstatite polymorph

As explained, enstatite has several polymorphs and therefore is important to determine for which polymorph the topotactic relationship between the enstatite host and majoritic garnet was determined. The polymorphs that were considered are orthoenstatite (Pbca), protoenstatite (Pbcn), low clinoenstatite ($P2_1/c$), and high clinoenstatite (C2/c). The systematic presence (fig. 6.2a) of 100 reflections in the [001] zone axis pattern indicate that it cannot be either the protoenstatite or high clinoenstatite polymorph. From the geometry of the zone axis pattern it can also be excluded that the *h*00 reflections are caused by double diffraction. Figure 6.2b shows the diffraction pattern taken down the <013> zone axis. The spacing of the *h*31 reflections indicates that the d-spacing of the 100 planes is ± 9.2 Å. This d-spacing excludes the possibility that the investigated enstatite crystal is the orthoenstatite polymorph (where the d-spacing is 18.2 Å) and thus needs to be the low clinoenstatite polymorph.

6.4.2 Microstructure

Figure 6.3 shows a backscattered electron (BSE) image of the enstatite part of the sample of experiment H2975. The enstatite part contains a high density of garnet precipates with a The exsolved grains of majoritic garnet show a clear arrangement relative to the host pyroxene, the long axis of the precipitates are parallel to the (100) planes of the pyroxene host. The left side of the picture shows recrystallized grains of clinoenstatite that

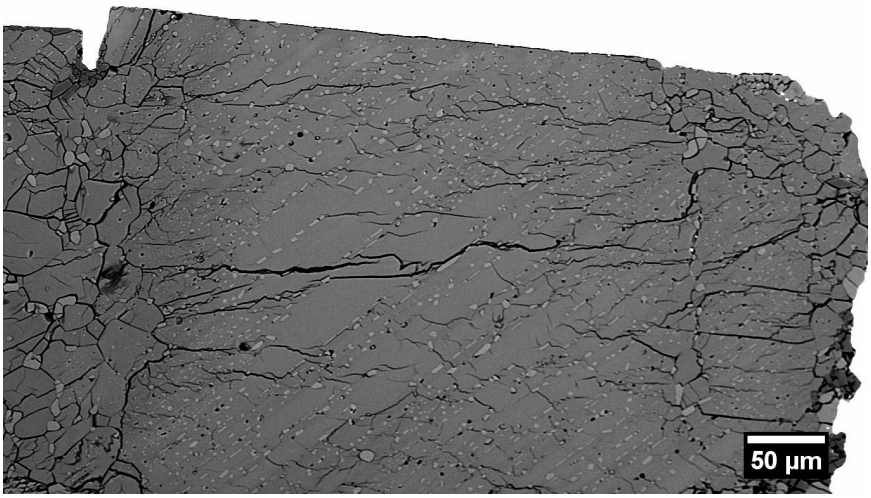

Figure 6.3: BSE image of the low clinoenstatite part of experiment H2975. The shape preferred orientation of the garnet precipitates in the undeformed single crystal part (center) is clearly visible. On the left the deformed part is visible. The middle gray phase is low clinoenstatite, the light gray phase majoritic garnet and the dark gray phase is stishovite.

Table 6.4:Composition of the exsolved majoritic garnet precipitates.

Oxide	**Wt%**
MgO	34.80
CaO	0.24
FeO	1.65
Al_2O_3	9.83
SiO_2	53.66
Total	*100.18*
Component	**Fraction**
Majorite	0.610
Pyrope	0.352
Almandine	0.032
Grossular	0.007

probably formed due to the indentation of the thermocouple. The composition of the majoritic garnet precipitates are listed in table 6.4. The component fractions are calculated using the method explained in chapter 5. The precipitates have a high majorite component (± 61 %), which is slightly higher than the equilibrium composition in the $Mg_3Al_2Si_3O_{12}$ – $Mg_4Si_4O_{12}$ system at the experimental conditions (chapter 2), based on data from Gasparik (2003). The thickness of the majoritic garnet layer that formed at the garnet – enstatite interface was generally thin (< 3 µm for the 19 hour experiments and absent within the resolution of the microprobe for the 1 hour experiment). This agrees well with the low majorite diffusivity in garnet that was determined from majoritic garnet – pyrope diffusion couples and of which the results are presented in chapter 5.

The recovered sample of run H2975 has been investigated in detail by TEM. Figure 6.4 shows a dark field (DF) image obtained using g = $\bar{6}\,\bar{1}3$ as diffraction vector. Twinning on the (100) mirror planes is pervasive in the sample, and is indicated by the short white arrows. Next to twinning, one can also observe stacking faults parallel to the twin plane throughout the sample (figure 6.4 and 6.5).

Figure 6.5a shows a DF image using g = 021 as diffraction vector, demonstrating again the pervasive nature of the stacking faults in this sample. The corresponding HRTEM image in an a^*-b projection (* denoting the reciprocal direction) of clinoenstatite shows a single stacking fault (fig. 6.5b). From this HRTEM image one can deduce that the displacement vector across the stacking fault is **R** = <½ ½ w>, the exact components can be

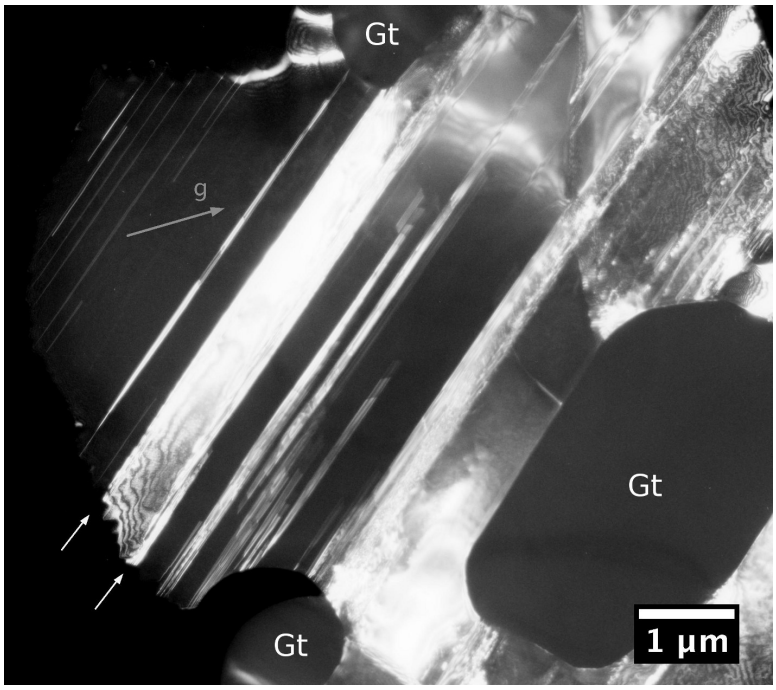

Figure 6.4: DF TEM image of twins (and stacking faults) parallel to (100) in clinoenstatite in experiment H2975. Two twin planes are indicated by the white arrows. The diffraction vector (g = $\bar{6}\,\bar{1}\,3$) is indicated by the light gray arrow. The garnet precipitates are indicated by Gt. As can be seen, the large precipitate on the right has its long axis (semi-)parallel to the twin planes and stacking faults in low clinoenstatite.

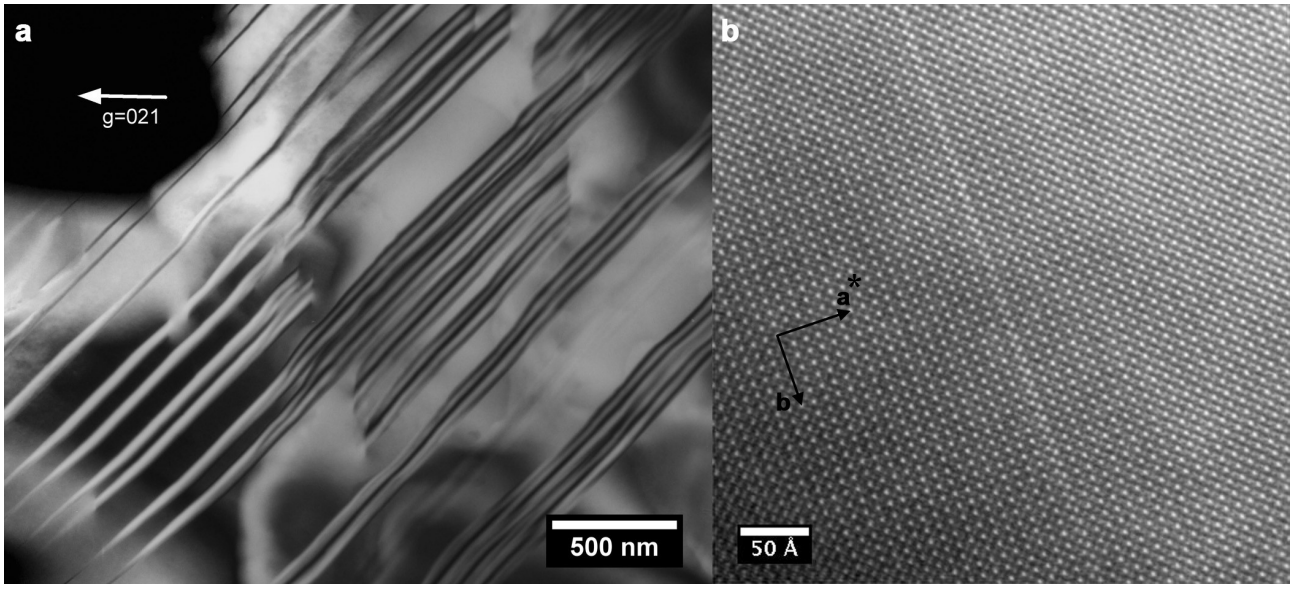

Figure 6.5: A more detailed view of the stacking faults in low clinoenstatite. a) A DF TEM image of the stacking faults, using g = 021 as diffraction vector. b) A HRTEM image of a single stacking fault, showing that the displacement vector is **R** = < ½ ½ w>.

determined from the fact that there is no offset of the spots across the stacking fault when looking in the <1*10> directions. The c-component was not determined in this study, but is required to be greater than zero. This is because if the c-component would be zero, the stacking fault would be out of contrast when using g = 021 as diffraction condition.

6.4.3 Majoritic garnet precipitates

As figure 6.3 shows, most of the majoritic garnet precipitates grew at high pressure during the experiments along predefined planes in the high clino-enstatite host. Further scrutinization by TEM showed that the precipitates grew with their long axes, in the case that there is a clear long axis visible, parallel to the (100) planes of the clino-enstatite host (figure 6.7). The typical spacing between the garnet precipitates is 5 – 20 µm for experiment H2975, though it varies with position. Experiment S4391 (figure 6.6) was run at the same conditions as H2975, but only for one hour. As expected the garnet precipitates are much smaller than in H2975,

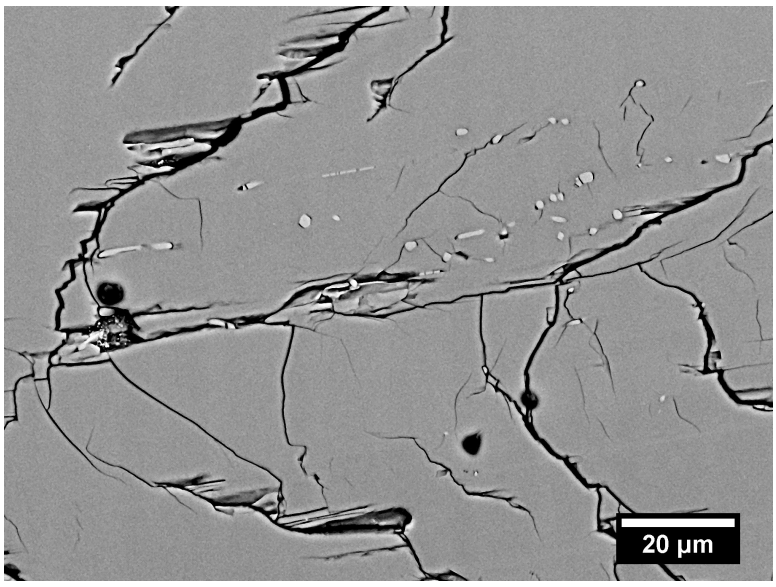

Figure 6.6: BSE image of garnet precipitates in experiment S4391, run for 1 hour. This image shows that the garnet precipitates start to nucleate within the first hour of the experiment. The size of the garnet precipitates is also significantly smaller than those from the longer experiments.

Figure 6.7: BF TEM images showing the orientation relationship between low clinoenstatite and the majoritic garnet precipitates. The insets of the diffraction patterns show the orientation of the reciprocal lattice with respect of the picture for the particular phase, the superimposed diffraction patterns show the relation between both phases on their interface. Diffraction patterns are taken on the approximate position of the insets. Zone axes of the diffraction patterns are: a) low clinoenstatite down [001] axis, garnet down the <111> zone axis. Garnet 110 reflection is coincident with low clinoestatite 010 reflection. b) Low clinoenstatite down the [001] zone axis, garnet down the <111> zone axis. Rotation of garnet grain with respect to figure a is ± 10°. c) Low clinoenstatite down the [001] zone axis, garnet down the <121> zone axis. Garnet 110 reflection nearly coincides with 110 of clinoenstatite.

however it shows that the first garnet precipitates start to form within the first hour of the experiment. There are however regions where there is a lack of garnet precipitates, mainly towards the end of the capsule. This might be caused by temperature gradients within the capsule. In this particular sample the spacing between the garnet precipitates was between 5 – 10 µm in the regions where garnet precipitates are present.

Diffraction patterns of the clinoenstatite host and garnet precipitates have been collected to determine the orientation relationship between the two phases. Figure 6.7 shows BF images of garnet precipitates in clinoenstatite with insets of the diffraction patterns. As can be seen from the diffraction patterns in figure 6.7a, the [001] zone axis of enstatite is parallel to the [111] zone axis of the garnet precipitate and the 110 reflection (d = 8.1 Å) of garnet nearly coincides with the 010 (d = 8.6 Å) reflection of clinoenstatite. Figure 6.7b shows the topotactic relation of another garnet precipitate to the clinoenstatite host. Again the <111> zone axis of garnet is parallel to the [001] zone axis of clinoenstatite, however the garnet grain is rotated around the <111> zone axis by 10° clock wise relative to figure 6.7a and the clinoenstatite host, which has the same orientation in both

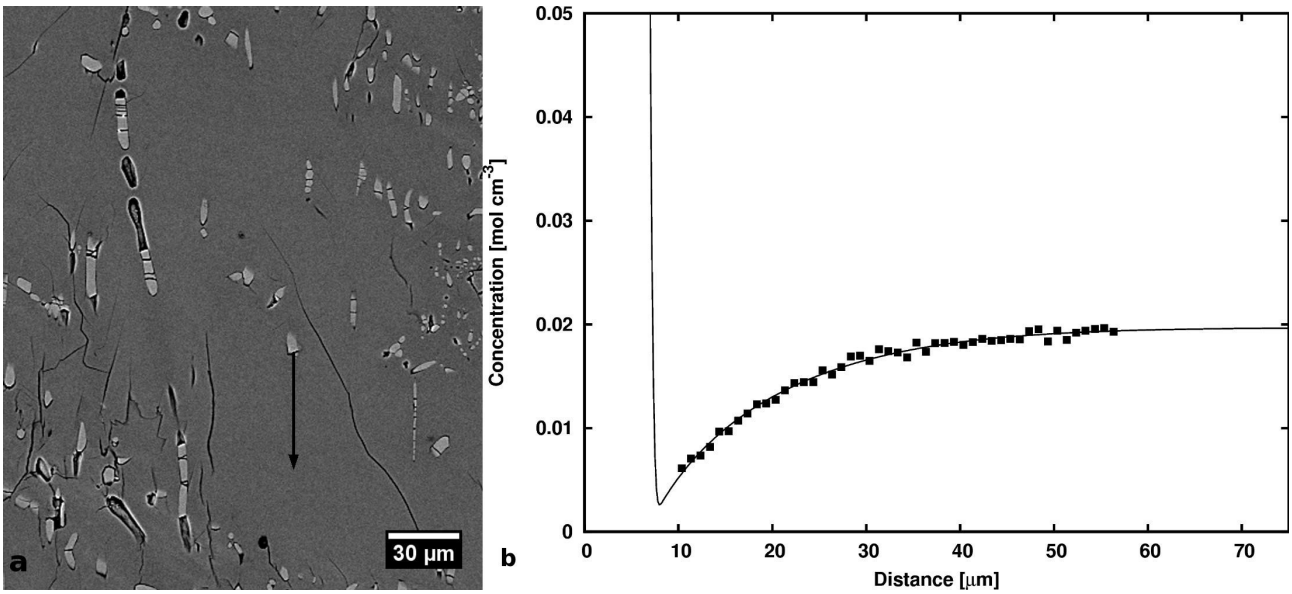

Figure 6.8: Location of the diffusion profile (black arrow) and the measured aluminium concentration profile expressed in mol cm^{-3} (b). The solid line in b is the fitted profile, the vertical line around 7 µm corresponds to the boundary between the garnet precipitate and the low clinoenstatite host.

figures. Although the dominant topotactic relationship between the clinoenstatite host and the majoritic garnet is the one depicted in figures 6.7a-b, i.e. <111> of garnet parallel to [001] of clinoenstatite, also some garnet precipitates were observed which had a different relation to the clinoenstatite host. Figure 6.7c shows such a garnet precipitate, where the <121> zone axis of garnet is parallel to the [001] zone axis of clinoenstatite. In this case the 110 reflection of garnet nearly coincides with the 110 (d = 6.3 Å) reflection of enstatite. However, the topotactic relation determined in figure 6.7a-b is the most dominant found in the samples that have been examined by TEM. Experiment S4391

6.4.4 Diffusion of Al in high clinoenstatite

In the recovered sample from experiment S4378 several diffusion profiles were measured around the garnet precipitates. Figure 6.8 shows the location and the longest diffusion profile that has been measured with the electron microprobe. The measured diffusion profile has been fitted using a numerical finite difference model, to determine the diffusivity of Al in high clinoenstatite at the experimental conditions (15 GPa and 1700 °C). The numerical model assumed cylindrical symmetrical diffusion of Al in the high clinoenstatite host and growth of the garnet precipitate, which is controlled by the diffusion of Al across the precipitate – host interface. A more detailed description of the program is given in section 4.2. The calculated diffusion profiles have been convoluted with a Gaussian function with a FWHM of 1.0 µm to account for the finite size of the activation volume for electron microprobe analyses. The crystallographic direction of the diffusion profile was determined by TEM by orienting diffraction patterns relative to known features in the BSE image of figure 6.8. Fitting of the measured profile gives a diffusivity for Al in high clinoenstatite along the $[\bar{1}01]^*$ (i.e., $[\bar{1}01]$ direction in reciprocal space) direction of 6×10^{-11} cm^2 s^{-1}. This value is 3-4 orders of magnitude faster than the diffusivity of the majorite component in garnet at the same conditions.

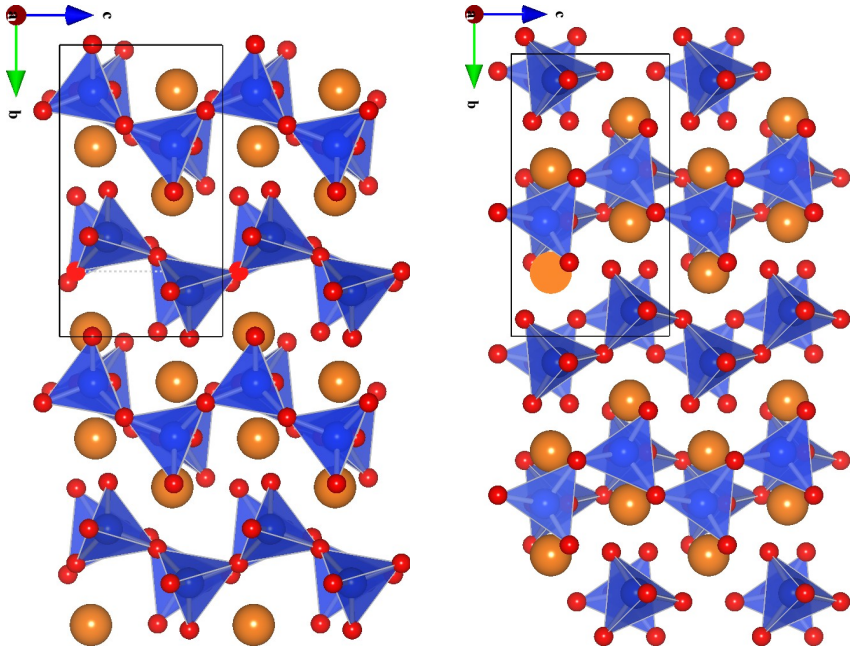

Figure 6.9: The crystal structure of a) low clinoenstatite and b) high clinoenstatite viewed down the [100] direction. Blue tetrahedra are silica tetrahedra, large spheres in between the tetrahedra are Mg cations and small spheres are oxygen. Note the difference in rotation of tetrahedra related by the vector ½ <111> between both structures.

6.5 Discussion

6.5.1 Pyroxene microstructure

In the recovered sample studied by TEM (H2975) twinning and stacking faults parallel to (100) in low clinoenstatite were pervasive. The twinning may have been caused by the transition from the low pressure orthorhombic phase (Pbca space group) to the high pressure monoclinic phase (C2/C space group), which is the stable enstatite polymorph at pressures above ± 10 GPa at the 1700 °C (Kanzaki 1991, Angel et al. 1992). Furthermore, it is also possible that the stacking faults were the result of the C2/C to $P2_1/c$ phase transition in clinoenstatite during decompression, since the C2/c phase of clinoenstatite is non quenchable and transforms back to $P2_1/c$ during decompression (Angel et al. 1992). Thomson and Downs (2003) showed that the C2/c and $P2_1/c$ phases of clinoenstatite have a different oxygen stacking sequence, which can be the cause of the appearance of stacking faults during the transformation between both phases.

The displacement vector across the stacking faults was determined to be **R** = <½ ½ w>.Though it was not possible to determine the exact value of *w* from the electron photographs directly, one can make an educated guess based on geometrical considerations. The distance between two silicon tetrahedra in along the silica chains is c/2. If the stacking fault plane would run through the silica tetrahedra parallel to (100) any c-component other than ½ would cause a severe distortion of the silica tetrahedra. A zero c-component would in addition not cause a stacking fault. A similar argument can be held in the case the fault alone would run in between the tetrahedral and octahedral layers as well as when it would run through the octahedral layers. The displacement vector should thus be **R** = ½ <111>. A closer look at the rotations of the individual silica tetrahedra in the silica chains shows how such displacement vector can be produced when going from high clinoenstatite to low clinoenstatite (figure 6.9). In the low clinoenstatite form the silica tetrahedra related to each other by the ½ <111> lattice vector have an opposite rotation, i.e. the triangular base of the tetrahedron point in opposite directions. For the high clinoenstatite form the silica tetrahedra related by the same vector have the same

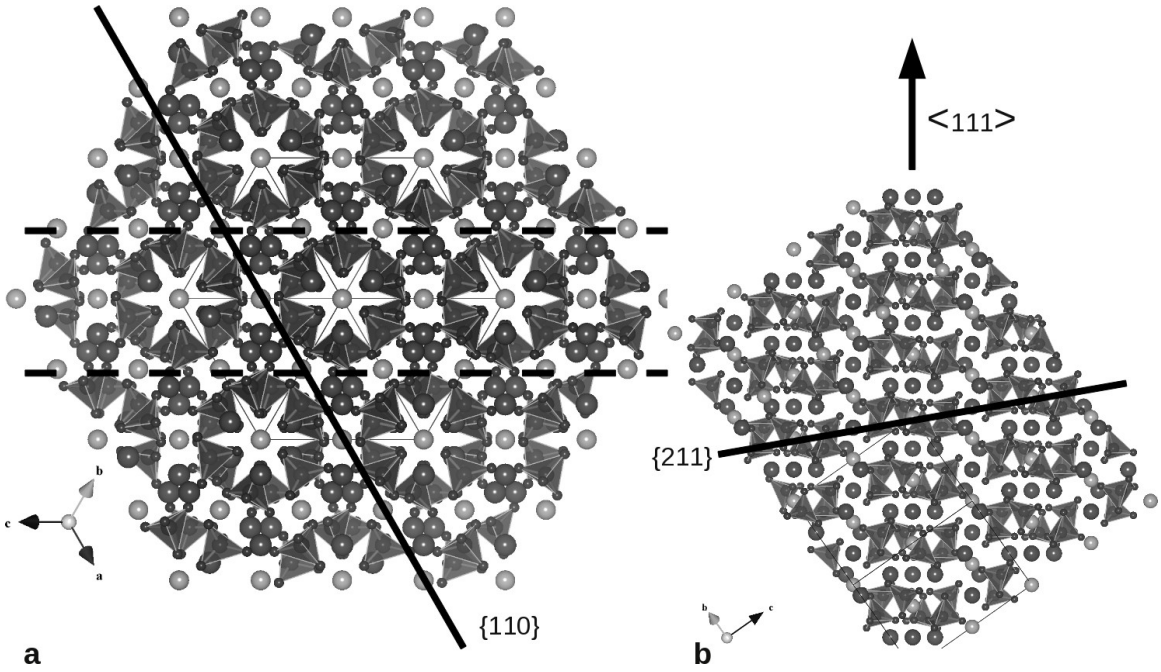

Figure 6.10: Projections of the garnet (pyrope) model down the <111> direction (a) and <110> direction (b).Small dark gray spheres are oxygen atoms, big dark gray spheres magnesium atoms, light gray atoms spheres aluminium atoms and the tetrahedra are silica tetrahedra. Figure b is a projection of a single row of silica tetrahedra tubular columns between two parallel {110} planes, indicated in figure a by the dashed lines. Every tubular column in b has an offset of 1/3 of a tetrahedral plus octahedral layer (i.e. 1/12 <111>) from its neighbouring column.

rotation. Introducing a stacking fault on (100) with displacement vector ½ <111> in the low clinoenstatite structure will thus result in the tetrahedra being related by the ½ <111> vector across the stacking having the same rotation, i.e. adding a high clinoenstatite layer in between the low clinoenstatite layers.

Several studies have addressed planar defects in pyroxenes, mostly related to deformation studies of pyroxene at relatively low pressures. Coe and Kirby (1975) determined a displacement vector of **R** =0.83[001] for stacking faults on (100) in experimentally deformed orthopyroxenes. Steuten and Van Roermund (1989) determined a displacement vector of **R** = ¼ [001] for stacking faults on (100) in a naturally deformed orthopyroxene. Both stacking faults in these studies are produced by the dissociation of **b** = [001] Burgers vectors. Van Duysen et al. (1985) conducted an indentation experiment on orthopyroxene at ambient conditions and found that dislocations with **b** = [001] Burgers vector dissociate into 4 partial dislocations, producing stacking faults on (100) with displacement vectors $\mathbf{R_1}$ = [0, β, γ], $\mathbf{R_2}$ = [0, ν, ½] and $\mathbf{R_3}$ = [0, -β-ν, ½-γ] with β = 0, ν = $^1/_6$ and ¼ < γ < $^1/_3$ based upon a FCC structural model for the sublattices. Skrotzki (1994) found in naturally deformed orthoenstatite stacking faults on (100) with displacement vectors **R** = 0.83 [001], **R** = ½ <101> and **R** = ¼ <121>, producing clinoenstatite and (partial) protoenstatite lamellae in orthoenstatite. In clinopyroxenes he describes stacking faults on (010), forming amphibole type chain multiplicity faults by the dissociation of [001] perfect dislocations into ½ <01w> (w ≠ 1), and stacking faults on {110} by the dissociation of <111> dislocations into ½ <111> partials. Clearly, none of these studies find a combination of stacking fault plane and displacement vector as in this study. Iijima and Buseck (1975) did a study on low clinoenstatite obtained by direct quenching

after bringing orthoenstatite either into the high temperature clinoenstatite or protoenstatite fields. They observe similar stacking faults and twins as observed in this study, and from HRTEM images they determined the b-component of the stacking fault vector to be ½ b, and interpreted this as the b-glide component of twinning in low clinoenstatite and across the twin plane there is an additional 4.5 Å layer, which is equal to an a/2 offset across the twin plane. The displacement over the composition plane can thus also be described by a < ½ ½ w> displacement vector. They however did not attempt to determine whether there was a c-component too in the displacement across the stacking fault. Having a look at the high temperature high clinoenstatite structure however shows that it cannot be precluded that the same line of arguments as with the high pressure high clinoenstatite structure can be used and that the displacement vector across the composition plane of the 'clinoenstatite twins' is ½ <111>. Comparing the high clinoenstatite structure to the orthoenstatite structure shows that the tetrahedra related to each other by the ½ <111> vector have the same rotation in both structures. Therefore it is considered more probable that the stacking faults formed during the high clinoenstatite to low clinoenstatite phase transformation than from the orthoenstatite to high clinoenstatite transformation in our experiments.

Though most of the stacking faults are not overgrown by garnet precipitates, some of them are. So at least some of the stacking faults must have grown before garnet started to precipitate. Many of the garnet precipitates have overgrown twin boundaries, indicating that the twins, like some of the stacking faults, also formed during compression or the initial stages of heating. The twin boundaries, and stacking faults to a lesser extent, thus appear to have played a significant role in the exsolution of garnet from enstatite. This can also be concluded from the fact that most garnet precipitates have their long axis parallel to the (100) plane of clinoenstatite, i.e. the twinning and stacking fault plane. Previous studies have shown that nucleation of new phases often occur heterogeneously on pre-existing defects in grains, which lowers the activation energy for nucleation (Putnis 1992, Kerschhofer et al. 2000), which can explain the preference of garnet nucleating on twin boundaries or stacking faults.

6.5.2 Garnet precipitates

A unique topotactic relationship between the garnet precipitate and the clinoenstatite host is not observed. The lack of an oxygen close packing direction in garnet may be the reason that there is no such topotactic relationship between garnet and the low clinoenstatite host. It was however observed that the dominant topotactic feature was that the <111> direction in garnet is parallel to the [001] direction in clinoenstatite. Comparing the length of the clino-enstatite c lattice parameter (c = 4.9 Å) to that of the unit cell body diagonal length of garnet (19.8 Å) shows that the latter one is almost exactly four times as long. Figure 6.10a shows a structural model of garnet down its <111> zone axis. The silicon tetrahedra form tubular columns down the <111> direction with octahedral sites in the centre of them. The columns of silica tetrahedra are interconnected by octahedra. The silica tabular columns themselves are made up of layers of silica tetrahedra with their apices pointing inward toward the central octahedral site and layers of dodecahedral site (see figure 6.10b) between the tetrahedral layers. The layering in a single tubular column is parallel to {111}, however the layering in a

complete crystal is parallel to {211} since every tubular column is shifted relative to a neighbouring tubular column by 1/3 of the tetrahedra plus octahedra layer thickness. In the view down the <111> direction the space between the tubular columns forms channels parallel to {110}. Though the structures of pyroxene and garnet are vastly different, silica tetrahedra also form a linear structure in garnet structure down the <111> direction. For the transformation from pyroxene to garnet, the chains of silica tetrahedra down the c-axis in pyroxene need to be broken into isolated silica tetrahedra. The distance over which the silica tetrahedra need to be diffused (or translated and rotated) may thus be minimal when the new garnet crystal forms with its <111> direction down the original c-axis of high clinoenstatite. The topotactic relationship would in this case thus not be controlled by minimization of the strain energy on the interface between both phases, but by the diffusion kinetics of silicon, because silicon is usually the slowest diffusing species.

6.5.3 Aluminium diffusivity in clinoenstatite

The diffusion in high clinoenstatite down the $[\bar{1}01]^*$direction was determined to be 6×10^{-11} cm^2 s^{-1} at 15 GPa and 1700 °C, which is 3 – 4 orders of magnitude faster than the diffusion of the majorite component in garnet. The reported diffusivity is a lower limit, since the exact time required before a majoritic nucleus formed is unknown. However, the measured profile used in the fit model was the longest that was found in the sample and thus probably also corresponds to one of the nucleus that formed first during the experiment. The region around the measured precipitate is relatively devoid of other precipitates, which also indicates that the precipitate from which the profile was measured nucleated during an early stage of the experiment. Experiment S4391 (figure 6.6) was run at the same conditions, but only for 1 hour. The presence of garnet precipitates in this experiment indicate the first precipitates nucleate within the first hour. Since the run duration of experiment S4378 was 19 hours, it is thought that the error due to the uncertainty about the exact time of nucleation of the precipitates is not significant.

To project the diffusion coefficients to subduction zone conditions one needs the activation energy for diffusion of aluminium in pyroxene (or ideally high clinoenstatite). There is, however, a general lack of diffusion data on aluminium in minerals in the literature, the only data on aluminium diffusion in diopside is by Sautter et al. (1988) and Jaoul et al. (1991) over a limited temperature range between 1000 – 1180 °C at 1 bar. They obtain an activation energy of 273 kJ mol^{-1}. The activation enthalpy, describing the temperature dependence, for diffusion of aluminium in high clinoenstatite will probably be higher, since the experiments in this study were conducted at a pressure of 15 GPa. Therefore a typical range of activation enthalpies have been assumed, i.e. between 275 kJ mol^{-1} and 350 kJ mol^{-1}, corresponding to an activation volume for the diffusion of aluminium in clinoenstatite between 0 – 5 cm^3 mol^{-1}. For the upper part of the subducting slab at a temperature of 1000 °C (Emmerson and McKenzie 2007), corresponding to the subducted oceanic crust, it gives an aluminium diffusion coefficient in the range of 5×10^{-16} cm^2 s^{-1} to 6×10^{-15} cm^2 s^{-1}. For the middle to lower part of the subducting slab at 1400 °C (Emmerson and McKenzie 2007), corresponding to the subducted mantle lithosphere, the range is smaller due to a smaller temperature difference between the extrapolated temperature and the experimental condition, and is in the range between 3×10^{-12} cm^2 s^{-1} and 4×10^{-12} cm^2 s^{-1}. Again this shows that diffusion of aluminium in

high clinoenstatite (in the $[\bar{1}01]^*$ direction) is significantly faster than the diffusion of the majorite component in garnet, i.e. 3 – 4 orders of magnitude slower. Since the distance over which a component can diffuse can be approximated by $x = \sqrt{(Dt)}$, with t the time for which the component is allowed to diffuse, one can calculate the distance over which aluminium can diffuse in pyroxene. At 1000 °C and 10 Myr, which is a typical time scale for subduction (see chapter 5), this is between 0.5 – 1.5 cm and at 1400 °C between 20 – 30 cm. If grain boundary diffusion plays a significant role, the values will be a factor 100 larger, i.e. at the meter scale at 1000 °C and at the decameter scale at 1400 °C.

Comparing the absolute values of the diffusion study by Jaoul et al. (1991) to the data presented in this study shows that our data is significantly faster, Jaoul et al. obtained a diffusivity of 3.7 x 10-17 $cm^2\ s^{-1}$ at 1180 °C at 1 bar and our study 6 x 10^{-11} $cm^2\ s^{-1}$ at 1700 °C. This would correspond to an activation energy for diffusion of aluminium in clinopyroxene of 655 kJ mol^{-1} (when the effect of pressure is neglected), which is anomalously high, or when using their activation energy for Al diffusion this corresponds to an activation volume for diffusion of aluminium in clinopyroxene of -25 $cm^3\ mol^{-1}$, which would mean that with increasing pressure diffusion would become faster. From this it can be concluded that there is a large difference in diffusivity between that of aluminium in HP clinoenstatite at high pressure and that of aluminium diffusion in diopside at low pressure, which possibly can be attributed to different diffusion mechanism in both clinopyroxene phases at the different conditions or a strong dependence of the diffusivity of aluminium in clinopyroxene on the calcium content.

6.6 Conclusions

- Twins and stacking faults on (100) are pervasive throughout the enstatite sample after quenching and decompression from 15 GPa and 1700 °C. The displacement vector across the stacking fault boundary was determined to be <½ ½ w>, most likely being ½ <111>. This displacement vector can be explained be the transformation of high clinoenstatite to low clinoenstatite.
- The twin boundaries and stacking faults that formed in high clinoenstatite parallel to the (100) planes during the transition from Pbca orthorombic to the C2/c high pressure phase seem to have acted as nucleation sites for majoritic garnet precipitates.
- In the case that there was a well defined long axis of the garnet precipitate in the observed TEM section, this long axis was predominantly oriented parallel to (100) and the twin planes / stacking faults in low clinoenstatite.
- There is no unique topotactic relationship between the low clinoenstatite host and the majoritic garnet precipitates. However, a dominant linear relationship was found with the <111> direction in garnet being parallel to the [001] direction in low clinoenstatite. This direction is probably controlled by the diffusivity of silicon in pyroxene and not by minimization of strain energy at the interface between the clinoenstatite host and majoritic garnet precipitates. The latter is probably due to the absence of a well defined oxygen close packing direction in garnet.

- The diffusivity of aluminium in C2/c HP-clinoenstatite in the $[\bar{1}01]^*$ direction at 15 GPa and 1700 °C was determined to be at least 6 x 10^{-11} cm^2 s^{-1}, which is 3 – 4 orders of magnitude faster than the diffusivity of the majorite component in garnet at the same conditions.
- There is a large difference in the diffusivity of aluminium in clinopyroxene at high pressure and the diffusivity of aluminium in clinopyroxene at room pressure, which eventually indicates a change in diffusion mechanism with pressure or a strong dependence of the diffusivity of aluminium on calcium content in clinopyroxene.

6.7 References

Angel, R.J., Chopelas, A., Ross, N.L. (1992), Stability of high-density clinoenstatite at upper-mantle pressures. Nature 358:322-324. doi: 10.1038/358322a0

Arlt, T., Angel, R.J., Miletich, R., Armbruster, T., Peters, T. (1998), High-pressure $P2_1/c$-$C2/c$ phase transitions in clinopyroxenes; influence of cation size and electronic structure. Am Mineral 83:1176-1181

Coe, R.S., Kirby, S.H. (1975), The orthoenstatite to clinoenstatite transformation by shearing and reversion by annealing: Mechanism and potential applications. Contrib Mineral Petrol 52:29-55. doi: 10.1007/BF00378000

Duysen, J.C. Van, Doukhan, N., Doukhan, J.C. (1985), Transmission electron microscope study of dislocations in orthopyroxene $(Mg, Fe)_2Si_2O_6$. Phys Chem Miner 12:39-44

Emmerson, B., McKenzie, D. (2007), Thermal structure and seismicity of subducting lithosphere. Phys Earth Planet Inter 163:191-208. doi: 10.1016/j.pepi.2007.05.007

Ganguly, J., Ghose, S. (1979), Aluminous orthopyroxene: Order-disorder, thermodynamic properties, and petrologic implications. Contrib Mineral Petrol 69:375-385. doi: 10.1007/BF00372263

Gasparik, T. (2003), Phase diagrams for geoscientists: an atlas of the earth's interior. Springer, Heidelberg-Berlin

Gasparik, T., Lindsley, D.H. (1980), Phase equilibria at high pressure of pyroxenes containing monovalent and trivalent ions. in: Prewitt C.T.(ed.) Reviews in Mineralogy and Geochemistry, pp. 309-339

Iijima, S., Buseck, P.R. (1975), High Resolution Microscopy of Enstatite I: Twinning, Polymorphism, and Polytypism. Am Mineral 60:758 - 771

Irifune, T. (1987), An experimental investigation of the pyroxene-garnet transformation in a pyrolite composition and its bearing on the constitution of the mantle. Phys Earth Planet Inter 45:324-336. doi: 10.1016/0031-9201(87)90040-9

Irifune, T., Sekine, T., Ringwood, A.E., Hibberson, W.O. (1986), The eclogite-garnetite transformation at high pressure and some geophysical implications. Earth Planet Sci Lett 77:245-256. doi: 10.1016/0012-821X(86)90165-2

Jaoul, O., Sautter, V., Abel, F. (1991), Nuclear Microanalyses: A Tool for Measuring Low Atomic Diffusivity. in: Ganguly J.(ed.) Diffusion, Atomic Ordering and Mass Transport, Advances in Physical Geochemistry 8, Springer-Verlag, Heidelberg-Berlin, pp. 198-220

Kanzaki, M. (1991), Ortho/clinoenstatite transition. Phys Chem Minerals 17:726-730. doi: 10.1007/BF00202244

Kerschhofer, L., Rubie, D.C., Sharp, T.G., McConnell, J.D.C., Dupas-Bruzek, C. (2000), Kinetics of intracrystalline olivine-ringwoodite transformation. Phys Earth Planet Inter 121:59-76. doi: 10.1016/S0031-9201(00)00160-6

Okamura, F.P., Ghose, S., Ohashi, H. (1974), Structure and Crystal Chemistry of Calcium Tschermak's Pyroxene,

$CaAlAlSiO_6$. Am Mineral 59:549 - 557

Putnis, A. (1992), An Introduction to Mineral Sciences. Cambridge University Press, Cambridge

Rauch, M. (2000), Der Einbau von Wasser in Pyroxene.

Sautter, V., Jaoul, O., Abel, F. (1988), Aluminum diffusion in diopside using the $^{27}Al(p,\gamma)^{28}Si$ nuclear reaction: preliminary results. Earth Planet Sci Lett 89:109-114. doi: 10.1016/0012-821X(88)90036-2

Skrotzki, W. (1994), Defect structure and deformation mechanisms in naturally deformed augite and enstatite. Tectonophysics 229:43-68. doi: 10.1016/0040-1951(94)90005-1

Spengler, D. (2006), Origin and Evolution of Deep Upper Mantle Rocks from Western Norway. Utrecht

Steuten, J.M., Roermund, H.L.M. Van (1989), An optical and electron microscopy study of defect structures in naturally deformed orthopyroxene. Tectonophysics 157:331-338. doi: 10.1016/0040-1951(89)90148-0

Thompson, R.M., Downs, R.T. (2003), Model pyroxenes I: Ideal pyroxene topologies. Am Mineral 88:653-666

Ich erkläre hiermit, dass ich die vorliegende Arbeit ohne unzulässige Hilfe Dritter und ohne Benutzung anderer als der angegebenen Hilfmittel angefertigt habe. Die aus fremden Quellen direkt oder indirekt übernommenen Gedanken sind als solch kenntlich gemacht.

Die Arbeit wurde bisher weder im Inland noch im Ausland in gleicher oder ähnlicher Form als Dissertation eingereicht und ist als Ganzes auch noch nicht veröffentlicht.

Ferner erkläre ich hiermit, dass ich nicht bereits anderweitig mit oder ohne Erfolg versucht habe, eine Dissertation einzureichen oder mich der Doktorprüfung zu unterziehen.

Ulm, 29. März 2012

Willem Louis van Mierlo